EXPERIMENTAL INVESTIGATION OF FORCED CONVECTION HEAT

TRANSFER OF NANOFLUIDS IN A MICROCHANNEL USING TEMPERATURE

NANOSENSORS

A Dissertation

by

JIWON YU

Submitted to the Office of Graduate Studies of
Texas A&M University
in partial fulfillment of the requirements for the degree of

DOCTOR OF PHILOSOPHY

Approved by:

Chair of Committee,	Debjyoti Banerjee
Committee Members,	Kalyan Annamalai
	Akhil Datta-Gupta
	Partha Mukherjee
Head of Department,	Jerald Caton

December 2012

Major Subject: Mechanical Engineering

ABSTRACT

Experiments were performed to study forced convective heat transfer of de-ionized water (DI water) and aqueous nanofluids flowing in a microchannel. An array of temperature nanosensors, called "Thin Film Thermocouples (TFT)", was utilized for performing the experimental measurements. TFT arrays were designed (which included design of photomask layout), microfabricated, packaged and assembled for testing with the experimental apparatus. Heat removal rates from the heated surface to the different testing fluids were measured by varying the coolant flow rates, wall temperatures, nanoparticle material, nanoparticle morphology (shape and nanoparticle size) as well as mass concentrations of nanoparticles in the coolants.

Anomalous thermal behavior was observed in the forced convective heat transfer experiments. Precipitation of the nanoparticles on the heat exchanging surface was monitored using Scanning Electron Microscopy (SEM) and Energy Dispersive X-Ray spectroscopy (EDX). Isolated precipitation of nanoparticles is expected to cause formation of "nanofins" leading to enhancement of surface area and thus resulting in enhanced convective heat transfer to the nanofluid coolants. However, excessive precipitation (caused due to the agglomeration of the nanoparticles in the nanofluid coolant) causes scaling (fouling) of the heat exchanging surfaces and thus results in degradation of convective heat transfer. This study shows that the surface morphology plays a crucial role in determining the efficacy of convective heat transfer involving suspensions of nanoparticles in coolants (or nanofluids).

Flow visualization and quantitative estimation of near-wall temperature profiles were performed using quantum dots and fluorescent dyes. This non-contact measurement technique for temperature and flow profiles in microchannels using quantum dots is expected to make pioneering contribution to the field of experimental flow visualization and to the study of micro/nano-scale heat transfer phenomena, particularly for forced convective heat transfer of various coolants, including nanofluids.

Logical extensions of this study were explored and future directions were proposed. Preliminary experiments to demonstrate feasibility showed significant enhancement in the flow boiling heat flux values for nanofluids compared to that of pure solvent (DIW). Based on the novel phenomena observed in this study several other topics for future research were suggested, such as, using Surface Plasmon Resonance (SPR) platforms to monitor precipitation of nanoparticles on microchannel surfaces in real time (e.g., for generating surface isotherms).

DEDICATION

To my beloved family and friends for their endless support

ACKNOWLEDGEMENTS

NOMENCLATURE

c_p	Specific heat (J/kg·K)
$c_{p,bf}$	Specific heat of base fluid (J/kg·K)
$c_{p,nf}$	Specific heat of nanofluids(J/kg·K)
$c_{p,s}$	Specific heat of nanoparticle (J/kg·K)
D_h	Hydraulic diameter (m)
H	Height of a microchannel (m)
h	Convective heat transfer coefficient (W/m²·K)
k	Thermal conductivity (W/m·K)
L	Length of the microchannel (m)
NA	Numerical aperture
Q	Heat energy (W)
q''	Heat flux (W/m²)
$\bar{u}$	Mean velocity (m/s)
w	Width of a microchannel (m)

Greek Symbols

ρ	Density (kg/m³)
ω	Uncertainty (%)
ϕ	Volumetric mass concentration
μ	Viscosity

μ Wavelength of light

Subscripts

b	Bulk (mean) temperature
f	Properties of fluids
in	into the control volume
out	from control volume to out of control volume
s	Properties of solid (nanoparticles)
w	Heat exchanging surface (wall)

Dimensionless Parameters

Nu	Nusselt number
Pê	Peclet number
Re	Reynolds number

TABLE OF CONTENTS

Page

LIST OF FIGURES

LIST OF TABLES

1. INTRODUCTION AND LITERATURE REVIEW

Recent advances in micro/nano technology have posed a challenge for the development of novel cooling platforms for efficient thermal management of high heat flux devices. These devices include integrated circuit (IC) chips for electrical/computational applications, optical devices (e.g., laser cutting and manufacturing using light emitting diodes/ "LED" and high power lasers), and advanced energy storage systems (e.g., high temperature thermal storage, batteries and fuel cells). These devices have significantly higher thermal loads because typically their size is much smaller than conventional devices (i.e., less surface area available for cooling) while the total amount of heat generated has remained the same or increased (i.e., higher volumetric heat generation). Non-uniformity in the temperature distribution within these devices (due to inefficient cooling) leads to formation of localized "hot-spots" which can jeopardize the reliability for device operation and often leads to device failure as well as reduced speed of device operation. Thus, it is of great concern for systems level device management to effectively remove heat from these compact devices.

Forced convective heat transfer is a cheap, reliable and effective method for heat removal. Thus, a significant number of studies have been reported on utilizing forced convective heat transfer for cooling applications. However, forced convection in single phase flows are insufficient to meet cooling requirement to ensure optimum device operation. Two approaches have been employed traditionally to improve the cooling efficacy of the thermal management platforms (in single phase flows):

(1) Enhancing the thermal properties of heat transfer media (coolant); or

(2) Increasing the effective surface area for heat exchanging surfaces.

A brief literature review of these approaches is presented next.

1.1. Review of Heat Transfer of Nanofluids

Solid phase of materials typically have significantly higher thermal conductivity(especially for metals) than materials in the liquid phase for the same temperature. Hence, in an effort to improve the thermal conductivity of liquid coolants various studies have been reported in the literature where solid particles (micron-scale or nano-scale size) were mixed with liquid solvents to obtain slurries or colloidal suspensions. However, micron-scale solid particles tend to precipitate in the solvent. This lack of stability of the micro-particles in the solvents led to problems such as fouling and clogging of heat exchanging surfaces and flow conduits, respectively [1, 2].Eastman et al. first proposed the synthesis of stable heat transfer fluids that were obtained by doping conventional heat transfer fluids with minute concentration of metallic nanoparticles to obtain stable colloidal suspensions[3].The stable colloidal liquid suspensions containing nanoparticles are often called "nanofluids" (or "complex fluids"). The subject of nanofluids has been an active topic for research in the past two decades for various applications – ranging from coolants, to thermal energy storage materials, to lubricants, to emulsifiers and to biomedical drug delivery agents (to name a few).

2

Numerous reports exist on the experimental investigation of thermal conductivity of various types of nanofluids that were obtained by mixing a variety of solvents (e.g., aqueous solvents with or without glycols, organic liquids/ oils, ionic liquids and molten salts) with nanoparticles (e.g., metallic, organic and ceramic). Eastman et al. observed up to 40 % increase in thermal conductivity of ethylene glycol nanofluids containing copper nanoparticles at 0.3 vol. %[4].Also, Hong et al. mixed iron nanoparticles with ethylene glycol (at up to 0.55 vol. %) and observedenhancement inthe thermal conductivity by 18 % [5]. Patel et al. and Shalkevich et al. investigated thermal conductivity of water containing gold nanoparticles and reported enhancement in the thermal conductivity by 21 % and 1.4 %, respectively [6, 7].Several other research groups have investigated the synthesis of nanofluids using oxide nanoparticles –such as Al_2O_3, CuO, and TiO_2. Das et al. measured the thermal conductivity of aqueous nanofluids containing Al_2O_3 and CuO nanoparticles as a function of temperature[8].This study reported that the enhancement of thermal conductivity increases with increasing temperature which was up to 24.3 % and 36 % for Al_2O_3 and CuO nanofluids, respectively. Li and Peterson, Wang et al., and Lee et al. also investigated thermal conductivity of Al_2O_3 and CuO containing nanofluids for various base fluids including water, ethylene glycol, pump fluid, and engine oil [9-11].In addition, Murshed et al. explored thethermal conductivity enhancement of water when mixed with TiO_2 nano-rods [12]. These studies reported marginal enhancement of thermal conductivity of nanofluids compared to the base fluids.

Thermal conductivity of organic solvents containing nanoparticle suspensions were also investigated and reported in the literature. The thermal conductivity of various

oils and water –mixed with carbon nanotube (CNT) –were explored in various studies since CNT are considered to have the highest thermal conductivity among all material classes[13].Assael et al. as well as Wen and Ding reported that the thermal conductivity of water was enhanced by 31% and 38%, respectively, when mixed with multi-walled carbon nanotubes (MWNT)[14, 15].Xie et al. succeeded in obtaining stable dispersions of CNT nanofluids without using surfactants by acid treatment of CNT prior to mixing and reported that the thermal conductivity was enhanced by 19.6%[16].Choi et al. mixed single-walled carbon nanotube (SWNT) with epoxy at 3% mass concentration and observed 300 % enhancement in the thermal conductivity[17]. Furthermore, Nelson et al. reported significant enhancement in thermal conductivity of polyalphaolefin nanofluids containing exfoliated graphite nanoparticles at 0.6 % by weight [18].

However, several research groups have highlighted that thermal conductivity is not always enhanced on addition of nanoparticles (with high thermal conductivity) into the base fluid. Wang and Wei reported that the thermal conductivity of water based nanofluids containing $CePO_4$ nanofibers is degraded by up to 33 % [19]. According to this report, thermal conductivity of thesenanofluidswere enhanced by 13 % at 20 °C and degraded at other temperatures. Wei and co-workers have also reported degradation in thermal conductivity of various nanofluids [20, 21]. In these reports, the researchers observed that the ratio of thermal conductivity of nanofluids to that of the base fluid (water) varies from 0.83 to 1.24 and from 0.82 to 1.21 when Cu_2O and CuS/Cu2S core/shell nanoparticles were added, respectively. The literature data of the thermal conductivity measurements of nanofluids are summarized inTable 1-1.

4

Table 1-1 Summary of previous studies on thermal conductivity of nanofluids

Authors	Nanoparticle /Base Fluid	Particle Size [nm]	Concentration [vol. %]	Enhancement [%]
Lee et al.[11]	Al_2O_3/Water	38.4	1 ~ 4	~ 10
	CuO/Water	23.6	1 ~ 3	~ 10
	Al_2O_3/EG[a]	38.4	1 ~ 5	~ 15
	CuO/EG[a]	23.6	1 ~ 4	> 20
Eastman et al.[4]	Cu/EG[a]	< 10	0.3	~ 40
Patel et al.[6]	Au/Water	10 ~ 20	0.00026	5 ~ 21
	Ag/Water	60 ~ 80	0.001	3.2 ~ 16.5
Das et al.[8]	Al_2O_3/Water	38.4	1 ~ 4	2 ~ 24.3
	CuO/Water	28.6	1 ~ 4	6.5 ~ 36
Choi et al.[17]	SWNT/Epoxy	$\varnothing$ 2	3 wt. %	300
Wen and Ding[15]	MWNT/Water	$\varnothing$ 20 ~ 60	0 ~ 0.84	~ 31
Assael et al.[14]	MWNT/Water	$\varnothing$ 80	~ 0.6	~ 38
Hong et al.[5]	Fe/EG[a]	10	~ 0.55	~ 18
Murshed et al.[12]	TiO_2/Water	$\varnothing$ 10	0.5 ~ 5	5 ~ 33
	TiO_2/Water	$\varnothing$ 15	0.5 ~ 5	5 ~ 30
Li and Peterson[9]	CuO/Water	29	1 ~ 6	30 ~ 52
	Al_2O_3/Water	36	2 ~ 10	7 ~ 30
Shalkevich et al.[7]	Au/Water	2 ~ 45	0.00025 ~ 1	1.4
Nelson et al.[18]	EG[b]/PAO[c]	100 (thickness)	0.6 wt. %	~ 1000
Wei et al.[20]	Cu_2O/Water	200.5	0.02 mol/L	-17 ~ 24
Buongiorno et al.[22]	Al_2O_3/Water	$\varnothing$ 10	1	3.6
	Al_2O_3/EGa	10	1~3	3.9 ~ 12.1
	Al_2O_3/PAO[c]	$\varnothing$ 10	1~3	5.1 ~ 17.6
	Au/Water	10	0.001	0.7
	SiO_2/Water	22	31	20.4

[a]EG : Ethylene Glycol; [b]EG : Exfoliated Graphite; [c]Polyalphaolefin

Hence, the reports showing enhancement in the thermal conductivity of nanofluids (compared to that of the neat solvent) have been controversial due to contradictions in the reported results between various research groups. Recently, Boungiorno et al. reported an extensive set of thermal conductivity measurements for multiple nanofluids (aqueous nanofluid samples and olefin-nanofluid samples) using different benchmark measurement techniques –which are primarily variants of the hot-wire technique (and all of the measurements involve a measurement probe in physical contact with the nanofluid samples)[22]. The measurements were performed by multiple investigators in different research laboratories using "blind" samples. The authors concluded after compiling the experimental results from various investigators participating in this study that the thermal conductivity values were consistent with the Maxwell's model and the authors concluded that the anomalous enhancement reported in prior studies was not observed for the nanofluids considered in that study. It is not clear if the conclusions from the study of Boungiorno et al.can be applied to all classes of nanofluids or if this study was relevant and valid for only the nanofluids used in that study. Also, it may be noted that the data sets that proved to be outliers were discarded from the compiled data sets – since they were obtained from multiple investigators participating in this study (while the discarded data sets were not reported in this paper).

From an applications perspective (e.g., for cooling applications) the investigation of forced convective heat transfer coefficient is a more important parameter – which in turn is a function of thermal conductivity and other thermophysical parameters (e.g., viscosity, specific heat capacity, density, etc.). However, relatively only a small number

of reports exist in the literature on the investigation of convective heat transfer of nanofluids. For example, the ISI Web of Knowledge reveals that there are only 318 publications relating to the measurement ofconvective heat transfer of nanofluids out of 1951 publications (including journal articles, conference papers, and reviews) on nanofluids as of June25[th] on 2012.

Pak and Cho pioneered the study of convective heat transfer of nanofluids in the turbulent flow regime [23]. They observed up to 75 % enhancement in the values of Nusselt number compared to that of pure solvent at the same Reynolds number. However, they reported that heat transfer coefficient of nanofluids decreased by 12 % for a given fluid velocity. However, other research groups have demonstrated marginal enhancement in the value of heat transfer coefficient of nanofluids.Xuan and Li reported up to 39 % increase in the heat transfer coefficient of aqueous nanofluids containing copper nanoparticles [24]. Wen and Ding, Kulkarni et al., Hwang et al., and Nassan et al. reported significant enhancement in the convective heat transfer coefficient of aqueous nanofluids mixed with oxide nanoparticles [25-28]. In the laminar flow regime, Wen and Ding and Nassan et al. observed increase in heat transfer coefficient of Al_2O_3nanofluids by up to 47 % and 20 % at 1.6 vol. % and 2.5 vol. %, respectively [25, 28]. Enhancement of heat transfer using oxide nanoparticles in turbulent flow regime was also reported by Kulkarni et al. By mixing with SiO_2at 10 % volume concentration nanoparticles into the solvent (a mixture of ethylene glycol and water with 60:40 ratio by mass concentration), they observe that convective heat transfer coefficient increased by 16 % [26].

Several research groups demonstrated the enhancement of convective heat transfer of organic nanofluids. Ding et al. first reported convective heat transfer characteristics of nanofluids containing CNT[29]. They observed notable enhancement of heat transfer coefficient by up to 350 % by mixing CNT nanoparticles with water (0.1 ~ 0.5 wt. %) at laminar flow regime (Re = 800). Amrollahi et al. later investigated convective heat transfer of MWNT nanofluids for turbulent flow regime (Re = 4778) [30].Marginal enhancement of heat transfer coefficient from 33 % to 40 % was also observed in the turbulent regime. Nelson et al. investigated polyalphaolefin (PAO) mixed with exfoliated graphite (EG) nanoparticles and reported enhancement of convective heat transfer by up to 10 %[18]. Nelson et al. also reported that specific heat capacity of nanofluids was enhanced by ~50 % compared to neat PAO. Table 1-2summarizes the results from prior studies in the literature.

In general, enhancement of thermal conductivity correlates fairly well with the anomalous enhancement of convective heat transfer of nanofluids[31].Various attempts in developing theoretical models for nanofluids remain incomplete and controversial since none of the theoretical models provide a comprehensive explanation for the observed anomalous behavior for various experiments performed using nanofluids. Part of the reason is due to faulty experiments performed using nanofluids where the relevant experimental parameters were not controlled or monitored diligently. Hence, considerable uncertainties exist about the relevance and validity of some of the experimental results reported in the literature. Buongiorno suggested seven transport (and slip) mechanisms which can cause anomalous behavior of nanofluids[32]. These

mechanisms are: (1) inertia, (2) Brownian diffusion, (3) thermophoresis, (4) diffusiophoresis, (5) Magnus effect, (6) fluid drainage, and (7) gravity. The report claims Brownian diffusion and thermophoresis are the only dominant slip mechanisms in nanofluids. Heyhat and Kowsary also noted the effect of particle migration caused by Brownian motion and thermophoresis on convective heat transfer of nanofluids[33]. In contrast, Nelson et al. presented the influence of surface modification by precipitation of nanoparticles on convective heat transfer [18].

Table 1-2 Summary of previous studies on convective heat transfer of nanofluids (solvent is water if it is not noted explicitly)

	Material	Concentration [vol. %]	D_h [mm]	Re	Enhancement [%]
Pak and Cho[23]	Al_2O_3 TiO_2	1 ~3	10.66	$10^4 \sim 10^5$	45 ~ 75 % for given Re
Xuan and Li[24]	Cu	0.3 ~ 2	10	10000 ~ 25000	~ 39
Wen and Ding[25]	Al_2O_3	0.6 ~ 1.6	4.5	500 ~ 2100	~ 47
Ding et al.[29]	CNT	0.1 ~ 0.5 wt. %	4	800	350
Kulkarni et al.[26][a]	SiO_2	2 ~ 10	3.14	3000 ~ 12000	~ 16
Hwang et al.[27]	Al_2O_3	0.01 ~ 0.3	1.812	600 ~ 700	8
Nelson et al.[18][b]	Graphite	0.3 ~ 0.6 wt. %		72 ~ 365	~ 10
Nassan et al.[28]	Al_2O_3 CuO	0.2 ~ 2.5 0.1 ~ 1.5	1 cm^2 square	660 ~ 2050	~ 20
Amrollahi et al.[30]	MWNT	01 ~ 0.25 wt. %	11.42	1592 ~ 4778	33 ~ 40

Base Fluid :[a]60:40 (% by weight) EG/water mixture; [b]Polyalphaolefin (PAO)

1.2. Review of Heat Transfer in Microchannel

Since the first report in the literature proposing the employment of microchannel heat sinks for enhanced dissipation of heat at high power densities [34],numerous studies have been performed on this topic. These studies have primarily focused on comparison of numerical predictions from theoretical models with experimental results. Most experimental measurements of friction factor and Nusselt number in microchannels were inconsistent with the theoretical predictions. Controversies exist since several research groups reported higher values of Nusselt number in the experimental observations than predicted by conventional theory[35-37] whereas other research groups reported lower values of Nusselt number [38, 39].

Various transport mechanisms have been suggested to reconcile the anomalous and inconsistent behaviors observed in the microchannel heat transfer experiments. Viscous dissipation effects, property variation effects, and surface roughness are typically suggested as the underlying factors responsible for the observed anomalous phenomena[40-44].Specifically, Qu et al. suggested that the surface roughness generally affects: (1) the velocity profile near the wall (velocity gradient decreases near the wall); (2) the temperature profile near the wall (temperature gradient decreases); and therefore (3) the resultant Nusselt number (which is smaller than the value predicted by conventional heat transfer theory)[38].Also, Liu et al. numerically evaluated the role of surface microstructures on forced convective heat transfer characteristics in microchannels and showed that the grooved microstructures provide more uniform heat transfer along flow direction compared to that of the plane surface[45].Systematic

studies are required to provide more accurate insights into the transport mechanisms responsible for the anomalous behavior of fluids (particularly nanofluids) in microchannels.

A few pioneering studies have provided insights on the forced convective heat transfer for flow of nanofluids in microchannels. Jang and Choi first reported experimental results that demonstrated enhancement in the cooling performance of a microchannel heat sink by approximately 10 % when aqueous nanofluids containing diamond nanoparticles at 1% volume concentrationwere employed [46]. Subsequently, other research groups reported similar results for the enhancement of convective heat transfer in microchannels using nanofluids [47, 48].

Lee and Mudawarexperimentally evaluated effectiveness ofAl_2O_3 nanofluids for enhancing heat transfer in a microchannel [49].They reported that heat transfer coefficient was enhanced by nanofluids for flow in a microchannel; however, marginal increase in pressure drop was also observed. Considering overall cooling effectiveness they remained inconclusive about the efficacy of using nanofluids for enhancing cooling in microchannel heat sinks. Similar to the observations from other research groups – the values of heat transfer coefficient were observed to decrease with decrease in the Reynolds number.

Jung et al. studied convective heat transfer characteristics of Al_2O_3 nanofluids flowing in a rectangular microchannel[50]. By mixing Al_2O_3 nanoparticles with two different base fluids, DI water and a mixture of 50% water and 50% ethylene glycol, convective heat transfer coefficient of nanofluids flowing in rectangular microchannel

(dimension is 50 μm x 50 μm and 100 μm x 100 μm with 15 mm length) was increased by approximately 32 % in the laminar flow regime. The enhancement was observed to be more significant in the entrance region and at higher Reynolds number. Other significant observations from this study are:(1) heat transfer coefficients are higher in relatively small microchannels than in larger microchannels and (2) Nusselt number in laminar flow regime is no longer constant and considerably less than the theoretical value of 4.0–5.6 in microchannel (reported Nusselt number is less than 0.5), which is consistent with the previous study done by Lee and Mudawar[49].

Singh et al. experimentally and numerically studied convective heat transfer of EG (ethylene glycol) based Al_2O_3 nanofluids[51]. Al_2O_3 nanofluids at concentration of 0.25 vol. %, 0.5 vol. %, and 1.0 vol. % flowing trapezoidal microchannel with hydraulic diameter of 218 and 303μm showed enhancement of heat transfer. The enhancement washigher when either the concentration or Reynolds number is increased.The authors suggested from the numerical simulations that this enhancement is caused by thermal dispersion due to shear induced particle migration, which Wen and Ding [52] had demonstrated in an earlier study. Numerical simulations also predicted that Brownian motion and thermophoresis are dominant mechanisms responsible for the migration of nanoparticles and enhanced heat transfer.

Although investigation of convective heat transfer in microchannels or using nanofluids have been explored intensively as separate topics, studies combining the two topics (i.e.,convective heat transfer of nanofluids flowing in microchannel) are comparatively rare. To illustrate, only 99 reports including journal papers, articles, and

conference reports are availableas of June25[th] on 2012 in ISI Web of Knowledge when searched with keywords nanofluids and microchannel.Detailed investigations scrutinizing convective heat transfer characteristics of nanofluids flowing in microchannels (including those for clarifying the transport transfer mechanisms) are required in order to enhance their adoption in various applications such as: electronic chip cooling, lab on a chip, drug delivery, and energy storage systems

1.3. Review of Temperature Measurement Technologies

Miniaturization of sensors (including temperature sensors) are required for various applications due to the concomitant advantage accruing from the high-speed and high spatial density of these devices (i.e., they enable high spatial and temporal resolution of the experimental parameter being monitored). In addition to the lower power consumption by the miniaturized sensors, the small form factors of the micro/nano-sensors minimize the perturbation of the phenomena under observation. Especially, novel measurement platforms are required for monitoring fluid flow and temperature profiles during flow of colloidal suspensions in microchannels while minimizing any perturbations of the transport mechanisms that can occur due to the act of measurement. However, current commercial measurement instruments are not amenable to meet these requirements. Various studies have been reported to overcome these challenges. Glaninger et al. developed thin film germanium thermistors with high flow sensitivities and short response times [53]. Wu et al. integrated flow sensors within a microchannel, where the response time of the flow sensors was modified by

controlling doping thickness [54]. Ernst et al. introduced thin film sensors with high resolution for Bio-MEMS applications [55].

Temperature sensors are indispensable for monitoring and measuring heat transfer in various applications. Thermocouples are one of the most widely used temperature sensors because they are applicable for wide range of temperatures up to 1700 °C, durable in harsh conditions, are convenient to use and fabricate. However, conventional wire-bead thermocouples tend to disturb flow profiles near the wall. Although these errors can be neglected in macro scale studies, differences between measured (apparent) value and real value can become significant as the scale of overall system becomes small (micro/nano scale). Various technologies have been introduced in order to overcome these disadvantages. For example, thin film thermocouple (TFT) was introduced in 1960s [56]. Other research groups developed micro-scale resistance temperature detector (RTD) for measuring temperature difference on a chip [57].

Thin film thermocouple (TFT) has been developed and utilized by many research groups because of its attractive features [56, 58-64]. Kumar and Kasiviswanathan fabricated transparent TFT using indium tin oxide (ITO) and manganese [63]. Heichal et al. addressed that TFT is expected to provide high response speed to temperature fluctuation because of its small thermal inertia [60]. Sunder and Banerjee developed thin film thermocouples (TFTs) and utilized them to measure surface temperature fluctuations in flow boiling experiments, which had been assumed using heat conduction equation in general [64]. In this study, Sunder and Banerjee fabricated K-type TFT using Alumel and Chromel alloys. Various micro/nano fabrication techniques such as

14

photolithography and Physical Vapor Deposition (PVD) were utilized in the fabrication processes.

Diode temperature sensors (DTS) were developed for measuring transient surface temperature fluctuations [65, 66]. DTS renders two significant advantages over TFT: (1) packaging requirements are dramatically reduced; and (2) the sensors are located flush under the surface (causing minimal disruption of the flow features). Specifically, perturbation of flow and heat transfer (transport mechanisms) is minimized due to the location of the sensors being flush under the surface. Recently, Jeon and Hansen developed diode temperature nanosensors and utilized it in droplet cooling experiments [67, 68].

Intrusive measurement devices that are embedded in the flow apparatus can cause perturbations of the transport mechanisms. This problem can be resolved if non-contact temperature measurement (or non-intrusive) technology is adapted. Thermochromic Liquid Crystal (TLC), infrared, and laser induce fluorescence thermography are the most widely used non-contact temperature measurement techniques. Due to unique optical characteristic of TLCs, – their optical properties are dependent on temperature – many researchers have exploited TLCs for experimental measurement of surface temperature transients [69-72]. Painting TLCs on the surface enables temperature measurement with high spatial (~1μm) and temporal (~10 ms) resolution. Infrared (IR) thermography is one of the most popular and well known temperature measurement techniques [73, 74]. This thermography technique has recently been utilized for measuring surface temperature in microchannel heat sinks as well as

capillary tubes [75, 76]. Surface temperature can be easily measured with high accuracy when accurate value of emissivity is available. However, both TLC and infrared thermography techniques have limitations in that they can measure only surface temperature.

Laser induced fluorescence (LIF) technique utilizes the temperature dependence characteristic of fluorescent intensity. In general, the overall intensity of fluorescent dye decreases and the peak wavelength of emission (wavelength corresponding to maximumintensity) moves to higher wavelength as temperature increases. LIF provides non-contact three dimensional visualization of temperature field inside miniaturized flow conduits. It has been successfully applied for combustion study or measuring temperature in liquids[77-79]. Specifically, Omenetto et al. measured and calculated the electronic excitation temperature of several flames using fluorescence method [78]. Sakakibara et al. visualized both velocity and temperature fields by combining laser induced fluorescence technique and particle image velocimetry (PIV) technique [80]. Also, Ozturk et al. recently utilized fluorescein to monitor transport properties of suspensions including nanoparticles, surfactant, and dye in microfluidic architectures [81]. Hardin et al. measured three dimensional (3-D) profile of ion flow field (distribution of velocity vectors) and temperature distribution using laser induced fluorescence technique by using different laser injection orientations at a single spatial location[82]. Chamarthy et al. used Rhodamine B and Rhodamine 110 as a laser induced fluorescence dye when they visualized mixing phenomenon between a hot and a cold fluid at a microfluidic T-junction [83].

16

Recently, Quantum Dots (QDs) have gained interest in the research community. QDs have higher photo-stability for longer durations, provide brighter emission of light in visible wavelengths, and are capable for wide range of excitation and emission wavelengths compared to organic dyes [84-86]. QDs have been utilized widely in the life science especially in biological research. Since emission spectrum of QDs generally changes with temperature, several reports have demonstrated the use of individual QDs as temperature sensors. For instance, Yang et al. used CdSe quantum dot as nano-thermometers to observe thermal gradient in individual living cells [87]. CdSe quantum dots provide red-shifted emission spectrum at elevated temperatures. Li et al. utilized CdSe quantum dots to sense localized variation of temperature on aluminum micro-heater [88]. Li et al. used water soluble CdSe quantum dots encapsulated by ZnS shell, which have emission peak at 655 nm. According to this report, precision in temperature measurement of 1 °C can be achieved, provided ~1200 (or larger numbers of) quantum dot particles are used.

In this sense, thin film nano-sensors, laser induced fluorescence dye, and quantum dot thermography have significant potential for temperature measurement applications in heat transfer research for micro/ nano-scale devices. These metrology techniques can minimize the perturbation of transport mechanisms that can potentially be perturbed by the introduction of these measurement probes. These techniques are amenable for the development of non-contact metrology of temperature profiles (especially near the wall) with high spatial and temporal resolution as well as high levels accuracy (when combined with high speed digital data acquisition systems). In this study,

these promising technologies are developed and adapted for the experimental apparatus that were utilized for measuring the convective heat transfer of coolants (water and aqueous nanofluids) flowing in the microchannels with rectangular cross section.

1.4. Objective of the Study

The goal of this study is to measure the forced convective heat transfer coefficient based on experiments performed for flow of coolants (water and aqueous nanofluids) in straight microchannels with rectangular cross sections. The objective of this study is to explore and scrutinize the thermo-fluidic behavior of various nanofluid coolants; as well as, to compare the thermal efficacy of nanofluid coolants with that of the pure solvent (De-Ionized Water or "DIW") in microchannel flows.

It is hypothesized that the modification of surface geometry on heat exchanging surface by precipitation of nanoparticles are responsible for the anomalous enhancements in convective heat transfer observed for the flow of nanofluids in microchannels. In order to prove (or disprove) the hypothesis, the levels of heat flux enhancements obtained from the flow of pure water solvent (water) in the microchannels containing the engineered nanostructures; were compared to that of the flow of aqueous nanofluids in the plain microchannels (without surface nanostructures).

In order to verify the hypothesis, materials characterization was performed using Scanning Electron Microscopy (SEM) and Energy Dispersive X-Ray Spectroscopy (EDX). Surface nanostructures were nanofabricated on the heat exchanging surface using Step and Flash Imprint Lithography (SFIL). Scanning probe microscopy (SPM)

techniques (such as Atomic Force Microscopy or "AFM") were also utilized. Temperature measurements were performed using various miniaturized metrology techniques (temperature nano-sensors/ TFT, LIF and QD). The microchannel apparatus was integrated with TFT array for measuring the wall temperature gradient in the flow direction and to obtain the wall heat flux during the flow of coolants. Soft lithography techniques were used to fabricate the microchannels.

1.5. Overview

Temperature nano-sensors, such as Thin Film Thermocouple (TFT) were integrated into the experimental apparatus by in-situ nanofabrication. The TFT were used to measure the wall temperature gradient in the axial direction (along the flow direction) on the heat exchanging surface (bottom surface) of the microchannel. TFT (~ 200 nm thickness) are expected to provide the necessary spatial and temporal resolution with minimal intrusion and impact (perturbation) on the flow fields (and temperature profiles) within the microchannels. Quantum Dots (QD) were dispersed in the test fluids and the QD nanofluids were explored for flow visualization using confocal microscopy. Similar experiments were also performed using fluorescent dyes. These nano-scale flow visualization techniques enabled the estimation of the flow profiles and temperature profiles of the test fluids during flow in microchannels. In particular, the near-wall estimates for velocity and temperature gradients are crucial for estimating the variations in the local values of heat-flux and friction coefficients. These parameters were used to determine the efficacy of the various test fluids for thermal management applications.

Various nanofluids were explored by varying the composition (material), concentration, shape and size of the nanoparticles.

The engineered surface nanostructures (nano-fins) were fabricated at the NSF-NNIN (National Nanotechnology Infrastructure Network) facility located at the "Microelectronics Research Center (MRC)" at the University of Texas at Austin. At the NNIN facility, Step and Flash Imprint Lithography (SFIL) and Electron Beam Lithography (EBL) techniques were used to perform nanolithography and nanofabrication of the engineered surface nanostructures and the templates, respectively. TFT were fabricated using the "lift-off" process by using a combination of photolithography and Physical Vapor Deposition (PVD). These fabrication protocols were developed at the Materials Characterization Facility (MCF) at Texas A&M University. The engineered nano-structured surfaces (using SFIL) and the associated surface characteristics (e.g., due to precipitation of nanoparticles from nanofluids) were monitored before and after the experiments. The nanostructures (engineered or precipitated from nanofluids) were characterized using electron microscopy instruments that are available at the Microscopy and Imaging Center (MIC) at Texas A&M University. The nanofluids samples were procured from commercial suppliers and also synthesized using facilities located at the "Multiphase Flows and Heat Transfer Lab." at Texas A&M University (under the supervision of Dr. Banerjee). The flow visualization experiments (for flow and temperature profiles) and experiments using QD – were performed using a shared-user-instrument – confocal microscope located in the "Multiphase Flows and Heat Transfer Lab." The flow visualization experiment using

QD that were developed as a part of this study,is a novel contribution to the field of experimental flow visualization and to the study of nano-scale convective heat transfer phenomena.

In addition, flow boiling experiments in microchannels were performed in this study using pure solvent (DI Water) and nanofluids. The temperature profiles within the microchannels were measured using the TFT array (which were fabricated in-situ in the microchannels). This is the first study of this kind in the literature combining flow boiling, microchannels, nanofluids and integrated nanosensor array.

1.6. Significance of Current Study

This study is expected to make fundamental contributions to the field of thermal-fluids sciences in the following ways:

- Development of nano-scale temperature metrology platform for monitoring convective heat transfer phenomena of simple (Newtonian) fluids and complex fluids (nanofluids).

- Design and fabricate high quality and stable thin film nano-sensors which can be utilized to measure temperature of coolants in microchannel, while minimizing the perturbation of the transport mechanisms under investigation.

- Utilize nano-fabrication techniques using Step and Flash Imprinting Lithography (SFIL) for obtaining surface nanostructures (nanofins) with the aim of enhancing surface area for augmenting convective heat transfer.

- Evaluate the contribution of various parameters such as nanoparticle concentration, wall temperature, and flow velocity on the forced convective heat transfer characteristics of nanofluid coolants during flow in a microchannel.

- Address the effect of surface nano-structures ("nanofins") on heat transfer and correlate the behavior with the thermal efficacy of nanofluids flowing in a microchannel (i.e., prove that nanoparticle precipitates from nanofluids can act as "nanofins"). Hence, this can help prove that the surface interactions are more dominant in determining the thermal efficacy of nanofluids than their bulk property values.

- Demonstrate the feasibility of non-contact temperature metrology techniques for experimental flow visualization and heat transfer measurements (especially in the near wall region) using quantum dots (QDs) and laser-induced-fluorescence (LIF) techniques.

- Demonstrate the feasibility of using this experimental platform combining flow boiling, microchannels, nanofluids and integrated nanosensor array.

2. MICRO/NANO FABRICATION

2.1. Fabrication of TFT

A conventional temperature measurement approach is to employ "thermocouples" which utilize the Seebeck effect. When the two junctions of two different conductive materials (metals or alloys for example) are immersed into any media at two different temperatures – they develop an electrical potential drop between the two junctions (which is proportional to the temperature difference between the two junctions) – which is known as the "Seebeck effect" (and the proportionality constant is known as the "Seebeck coefficient"). The junction of two dissimilar materials used for measuring the electrical potential drop (in order to ascertain the temperature) is therefore called a "thermocouple".

In this study, K-type thin film thermocouple (TFT) arrays were microfabricated using conventional techniques – consisting of –photolithography, Physical Vapor Deposition (PVD), and "lift-off" process. K-type thermocouple is composed of two different alloys of nickel: chromel (90 % nickel and 10 % chromium) and alumel (95 % nickel, 2 % manganese, 2 % aluminum and 1 % silicon) as a positive leg and negative leg, respectively. K-type thermocouples were chosen for their strong resistance to oxidation which makes them ideal candidate for application in aqueous environment and at high temperatures. TFTs were fabricated on silicon and pyrex glass wafers. Pyrex glass wafers were chosen to minimize thermal conduction within the wafer (in the axial direction, i.e., the flow direction) – which enables better monitoring of the convective

heat loss into the fluid from the heated wafer and reduces the measurement uncertainty. Photolithography and physical vapor deposition (PVD) techniques were utilized in the fabrication process. Each layer for positive and negative elements of the thermocouple (chromel and alumel) were fabricated in separate steps (successively by photolithography, PVD and lift-off), and designed to overlap at specific locations to obtain the TFT junction with the desired pitch in the flow direction (axial direction) on the surface of the wafer substrate. Schematic diagram for the fabrication steps and the microfabrication procedure are shown in Figure 2-1. Since the performance of TFT is highly dependent on the quality of metal thin film, recipes for the fabrication procedure were optimized in multiple iterations of the fabrication that were performed in this study (as well as from information obtained in previous studies[89-92].

The specific steps involved in the fabrication of the temperature nanosensors are described next. These steps were performed at the Materials Characterization Facility (MCF) at Texas A&M University and the Microelectronics Research Center (MRC)/ National Nanotechnology Infrastructure Network (NNIN) node located at the University of Texas at Austin.
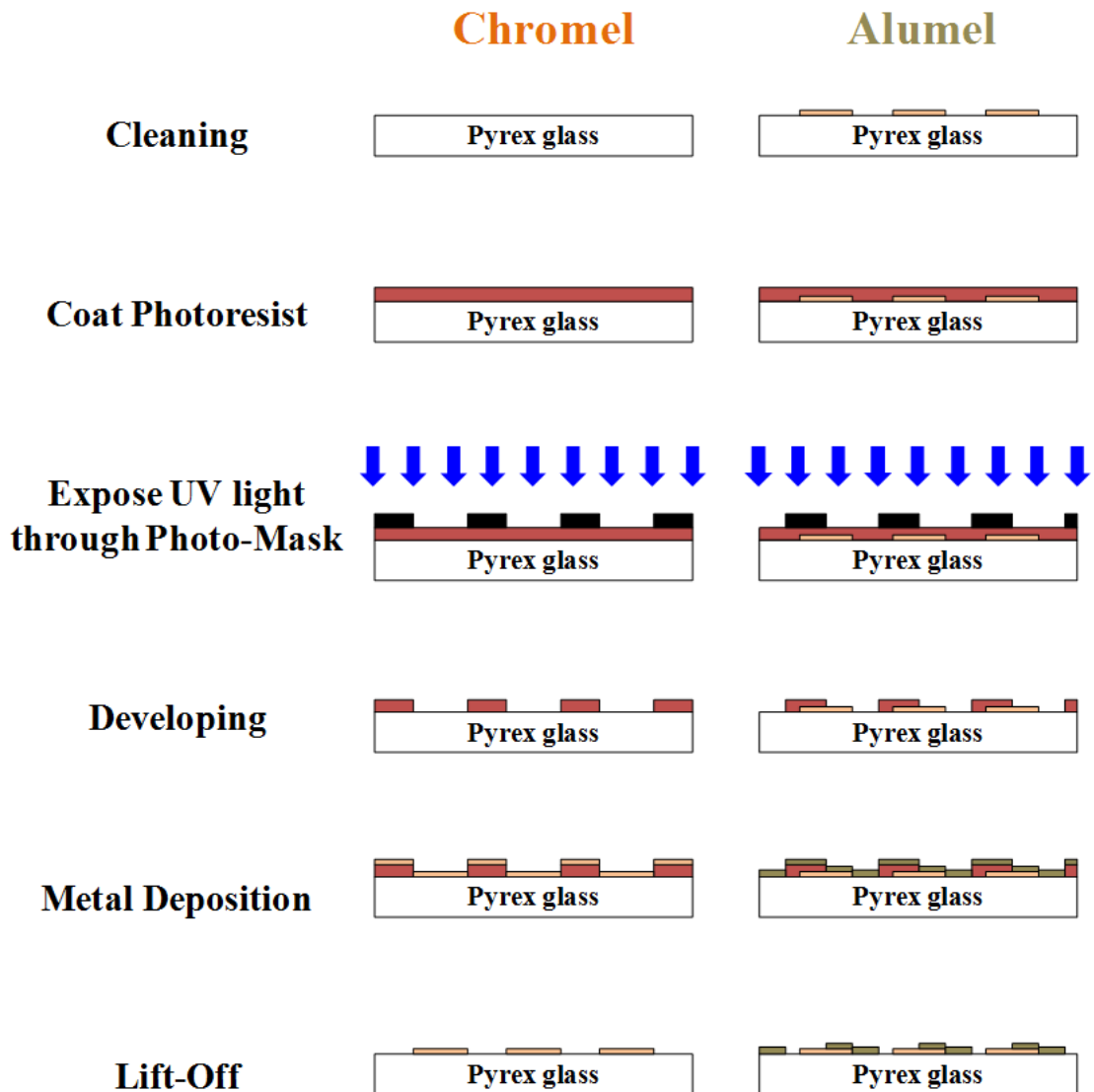
Figure 2-1 Schematic diagram of TFT fabrication process

2.1.1. Photolithography

Layout for the two photomasks used for fabrication of the TFT array was designed so that metal alloys can be deposited on a desired pattern. The photomasks were fabricated at "Southwest Printing" located in Bryan, Texas. After obtaining the

photomasks photolithography was performed. This process includes cleaning wafers, spin coating photoresist, UV exposure, and developing of the exposed substrates. Failure in mask alignment or improper developing could cause problem in the subsequent steps (e.g., failure in the lift-off process) or malfunctioning of the TFT. These steps were performed at the Materials Characterization Facility (MCF) at Texas A&M University.

2.1.1.1. Cleaning Wafer Using Reactive Ion Etching (R.I.E.)

The wafers shipped by vendors can be potentially contaminated with organic particles and dust/ dirt which is undesirable for micro/nano fabrication. To remove those impurities, the wafer is cleaned using acetone, DIW, and oxygen plasma. The wafer is first washed with acetone and DIW and then blow-dried using compressed nitrogen gas at least two times. Although nitrogen gas removes water from the wafer, it is possible that the wafer can contain residual moisture. So, the wafer is place on hot plate for ten minutes at 115 °C to remove residual moisture. After wet-cleaning of the wafer, reactive ion etcher (Model CS-1701, March Plasma Systems) is used for surface cleaning using oxygen plasma (dry-cleaning step for removing organic residues on the wafer surface). This process is performed using the recipe which is summarized in Table 2-1.

Table 2-1 Photolithography recipes for fabricating TFT layer

Reactive Ion Etching (R.I.E.)	Instrument	March Plasma Systems Model CS-1701
	Power	350 W
	Time	300 seconds
	O_2 Flow	20 sccm
Spin Coating	Instrument	Laurell WS-650S (8.5 inch bowel) Spin Processor
	Material	SC 1827 (Rohm and Haas Electronic Materials)
	Speed	3000 rpm
	Time	60 seconds
	Acceleration	500 rpm/s
Soft Bake	Temperature	115 °C
	Time	60 seconds
UV expose	Instrument	Quintel Q4000 Mask Aligner
	Power Density	14 mW/cm^2
	Expose Time	60 seconds
Develop	Material	MF-319 (Rohm and Haas Electronic Materials)
	Develop Time	60~90 seconds

2.1.1.2. Spin Coating

Positive photoresist (SC 1827, Rohm and Haas Electronic Materials) is spin-coated to form photoresist layer with a target thickness that exceeds 3μmon the wafer surface. According to the spin speed curve (manufacturer specification) this is achieved by spin coating the photoresist at 3000 rpm for 60 seconds. The wafer coated with the photoresist is than pre-baked on a hot plate at 115 °C for 60 second in accordance with

manufacturer specification (pre-exposure bake is performed to provide structural rigidity to the coated photo-resist).

2.1.1.3. Exposure to UV Light

When exposed to UV light with a certain amount of photo (radiation) energy, positive photoresist becomes soluble to the photoresist developer. Patterns are transferred to the wafer through photomasks containing the desired layout for the TFT array. For fabrication of TFTs, two independent photo-masks are required to pattern chromel and alumel layer. Designs for those masks are shown inFigure 2-2, (these layouts designed using Solidworks™ version 2010, DassaultSystèmes). Before exposure to UV light source, photo-masks and the wafer need to be aligned so that two patterns (i.e., chromel and alumel layer) overlap at desired position. Alignment is performed using a commercial Mask Aligner (Model: Q4000, Manufacturer: Quintel). Subsequently the wafer aligned with the mask is exposed to UV light for 60 seconds. The optical power rating (intensity) of the UV light source is 14 mW/cm^2. The wafer is marginally over exposed to UV light (compared to manufacturer specification) when this recipe is applied. This is intended to ensure that the exposed area can be completely developed and there is adequate reliability of the exposure process for the photoresist coating. For the recipe used in this study, over exposure can potentially limit the critical dimension ("CD" or minimum size of the features obtained in the fabrication process) to ~10μm. This is acceptable for this study because the size of the smallest pattern targeted for fabrication is ~100μm.
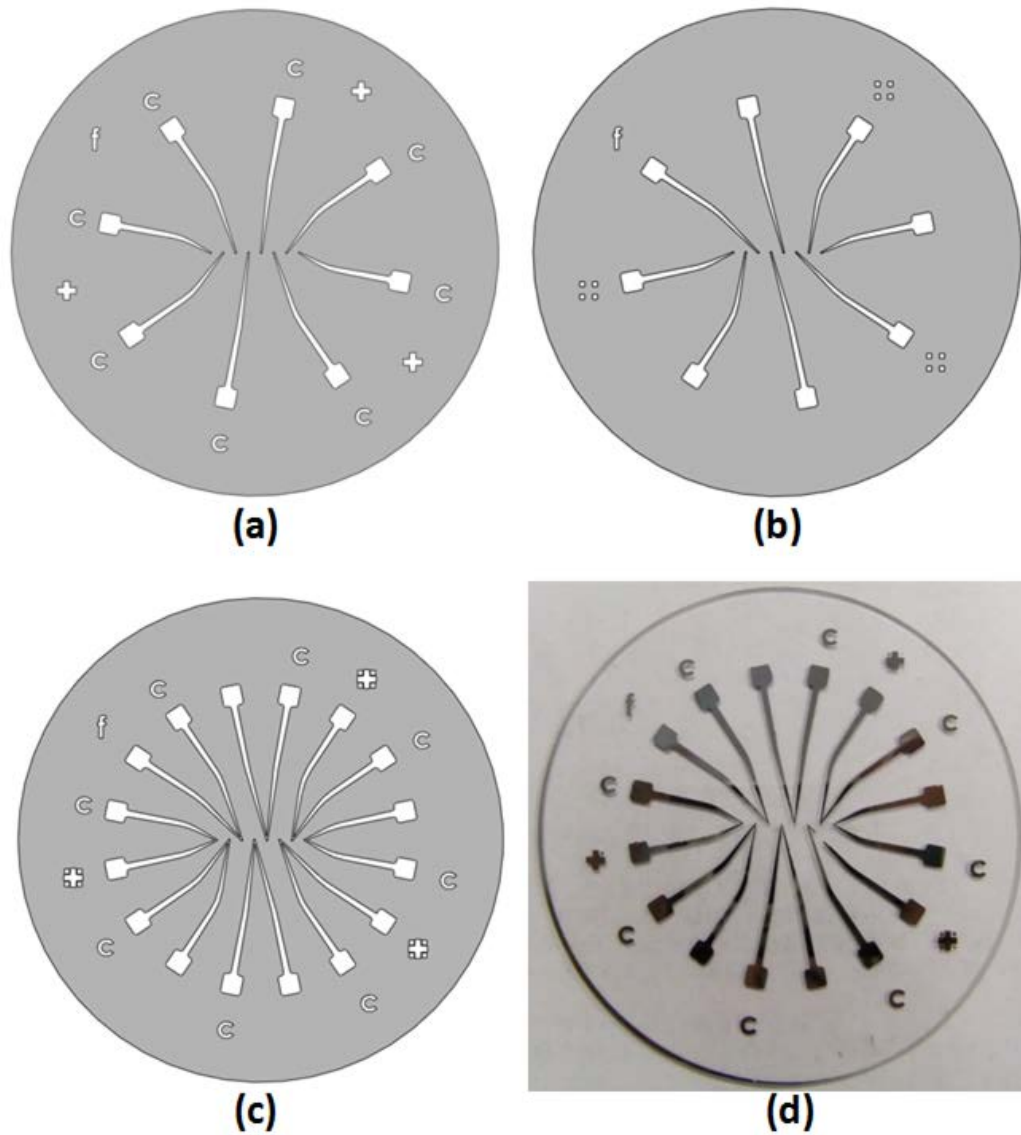
Figure 2-2 Mask layouts for (a) chromel layer, (b) alumel layer, and (c) completed TFT, and (d) picture of fabricated TFT on pyrex(glass) wafer

2.1.1.4. Development of Exposed Photoresist

The exposed wafer is immersed in the developer solution, MF-319 (Rohm and Haas Electronic Materials) for obtaining the exposed pattern. Portion of the (positive)

photoresist that is exposed to the UV illumination is dissolved when immersed in the developer solution. Developing time is estimated to be approximately 60 ~ 90 seconds. After the photochemical development step the wafer is washed using only DIW and blow-dried using a nozzle and compressed nitrogen gas. Developed pattern is examined using optical microscope to ensure the removal of residual photoresist. It is recommended that an UV filter is placed on the light source of the optical microscope while performing the visual examination of the wafer since the process may need to be repeated in the event of failure in the photolithography process. If the photolithography process is not successful (e.g., due to uneven coating of photoresist during spin coating, broken pattern due to over-exposure/ over-development, etc.), the wafer is cleaned using acetone and the process is repeated from the beginning. Images of the wafer after photolithography are shown in Figure 2-3, which is then ready for metal deposition.

2.1.2. *Physical Vapor Deposition (PVD)*

Metals (either chromel or alumel) are deposited on the wafer by thermal evaporation of the target materials and deposition on the wafer substrate (with patterned photoresist such that a portion of the wafer is exposed to the deposited metals/ alloys). However, metals generally have a weak bond with non-metallic materials (pyrex glass) hence an adhesion promoter (adhesion layer) is deposited prior to deposition of the target metal/ alloy. Titanium is deposited to a thickness of 20 nm and serves as the adhesion layer for pyrex (glass) substrates used in this study. Since the melting point of Titanium is higher than for conventional metal deposition processes (which is not amenable for a

resistive-filament thermal evaporator), an E-beam evaporator (CHA #1) is used for the PVD process: which is located in MRC/NNIN node at the University of Texas at Austin.

In accordance with the manufacturer's specification, Tiadhesion layer is initially deposited on the wafer to a thickness of 20 nm. This is immediately followed by a deposition of the target material (chromel or alumel). The goal is to form a 200 nm layer at a deposition rate of 0.7 ~ 0.9 Å/s. It is very important to properly control deposition rate in order to optimize theadhesion and quality (continuity) of the thin films. If the deposition rate is too high, deposited metals suffer from poor adhesion to the substrate or the adhesion layer. Especially, it is recommended that the deposition rate be restricted to 0.1 ~ 0.3 Å/s at theinitiation of the deposition process. Once metals are deposited by to sufficient thickness (~30-50 Å), it is acceptable to increase deposition rate to up to 1 Å/s. Special care should be taken when dealing with materials for metal deposition that require high quality of deposition (especially for successful lift-off). Each metal/ alloy target including titanium, chromel, and alumel should be restricted to separate cruciblesto prevent cross-contamination and to maintain the purity of the targets that are used while repeating the PVD process in each fabrication run. An image of the wafer coated with metal alloy (chromel) on titanium adhesion layer is shown in Figure 2-4 (a). This image is obtained just before lift-off process.
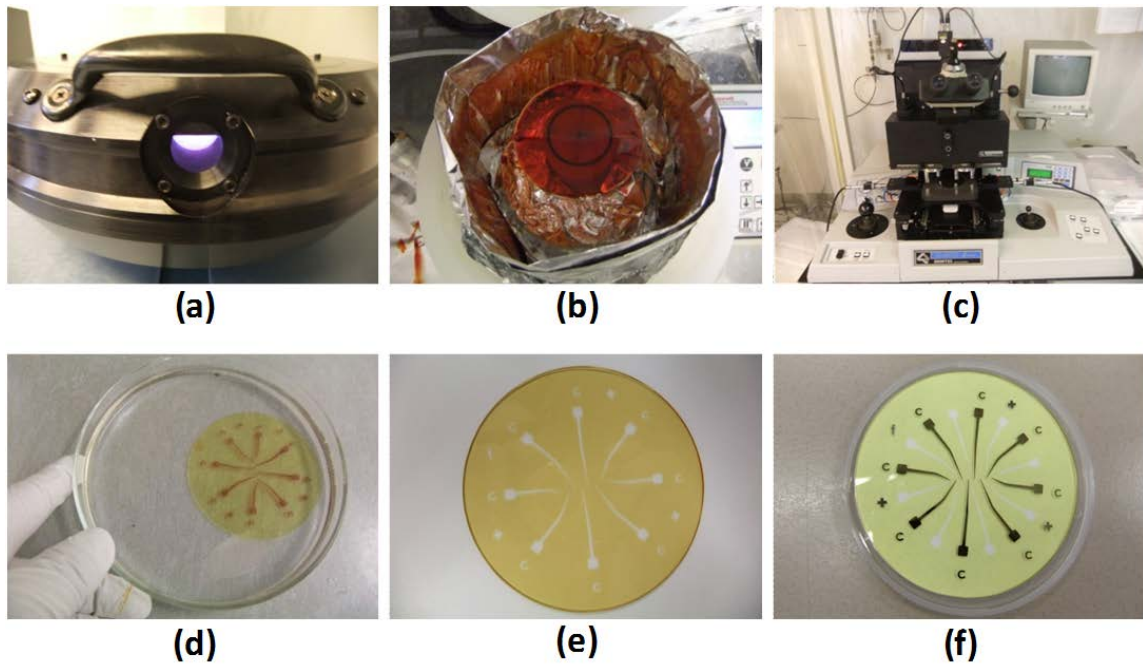
Figure 2-3 Sequence of images showing: (a) Reactive Ion Etcher (RIE) used for oxygen plasma cleaning. (b) Spin coater (SC-1827). (c) Mask Aligner. (d) Wafer immersed in developer solution. (e) Photoresist patterned for deposition of chromel. (f) Patterned chromel layer and photoresist patterned for deposition of alumel layer
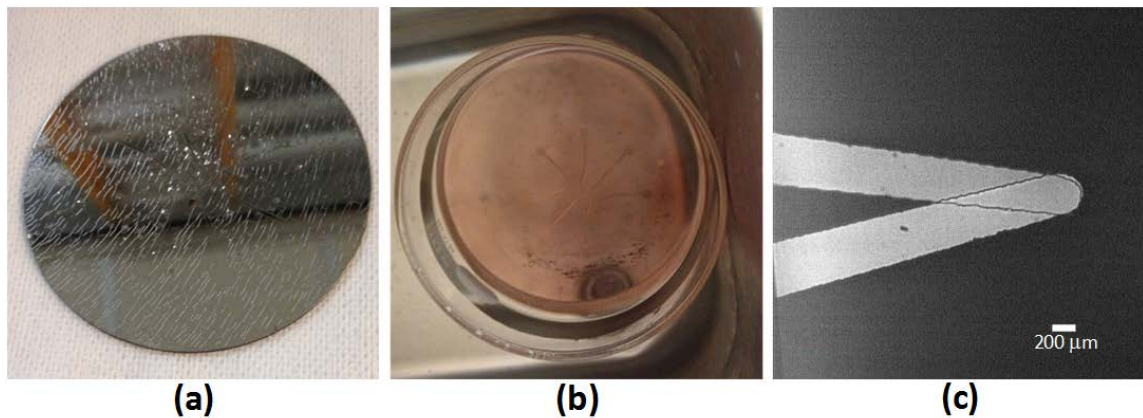
Figure 2-4 Sequence of images showing: (a) A wafer coated with metal alloy (chromel) on patterned photoresist. (b) A wafer immersed in photoresist remover and subjected to lift-off process in ultrasonicator. (c) Image of a TFT junction observed in a optical (confocal) microscope showing the overlap of the patterned chromel and alumel layer, that were obtained using lift-off process.

2.1.3. Lift-Off

After PVD of metal/ alloy, lift-off is performed to dissolve the photoresist and detach the thin film layers deposited on photoresist – such that the material deposited on the exposed parts of the wafer remain at the end of the process (and thus the desired pattern is replicated from the photomask onto the wafer substrate), and is shown in Figure 2-4 (b). In this study, the wafer is cleaned using PG remover solution (MicroChem Inc.) in an ultrasound bath for $15 \sim 20$ minutes until all undesired materials are removed. After lift-off, the wafer is cleaned by rinsing in DIW at least for three times and blow dried. Magnified image of one of TFT junctions using optical (confocal) microscope is shown in Figure 2-4 (c). As described before, the maximum width of the temperature nanosensor at the location of the TFT junction (where the patterned chromel and alumel layers overlap) is approximately $150 \sim 200\mu m$ while the thickness of the metal layers is ~ 200 nm (or ~ 400 nm at the location where the patterned layers overlap). These dimensions can be adjusted to smaller or larger sizes by changing the layout of the photomasks and controlling the deposition thickness targeted in the PVD process.

2.2. Fabrication of Microchannels

Soft lithography techniques [93, 94] using Polydimethylsiloxane (PDMS) is used to fabricate individual microchannels. PDMS is a visco-elastic material which can be cured (polymerized) using a resin. A mold is initially prepared on a silicon wafer by optical lithography technique using a negative photoresist (e.g., SU-8). PDMS is then poured on the mold and cured. The complementary pattern corresponding to the features

photo-patterned on the SU-8 mold is transferred to the imprinted PDMS after curing. The cured PDMS layer is then peeled from the mold and the mold can be reused multiple times. PDMS is preferred for soft lithography since it has several noble properties; i.e., PDMS is transparent, inert, non-toxic, and non-flammable.

2.2.1. *Preparation of a Mold*

In this study, a mold which contains desired shape of the microchannel is first prepared on silicon wafer using photolithography technique. Negative photoresist, SU-8 2050 (MicroChem), is used and photolithography procedure is performed according to the manufacturer's specification for achieving a target height of the SU-8 photoresist (i.e., the height of microchannel), which is 70μm. SU-8 2000 series is amenable for fabrication of high aspect ratio features for a wide range of film thickness values (25 ~ 225μm), and for very high optical transmission coefficients (above wavelength of 360 nm). This enables the patterning of nearly vertical sidewalls in very thick films. The photolithography procedure is identical to the description provided in Section 2.1.1. The recipes for the microchannel molds are summarized in in Table 2-2.

Table 2-2 Recipes for SU-8 2050 to form a mold with a thickness of 70µm

	Material	SU-8 2050 (MicroChem)
	Speed #1	500 rpm
	Time #1	8 seconds
Spin Coating	Acceleration #1	100 rpm/s
	Speed #2	2000 rpm
	Time #2	30 seconds
	Acceleration #2	300 rpm/s
Pre-Bake	Temperature	65 °C
	Time	3 minutes
Soft Bake	Temperature	95 °C
	Time	9 minutes
UV Expose	Power Density	14 mW/cm^2
	Expose Time	30 seconds
Post Bake 1	Temperature	65 °C
	Time	1 minute
Post Bake 2	Temperature	95 °C
	Time	7 minutes
Develop	Material	SU-8 Developer (MicroChem)
	Develop Time	60~90 seconds
Cure	Temperature	150 ~ 200 °C
	Time	15 ~ 30 minutes

2.2.2. *Fabrication of PDMS Microchannel Using Soft Lithography*

After preparing desired mold on the silicon wafer, soft lithography is adopted to fabricate microcahnnel.Sylgard 184 kit (Dow Corning) PDMS is mixed with the curing

agent with the ratio of 10:1 and then poured onto the mold. Before pouring, the mixture should be placed in partial vacuum (using a desiccator connected to a vacuum pump) for 30~60 minutes to completely eliminate the bubbles that may form in the mixture. Also, inlet and outlet ports should be placed and supported on top of the mold (prior to poring the PDMS) in order to embed the ports in the microchannel. PDMS mixture is then poured on the mold and heated for 10 minutes at 150 °C. The cured mixture is then allowed to cool to the room temperature. The cured PDMS layer is then carefully peeled off from the mold and cut to appropriate size using a razor blade. The PDMS substrate is them ready for assembly with a flat substrate to form a microchannel (flow conduit) and for performing the desired experiments. Table 2-3shows the dimensions of the microchannel fabricated and used in this study.

Table 2-3 Dimensions of fabricated microchannel

Height (H)	55.7μm (with standard deviation, 0.5 μm)
Width (W)	1000μm
Length (L)	24 mm
Hydraulic Diameter (D_h)	105.5μm
Aspect Ratio (H:W)	1:18

2.3. Fabrication of Nanofins

Monitoring and evaluating the effects of surface modification (i.e., the formation of nanofins) due to precipitation of the nanoparticles from nanofluid coolants, is a focus of this study. As described in Section 1, if the level of enhancement of convective heat

transfer during flow of de-ionized water (DIW, i.e., pure solvent) inside a microchannel containing surface nanostructures (nanofins) on the heat exchanging surfaces; is similar to that of the nanofluids flowing in a plain microchannel that does not have engineered nanostructures (i.e., if it can be shown that the nanofins are generated in-situ by precipitation of the nanoparticles from the nanofluid coolants), it can be reliably concluded that the observed enhancements in forced convective heat transfer for nanofluid coolants is essentially due to the resultant surface interactions and not primarily dominated by the bulk properties of the nanofluid coolants.

For this purpose, an array of surface nanostructures (nanofins) needs to be fabricated with well-defined diameter, height, and pitch. This is a costly endeavor and can be quite time consuming requiring a series of complicated fabrication steps as well as intricate process recipe. Photolithography is one of the most widely used methods for patterning. However, the resolution (CD) of the patterns obtained in photolithography is limited by the wavelength of the illumination source (which is approximately ~ 300 nm). Considering that using light source with extremely short wavelength (deep UV or "DUV") requires complicated processes and elaborate clean room infrastructure that is associated with considerable capital and operational costs; this option is incompatible with the requirements of this study. Another widely used patterning method is Electron Beam Lithography (EBL). Complicated patterns with very small size (CD under 100 nm) can be patterned using EBL.However, it is very slow and costly.

Nano Imprint Lithography (NIL) has been invented as an alternative technique for nano-patterning at low cost. Chou et al. developed thermal nano imprint lithography

and succeeded in creating patterns with 25 nm CD [95]. However, the process requires the heating of the substrate beyond the glass transition temperature of the imprinting resist (PolyMethyMethAcrylate, PMMA). Although the use of bi-layer could allow greater etch selectivity, the high pressures and temperatures make it ineffective because the substrate is exposed to thermal and mechanical stress which can potentially affect the alignment procedure and compromise the CD that can be achieved using this technique.

Step and Flash Imprint Lithography (SFIL), which was developed at the University of Texas at Austin, confers several advantages over conventional techniques such as NIL. The SFIL process can be performed at room temperature by utlizing imprinting resists that have low viscosity at room temperature [96]. This method uses bi-layer coating (one for transfer layer and the other for imprinting resist). A schematic of the steps in the fabrication procedure for pattering and etching nano-structures using SFIL process is shown in Figure 2-5.

The substrate is first spin-coated with a transfer layer and tiny volume of imprinting resist is dispensed on the substrate just before the pattern is imprinted using a mold (fabricated apriori). Silicon containing imprinting resist is used since it has low viscosity and is photo-curable using Ultra Violet (UV) illumination. The template is fabricated using patterned features that are complementary to the desired nanostructures. The "negative" features are patterned on a quartz plate (which is transparent to UV light) by utilizing Electron Beam Lithography (EBL). Since the viscosity of imprinting resist is low, it can flow during imprinting step to fill the patterned recesses in the mold (quartz template). After curing the imprinting resist using UV from an illumination source

(which confers mechanical strength to the patterned resist), the template is released. After substrate with the patterned resist is subjected to appropriate dry etching processes, the imprinted nano-patterns are thus "chemically embossed", i.e., transferred to the silicon wafer. Details for each process are explained in following subsections.
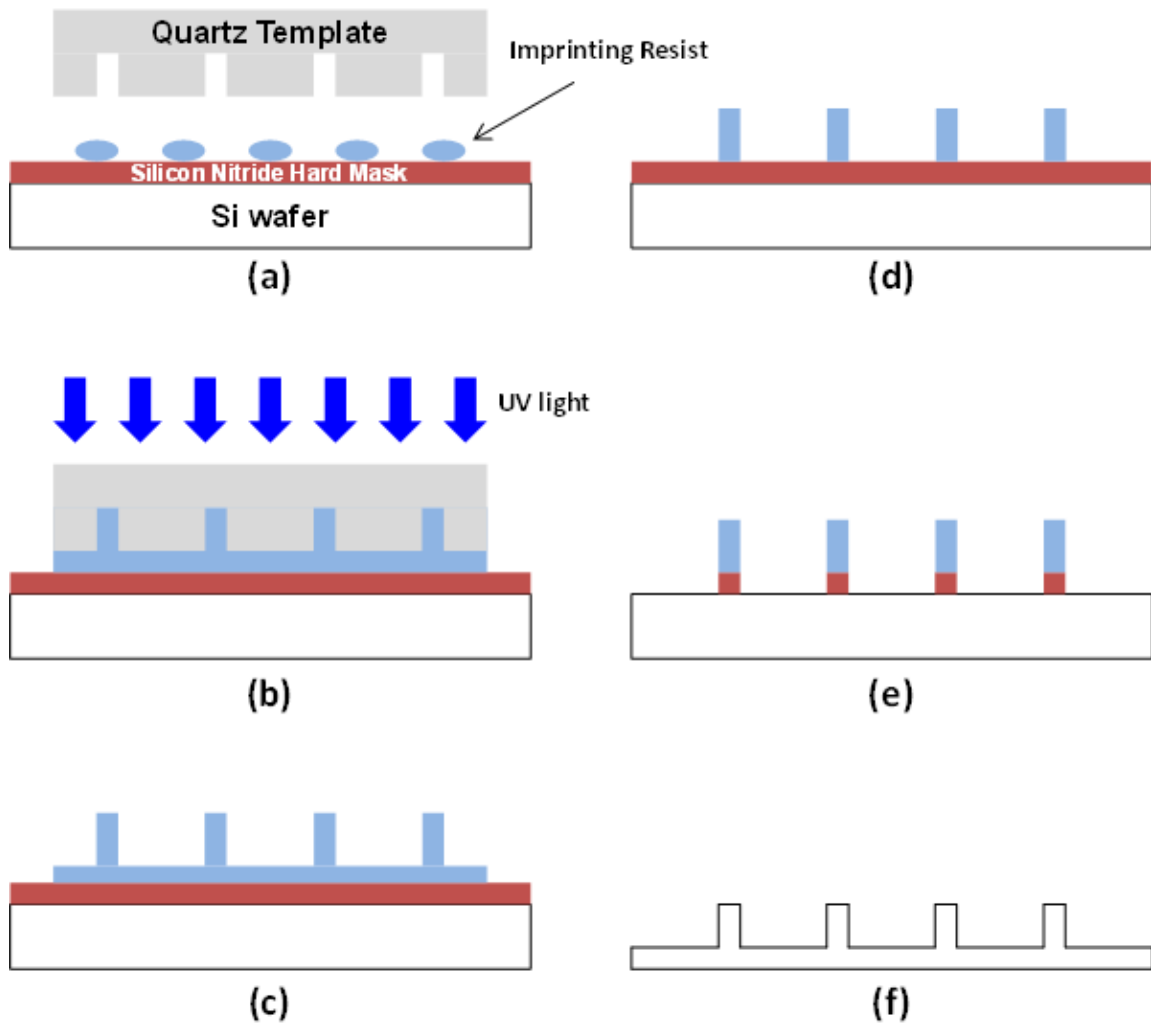
Figure 2-5 Schematic diagram showing individual steps in the Step and Flash Imprint Lithography (SFIL) process (figures not to scale)

2.3.1. Preparation of Template (Mold)

The template is prepared using E-Beam Lithography (EBL). The help of Dr. Marylene Palard, a research staff member in MRC/NNIN at the University of Texas at Austin in performing the EBL and realization of the mold is gratefully acknowledged. The mold (template) was fabricated to obtain circular nanofins with a nominal diameter of 200 nm and a pitch of 1μm.

2.3.2. Piranha Clean

The wafer is first cleaned using piranha solution to remove organic residues. Piranha solution is a strong oxidizer, which contains a mixture of hydrogen peroxide (H_2O_2) and sulfuric acid (H_2SO_4) in 2:1 (H_2O_2:H_2SO_4) volumetric ratio. Piranha cleaning allows reclamation of wafers if the prior imprinting process is unsuccessful. However, this should be performed in an acid hood with adequate precaution and protective gear.

Piranha solution is prepared by slowly and carefully adding 1650 ml sulfuric acid (H_2SO_4) into quartz bath containing 825 ml hydrogen peroxide (H_2O_2). The mixture starts to generate bubbles due to exothermal reaction. After allowing the mixture to stabilize for five minutes, the wafer is immersed into the solution using a wafer holder. Piranha solution is left in the bath for 8~10 minutes to react with any organic particles.

The cleaned wafer is then rinsed with DIW in the cascade washer which is placed in the acid hood. Rinsing is repeated five times to completely wash out the piranha solution from the wafer and then spin-dried using Verteq Spin Rinser Dryer (Akrion, Inc.). The wafer is then ready to be used for subsequent processing steps.

2.3.3. Deposition of Etch-Resist (Silicon Nitride Hard Mask Coating)

The imprinting resist is not durable enough to endure the harsh processing conditions during the dry etching step. This is an impediment to achieving nanofins that are more than 100 nm length. In order to solve this problem, silicon nitride is coated on the silicon wafer to be used as a hard mask for obtaining the nanofins of sufficient length (nanofins). In this study, silicon nitride (deposition thickness of 100 nm) is used as an etch mask. The silicon nitride layer is deposited using LPCVD furnace in the north cleanroom at MRC/NNIN at UTA (the help and technical advice of Dr. Marylene Palard for this endeavor is gratefully acknowledged).

2.3.4. Coating of Transfer Layer

Anti-reflective coatings are spin-coated ("transfer layer") on the 4 inch wafer immediately after piranha-cleaning. The transfer layer is used to achieve high aspect ratio features and get good adhesion of the cured imprint resist to the substrate. Also, the transfer layer plays a key role during dry etching and serves as an etch mask. Requirements of the material for the transfer layer are as follows:

a. Provide good adhesion of imprint resist to the silicon wafer after UV curing.
b. Provide high etch selectivity relative to the substrate.
c. Provide enough thickness for obtaining high aspect ratio features.
d. Does not dissolve or swell during imprinting.

41

In this study, AP410 is used as a material for transfer layer. Since this material is easily spin coated on the substrate, small amount of AP410 is first dispensed on the silicon wafer and spin coated at 2600 rpm for 60 seconds. After coating, the transfer layer needs to be soft-baked at 180 °C for one minute and then the wafer become ready for imprinting.Since AP410 forms a monolayer, it is very thin (thickness is only a few angstroms) and can be removed using O_2 plasma dry etching after imprinting

2.3.5. *Imprinting*

After cleaning, coating silicon nitride, and AP410 coating, the patterns in the template are imprinted on the wafer using IMPRIO 100. First, the template is cleaned using IPA and then blow-dried using nitrogen. The cleaned template is loaded onto IMPRIO 100 and aligned so that the sides of imprinted squares are parallel to the flat of the wafer. After wafer alignment, the template is transferred to the tool and mounted on a vacuum chuck. Next, the template is leveled. The leveling procedure is complicated and time consuming step. However, this is the most crucial procedure during imprinting because perfect leveling ensures more uniform imprints. In this study, 4-point measurement was chosen for the leveling operation. The relative height at four points outside of the mesa is measured and the slope along planar direction (x and y direction) is measured. After each measurement, leveling screws are manually adjusted/ rotated slightly (typically less than three steps). This process is repeated until slope of the template along x and y direction reaches the desired level. The minimum requirement of the tool for the leveling is slope below 250 nm/100μm for each direction. When the

template is leveled with slopes below 100 nm/100µm, imprinting results have proved to be quite uniform and repeatable. The aligned wafer is then loaded into the tool. IMPRIO 100 provides automatic leveling of the wafer by aligning it to the leveled template; so, no further manual adjustment is required.

The imprinting process is controlled following a specified standardized recipe (programmed into the control software) which describes the volume, the position, and the type of imprinting resist dispensed on the wafer as well as the layout for imprinting. In this study, dispenser #2 is selected which does not contain silicon so that it can be etched using only O_2 plasma. When the selected recipe is implemented, the selected dispenser dispenses droplets of specified pitch and volume (predetermined by the control software) in accordance with the standardized recipe and the template approach routine on to the surface of the wafer is implemented by the instrument controller. The tool imprints the template with a specified force (9 N in this study) for 2 minutes so that the droplet of imprinting resist can completely fill the recesses within the template. Then, UV light illumination is performed to cure the imprinting resist for ~10 seconds. This process, starting from dispensing imprinting resist to curing, is repeated at another position on the substrate after stepping the tool assembly by a pre-specified length of travel. The results from each imprinting should be examined so that the recipe can be modified and optimized for the next "step", "imprint" and "flash" operation. This is necessary because occasionally surface contamination, impurities and dust particles can affect the process yield. When particles are detected, they can be removed using kapton tape. As described earlier, imprinting is performed for complete surface coverage of the

43

substrate using this stepping scheme – thus justifying the name of the process as: "Step and Flash Imprint Lithography (SFIL)".

2.3.6. *Transfer of Patterns to the Wafer Substrate (Dry Etching)*

The patterns (nanofins) are now nano-imprinted onto the imprinting resist. The next step is to transfer this pattern to the silicon wafer substrate using dry etching (i.e., this is a "chemical embossing" technique). In this study, dry etching is performed using Reactive Ion Etching (RIE). Three steps are needed to etch imprinting resist and transfer layer (breakthrough etch), the silicon nitride etch-resist, and the silicon substrate, successively. First two layers are dry etched using normal procedure in RIE (Plasma Therm #2, MRC/ NNIN at UTA) and the specified recipe is summarized in Table 2-4. Recipe for silicon nitride etching is implemented to provide 30 % over-etching. This is to ensure the complete removal of the silicon nitride etch resist layer. Silicon substrate is etched using RIE to obtain nanostructures with low aspect ratios. Deep RIE (DRIE) is used for obtaining high aspect ratio structures in the silicon substrate. The depth of etching using DRIE is controlled by varying number of etching cycles (6, 12, 18, and etc.). The more the number of etching cycles, the higher the height of fabricated nanofins.

Table 2-4 Recipe for dry etching

Breakthrough Etching	Instrument	Plasma Therm #2
	Recipe name	YJ_O2.prc
	DC	400 V
	Time	30 ~ 45 seconds
	Gas	O_2 8 sccm
Silicon Nitride Etching	Instrument	Plasma Therm #2
	Recipe name	TA_NIT1.prc
	Power	400 W
	Time	1 minute 50 seconds
	Gas	CHF_3 40 sccm / O_2 2 sccm

Although it is very important to completely etch the imprinting resist layer and the transfer layer (when performing breakthrough etching), it is difficult to ascertain if there is any residue on the substrate since they are very thin (below 100 nm). In this study, a dummy pattern is obtained by scratching the surface on the periphery of the wafer using thin and sharp pen to physically remove imprinting resist and transfer layer. This is performed in order to ascertain the complete removal of the residual layers. The region with the scratch mark is examined using AFM after breakthrough etching to check if resists are indeed completed removed. Figure 2-6 and Figure 2-7 show AFM images showing the thickness of imprinting resist as well as the height of nanofins before and after breakthrough etching, respectively. Figure 2-6 shows the results after nano-imprinting is completed. According to this figure, the height of imprinted nanofins is 66.3 nm immediately after imprinting. The thickness of imprinting resist and transfer layer (difference of height between scratched region and imprinted region) is

approximately 70 nm. After O_2 plasma etching for 45 seconds, imprinting resist and transfer layers are ascertained to be completely removed, as shown in Figure 2-7. Height of nanofins is also significantly decreased from 66.3 nm to 19.5 nm. This shows that breakthrough etching for 45 seconds results in over-etching. After multiple iterations, it was determined that the recipe used for breakthrough etching provides etching rates ofapproximately 2.5 nm/s. Since the thickness of imprinting resist varies for each sample due to different wafer thickness and other fabrication conditions, breakthrough etching has been optimized to a value of 30 ~ 45 seconds.
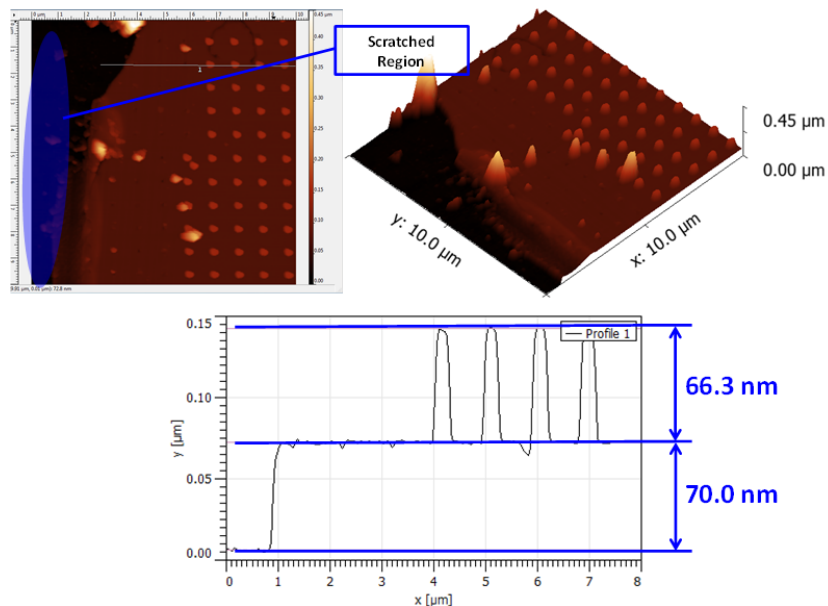
Figure 2-6 AFM images before breakthrough etching (right after imprinting). Height of the imprinting resist and transfer layer is 70 nm. Height of nanofins is 66.3 nm.

46
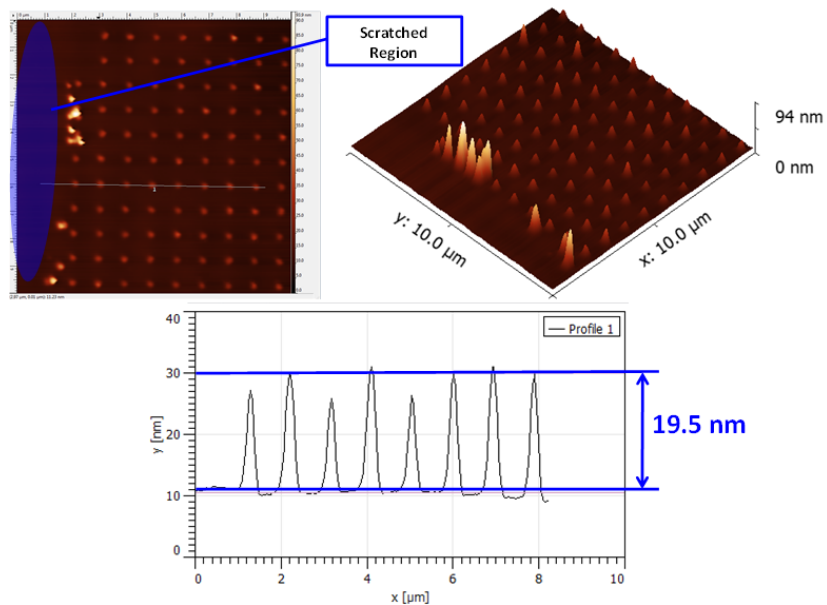
Figure 2-7 AFM images after breakthrough etching for 45 seconds. Imprinting resist and transfer layers are completely removed. Also, the height of nano-imprinted nanofins is reduced from 66.3 nm to 19.5 nm.

After successfully accomplishing the transfer of patterns, residues on the nanofins which had been utilized as etch-mask should be removed. Imprinting resists can be removed using piranha clean, O_2 plasma, or RS111. However, fabricated nanofins are susceptible to damage due to harsh environmental conditions and chemical reactions when the sample is subjected to piranha cleaning (cf. Appendix A). Thus, RS111 solution is used to removal of the imprinting resist. By immersing the substrate into RS111 solution at 50 °C for 20 minutes, imprinting resist slowly removed from the substrate. The silicon nitride hard mask is removed using dry etching with same recipe described earlier in this section. Although fabrication of silicon nanofins with specified dimension (200 nm in diameter with 1 μm pitch) is now completed, one more step remains; i.e., dicing of the silicon wafer is required to obtain the appropriate form factor.

This is required for packaging and assembling the fabricated wafer in the experimental apparatus. The wafer is cut using dicing saw (ADT Dicing Saw, MRC/ NNIN at UTA) for obtaining the desired shape and size that is suitable for the assembly and packaging process.

2.3.7. *Characterization of Fabricated Nanofins*

Fabricated nanofins were subsequently characterized. Scanning Electron Microscopy (SEM) is used to measure the dimensions of the nanofins (height, diameter, pitch, yield, etc.).

Although top-view of the nanofins obtained from the SEM images can be used to obtain the required geometrical information, images obtained by tilting the platform at 45° can be sued to estimate the height of the nanofins. Cross-section image can also be examined if required. Selected SEM images for fabricated samples are shown in Figure 2-8. The image shows that the diameter of the nanofins is marginally smaller (140~150 nm) than that of the template (200 nm).

Utilizing the SEM images from the tilted platform, the height of the nanofins was estimated in this study. As mentioned earlier, 4 batches consisting of different number of etch cycles (6, 12, 18, and 24) were used for DRIE. The average heights of the nanofins in the 4 batches were 208 nm, 354 nm, 464 nm, and 750 nm (for 6, 12, 18, and 24 cycles, respectively). Figure 2-9shows the height of the nanofins plotted as a function of the number of cycle of DRIE (the results were obtained from the 4 batches of DRIE). From the slope of the graph it is estimated that the nominal value of the average etch rate for

each etch-cycle during the DRIE process is 29~30 nm (with a standard deviation of ~3 nm) during etching of Si (the average value of the nominal etch rates for the 4 batches of DRIE of Si are: 35, 30, 26 and 31 nm). This is to be expected since the etch rates in DRIE are faster in the initial cycles and are slower as the etch depth increases with each cycle due to diffusion limited kinetics and stearic hindrance in the etch reactions. Hence, the average values of the etch rate decreases as the number of cycles is increased in the different batches. Although maximum height of nanofins realized in this study is ~750 nm, higher values of nanofin height can be realized (which can exceed several micrometers) when more than 35 cycles are implemented for the DRIE of Si.
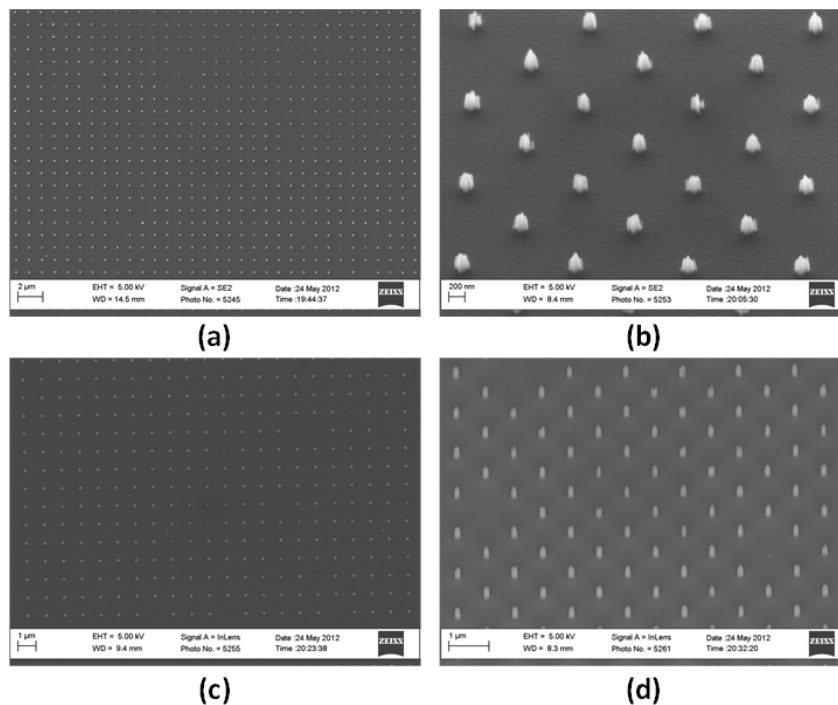
Figure 2-8 SEM images: (a) After 6 cycles of DRIE (without tilting), (b) After 6 cycles of DRIE (SEM stage tilted at 45°), (c) After 12 cycles of DRIE (without tilting), (d) After 12 cycles of DRIE (SEM stage tilted 45°)
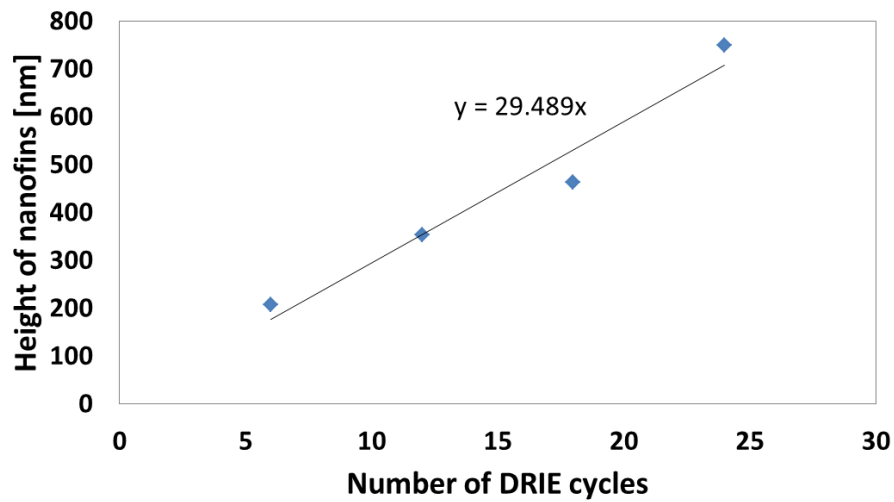
Figure 2-9 Plot of height of nanofins as a function of the number of cycles in the 4 batches of DRIE of Si

Visual observation can provide a rough estimate of the process yield. Figure 2-10shows an image sequence of the silicon wafer that was obtained at the conclusion of each step during the implementation of the SFIL process, including: imprinting, breakthrough etching, silicon nitride etching, and Si deep RIE etching. The images show that the imprinted patterns emit a brownish hue in Figure 2-10 (a) which is a result of good (uniform) nano-imprinting, compared to that with bluish color (non-uniform imprinted region). Figure 2-10 (b) also confirms that the regions with brownish hue are etched uniformly after breakthrough etching. In Figure 2-10 (c), after etching the silicon nitride region (emitting dark blue hue) is removed and the substrate appears to have a mirror-finish - identical to that of a silicon wafer. However, closer examination reveals the existence of shiny diffraction patterns, as shown in Figure 2-10 (d) after DRIE of Si

50
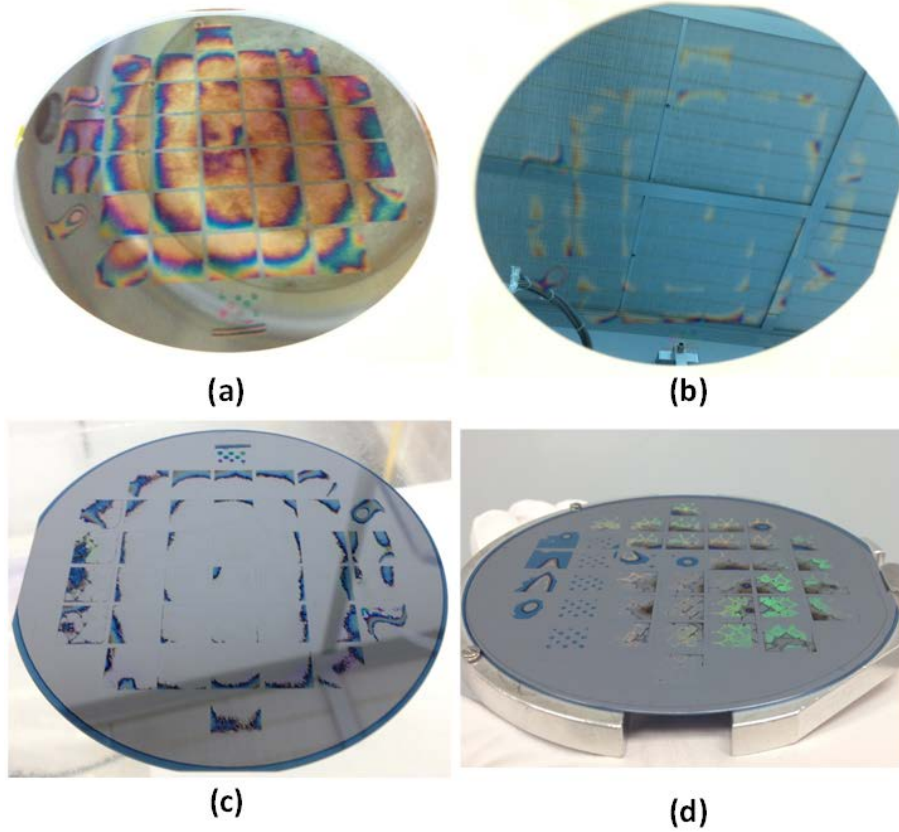
Figure 2-10 Sequence of images showing the wafer after: (a) Nano-Imprinting (SFIL); (b) Breakthrough etch (oxygen plasma); (c) Silicon nitride etching (RIE); and (d) DRIE of Si (diffraction of the incident light by the nanofins cause bright hues to emanate from the wafer surface in the regions containing the nanofins with ~700 nm height)

3. EXPERIMENTAL APPARATUS AND PROCEDURE

3.1. Experiments Using Thin Film Thermocouples (TFT)

3.1.1. Description of Experimental Setup

The experimental setup initially used for measuring the convective heat transfer in microchannels consists of the main test section (microchannel integrated with TFT array with film heaters attached below the wafer substrate), flow apparatus consisting of tubing connected with syringe pump (Pump 11 Pico Plus, Havard Apparatus), film heater (KHR-2/10-P, Omega), DC power supply (SPS 200-50-K025, American Reliance Inc.), and DAQ (Data acquisition) system (NI SCXI-1303, National Instrument). Syringe pump and film heater were used for providing constant flow rate of the coolants and constant heat flux to the bottom of the main test section, respectively. DC power supply is connected to the heater. Temperature data is monitored and recorded using high speed DAQ system (nominal sampling frequency of 200 Hz, but capable of sampling frequency up to 1 kHz). Figure 3-1shows the schematic configuration of the entire experimental setup.

Main test section is composed of two parts: temperature measurement part (TFT) and microchannel. The fabrication procedure for TFT and microchannel are described in section 2. Fabricated PDMS microchannel is placed on the pyrex wafer containing TFT array that was fabricated in-situ and apriori. It is important to prevent leakage from the channel. However, physical bonding is unable to provide adequate bonding force between PDMS and pyrex wafer to overcome the pressure drop in the microchannel

arising from the flow of the coolants, thus causing fluid leakage through unexpected regions of the wafer substrate. PDMS can be chemically functionalized, i.e., temporarily converted to hydrophilic surface from hydrophobic state using oxygen plasma treatment [97, 98]. In this study, PDMS microchannel and pyrex glass (which contains TFT array) are treated using oxygen plasma. The various parameters, such as, flow rate of oxygen gas, applied power for generating oxygen plasma, and treatment time, are: 10 sccm, 100 W, and 40 seconds, respectively. For best results, both PDMS and pyrex glass are cleaned twice or thrice before subjecting the substrates to RF plasma. Bonding should be performed immediately after plasma treatment to ensure that the surfaces are hydrophilic during the bonding process. No leakage of coolants was detected during the experiments after this bonding procedure was implemented.

For data acquisition of the steady state temperature data from the TFT array, wires are connected to the bond pads of the TFT array and the high speed data acquisition system. The electric wires are connected to the TFT by aligning them with the bond pads of the TFT array and placing them between two acrylic plates which contain the electric wire leads. By applying pressure using bolts and nuts the electrical wire leads were secured in place over the bond pads. Figure 3-2 shows the main test section connected to the electric wires as well as the electrical heater. It is important to connect the wires by following the appropriate polarity; that is, chromel layer works as positive polarity junction and alumel layer works as a negative polarity junction. In Figure 3-2, yellow cable and red cable are for chromel line and alumel line, respectively. If the electric cables are connected in reverse, output voltage may decrease as

temperature increases. Flexible film electrical heater (KHR-2/10-P, Omega) is attached at the bottom side of the pyrex glass to provide uniform heat flux into the microchannel. The nominal heater size is two inches (50.8 mm) and the maximum power rating is 10 W. Polymer tube with 400μm inner diameter (PM-1073, IDEX Health & Science) is connected to the inlet of the microchannel to pump coolants from the syringe pump at constant volumetric flow rate (i.e., independent of the pressure drop in the flow apparatus).
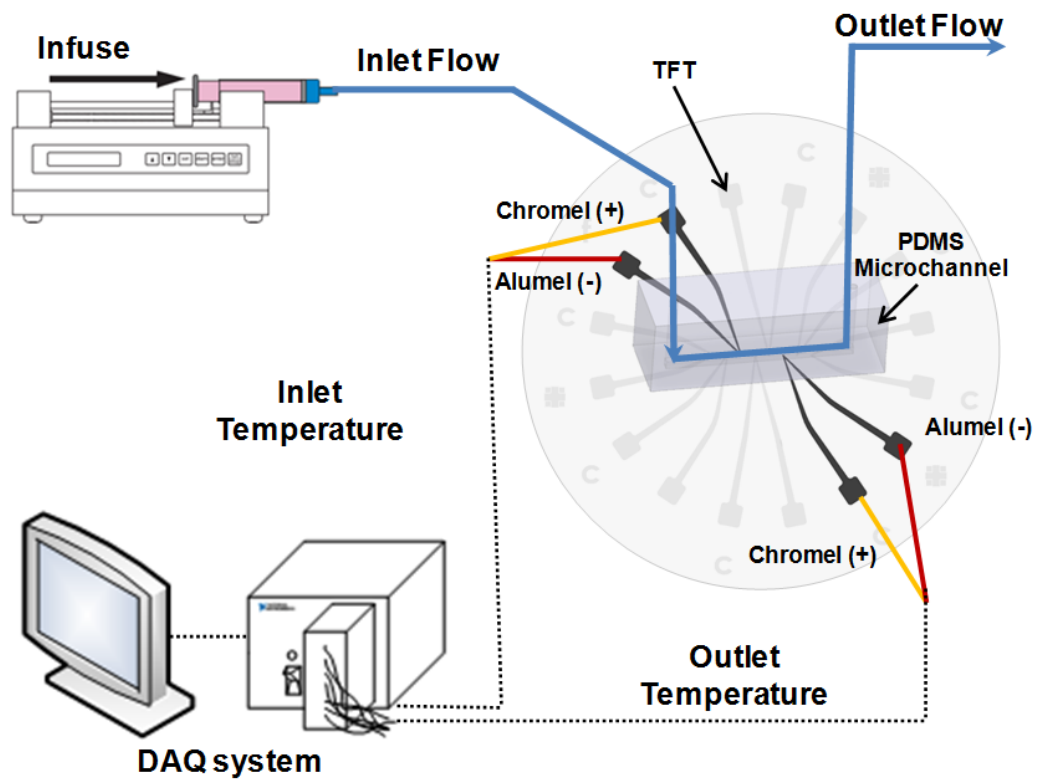
Figure 3-1 Schematic diagram of the experimental setup for measuring convective heat transfer in the microchannel (figure not to scale)
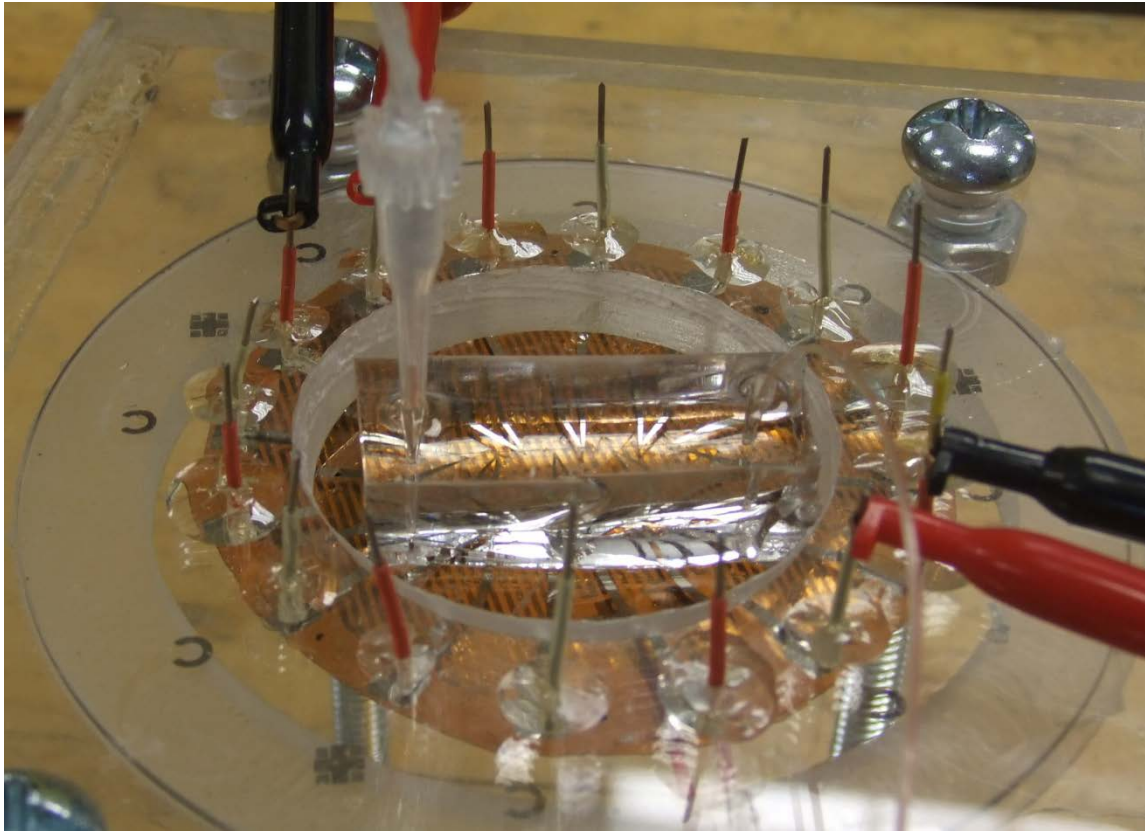
Figure 3-2 Image of the main test section. PDMS microchannel is bonded on pyrex (glass) wafer containing TFT fabricated apriori in-situ. Each junction of TFT is physically connected to electrical wires for connection to the high speed data acquisition apparatus. The acrylic plates are used to align the wires with the bond pads of the TFT array and for mounting the wires for connection to the data acquisition system. Flexible film electrical heater is attached under the wafer

Syringe pump provides constant flow rate up to 40μl/min. In order to monitor the inlet and outlet temperature of fluids, micro thermocouples (5SRTC-TT-K-40-72, Omega) are embedded with polymer tube at the inlet and outlet flow as can be seen in Figure 3-2. DAQ system collects whole information to monitor and record measured temperatures at each TFT junction as well as inlet and outlet temperature of fluids with a sampling rate of 200 Hz using LABVIEW program.

3.1.2. Data Analysis

The acquired data for the temperature readings from the TFT array are used for post-processing. Reasonable assumptions consistent with the experimental conditions are used to develop the theoretical models that are used for post-processing of the experimental data. First of all, it is assumed that top and lateral sides of the microchannel walls are insulated since PDMS has very low thermal conductivity (0.15 W/mK) and heat transfer through these sides are negligible (compared to heat loss to the coolant flowing in the microchannel). The bottom side of the microchannel is exposed to a constant heat flux boundary condition provided by the film heater. Flow rate is also considered to be constant and all surfaces are assumed to be smooth (since the flow is essentially in the laminar regime). In addition, the flow is assumed to be similar to the internal flow configuration for flow between two infinite parallel flat plates since the width of microchannel is approximately 20 times larger than the height of microchannel, that are in used this study. Figure 3-3 shows the schematic of the microchannel used in this study and is used for the development of the theoretical models. Qi_n and Q_{out} represent the heat input and heat loss through the control volume due to flow of coolants and Q_w is the thermal energy input into the control volume from the heating surface. Under steady state conditions, the heat removed by the fluids should match the heat input from the heat exchanging surface in the microchannel (bottom wall of the microchannel). Since the flow is modeled to be between two infinite parallel flat plates, it is assumed that there is negligible heat loss in the lateral directions

56
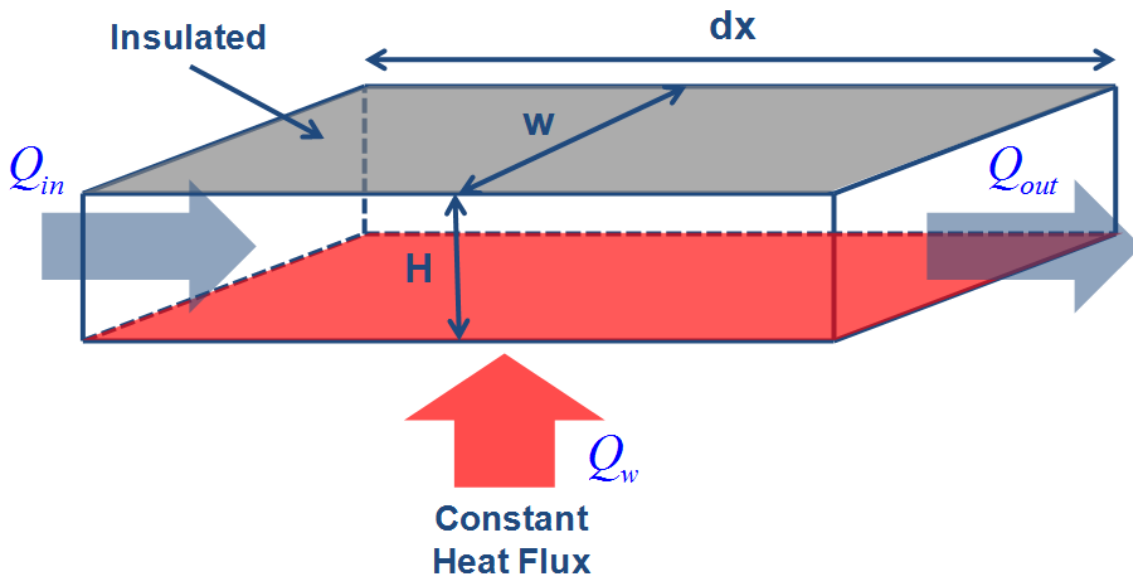
Figure 3-3 Schematic diagram for energy balance within the control volume corresponding to the extent of the microchannel geometry

By applying energy balance to the control volume:

$$Q_w + Q_{in} = Q_{out} \tag{1}$$

Q_w, Q_{in}, and Q_{out} can be expressed as follows.

$$Q_w = q_w^{"} \cdot w \cdot dx \tag{2}$$

$$Q_{in} = \rho \overline{u} H w c_p T_b \tag{3}$$

$$Q_{out} = \rho \overline{u} H w c_p T_b + \frac{\partial}{\partial x} \left(\rho \overline{u} H w c_p T_b \right) dx \tag{4}$$

From equation (2) ~ equation (4), w and H corresponds to the width and height of the microchannel, respectively. Heat removal rate (heat removal flux) is represented by $q_w^{"}$. The density and specific heat capacity of the fluids (either pure water or nanofluids) is denoted as ρ and c_p, respectively. Also, $\overline{u}$ and T_b represent flow velocity and bulk

mean temperature of flowing fluids, respectively. Since this energy balance analysis in the control volume is conducted within infinitesimally small segment along the flow direction, Taylor series expansion is applied to derive outgoing heat energy (Q_{out}) and by neglecting the higher order terms (above the second derivative). If we assume all thermo-physical properties including density and specific heat of fluids are constant within the control volume, equation (1) is rearranged by substituting for Q_w, Q_{in}, and Q_{out} from equation (2) ~ equation (4).

$$q_w^{''} \cdot w \cdot dx + \rho \overline{u} H w c_p T_b = \rho \overline{u} H w c_p T_b + \frac{\partial}{\partial x}\left(\rho \overline{u} H w c_p T_b\right) dx \tag{5}$$

$$q_w^{''} = \rho \overline{u} H c_p \frac{\partial T_b}{\partial x} \tag{6}$$

Equation (6) shows that the gradient of fluid temperature, $\frac{\partial T_b}{\partial x}$, is needed in order to calculate , the total heat dissipation from the bottom surface of the microchannel to the working fluids. Temperature measurements using the TFT array can be used to estimate the value of wall temperature gradient in the axial direction (flow direction): $\frac{\partial T_w}{\partial x}$.

Fortunately, for the steady state and fully developed conditions, it can be shown that $\frac{\partial T_b}{\partial x} = \frac{\partial T_w}{\partial x}$ for internal flow under constant heat flux boundary condition[99]. Thus, the total heat dissipation from the bottom surface of the microchannel to the coolants can be calculated using the following equation.

$$q_w^{''} = \rho \overline{u} H c_p \frac{\partial T_w}{\partial x} \tag{7}$$

$$q_w'' = \rho \bar{u} H c_p \frac{\Delta T_w}{\Delta x} \qquad (8)$$

For a segment of the control volume of length, Δx, equation (7) is modified to obtain

equation (8).

In equation (8), $\frac{\Delta T_w}{\Delta x}$ is a gradient of temperature on the bottom surface of the

microchannel along the flow (axial) direction. This value of temperature gradient can be

estimated by using the temperature data recorded by the TFT array and the distance

between the thermocouple junctions in the TFT array (obtained from the mask layout

and design of the photolithography process, as described in section 2). Mean velocity, $\bar{u}$,

is directly calculated from the flow rate set on the controller for the syringe

pump.Density of the nanofluids is assumed to be the same as that of the base fluid since

the mass fraction of the nanoparticles in the nanofluids coolants are not at significant

levels to have considerable effect on density.However, the other thermophysical

properties (such as the specific heat capacity, viscosity, and thermal conductivity) of

nanofluids should be evaluated carefully since literature reports have demonstrated that

mixing with minute concentration of nanoparticles to solvents can significantly change

these property values.

A general misconception in the literature relates to the decrease of specific heat

capacity of solvents when mixed with nanoparticles[100]. However, such reduction in

the values of specific heat capacity of nanofluids is potentially limited to aqueous

nanofluids – while the specific heat capacity of oil-based and molten-salt based

nanofluids have been measured to increase dramatically when mixed with nanoparticles at minute concentrations (0.1% ~ 5%).

For example, Zhou and Ni reported dramatic decrease in the specific heat capacity of aqueous nanofluids containing Al_2O_3 nanoparticles[101] and also concluded that the predictions from the simple mixing rule were consistent with the experimental observations in this study. Also, Namburu et al. observed 12 % reduction in the specific heat capacity when SiO_2 nanoparticles are dispersed in a fluid (60:40 ethylene glycol and water) [102]. It may be noted that these studies were restricted to the aqueous nanofluids. In contrast, Nelson et al. reported that the specific heat capacity of PAO (oil) was enhanced by up to 50% when mixed with exfoliated graphite (EG) nanoparticles at mass concentration of 0.6 % [18]. Subsequently, Shin and Banerjee reported enhancement of the specific heat capacity of a eutectic of lithium carbonate and potassium carbonate (62:38 ratio) by 19~24% when mixed with silica (SiO_2) nanoparticles at a mass concentration of 1% [103]. Recently, Fox et al. demonstrated similar enhancement in the specific heat capacity of ionic liquids when mixed with nanoparticles at minute mass concentrations [104].It may be noted that these results showing enhancement in the specific heat capacity of nanofluids were observed for non-aqueous nanofluids. Also, theoretical analyses have shown that the observed levels of enhancements in the specific heat capacity of nanofluids are amplified as the size of the nanoparticles are decreased, preferably below 10 nm in diameter and ideally below 5 nm in diameter (and is more likely to be higher than predicted by the simple mixing rule)[105]. If the size of the

60

nanoparticles exceeds 10 nm – the resultant mixture properties (especially for specific heat capacity) are likely to be more consistent with the simple mixing rule [105].

In order to estimate the value of the forced convective heat transfer coefficient from the experimental data, following equation (Newton's law) is utilized.

$$h_x = q''_w / \left(T_w(x) - T_b(x) \right) \tag{9}$$

At given position x, $T_w(x)$ and $T_b(x)$ represent the local temperature for the heat exchanging surface and the bulk temperature of the coolant, respectively. Temperature of the wall is directly measured using TFT and bulk fluid temperature is calculated assuming linear temperature variation along the flow direction, i.e., thermally fully developed condition. Bulk fluid temperature can be calculated using equation (10).

$$T_b(x) = T_{in} + \frac{T_{out} - T_{in}}{L} x \tag{10}$$

Dimensionless parameter, Nusselt number, is calculated using following equation:

$$Nu = \frac{hD_h}{k} \tag{11}$$

where D_h is hydraulic diameter of microchannel and k is thermal conductivity of fluids (k_f for pure water and k_{nf} for nanofluids).

3.1.3. Measurement Uncertainty

The measurement uncertainty for heat removal rate from the heat exchanging surface is evaluated by following the Kline and McClintock method [106]. The

following equation expresses the measurement uncertainty in this study that was estimated using this method.

$$w_q = \left[\left(\frac{\partial q_w}{\partial x_1} w_1 \right)^2 + \left(\frac{\partial q_w}{\partial x_2} w_2 \right)^2 + \cdots + \left(\frac{\partial q_w}{\partial x_n} w_n \right)^2 \right]^{\frac{1}{2}}$$ (12)

In equation (12), x_1, x_2, ..., and x_n represent variables which heat removal rate, q_w, depends on. In this study, those variables are density, specific heat, height of microchannel, and flow velocity. When estimating the measurement uncertainty values, thermo-physical properties of fluids such as density and specific heat capacity are considered as constants (since they are obtained from property tables). It is reasonable assumption because density and specific heat is constant for a given experimental set although they differ from each experimental run to the next (depending on the choice of coolants and their material properties). Also, the height of the microchannel is fixed and it is assumed that syringe pump provides constant flow rate. Therefore the only variable in the equation that affects the measurement uncertainty for the values of heat flux is the surface temperature gradient on the heat exchanging surface. Thus, equation (12) is reduced as follows:

$$\frac{w_q}{q_w} = \frac{w_{\left(\Delta T_w / \Delta x \right)}}{\Delta T_w / \Delta x}$$ (13)

The value for measurement uncertainty for the heat removal rate on the heat exchanging surface is estimated using equation (13) to be 13 %.

The uncertainty of convective heat transfer coefficient is derived from equation (9) and equation (14) by using Kline and McClintock's method

$$\frac{w_h}{h} = \left[\left(\frac{w_q}{q_w} \right)^2 + \left(\frac{w_{\Delta T_b}}{\Delta T_b} \right)^2 \right]^{\frac{1}{2}} \qquad (14)$$

The estimated uncertainty of the convective heat transfer coefficient calculated using equation (14) is 13.2 %. With the assumption that there is no uncertainty in hydraulic diameter of microchannel and thermal conductivity of a given coolant, the uncertainty of Nusselt number is then expected to be the same as that of the convective heat transfer coefficient

3.1.4. Experiment Details

In this experimental study, the forced convective heat transfer characteristics for the flow of two different classes of aqueous nanofluids have been explored. The two classes of aqueous nanofluids consist of: (1) SiO_2 and (2) TiO_2 nanoparticles – at several different mass concentrations. The results are compared with that of the neat solvent (DIW). As illustrated (and discussed) earlier in this section, constant heat flux is applied from the bottom of the microchannel. In order to examine the effect of heat flux, three different heat fluxes were applied by setting constant input voltage by 20 V, 25 V, and 30 V to the flexible film electrical heaters. The resistance of the heater is 450 Ω. Although resistance changes as temperature varies, it was observed that the resistance does not change significantly for the range of temperatures used in this study. Hence, the heat input can be evaluated using Ohm's Law. Hence the heat input is estimated to be

0.9 W, 1.4 W, and 2.0 W. However, heat loss from the heater to the ambient is expected to reduce the estimated value of the heat input to the microchannel under steady state conditions. These losses can be due to natural convection to the ambient air from the heater and the heat conduction within the wafer in the axial as well as transverse direction. In addition contact resistance between the heater and the wafer surface is expected to reduce the net heat input to the coolant for the same temperature drop. Since evaluation of these losses with sufficient accuracy is difficult, it is inappropriate to say input heat energy is exactly 0.9 W, 1.4 W, and 2.0 W, which is the total heat input from the heater. Instead, wall temperatures corresponding to each case of heat input has been used to represent the different boundary conditions. The wall temperatures are measured (or set to) 45 °C, 60 °C, 75 °C, corresponding to these values of the heat input.

The effect of varying the flow rates of the coolants have also been investigated, and will be represented by the corresponding Reynold's number. By setting flow rate of the syringe pump, three different sets of flow rates (30μl/min, 35μl/min, 40μl/min) were used in the experiments. All the experimental conditions including type of nanoparticles, concentrations, boundary conditions, and flow rates are listed in Table 3-1.

Table 3-1 Experimental conditions used in this study

Nanoparticles	Concentration	Base Fluid	Flow Rate	Wall Temperature
SiO_2	0.05 wt%			
	0.1 wt%			
	0.3 wt%	DIW	30μl/min	45 °C
	0.001 wt%		35μl/min	60 °C
TiO_2	0.005 wt%		40μl/min	75 °C
	0.01 wt%			
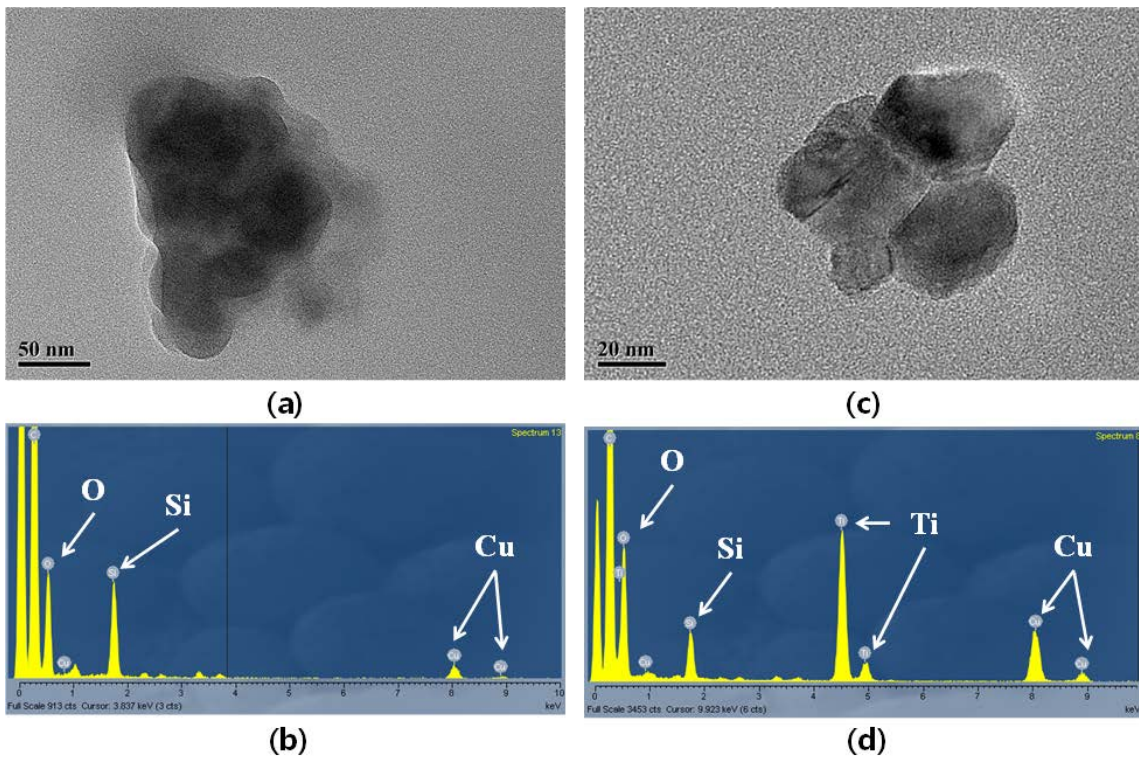
Figure 3-4 Transmission Electron Microscopy (TEM) images of: (a) SiO₂ and (c) TiO₂ nanoparticles used in this study; Corresponding Energy Dispersive X-Ray (EDX) spectroscopy measurement for (b) SiO₂ and (d) TiO₂ nanoparticles

The nanoparticles used in this study are shown in Figure 3-4. The presence of copper in the EDX measurements in Figure 3-4 (b) and (d) arises from the copper contained in the TEM grid (which is composed of copper). Since this grid is coated with silicon, silicon peak is also found in Figure 3-4 (d) when measuring the chemical composition of the samples containing TiO_2 nanoparticles.

As discussed earlier, thermo-physical properties of nanofluids can be significantly different from those of the neat solvent. Density of nanofluids is considered to be that of DIW (as discussed earlier) due to the small mass concentration of nanoparticles, being less than 0.5 %. The density of water is assumed to be at a constant value of 998.2 kg/m^3(for the range of temperature in this study) –although it varies marginally with the operating (or mean film) temperature.Thermal conductivity of water is also considered to be at a constant value of 0.58 W/m·K. However, dynamic viscosity of water changes significantly with temperature. Thus, the following equations are used to evaluate the dynamic viscosity of water [107].

$$\mu = A10^{B/(T-C)} \tag{15}$$

In equation (15), μ is the dynamic viscosity of water, T is absolute temperature of water, and A, B, and C are constants. The values of the constant are A = 2.414 × 10^{-5} N·s/m^2, B = 247.8 K, and C = 140 K.The prediction from this equation match the physical values of the viscosity of water to within ± 2.5 %for the temperature range from 0 °C to 370 °C.

Thermal conductivity, viscosity, and specific heat capacity values of aqueous nanofluids are known to be significantly different from those of DIW. Thus, care should be taken to determine these properties. For SiO_2 nanofluids, experimental data for the

specific heat capacity values are available in the literature. Vajjha and Das suggested a correlation for the specific heat capacity of SiO_2 nanofluids based on their experimental data, which is valid from 315 K to 363 K, and at volume concentrations ranging from 0~ 10% [108]. Correlations for the specific heat capacity of aqueous silica nanofluids as a function of particle concentration and temperature are expressed in Equation (16) and the values of the fitting coefficients are summarized in Table 3-2. It is known that the specific heat capacity of SiO_2 nanoparticles are higher by 4 ~ 10% (depending on the size of the nanoparticles) than that of the bulk SiO_2 (745 J/kg·K). In this study, the constants for specific heat capacity of SiO_2 nanoparticles ($C_{p,s}$) and base fluid ($C_{p,f}$, DIW) are estimated to be 819.5 J/kg·K and 4182 J/kg·K, respectively.

$$\frac{C_{p,nf}}{C_{p,f}} = \frac{AT + B\left(\frac{C_{p,s}}{C_{p,f}}\right)}{C + \phi} \tag{16}$$

Table 3-2 Fitting coefficients for equation (16)

A	B	C	Maximum Error [%]	Average Absolute Error [%]
0.001769	1.1937	0.8021	3.1	1.5

Although numerous reports exist regarding thermal conductivity of nanofluids, these are often contradictory and this essentially remains as a controversial topic in the literature. In a recent experimental study, Ferrouillat et al. reported that thermal conductivity of water based SiO_2 nanofluids is consistent with Maxwell's effective medium theory [109]. Thermal conductivity of SiO_2 nanofluids also showed good agreement with molecular

dynamics simulation in well dispersed nanofluids [110]. Maxwell's equation is expressed as follows:

$$k = k_f \frac{k_s + 2k_f - 2(k_f - k_s)\phi}{k_s + 2k_f + (k_f - k_s)\phi}$$ (17)

Hamilton and Crosser suggested a model for non-spherical particles by introducing shape factor, β [111].

$$k = k_f \frac{k_s + (\beta-1)k_f - (\beta-1)(k_f - k_s)\phi}{k_s + (\beta-1)k_f + (k_f - k_s)\phi}$$ (18)

For spherical particles, β is 3 and equation (18) becomes identical to equation (17). In this study, thermal conductivity of SiO_2 nanofluids is evaluated by using equation (17) following Maxwell's effective medium theory for spherical nanoparitcles. In addition, Einstein suggested that the viscosity of a dilute suspension of uncharged particles is expressed as follows:

$$\mu_{nf} = \mu_f (1 + 2.5\phi)$$ (19)

Viscosity of SiO_2 nanofluids are therefore evaluated using equation (19).

Regarding aqueous TiO_2 nanofluids, adequate experimental dataforthe specific heat capacity is not available in the literature. Thus, conventional mixing model is used to evaluate the specific heat capacity of TiO_2 nanofluids [112]. Based on the literature data, mass averaged formulation – as expressed in equation (20), can also be used to predict the values for the specific heat capacity of the aqueous nanofluids [100].

$$c_{p,nf} = \frac{\phi\rho_s c_{p,s} + (1-\phi)\rho_f c_{p,f}}{\phi c_{p,s} + (1-\phi)c_{p,f}}$$ (20)

Also, the thermal conductivity and viscosity of TiO_2 nanofluids is calculated using the following correlation suggested by He et al. [113].

$$k_{n,f} = k_f \left(125.62\phi^2 + 4.82\phi + 1.0 \right) \tag{21}$$

$$\mu_{nf} = \mu_f \left(199.21\phi^2 + 4.62\phi + 1.0 \right) \tag{22}$$

Thermophysical properties of SiO_2 nanofluids and TiO_2 nanofluids calculated using equation (16) ~ equation (22) are described in Table 3-3 and Table 3-4, respectively. Since mass concentration at 0 wt% means pure solvent, properties at $\phi = 0$ wt% represent density, specific heat , thermal conductivity, and viscosity of water at room temperature (20 °C).

Table 3-3 Thermophysical properties of SiO₂ nanofluids at various mass concentration of nanoparticles at 20 °C

	$\phi = 0$ wt%	$\phi = 0.05$ wt%	$\phi = 0.1$ wt%	$\phi = 0.3$ wt%
ρ_{nf}[kg/m³]	998.2	1025.4	1052.7	1161.9
$c_{p,nf}$[J/kg·K]	4182	3978	3785	3102
k_{nf}[W/m·K]	0.58	0.61	0.65	0.81
μ_{nf}[kg/m·s]	1.01E-03	1.06E-03	1.12E-03	1.35E-03

Table 3-4 Thermophysical properties of TiO₂ nanofluids at various mass concentration of nanoparticles at 20 °C

	$\phi = 0$ wt%	$\phi = 0.001$ wt%	$\phi = 0.005$ wt%	$\phi = 0.01$ wt%
ρ_{nf}[kg/m³]	998.2	998.7	1000.9	1003.6
$c_{p,nf}$[J/kg·K]	4182	4174	4144	4106
k_{nf}[W/m·K]	0.58	0.58	0.59	0.59
μ_{nf}[kg/m·s]	1.01E-03	1.01E-03	1.02E-03	1.03E-03

3.2. Confocal Microscopy Experimental Setup

3.2.1. Experimental Setup

Either laser induced fluorescence (LIF) for flow of dyes or quantum dots (QD) can be used to estimate temperature profile at the focal plane. By stacking the images obtained at each focal plane, temperature distribution along the vertical direction of the microchannel can be obtained and used to calculate the heat flux. However, it is very difficult to obtain clear images at a chosen focal plane using normal optical microscope because of the relatively large depth of focus compared to the dimension of microchannel. Confocal laser scanning microscopy is therefore developed to obtain high resolution optical images at selective focal planes with limited depth of focus. In other words, one can acquire in-plane images with high quality for selected focal planes. The light from out-of-focus plane is blocked by small pinholes, which enables acquisition of sharper images than those obtained by conventional microscopes. As a result, it is possible to obtain clear three dimensional (3-D) images using confocal microscope.

In this study, confocal scanner unit model (CSU10, Yokogawa) which contains pinholes with 50 μm in diameter is used. Specifically, CSU10 has two disks, one with 20000 micro-lenses and the other with pinholes with same pattern as the micro-lenses, which are rotate synchronously at 1800 rpm by an electrical motor. Figure 3-5 schematically shows the operation and optical ray-diagram of the confocal scanner used in this study. The confocal microscope can produce two dimensional (2-D) confocal images since both excitation light (light from laser) and emitted light (light from the sample) pass through a single pinhole.
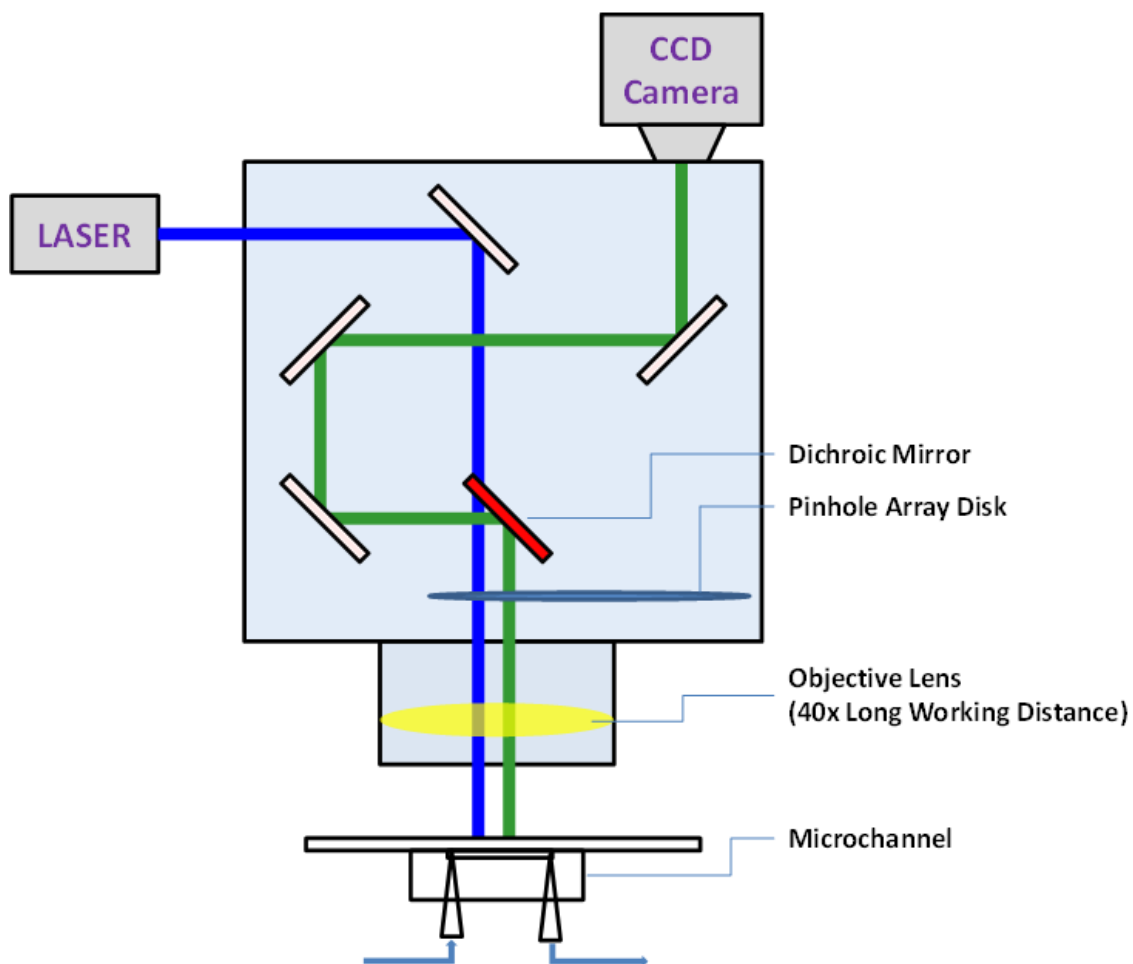
Figure 3-5 Schematic of confocal laser scanning microscopy setup

Dichroic mirror arrangement enables the reflection of specific wavelengths while transmitting rays at other wavelengths. The dichroic mirror enables correct detection of the emitted light while minimizing the noise from the excitation light. An optical microscope (BX-61, Olympus) is embedded in the confocal scanner (CSU10). Laser illumination source (150 nm select, LASERPHYSICS) is used to provide illumination with 488 nm wavelength (blue light) at 50 mW illumination power. CCD camera (UP-1830, UNIQ) is used for image acquisition at 1024 × 1024 pixel resolution at a frame

rate of 30 Hz. Spatial resolution of this CCD camera is 6.45µm by 6.45µm. The optical

arrangement consists of an array of objective lens and a 40× long working distance lens

(LUCPLFLN 40X PH, Olympus). Working distance of this lens arrangement is 2.7 mm

~ 4 mm and numerical aperture is 0.6. Since it is a dry lens (not an oil immersion lens),

this lens arrangement can be used for operation in air. The main test section (i.e.,

microchannel integrated with TFT on pyrex glass substrate) is mounted in the confocal

microscopy stage, as shown in Figure 3-6.
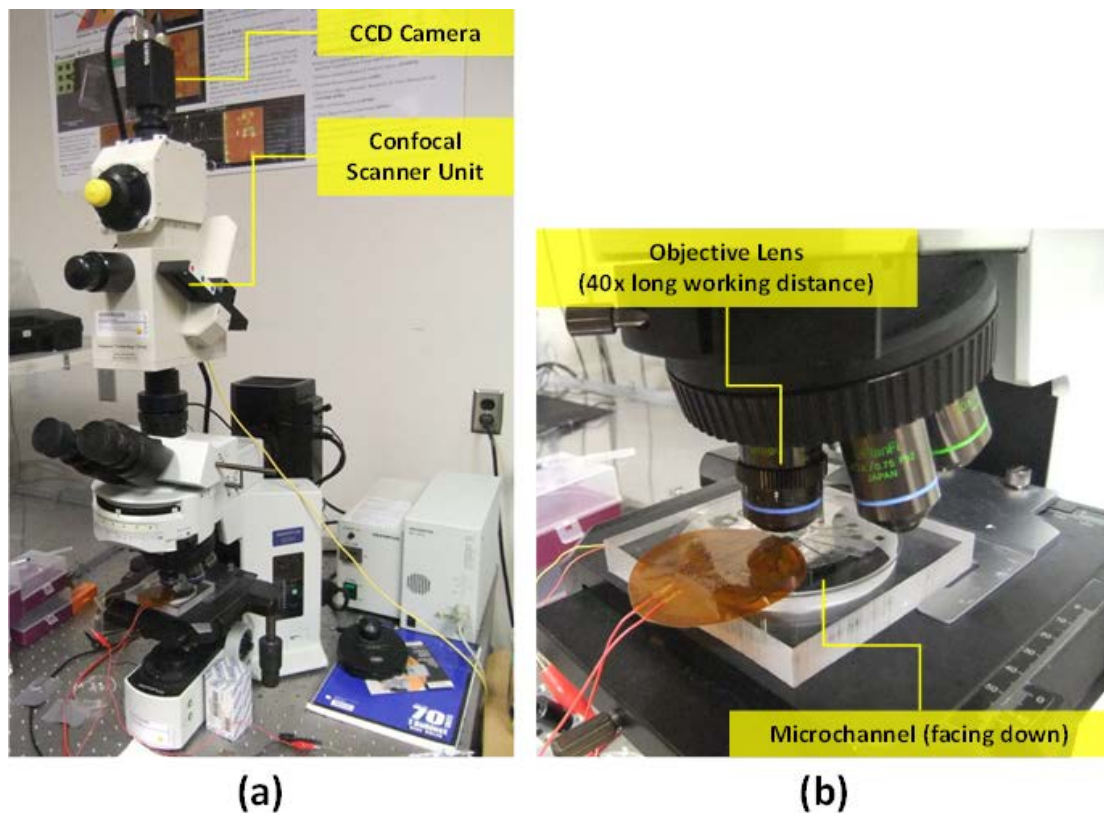
Figure 3-6 Images of experimental set-up integrated with the confocal microscope apparatus that was used in the current study: (a) CCD camera and confocal scanner unit. (b) Microchannel experimental setup placed under the objective lens

As shown in Figure 3-6 (b), the microchannel apparatus is facing down on the confocal microscopy stage – so that illumination from laser source can excite the fluorescence dye for the LIF experiments. Although it is possible to place the microchannel experimental apparatus in face-up orientation, the optical path in the PDMS substrate can be distorted and considerable extinction of the incident illumination would occur. These can also cause significant reduction in signal-to-noise ratio in this orientation. Flexible film heater (KHR-2/10-P, Omega) is attached under the inlet port to minimize interference with the incident illumination.

Images are acquired and analyzed using commercial software (QED image v1.8.3, Media Cybernetics). This software is used to control the motion of the mounting stage in the z-direction. This software therefore enables the selection of location of focal planes for image acquisition. Once the extents of the image acquisition (bottom plane and the top plane) as well as z-step (distance between each plane) are specified in the software settings, a series of confocal images are acquired. Axial resolution of the images is calculated using the following equation:

$$D_z = 1.4 \cdot \lambda \cdot \eta / \left(NA^2 \right) \tag{23}$$

In this equation, NA is the numerical aperture of the objective lens, λ is the wavelength of signal, and η is the refractive index of the immersion medium (air, 1.0; water, 1.33; oil, 1.515). Suggested z-step is expressed as equation (24).

$$D_{z\_suggest} = 1.4 \cdot \lambda \cdot \eta / \left(NA^2 \right) / 2.3 \tag{24}$$

73

In this study, the values for the wavelength of signal (λ), the refractive index of the immersion medium (η), and numerical aperture (NA) are: 0.488 μm, 1.0, and 0.6, respectively when 40x long working distance object lens is used. The z-step is set to a value of 0.83 μm. Thus, confocal images were obtained in steps of ~0.825 μm. In other words, the steady state temperature profile within the microchannel is measured with a spatial resolution of 0.825 μm.

Figure 3-7 shows the optical characteristics of fluorescence dyes used in this study. In this study, fluorecein dye (46955 FLUKA, Sigma-Aldrich) is used for the LIF measurements. The dye-particles are dissolved in deionized water at 0.1 % mass concentration. Spectral characteristics of fluorecein are shown in Figure 3-7 (a). For the experiments using quantum dots, water-soluble CdSe quantum dots (Q21341MP, Invitrogen) were employed in this study. The stock solution provided by manufacturer is rated for a concentration of 8μM. Since this quantum dot solution is expensive, it is diluted to 0.2μM concentration (1:40) in the experiments performed in this study. Fluorescence characteristic of these quantum dots is shown in Figure 3-7 (b). According to manufacturer's specification, the maximum temperature rating of the QD nanoparticles for providing stable emission is 60 °C. Above this temperature, it is stable for 1 hour at 65 °C and for 5 minutes at 100 °C. Since temperature range in the current study does not exceed 80 °C, this material is suitable for the current study. Figure 3-7 (a) and (b), shows that both fluorecein dyes and CdSe quantum dots emit green light (510 ~ 550 nm) when excited by blue light (488 nm).
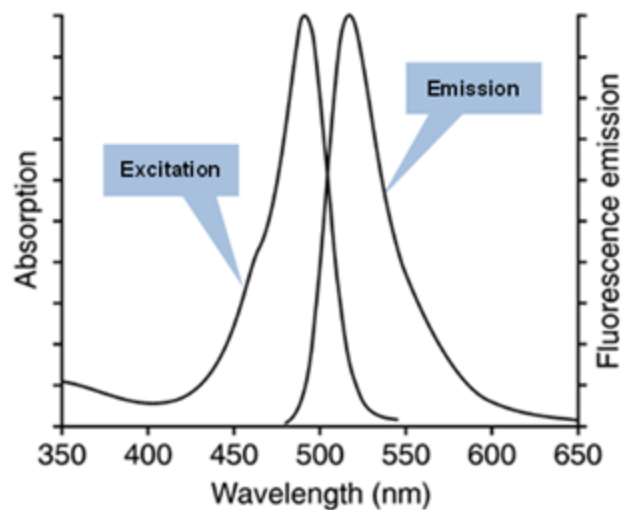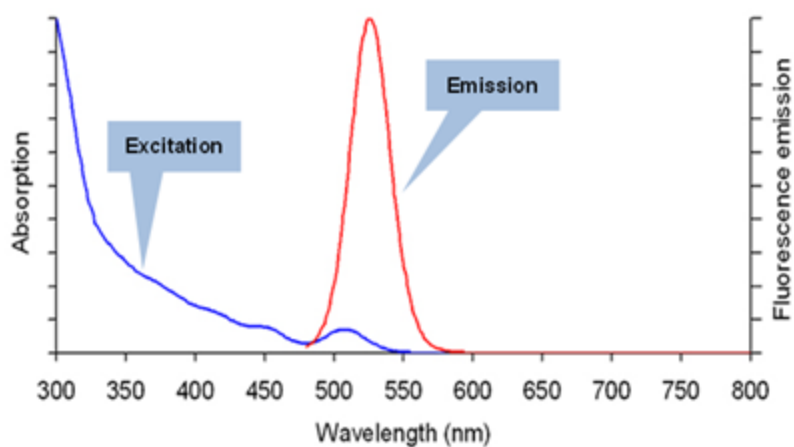
Figure 3-7 Spectral excitation and emission characteristics of (a) Fluorecein; and (b) CdSe quantum dot (QD); used in this study

The experiments were performed at a flow rate of 40 µl/min for various heat input (and wall temperature) conditions. Constant voltage is applied to the flexible film electrical heater in order to provide heat input into the microchannel apparatus. The

voltage values are fixed at 20 V, 30 V, and 40 V. Temperature is measured using a calibrated TFT array that was fabricated in-situ on the pyrex (glass) wafer. Based on the steady state surface temperature measurements obtained from the TFT array, the intensity values in the acquired images were calibrated for temperature measurement. This was achieved by using the acquired confocal images and the corresponding intensity values recorded for the bottom surface (heat exchanging surface) of the microchannel (and was correlated to the TFT data).

Literature reports have shownthat sensing oflocal temperature changescan be performed in biological applications using a single quantum dot [88]. Although this demonstrated that local temperature values can be measured using individual QD, emission characteristics are known tovary between individual QD. This variation is considered to be inherent due to the variation of size and shape of individual QD[114, 115]. Thus, it is inappropriate to evaluate absolute temperature using a single quantum dot (or the spatial gradient in temperature between two QD), and rather the relative temporal variation of temperature at a particular location can be measured using a single QD. The number of QD particles required to achieve a desired precision can be evaluated statistically. Literature reports have shown that 1200 QD particles are needed to measure temperature in a fluid to within 1 °C precision [88].

3.2.2. *Data Analysis and Measurement Uncertainty*

Post processing of the acquired images is performed by utilizing MATLAB (version R2012a). The values of the image intensity is averaged for each image and

plotted as a function of height of the microchannel. Measurement uncertainty is calculated using equation (25), by following the Kline and McClintock's method

$$\text{uncertainty} = \frac{\Delta Intensity}{Intensity} \qquad (25)$$

Maximum value of measurement uncertainty is estimated to be 5.2 % and 17.3 % for experiments using fluorecein dye (LIF) and quantum dots (QD), respectively.

It is unable to find uncertainty value for a focusing mechanism (a stepping motor and ball screw) in a user's manual. However, the recommended finest adjustment scale is 1 μm with 0.01 μm resolution according to user's manual. Also, the smallest value for adjusting focusing is 0.02 μm.

4. RESULTS[*]

4.1. Experiments Using Thin Film Thermocouples (TFT)

4.1.1. Calibration of TFT

Infrared (IR) camera (FLIR i50, FLIR SYSTEMS) is used as a reference for calibration of the TFT readings. The emissivity of pyrex glass is set to 0.95 in the control software for the IR camera. Every TFT is calibrated before use. Representative data for the calibration results is shown in Table 4-1, Figure 4-1, and Figure 4-2. Figure 4-1 shows images obtained from IR camera at room temperature and three different set wall temperatures.

In Figure 4-1 (b) ~ (d), it can be observed that pyrex wafer is heated, which is represented by red color. However, PDMS microchannel is observed to be at a constant temperature and is comparable to the room temperature even after heating for a considerable amount of time. To elaborate further, the color of PDMS microchannel is blue or green for all of images regardless of wall temperature. These images provide important clues about the assumptions used in the theoretical models that were developed in this study. As stated in Section 3.2, it is assumed that the upper surface of microchannels is insulated. By checking images obtained from IR camera, this assumption is validated since the upper surface of microchannel (i.e., the PDMS

---

substrate) remains at near room temperature even after the Pyrex wafer is heated from below.
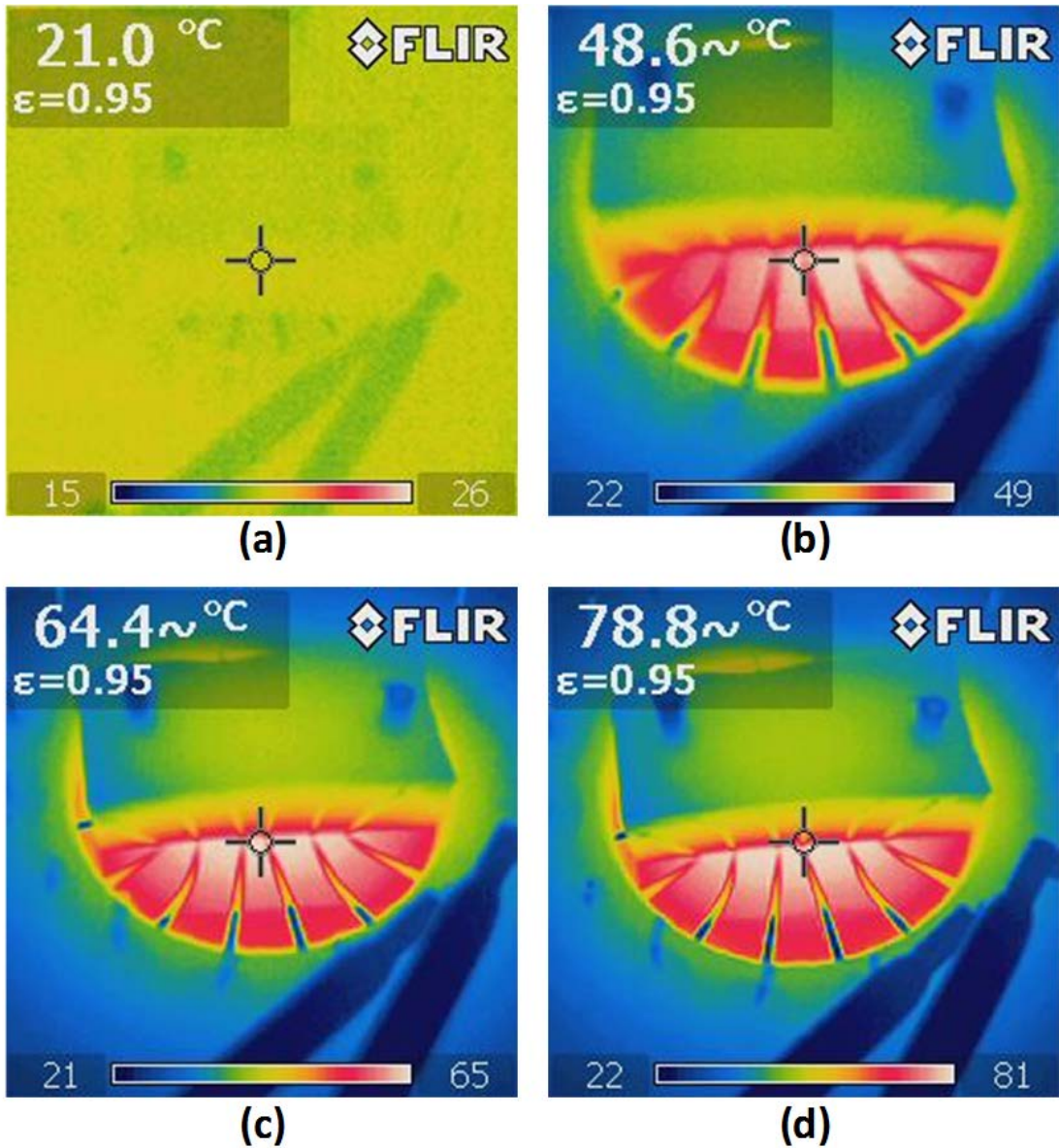
Figure 4-1 Images obtained from an IR camerafor different wall temperatures of pyrex wafer: (a) At room temperature, (b) $T_w \approx 45$ °C, (c) $T_w \approx 60$ °C, and (d) $T_w \approx 75$ °C

Table 4-1 Calibration of TFT array: Temperatures measured from IR camera and TFT before and after calibration

Reference Temperature from IR Camera [°C]	Ch 5			Ch6		
	T_{raw} [°C]	$T_{calibrated}$ [°C]	error	T_{raw} [°C]	$T_{calibrated}$ [°C]	error
21.0	27.4	20.9	-0.7%	27.4	20.9	-0.4%
48.6	47.5	49.4	1.7%	48.6	49.1	1.1%
64.4	57.2	63.3	-1.6%	59.5	63.7	-1.1%
78.8	68.3	79.2	0.5%	71.0	79.1	0.3%
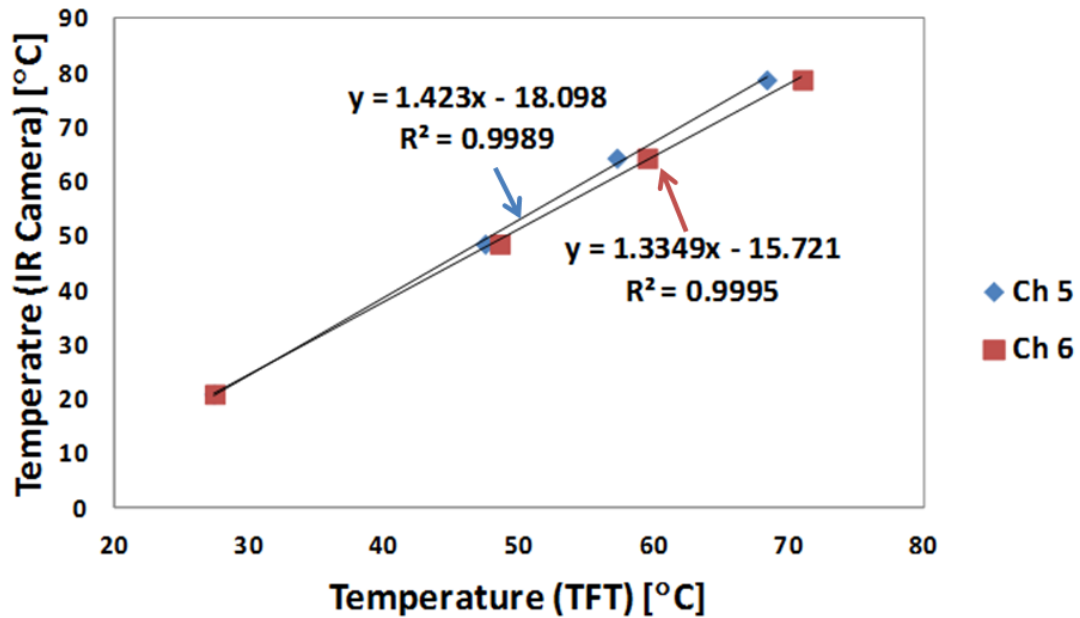
Figure 4-2 Calibration curve and equation

Calibration data is presented in Table 4-1 and Figure 4-2. The calibration data shows that TFT display excellent linearity in response with a bias error that tends to slightly under-predict the temperature of the Pyrex wafer substrate. Inspite of the bias error, the performance of TFT is quite accurate; as demonstrated by the high value of R^2

parameter in the calibration curve (more than 0.99) and relative errors between the calibrated temperature measured by TFT and the reference temperature values are within ±1.7 %. Since TFT can be contaminated by nanofluids, new (fresh uncontaminated) substrates with TFT were used whenever new working fluids was used. Although the performances are not exactly the same and appear to have small differences, all TFT arrays used in this study demonstrated fairly linear behavior (value of R^2 is more than 0.98 for all cases). All of the TFT arrays used in this study have very small values of variances compared to the reference temperature measured by the IR camera. Thus, it can be concluded that measured temperatures using TFT after calibration are reliable to within 1% and TFT array are suitable for the experiments performed in this study. Connections between TFT and DAQ system using electric wires are maintained for the experiments once calibration is finished – becausecalibration data could change otherwise.

4.1.2. Pure Water (DIW)

To perform baseline experiments (control experiments), forced convective heat transfer experiments were performed initially for the flow of DIW in the microchannel. In order to remove any bubbles (or dissolved gasses) in DIW which could possibly influence the results, DIW is degassed on hot plate at 200 °C before it is used for the experiments.Figure 4-3, Figure 4-4, and Figure 4-5show the axial gradient of wall temperature for each flow rate. The heat transfer values are shown in Figure 4-6 and Table 4-2.
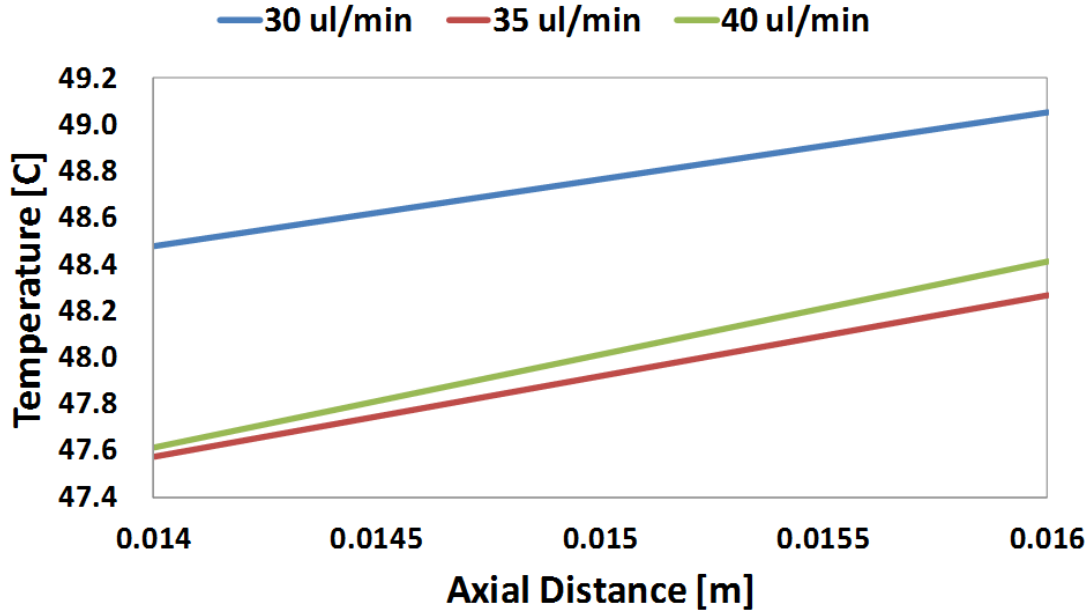
Figure 4-3 Wall temperature as a function of axial distance from the entrance of the microchannel for T$_w$≈ 45 °C when DIW is used as working fluid
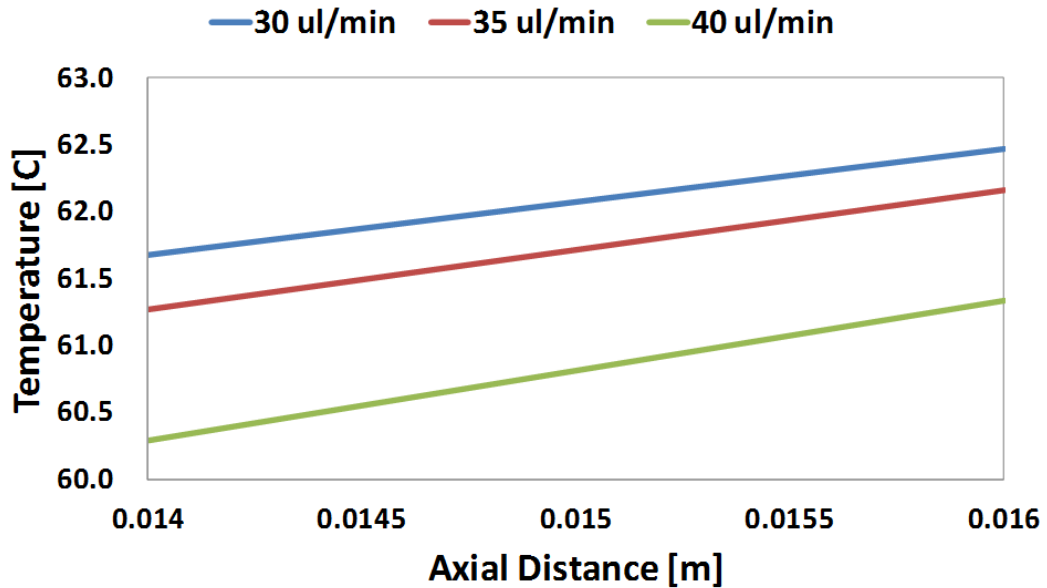
Figure 4-4 Wall temperature as a function of axial distance from the entrance of the microchannel for T$_w$≈ 60 °C when DIW is used as working fluid
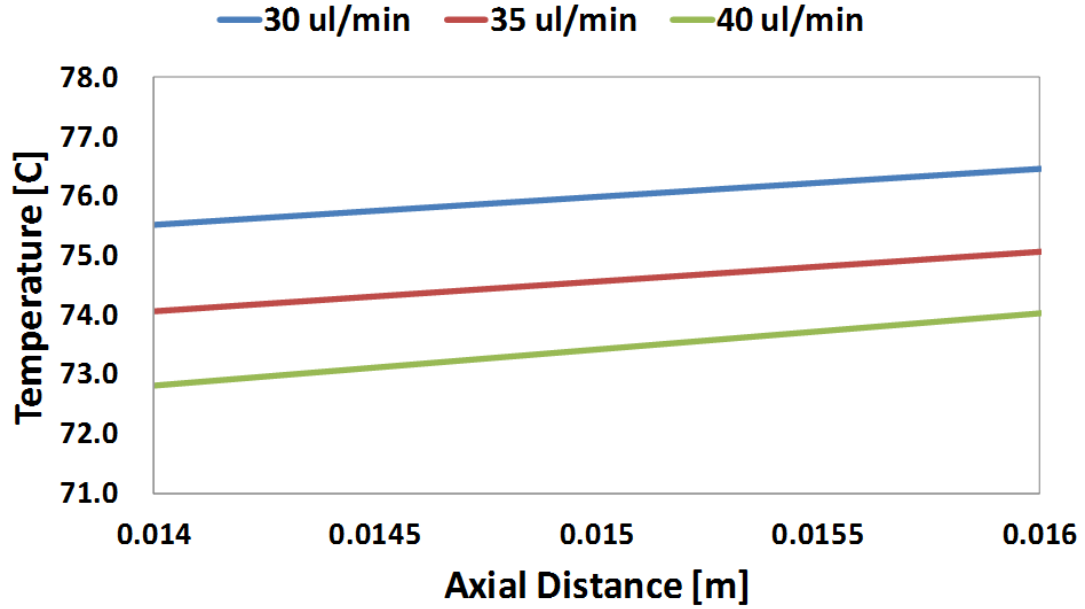
Figure 4-5 Wall temperature as a function of axial distance from the entrance of the microchannel for $T_w \approx 75\ °C$ when DIW is used as working fluid
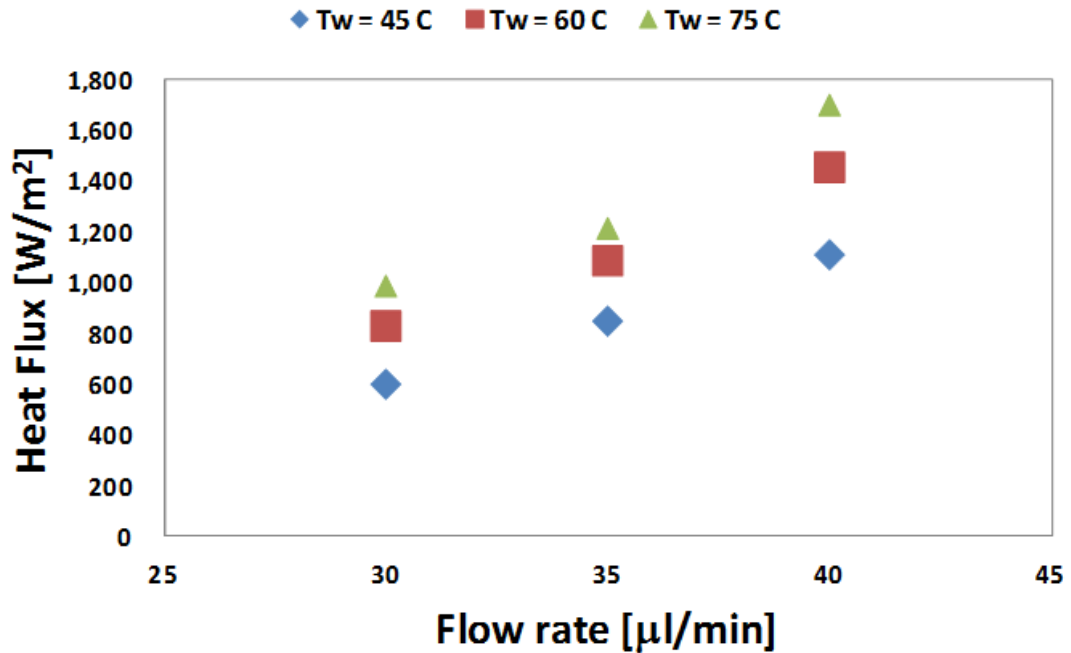
Figure 4-6 Heat removal rate as a function of flow rate and wall temperature when using DIW as a working fluid

Table 4-2 Convective heat transfer characteristics (heat removal rate, heat transfer coefficient, and Nusselt number calculated using equation (8) – equation (11)) for flow of DIW in a rectangular microchannel at different wall temperatures and different flow rates

T_w [°C]	Flow Rate [ml/min]	Heat Flux [W/m^2]	h [W/m^{2}K]	Nu
	30	599	31	0.006
45	35	734	41	0.008
	40	1012	58	0.011
	30	828	29	0.005
60	35	1085	39	0.007
	40	1452	53	0.010
	30	986	26	0.005
75	35	1212	33	0.006
	40	1697	47	0.009

It is apparent from the plots for the TFT measurements that DIW is progressively heated as it passes through the heated microchannel. Values for heat transfer coefficient and Nusselt number are calculated using equations introduced in Section 3.2 and the calculated values of heat removal rate is shown in Figure 4-6. Experimental results for convective heat transfer of DIW in the rectangular microchannel are summarized in Table 4-2. Figure 4-6 and Table 4-2 show that the heat flux increases as the flow rate increases. Higher heat flux values are obtained at higher wall temperature values. Nusselt number is observed to be vary from 0.005 ~ 0.11 which is smaller than the theoretical predictions (Nu = 5.384, cf. Appendix B).

Considering Reynolds number in this experiment is extremely small ranging from 1.7 to 3.3, this is definitely in the creeping flow regime for laminar forced internal

flows and convective heat transfer. In recent report, Sahu et al. summarized various correlations for prediction of the entrance length for low Reynolds number flows [116]. Most predictions from the correlations for entrance length are consistent with experimental measurements – essentially providing the coefficient of determination up to 0.898. One of them, Sparrow et al. suggested the following correlation [117]:

$$\frac{L}{D_h} = 0.056\,\text{Re} \tag{26}$$

where L is the entrance length. Following this correlation, maximum entrance length in this study is 20μm. Consideringthat the total channel length is 24 mm, the entrance length effects can be neglected. Thus, all experiments in this study can be assumed to be in the fully developed flow regime.Dimensionless parameters were used to represent the thermal-fluid flow behavior for DIW in a microchannel.Pêclet number (Pe) is a product of Reynolds number and Prandtl number. After converting all experimental data using the equations shown in section 3.2, they are plotted in a single graph. As shown in Figure 4-7 and Figure 4-8, Nusselt number values are observed to increase monotonously as a function of Pêclet number. However, prediction from theoretical (analytical) models show that Nusselt number should be constant regardless of flow rate (which is represented by Pêclet number) for fully developed internal forced convective heat transfer in microchannels in the laminar (or creeping flow regime). Furthermore, the value of Nusselt number obtained in this study for DIW is significantly smaller than the predictions from the analytical model.
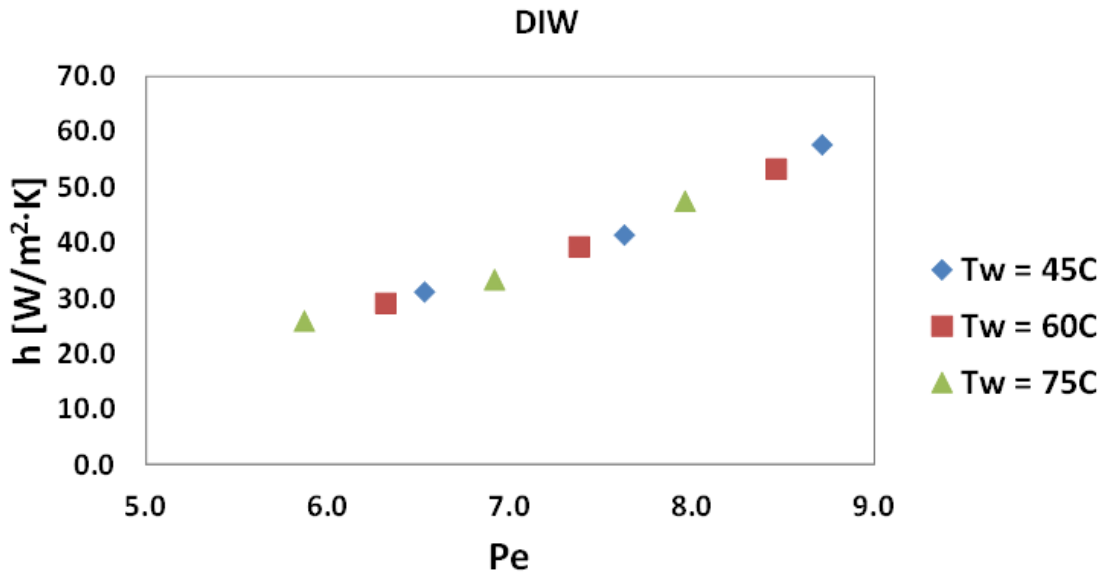
Figure 4-7 Heat transfer coefficient for DIW as a function of Pêclet number
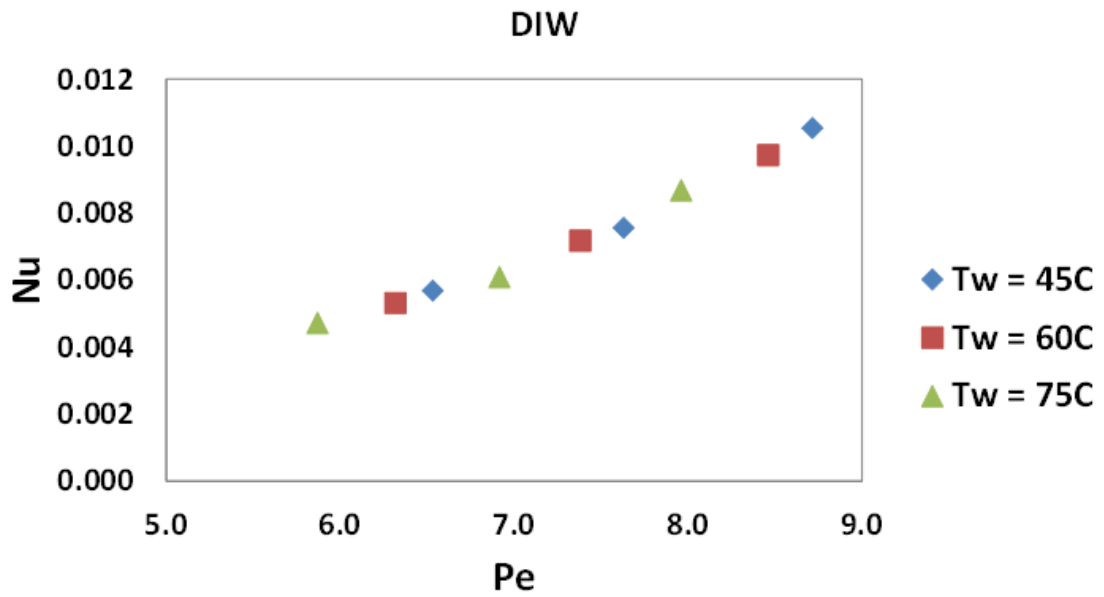
Figure 4-8 Nusselt number for DIW as a function of Pêclet number

For convective heat transfer between two parallel plates under constant heat flux boundary condition for bottom plate and insulated boundary condition for upper plate, theoretical value of Nusselt number is 5.384 (see Appendix B). Forced convective heat transfer values for flow of DIW in the rectangular microchannels are therefore observed to display anomalous behavior which is inconsistent with the predictions obtained from theoretical models. Similar discrepancies have already been reported in several literature reports [38, 39, 49, 50]. Especially, Jung et al.'s experimental data for convective heat transfer of fluids in the microchannel showed quite similar behavior to the current study[50]. Nusselt number values reported in their study was below 0.3 for pure water and below 0.5 for a mixture of water and ethylene glycol for Reynolds number less than 300. Nusselt number was observed to decrease as the Reynolds number decreased for both fluids. Nusselt number of water was under 0.1 at Reynolds number of ~10. Considering that the Reynolds number values in the current study is less than 3.3 and Nusselt number dramatically decreases with decrease in Reynolds number, the very low values of Nusselt number obtained in this study is therefore consistent with previous reports in the literature.

Qu et al. also obtained Nusselt number as low as 1~2 and argued that surface roughness is responsible for the small values of Nusselt number [38]. Nevertheless, Qu et al.'s results are different from Jung et al.'s work and both are inconsistent with the predictions from the theoretical model (i.e., the value of Nusselt number should be constant and independent of the Reynolds number). Jung et al. discussed that the low Nusselt number values (less than 0.5) indicates that the convective heat transfer

coefficient in micro/nano-channels do not linearly increase as the channel size decreases. This trend would appear to be more realistic since expectation of infinite heat transfer coefficient values (in the limit of the hydraulic diameter values approaching zero) is physically unrealistic.

Experimental results for DIW from the current study are compared to previous reported values by over-plotting them [50]. The results are compared for the different data sets (from the current study and from the literature) for different flow rates (and thus Reynolds number). The current experimental results are found to follow the same trend as the literature data as shown in Figure 4-9. The results from this study are observed to be for significantly lower values of Reynolds Number compared to the results reported in the literature.
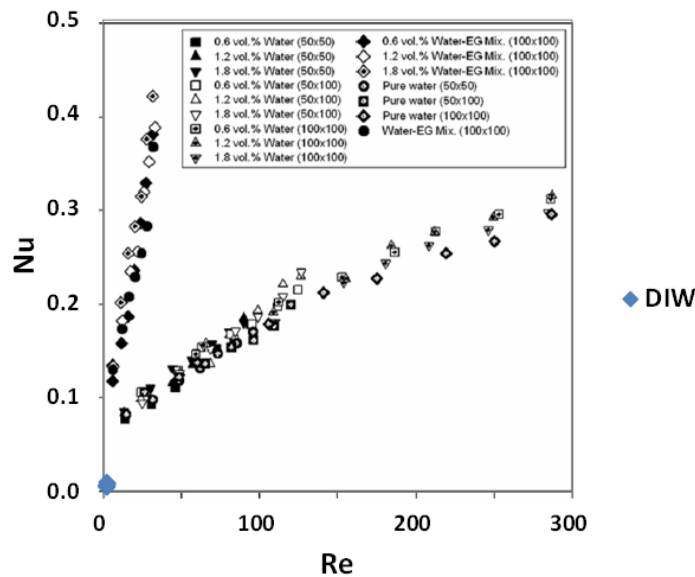
Figure 4-9 Overplot of the experimental results for DIW on previous reported values from the other literature [50]

4.1.3. SiO$_2$ Nanofluids

Experimental results for SiO$_2$ nanofluids are presented in this section. In order to investigate the role of nanofluid concentration on forced convective heat transfer, nanofluids with three different mass concentrations were used in the experiments. Figure 4-10, Figure 4-11, and Figure 4-12 show the measured temperature gradient on the heat exchanging surface using TFT for flow of SiO$_2$ nanofluids at each concentration. Wall temperature was observed to increase monotonously along the flow direction. Also, it was observed that the surface temperature decreases as flow rate increases at a given wall temperature. To elaborate, green line (which represents wall temperature for flow rate of 40 µl/min) is lower than blue line (30 µl/min) and red line (35 µl/min). This trend is observed to recur in every set of experiments except one case performed using SiO$_2$nanofluids with mass concentration of 0.3 % at a wall temperature of 60 °C, as shown in Figure 4-12 (b). This is probably due to a different ambient temperature when this experiment was performed.
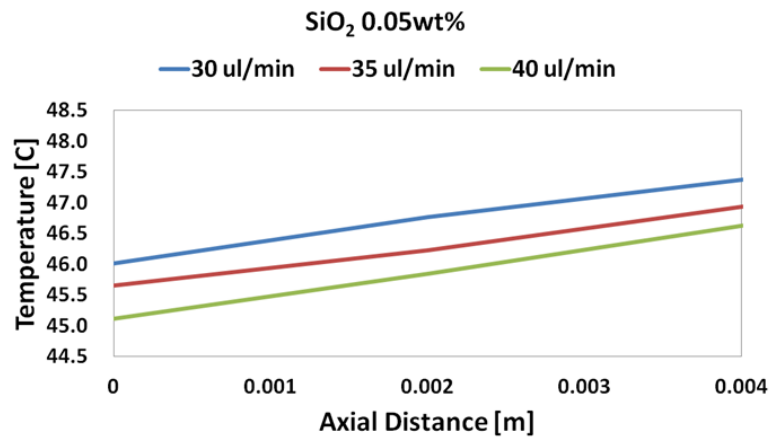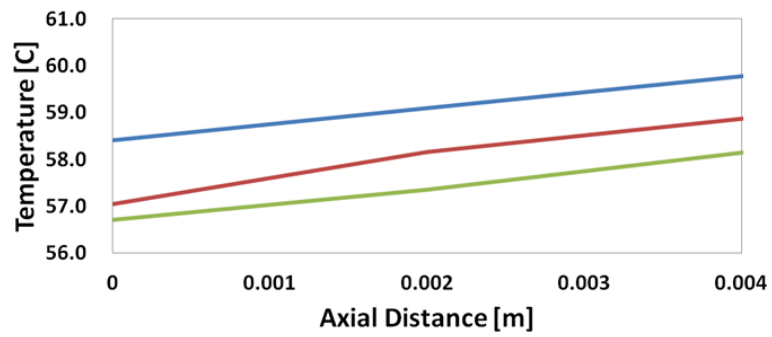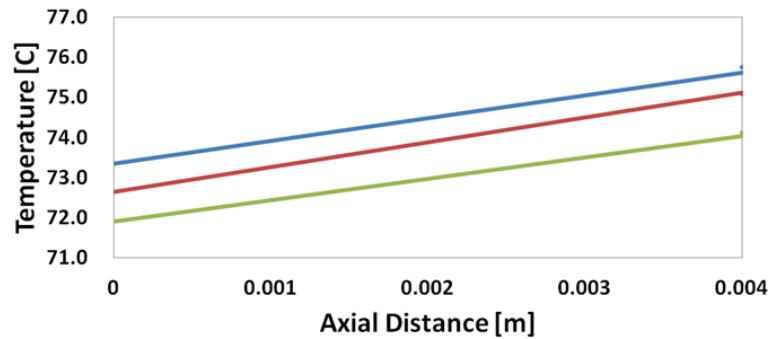
Figure 4-10 Wall temperature profile for experiments performed using SiO$_2$ nanofluid at mass concentration of 0.05 % for: (a) T$_w$ ≈ 45 °C, (b) T$_w$ ≈ 60 °C, and (c) T$_w$ ≈ 75 °C

90
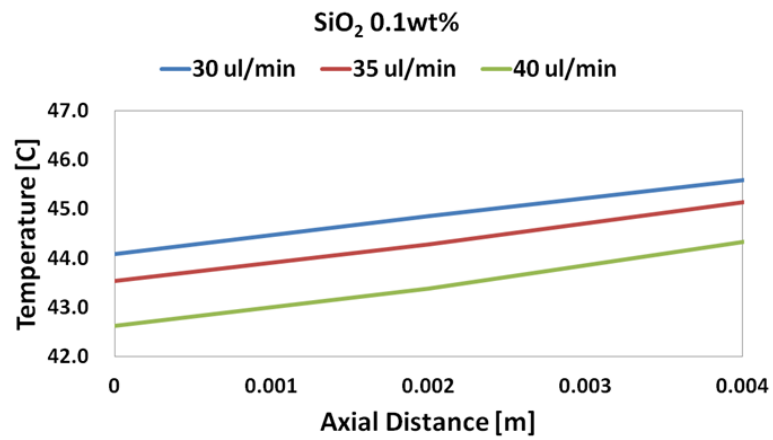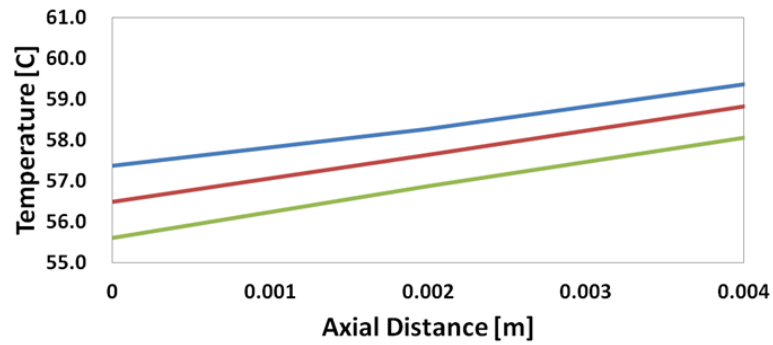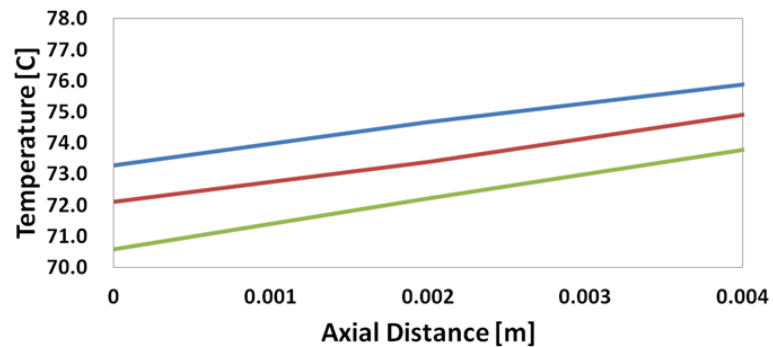
Figure 4-11 Wall temperature profile for experiments performed using SiO$_2$ nanofluid at mass concentration of 0.1 % for: (a) T$_w$ ≈ 45 °C, (b) T$_w$ ≈ 60 °C, and (c) T$_w$ ≈ 75 °C

SiO₂ 0.3wt%
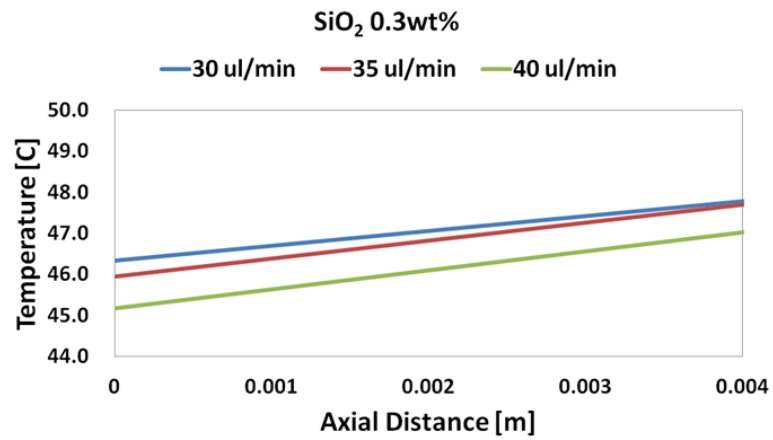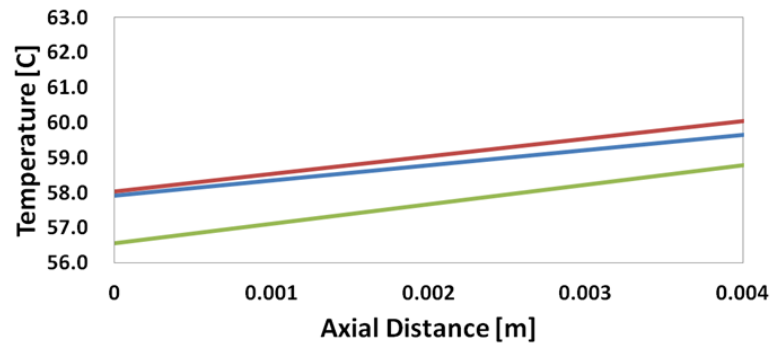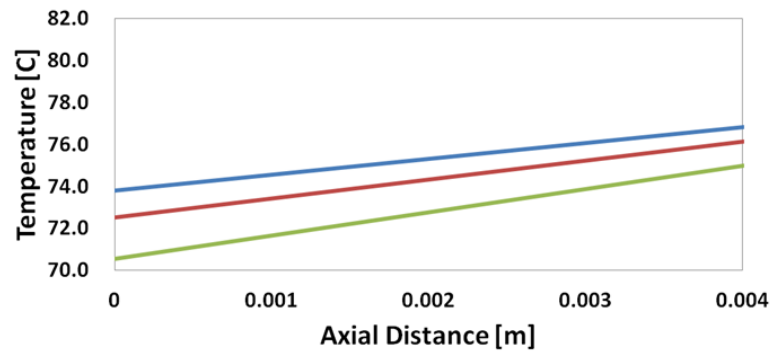
Figure 4-12 Wall temperature profile for experiments performed using SiO₂ nanofluid at mass concentration of 0.3 % for: (a) T$_w$ ≈ 45 °C, (b) T$_w$ ≈ 60 °C, and (c) T$_w$ ≈ 75 °C
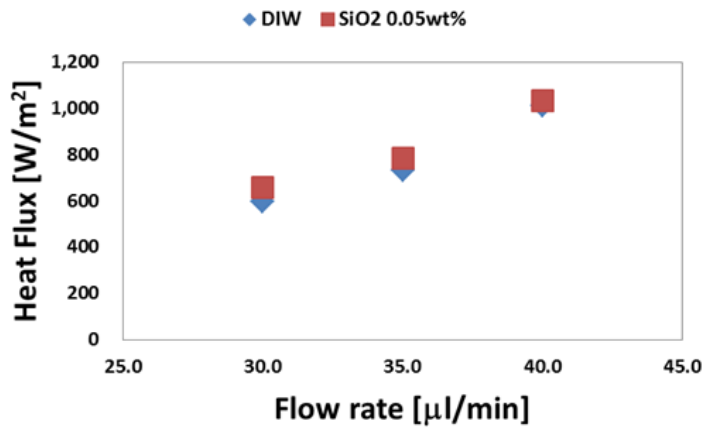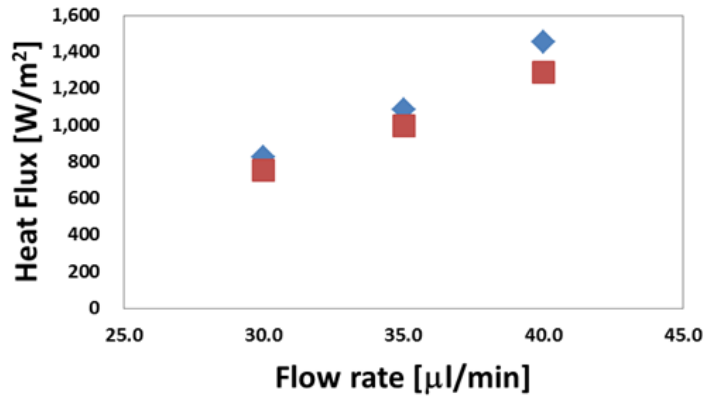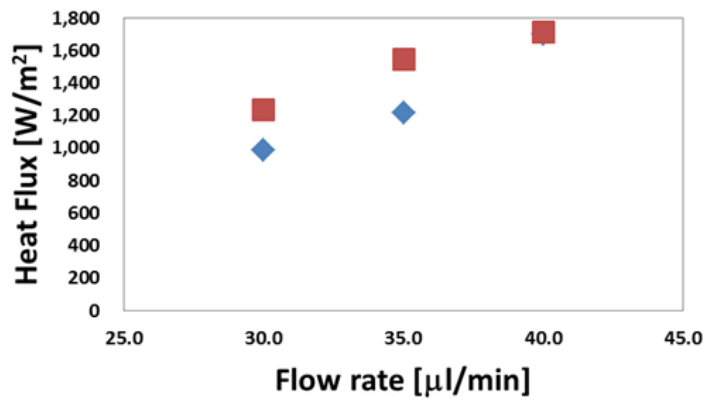
Figure 4-13 Heat flux values calculated using equation (8) plotted as a function of flow rate for SiO$_2$ nanofluids at mass concentration of 0.05% (a) T$_w$ ≈ 45 °C, (b) T$_w$ ≈ 60 °C, and (c) T$_w$ ≈ 75 °C
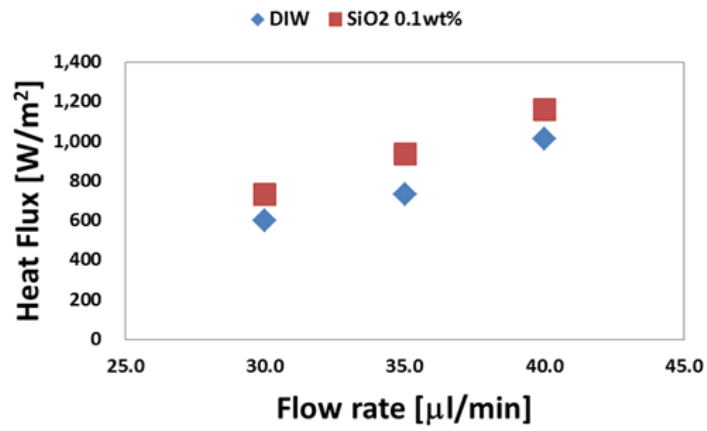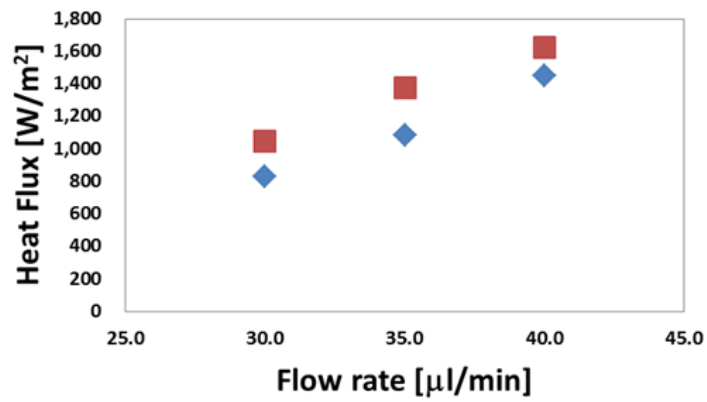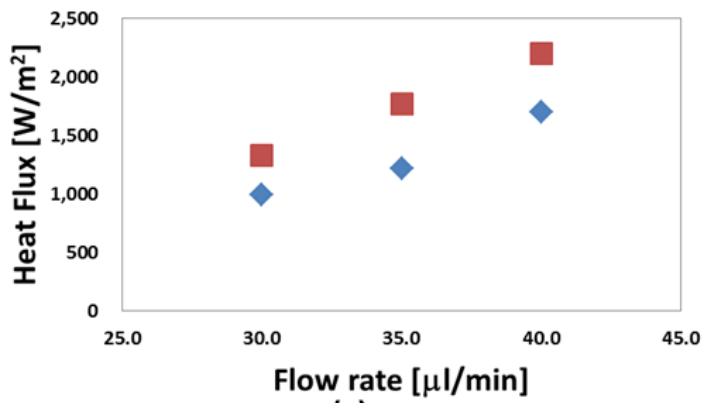
Figure 4-14 Heat flux values calculated using equation (8) plotted as a function of flow rate for SiO$_2$ nanofluids at mass concentration of 0.1 % (a) T$_w$ ≈ 45 °C, (b) T$_w$ ≈ 60 °C, and (c) T$_w$ ≈ 75 °C
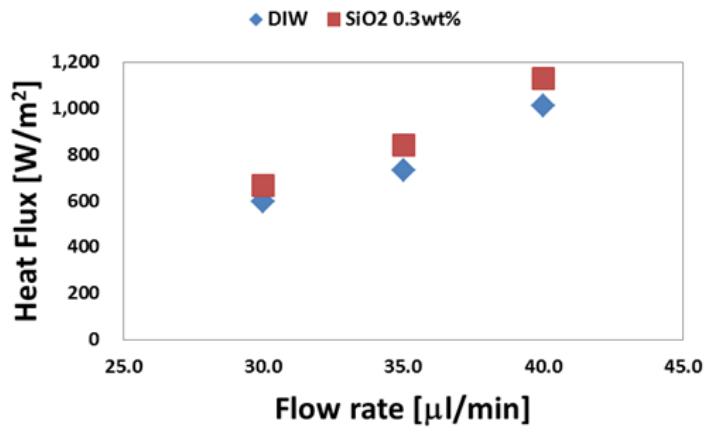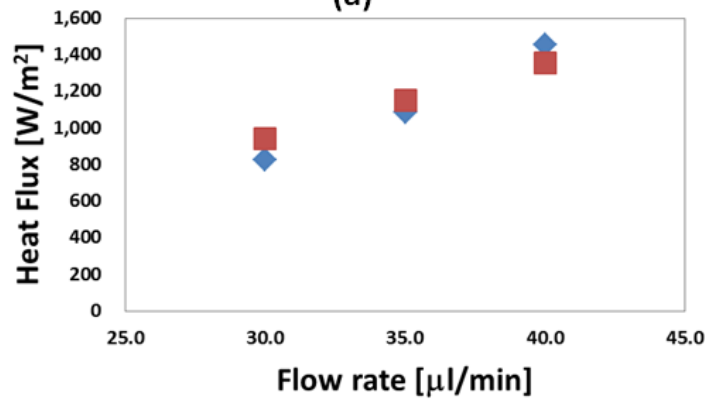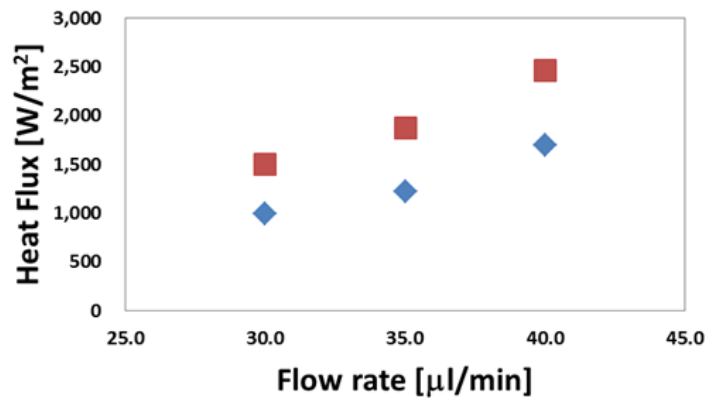
Figure 4-15 Heat flux values calculated using equation (8) plotted as a function of flow rate for SiO$_2$ nanofluids at mass concentration of 0.3 % (a) T$_w$ ≈ 45 °C, (b) T$_w$ ≈ 60 °C, and (c) T$_w$ ≈ 75 °C

95
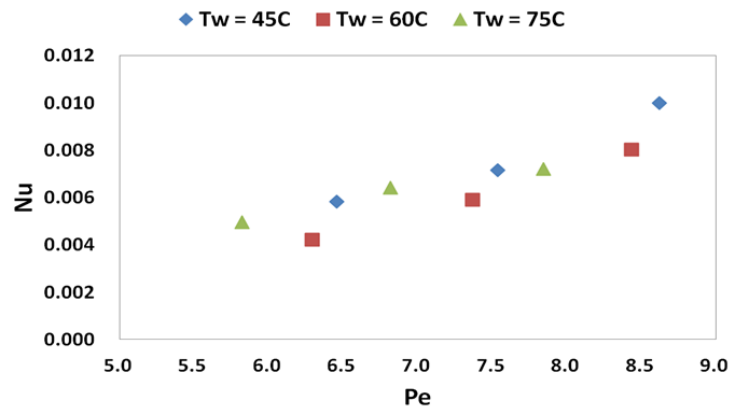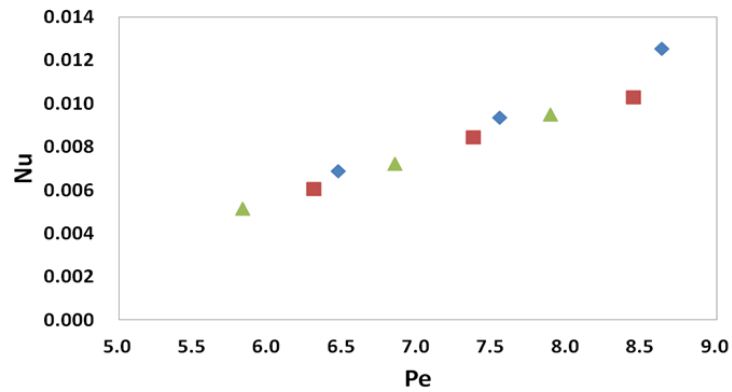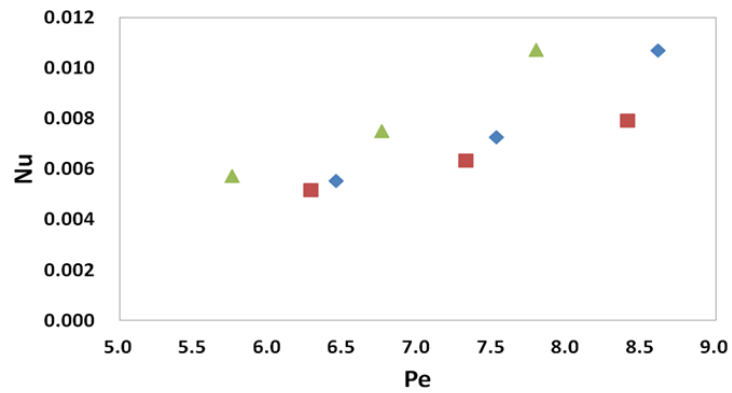
Figure 4-16 Nusselt number calculated using equation (11) as a function of Pêclet number for SiO₂ nanofluids at mass concentration of (a) 0.05 %, (b) 0.1 %, and (c) 0.3 %

Table 4-3 Heat removal rate calculated using equation (8) for various conditions including wall temperature and flow rate using SiO₂ nanofluids at mass concentration of 0.05 %, 0.1 %, and 0.3 % (enhancement levels in braces)

T_w [°C]	Flow Rate [µl/min]	Heat Flux [W/m²]		
		SiO₂ 0.05 %	SiO₂ 0.1 %	SiO₂ 0.3 %
45	30	658 (9.9%)	730 (21.9%)	666 (11.2%)
	35	787 (7.1%)	938 (27.8%)	843 (14.9%)
	40	1033 (2.1%)	1163 (14.9%)	1132 (11.8%)
60	30	756 (-8.8%)	1045 (26.2%)	940 (13.5%)
	35	995 (-8.2%)	1379 (27.1%)	1149 (5.9%)
	40	1292 (-11.1%)	1621 (11.6%)	1354 (-6.7%)
75	30	1232 (25.0%)	1324 (34.3%)	1496 (51.8%)
	35	1544 (27.4%)	1762 (45.3%)	1873 (54.5%)
	40	1710 (0.8%)	2196 (29.4%)	2454 (44.6%)

Table 4-4 Convective heat transfer coefficient calculated using equation (9) for various conditions including wall temperature and flow rate using using SiO₂ nanofluids at mass concentration of 0.05 %, 0.1 %, and 0.3 % (enhancement levels in braces)

T_w [°C]	Flow Rate [µl/min]	h [W/m²K]		
		SiO₂ 0.05 %	SiO₂ 0.1 %	SiO₂ 0.3 %
45	30	33 (5.2%)	40 (27.0%)	34 (10.6%)
	35	40 (-2.8%)	54 (29.6%)	45 (9.5%)
	40	56 (-2.7%)	72 (24.7%)	67 (15.9%)
60	30	24 (-18.4%)	35 (19.5%)	32 (10.9%)
	35	33 (-15.8%)	48 (23.2%)	40 (0.7%)
	40	45 (-15.2%)	59 (10.9%)	49 (-7.1%)
75	30	28 (7.5%)	30 (14.1%)	36 (38.1%)
	35	36 (8.0%)	41 (24.2%)	47 (40.4%)
	40	41 (-14.7%)	54 (14.5%)	67 (40.9%)

Table 4-5 Nusselt number calculated using equation (11) for various conditions including wall temperature and flow rate using SiO$_2$ nanofluids at mass concentration of 0.05 %, 0.1 %, and 0.3 % (enhancement levels in braces)

T_w [°C]	Flow Rate [μl/min]	Nu		
		SiO$_2$ 0.05 wt%	SiO$_2$ 0.1 wt%	SiO$_2$ 0.3 wt%
	30	0.006 (3.7%)	0.007 (23.5%)	0.006 (1.7%)
45	35	0.007 (-4.2%)	0.010 (26.0%)	0.008 (0.7%)
	40	0.010 (-4.1%)	0.013 (21.2%)	0.011 (6.5%)
	30	0.004 (-19.5%)	0.006 (16.2%)	0.005 (1.9%)
60	35	0.006 (-17.0%)	0.009 (19.7%)	0.007 (-7.4%)
	40	0.008 (-16.4%)	0.010 (7.8%)	0.008 (-14.7%)
	30	0.005 (6.0%)	0.005 (10.9%)	0.006 (26.9%)
75	35	0.006 (6.5%)	0.007 (20.7%)	0.008 (29.0%)
	40	0.007 (-15.9%)	0.010 (11.3%)	0.011 (29.5%)

$k_{SiO2\,0.05\,\%} / k_{DIW} = 1.014$, $k_{SiO2\,0.1\%} / k_{DIW} = 1.029$, $k_{SiO2\,0.3\,\%} / k_{DIW} = 1.088$

Heat removal rate from the heated surface to nanofluids is calculated using equation (8) and summarized in Table 4-3. This is also shown as a function of flow rate in Figure 4-13, Figure 4-14, and Figure 4-15. In addition, convective heat transfer coefficient and Nusselt number values are also calculated and summarized in Table 4-4 and Table 4-5, respectively. In these tables, percentage values between parentheses represent enhancement compared to those of DIW cases. As shown inTable 4-5, the ratio of evaluated thermal conductivity to that of pure water (0.58 W/mK) is 1.014, 1.029, and 1.088 when the mass concentration of SiO$_2$ nanoparticles are 0.05 %, 0.1 %, and 0.3 %, respectively.

Examination of the heat removal rates summarized in Table 4-3reveals marginal enhancements for SiO_2 nanofluids at mass concentration of 0.1% regardless of other experimental conditions such as flow rate and wall temperature. Enhancement of heat removal rate is larger at higher wall temperature (75 °C, 29.4 ~ 45.3 %) than low wall temperature (45 °C, 14.9 ~ 27.8 %). When the mass concentration of nanoparticles is 0.3%, enhancement in heat removal rate was also observed. It was observed that the level of enhancement is larger at higher wall temperature (75 °C, 44.6 ~ 51.8 %) than for lower wall temperatures (45 °C and 60 °C, up to 14.9 %) at this mass concentration. Marginal decrease in heat removal rate was also observed for 40 µl/min flow rate at wall temperature of 60 °C. However, heat removal rate of SiO_2 nanofluids at 0.05% is not significantly enhanced when compared to that at higher mass concentrations. At this mass concentration, heat removal capacity of the coolant tends to decrease marginally or increase only marginally at lower wall temperatures (45 °C and 60 °C, -11.1 ~ 9.8 %). Nevertheless, heat removal rate is enhanced when wall temperature is high (75 °C, 0.8 ~ 27.4 %), which is similar to that at other concentrations.

Dependence of Nusselt number on Pêclet number is shown in Figure 4-16. In general, Nusselt number tends to increase monotonously with Pêclet number for the SiO_2 nanofluids (which is similar to that of the DIW). However, this trend is found to be weaker at higher concentration (0.3 %) and at high wall temperature (75 °C).

The following results presented here are from a prior study and the following section is copied from this prior study published originally in the journal of Frontiers in Heat and Mass Transfer [118]. Experiments at lower flow rates are conducted on the

99

silicon wafer using the same experimental apparatus [118]. The calculated values of heat flux during flow of nanofluids are compared to that for DI water, and are plotted in Figure 4-17as well as listed in Table 4-6.Table 4-6 shows that the heat flux is significantly enhanced by the nanofluids at the lower temperature (~45 °C). The enhancement ranges from ~ 40 to 140% depending on the concentration of the nanoparticles and the flow rate. Although significant enhancement was observed at low wall temperatures ($T_w \approx 45$ °C), degradation of convective heat transfer was observed at higher wall temperatures ($T_w \approx 55$ °C and $T_w \approx 70$ °C). Nelson et al. suggested that the anomalous enhancements are caused by the precipitation of nanoparticles on the heat exchanging surfaces resulting in formation of nanoscale protrusions on the wafer surface[18]. The silicon wafer is originally perfectly smooth (i.e., to atomic scale roughness since it is a single crystal of silicon with exposed <100> crystal plane). These nano-scale protrusions (or roughness) enhance the effective surface area available for heat transfer – thus behaving like a nanofin. It is remarkable that nanofluids at lower concentration (0.05%) showed much higher enhancement (139.5%) than at higher mass concentration (0.1%), where the enhancement was only 21~58%. This result demonstrates that although precipitation of nanoparticles on heat exchanging surface forms nanofins and increases heat removal rate, excessive precipitation possibly leads to partial scaling (or fouling) of the heat exchanging surface as well as of the flow conduits –which causes degradation of the resulting heat transfer.Convective heat transfer coefficients were also calculated and listed in Table 4-7.
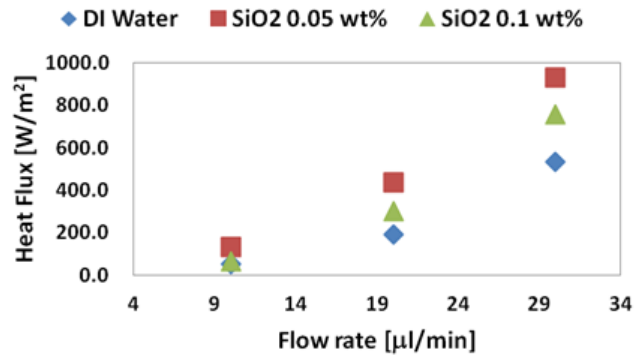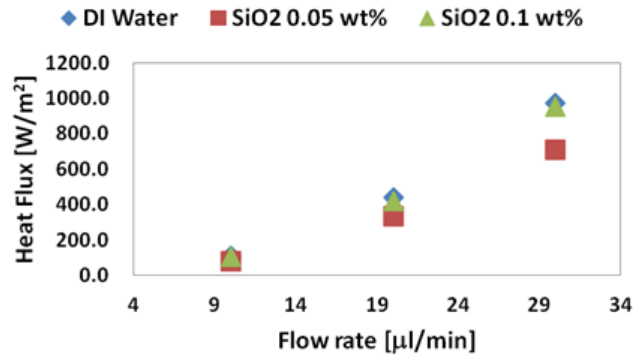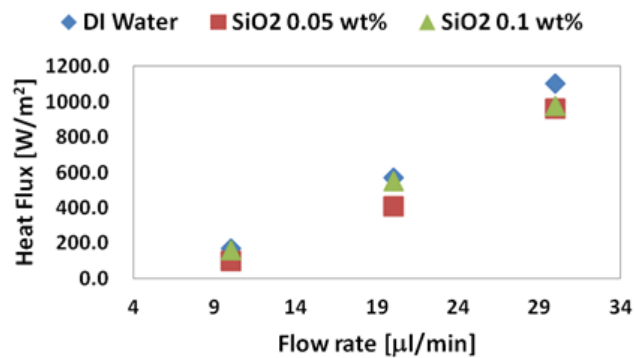
Figure 4-17 Heat flux calculated using equation (8) as a function of flow rate for: (a) $T_w \approx 45$ °C, (b) $T_w \approx 55$ °C, and (c) $T_w \approx 70$ °C

Table 4-6 Enhancement of convective heat transfer calculated using equation (9) as a function of flow rate and wall temperature for nanofluids containing SiO_2 nanoparticles with mass concentrations of 0.05 wt.% and 0.1 wt.%

T_w [°C]	Flow Rate [μl/min]	SiO_2 0.05 wt.%	SiO_2 0.1 wt.%
	10	139.50%	21.20%
45	20	129.90%	58.50%
	30	74.50%	41.60%
	10	-31.50%	-6.90%
55	20	-23.80%	-5.10%
	30	-27.10%	-2.10%
	10	-40.90%	-6.20%
70	20	-28.20%	-3.70%
	30	-12.90%	-11.30%

Table 4-7 Convective heat transfer coefficients calculated using equation (9) [W/m^{2}K]

T_w [°C]	Flow Rate [μl/min]	DI Water	SiO_2 0.05 wt.%	SiO_2 0.1 wt.%
	10	2.8	6.0	3.5
45	20	9.3	20.2	17.1
	30	29.9	47.1	49.2
	10	4.0	2.5	3.8
55	20	17.0	11.9	17
	30	40.0	27.6	42.3
	10	4.4	2.5	4.2
70	20	16.9	11.1	16.4
	30	36.7	29.7	33.4

As illustrated earlier, convective heat transfer coefficient for flow of Al_2O_3 nanofluids in microchannels at Re = 60 and Re = 200 were reported to be approximately 1000[50]and 7000~9000 [49], respectively. Hence, these two reports show that the value of heat transfer coefficient drops as Re decreases. Therefore, it can be expected that the experimental observations obtained from the current study would be significantly smaller compared to the results reported in the literature. Measurement of temperatures at inlet and outlet ports also provide an estimate for the heat flux values (however there is greater experimental uncertainly in this technique since the temperature rise is relatively "small" between the inlet and outlet ports), as shown in the following equation:

$$q_w^{''} = \frac{\dot{m}c_p\left(T_{out} - T_{in}\right)}{A} \tag{27}$$

Table 4-8 shows the comparison of the calculations from both equation (8) and equation (27). Additionally, the experimental uncertainty can be exacerbated when the thermocouples are embedded at the inlet and outlet ports, since the flow is possibly disturbed due to the presence of the thermocouples which could also influence the results. Also, the tips of each thermocouple are significantly larger (in comparison to the cross section of the microchannels); thus, leading to additional experimental uncertainties. For these reasons, the calculated values of heat flux using equation (8) and equation (27) are not always consistent – as shown in Table 4-8.

Table 4-8 Comparison of heat flux values [W/m²K] calculated using equation (8) and equation (27)

T_w [°C]	Flow Rate [μl/min]	q_{DIW}		$q_{SiO2\ 0.05wt\%}$		$q_{SiO2\ 0.1wt\%}$	
		Eq. (8)	Eq. (27)	Eq. (8)	Eq. (27)	Eq. (8)	Eq. (27)
	10	55	179	131	183	66	212
45	20	191	268	438	464	302	576
	30	535	731	934	952	758	1100
	10	112	162	76	148	104	212
55	20	439	496	335	440	417	693
	30	972	897	709	942	951	1255
	10	168	157	99	93	157	192
70	20	569	712	408	552	548	818
	30	1103	1524	960	1315	978	1666

4.1.4. *TiO₂ Nanofluids*

Experimental results for nanofluids other than SiO_2 are required to check and verify the effect of precipitation of the nanoparticles on the resulting heat transfer. In this sense, convective heat transfer characteristics of water based nanofluids containing TiO_2 nanoparticles are shown in this section. Mass concentrations used in the experiments are 0.001 %, 0.005 %, and 0.01 %. Surface temperature on the heated wall is measured using fabricated TFT. Figure 4-18, Figure 4-19, and Figure 4-20 shows the wall temperature gradient of the wall flowing TiO_2 nanofluids at mass concentration of 0.001 %, 0.005 %, and 0.01 %, respectively. The results show that wall temperature increases monotonously along flow direction for the nanofluid coolants. In general, the surface temperature gradient shows similar trend to that of DIW andSiO_2 nanofluids.
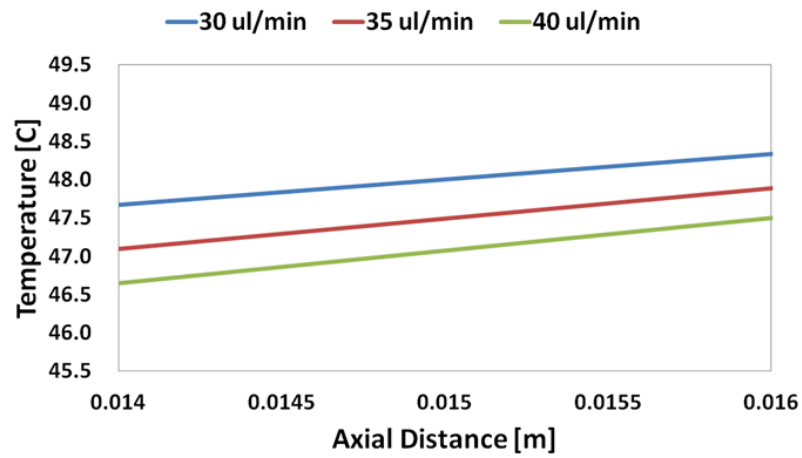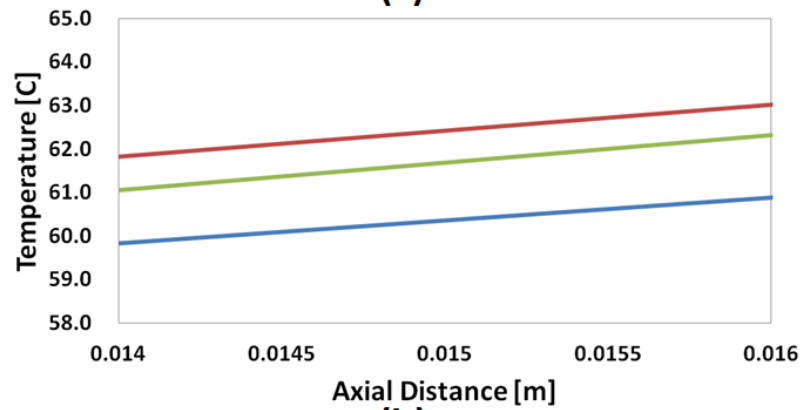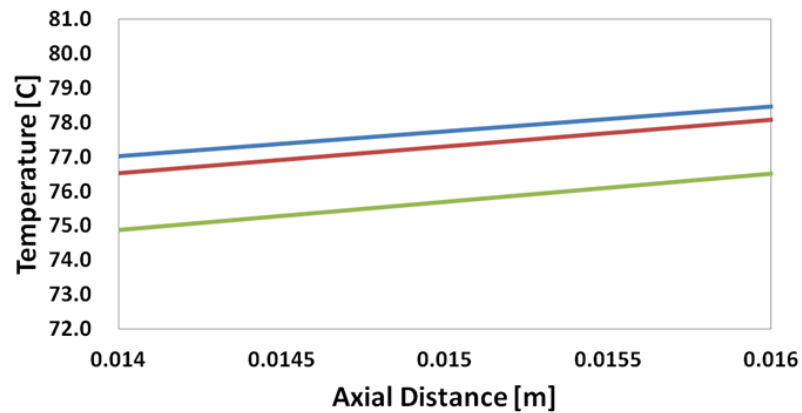
Figure 4-18 Wall temperature profile for experiments performed using TiO$_2$ nanofluid at mass concentration of 0.001 % for: (a) T$_w$ ≈ 45 °C, (b) T$_w$ ≈ 60 °C, and (c) T$_w$ ≈ 75 °C
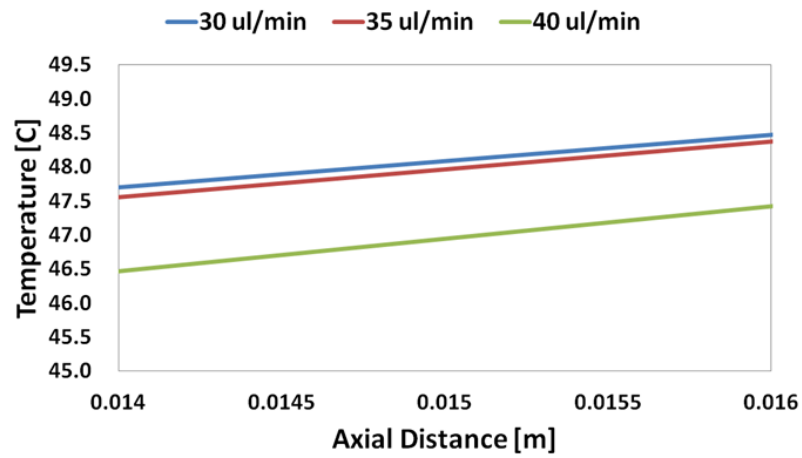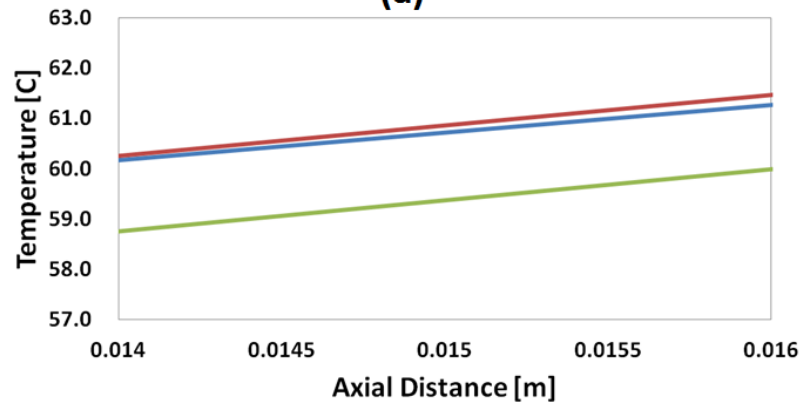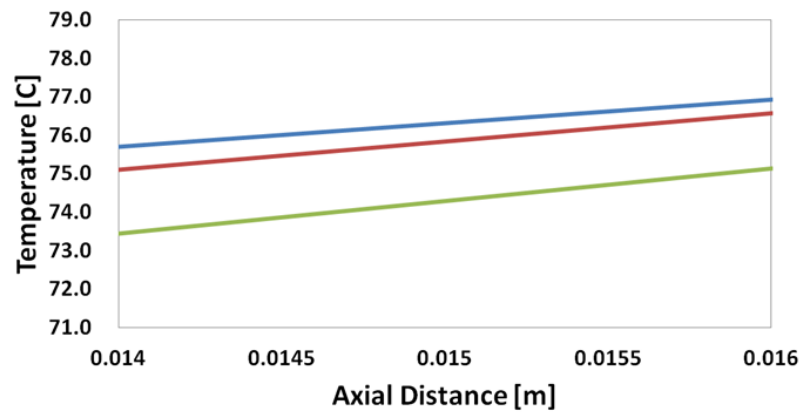
Figure 4-19 Wall temperature profile for experiments performed using TiO$_2$ nanofluid at mass concentration of 0.005 % for: (a) T$_w$ ≈ 45 °C, (b) T$_w$ ≈ 60 °C, and (c) T$_w$ ≈ 75 °C
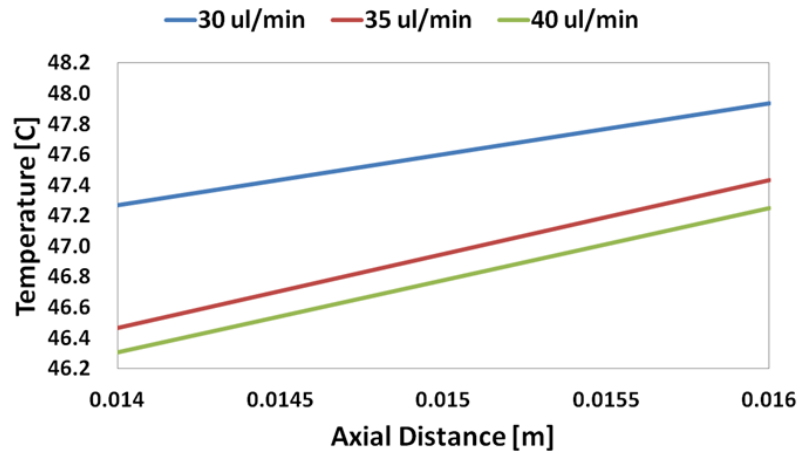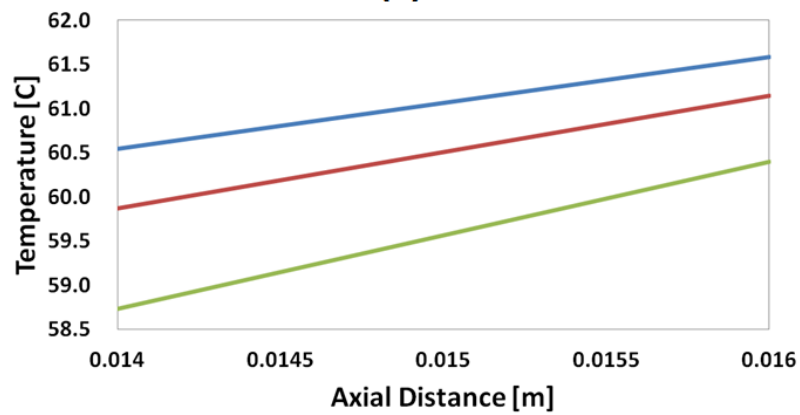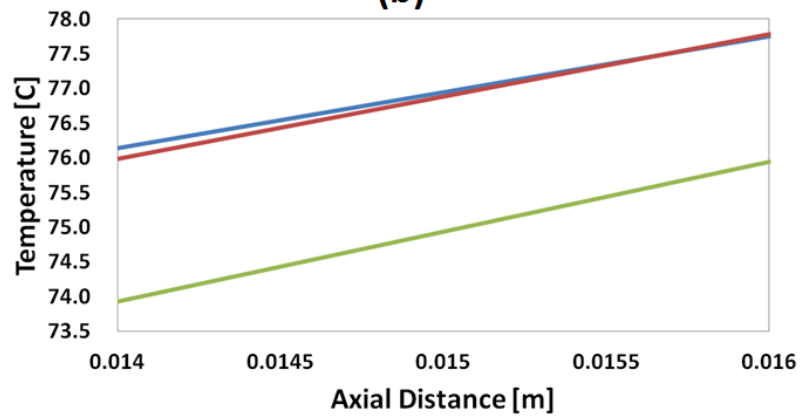
Figure 4-20 Wall temperature profile for experiments performed using TiO$_2$ nanofluid at mass concentration of 0.01 % for: (a) T$_w$ ≈ 45 °C, (b) T$_w$ ≈ 60 °C, and (c) T$_w$ ≈ 75 °C
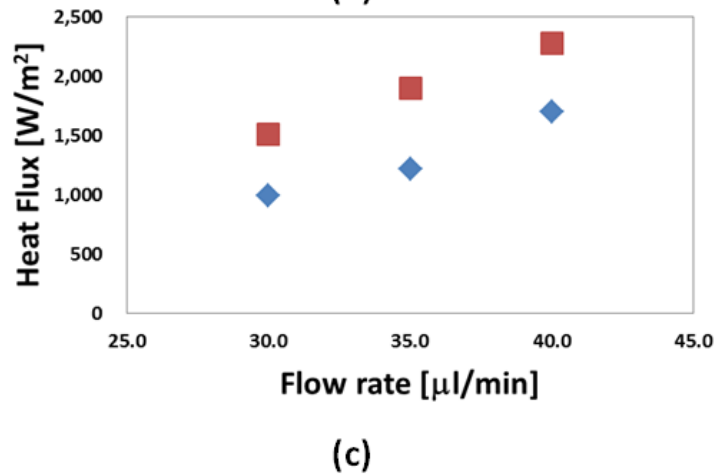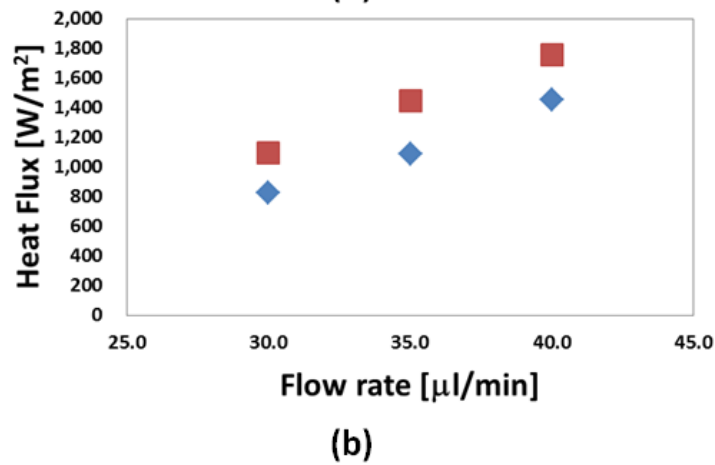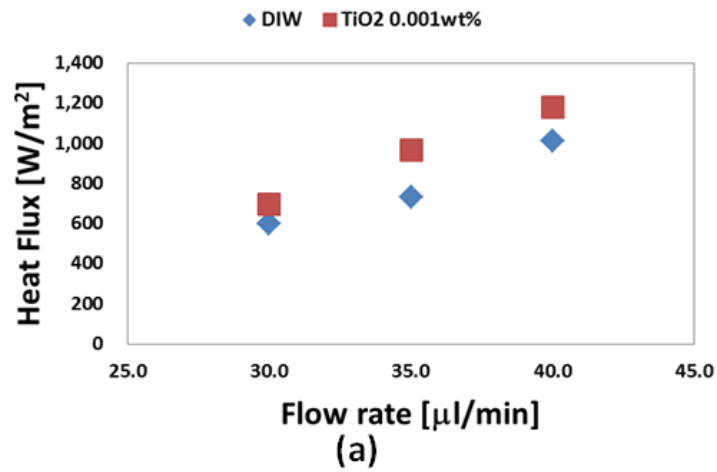
Figure 4-21 Heat flux values calculated using equation (8) plotted as a function of flow rate for TiO₂ nanofluids at mass concentration of 0.001% (a) $T_w \approx 45\ °C$, (b) $T_w \approx 60\ °C$, and (c) $T_w \approx 75\ °C$
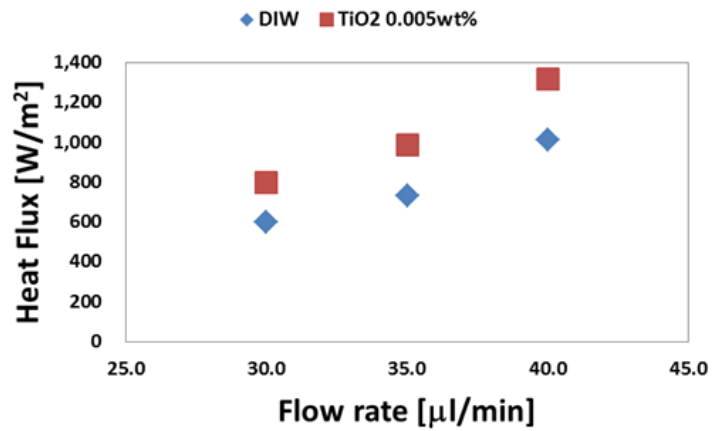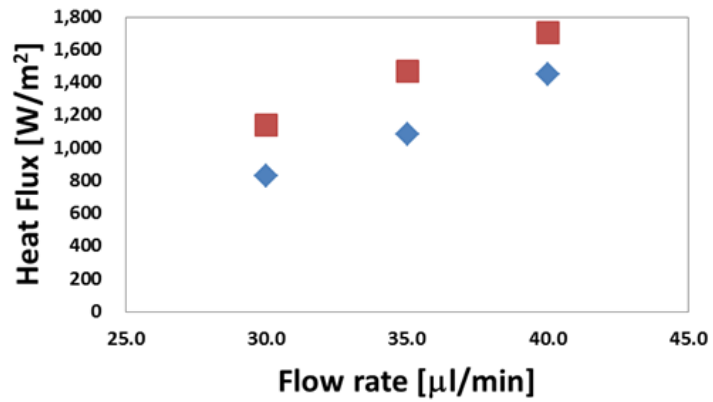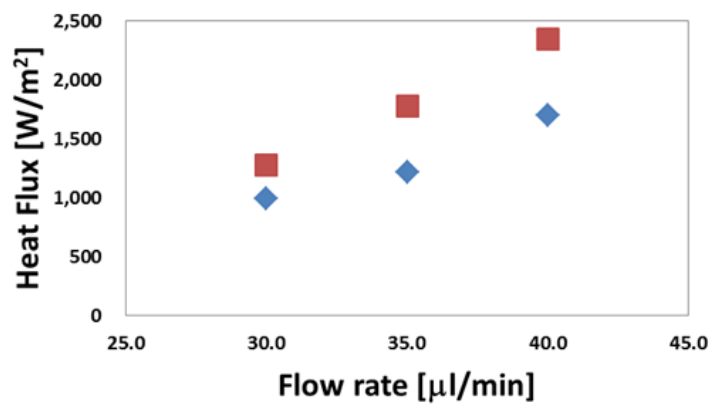
Figure 4-22 Heat flux values calculated using equation (8) plotted as a function of flow rate for TiO$_2$ nanofluids at mass concentration of 0.005 % (a) T$_w$ ≈ 45 °C, (b) T$_w$ ≈ 60 °C, and (c) T$_w$ ≈ 75 °C

109
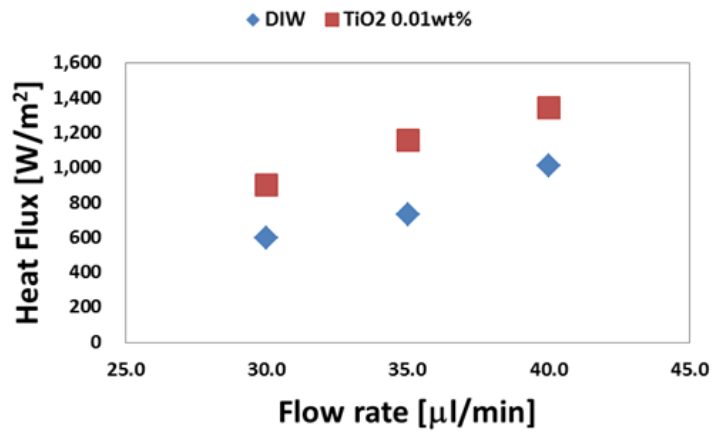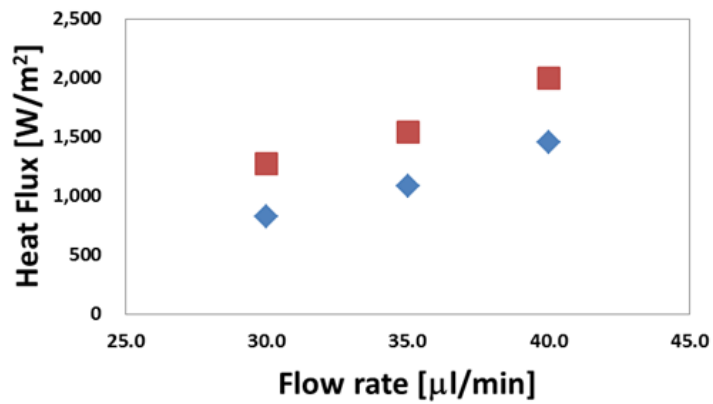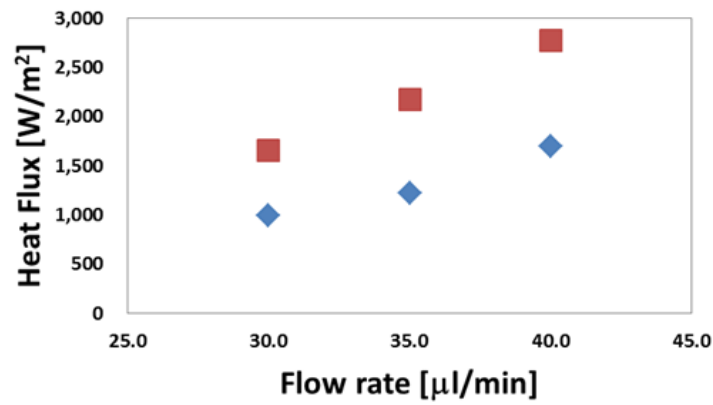
Figure 4-23 Heat flux values calculated using equation (8) plotted as a function of flow rate for TiO$_2$ nanofluids at mass concentration of 0.01 % (a) T$_w$ ≈ 45 °C, (b) T$_w$ ≈ 60 °C, and (c) T$_w$ ≈ 75 °C

110
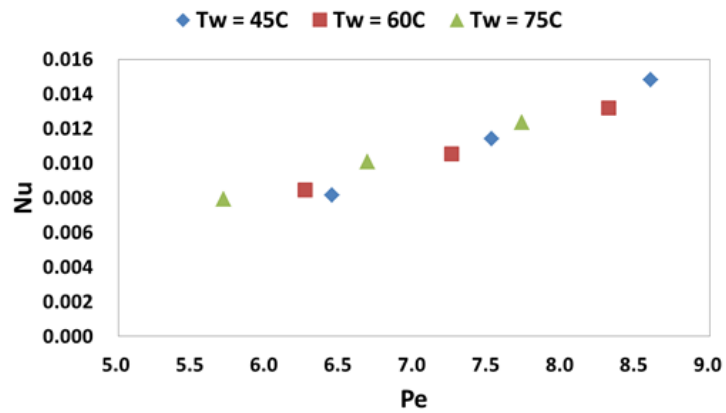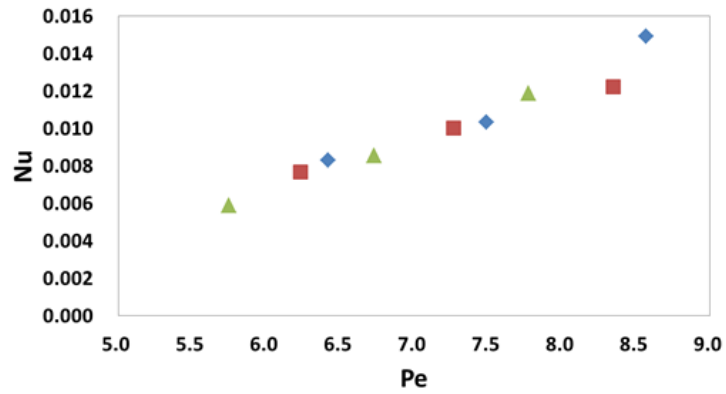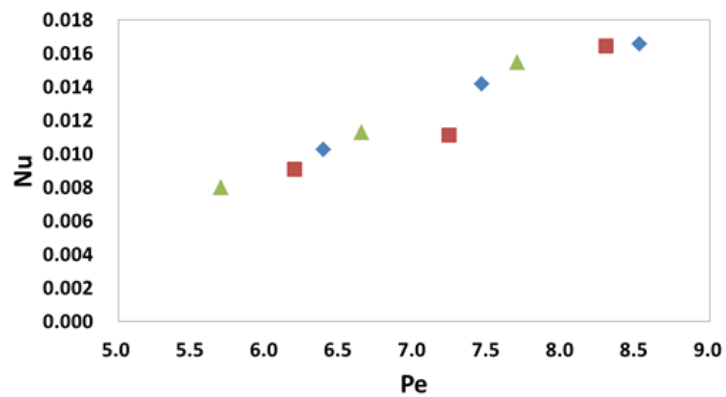
Figure 4-24 Nusselt number calculated using equation (11) as a function of Pêclet number for TiO₂ nanofluids at mass concentration of (a) 0.001 %, (b) 0.005 %, and (c) 0.01 %

Based on the measured temperature gradients, heat removal rate from the heated wall to the nanofluids was calculated and plotted in Figure 4-21, Figure 4-22, and Figure 4-23. The values for heat removal rate are summarized in Table 4-9. The results show that there is a marginal enhancement in the rate of heat removal by the TiO_2 nanofluid coolants at mass concentration of 0.001%, 0.005%, and 0.01%. Specifically, the level of enhancement increases from 15.9 % to 56.2 % as the wall temperature increases for low values of mass concentration (TiO_2 at 0.001%). Also, the level of enhancement is observed to be lower at higher flow rates (40 µl/min) at this mass concentration. For TiO_2 mass concentration of 0.005%, the enhancement in the heat removal rate is observed to range from 17.6 ~ 46.4 %. The heat removal rate increases dramatically to 78.5 % at higher mass concentration of nanoparticles (0.01%), compared to that of DIW. Interestingly, the level of enhancement is moderate at low wall temperature (at 45 °C, 32.5 ~57.8 %) whereas the level of enhancement is very high at higher wall temperature (at 75 °C, 62.8 ~ 78.5 %). This trend is similar to the results obtained for mass concentration of 0.001%. Average enhancement is 32.6 %, 33.5 %, and 53.6 % for mass concentration of 0.001%, 0.005%, and 0.01%, respectively. In addition, it is also observed that the average enhancement is 33.6 %, 34.4 %, and 51.6 % when the wall temperature is 45 °C, 60 °C, and 75 °C, respectively. These indicate that thermal energy is removed more efficiently as the concentration of TiO_2 nanoparticle increases and as wall temperature increases.

Table 4-9 Heat flux calculated using equation (8) for various conditions including wall temperature and flow rate using TiO$_2$ nanofluids at mass concentration of 0.001%, 0.005%, and 0.01% (enhancement levels in braces)

T$_w$ [°C]	Flow Rate [µl/min]	Heat Flux [W/m^2]		
		TiO$_2$ 0.001 %	TiO$_2$ 0.005 %	TiO$_2$ 0.01 %
	30	694 (15.9%)	800 (33.6%)	899 (50.0%)
45	35	966 (31.6%)	988 (34.5%)	1159 (57.8%)
	40	1181 (16.7%)	1317 (30.1%)	1342 (32.5%)
	30	1095 (32.2%)	1138 (37.4%)	1272 (53.6%)
60	35	1448 (33.5%)	1467 (35.3%)	1538 (41.8%)
	40	1758 (21.1%)	1705 (17.4%)	1998 (37.6%)
	30	1503 (52.5%)	1270 (28.8%)	1654 (67.9%)
75	35	1894 (56.2%)	1775 (46.4%)	2165 (78.5%)
	40	2270 (33.7%)	2338 (37.7%)	2763 (62.8%)

Table 4-10 Convective heat transfer coefficient calculated using equation (9) for various conditions including wall temperature and flow rate using TiO$_2$ nanofluids at mass concentration of 0.001%, 0.005%, and 0.01% (enhancement levels in braces)

T$_w$ [°C]	Flow Rate [µl/min]	h [W/m^{2}K]		
		TiO$_2$ 0.001 %	TiO$_2$ 0.005 %	TiO$_2$ 0.01 %
	30	45 (44.0%)	46 (47.6%)	57 (83.7%)
45	35	63 (51.7%)	57 (38.0%)	79 (90.4%)
	40	82 (41.6%)	82 (43.0%)	92 (59.7%)
	30	47 (60.1%)	43 (46.2%)	51 (74.1%)
60	35	58 (48.0%)	55 (41.0%)	62 (57.5%)
	40	73 (36.4%)	68 (27.1%)	91 (71.8%)
	30	44 (68.4%)	33 (26.2%)	45 (72.2%)
75	35	55 (66.2%)	47 (41.7%)	63 (88.2%)
	40	68 (43.1%)	66 (38.2%)	86 (81.1%)

Table 4-11 Nusselt number calculated using equation (11) for various conditions including wall temperature and flow rate using TiO$_2$ nanofluids at mass concentration of 0.001%, 0.005%, and 0.01% (enhancement levels in braces)

T_W [°C]	Flow Rate [μl/min]	Nu		
		TiO$_2$ 0.001 %	TiO$_2$ 0.005 %	TiO$_2$ 0.01 %
	30	0.008 (43.7%)	0.008 (45.9%)	0.010 (79.3%)
45	35	0.011 (51.4%)	0.010 (36.4%)	0.014 (85.9%)
	40	0.015 (41.3%)	0.015 (41.3%)	0.017 (55.9%)
	30	0.008 (59.8%)	0.008 (44.5%)	0.009 (70.0%)
60	35	0.011 (47.6%)	0.010 (39.4%)	0.011 (53.7%)
	40	0.013 (36.1%)	0.012 (25.6%)	0.016 (67.7%)
	30	0.008 (68.0%)	0.006 (24.8%)	0.008 (68.1%)
75	35	0.010 (65.9%)	0.009 (40.1%)	0.011 (83.7%)
	40	0.012 (42.8%)	0.012 (36.6%)	0.015 (76.7%)

$k_{TiO2\ 0.001\ \%} / k_{DIW} = 1.002$, $k_{TiO2\ 0.005\ \%} / k_{DIW} = 1.012$, $k_{TiO2\ 0.01\%} / k_{DIW} = 1.024$

Heat transfer coefficient and Nusselt number for TiO$_2$ nanofluids are calculated and summarized in Table 4-10 and Table 4-11, respectively. Both heat transfer coefficient and Nusselt number are turned out to be enhanced compared to that of DIW. Contrary to the results for heat removal rate, heat transfer coefficient and Nusselt number values are not significantly dependent on the wall temperature. Specifically, the average value of heat transfer coefficient is increased from 55.5 %,51.4 % and 58.4 % for a wall temperature of 45 °C, 60 °C, and 75 °C, respectively. Similarly, average enhancement of Nusselt number is 53.5 %, 49.4 %, and 56.3 % for a wall temperature of 45 °C, 60 °C, and 75 °C, respectively. Dependence of the level of enhancement of both heat transfer coefficient and Nusselt number on the nanoparticle mass concentration

shows different tendency compared to that of heat removal rate. Average value of the enhancement of heat transfer coefficient decreases from51.1 % to 38.8 % as nanoparticle mass concentration increases from 0.001% to 0.01%. Average value of the enhancement of Nusselt number also decreases from 50.7 % (TiO_2 at mass concentration of 0.001%) to 37.2 % (TiO2 at 0.01%). Hence, it is observed that heat removal rate, heat transfer coefficient, and Nusselt number is enhanced by adding minute amount of TiO_2 nanoparticles into the solvent (DIW). As shown in Figure 4-24, Nusselt number monotonously increases with increasingPêclet number, which is similar behavior to DIW and SiO_2 nanofluids.

4.2. Confocal Microscope Experiments

4.2.1. Calibration of Intensity to Temperature

The thermal response of optical emission from both fluorecein and CdSe quantum dots (for increasing temperature) are characterized in order to utilize these materials as temperature sensors. Figure 4-25 shows the calibration curve of the emission intensity for both fluorecein and quantum dots versus temperature. As shown in this figure, the emission intensity for both fluorecein and quantum dot is inversely proportional to increase in temperature. This behavior is in excellent agreement with previous reports where these materials are utilized as temperature sensor.
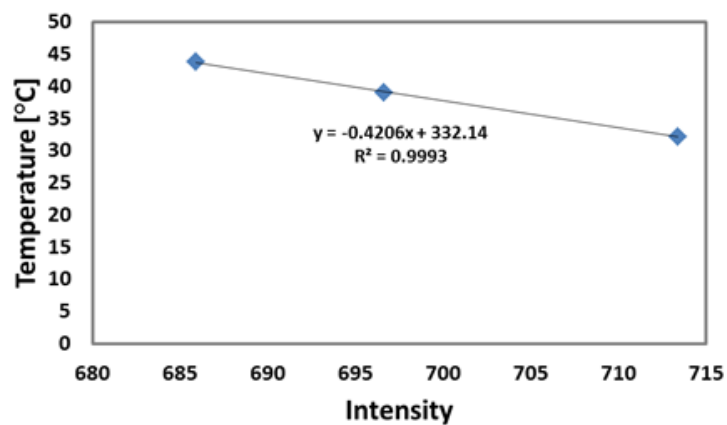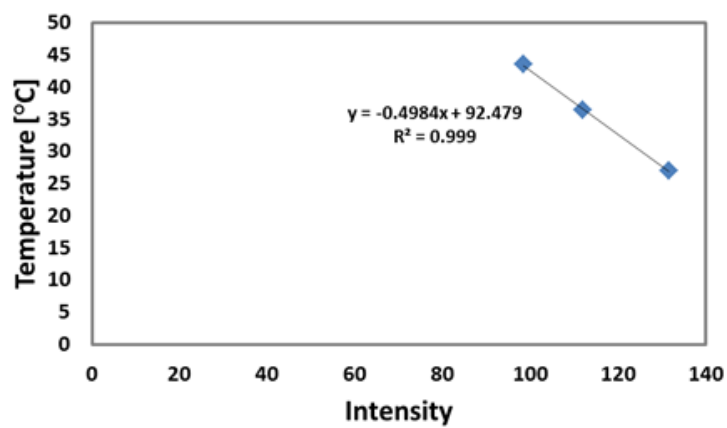
Figure 4-25 Calibration curve for (a) fluorecein and (b) quantum dots

Figure 4-26 and Figure 4-27show the recorded values of intensity profile from the fluorescence materials and QD near the heater wall.
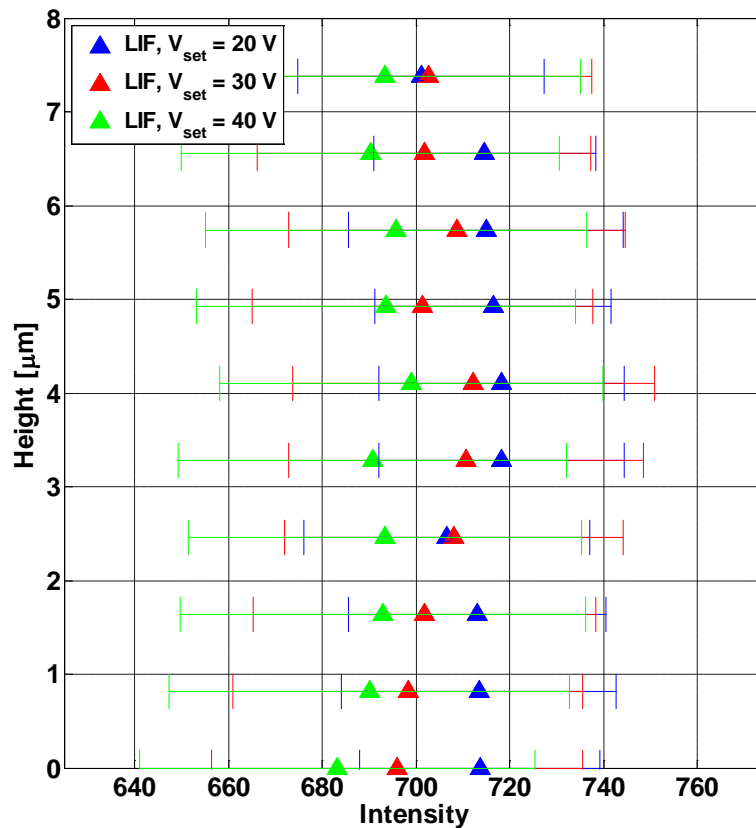
Figure 4-26 Intensity variation of fluorecein near the bottom surface of the microchannel at 40 µm/min
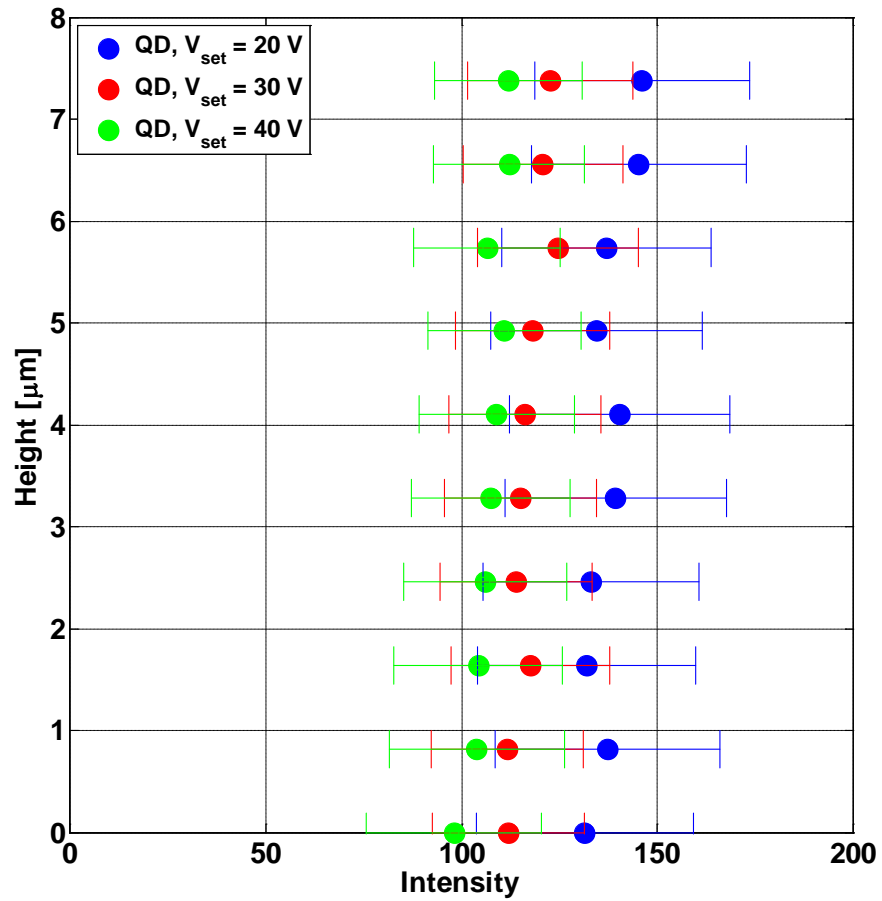
Figure 4-27 Intensity variation of quantum dots near the bottom surface of the microchannel at 40 µm/min

As shown in these figures, decrease in intensity is observed with increasing power input and increase in intensity is observed with increasing height (which corresponds to higher temperature and heat flux values). Recalling intensity is inversely proportional to temperature, this indicates that the temperature decreases in vertical direction near the heat exchanging surface.

4.2.3. *Temperature Data*

Intensity values are converted to temperature data using the calibration curve. Measured temperature is shown in Figure 4-28.
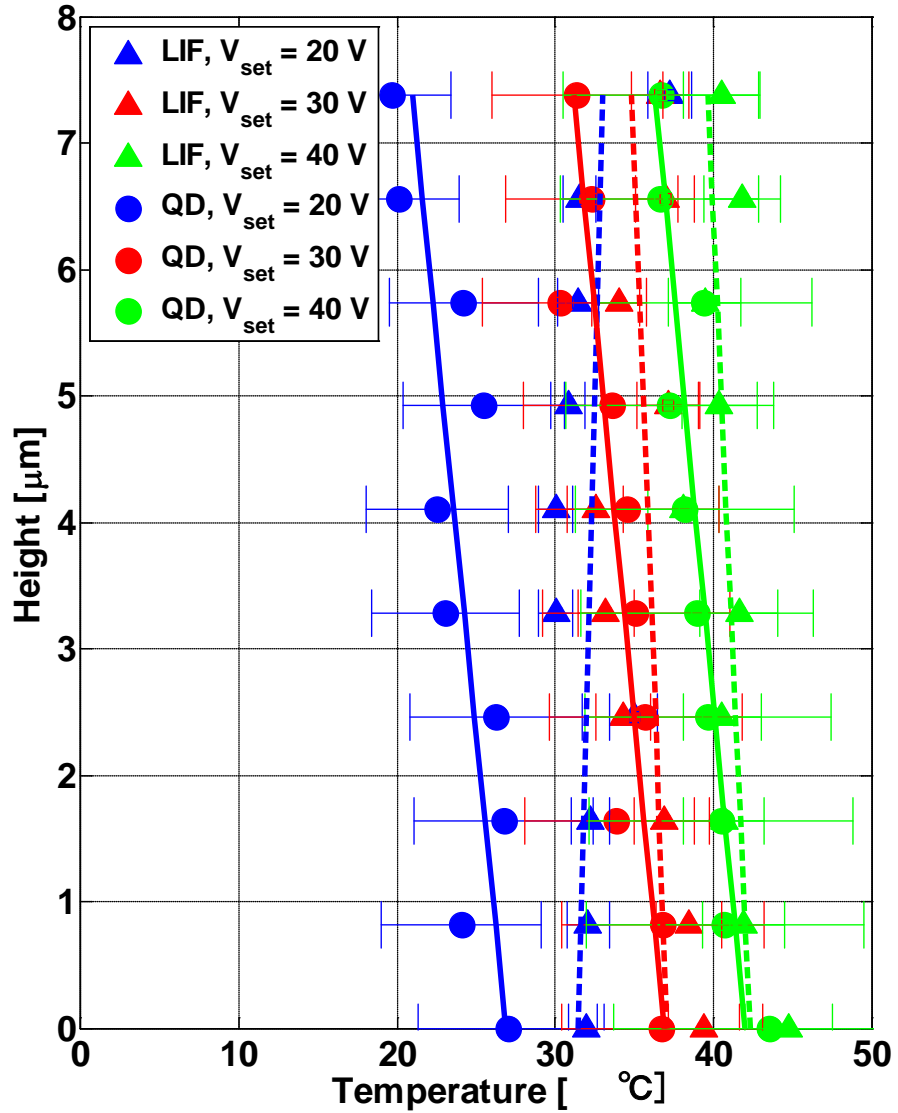
Figure 4-28 Temperature gradient near the heat exchanging surface

Table 4-12 Value of $\dfrac{\partial T}{\partial y}$ (°C/µm) at the bottom surface (heated wall) of the microchannel obtained from LIF and QD experiment (R^2 values in braces)

set voltage	Fluorecein	Quantum Dot
20 V	0.20 (0.05)	-0.80 (0.59)
30 V	-0.31 (0.11)	-0.77 (0.77)
40 V	-0.36 (0.26)	-0.77 (0.80)

In order to derive temperature gradient at the wall ($\dfrac{\partial T}{\partial y}$), temperature is plotted as a function of height in Figure 4-28. Since the measured region is very small (thin), linear approximation is applied for the curve fitting exercise. Using the curve fitting equation, temperature gradient at the wall is calculated and the values are summarized in Table 4-12. Anomalous results are observed for the data set for Fluorecein for supply voltage of 20 V (i.e., positive gradient in intensity and therefore negative gradient in temperature was recorded). This can potentially be induced by disturbances and extraneous noise while performing the experiment.

5.   DISCUSSION[*]

5.1.   Experiments using Thin Film Thermocouples (TFT)

5.1.1.   *Precipitation of Nanoparticles and Nanofin Effect*

As discussed earlier, only a few studies exist in the literature regarding heat transfer of nanofluids in microchannels. Although those studies report on the anomalous behavior of nanofluids for forced convective heat transfer, the understanding of the underlying transport mechanisms remains unclear. Several research groups proposed that the thermal dispersion due to shear induced particle migration could be a dominant transport mechanism for nanofluids [51, 52]. Brownian motion of nanoparticles and thermophoresis were also proposed in these studies to be dominant transport mechanisms that influence nanoparticle migration. However, these models were inconsistent with some of the results showing degradation of heat transfer for nanofluids [119-121].

Nelson et al. suggested that the anomalous enhancements in the heat transfer characteristics are caused by the precipitation of nanoparticles on the heat exchanging surface [18]. Bare silicon wafers on which pure water and nanofluids are tested have inherently atomic scale roughness; so, there is no surface roughness effect when performing experiments on pure water since there is nothing to precipitate on the heat

exchanging surface. However, nanoparticles precipitate on heat exchanging surface as they flow through the microchannel and act as "nanofins". These nano-scale protrusions enhance the effective surface area for the heat exchanging surfaces, and thus behave like nanofins.

(The following results presented here are from a prior study and the following section is copied from this prior study published originally in the journal of Frontiers in Heat and Mass Transfer [118].) To elaborate further, Yu et al. proposed that excessive precipitation of nanoparticles possibly leads to loss of the nanofin effect and instead are replaced by a continuous film of precipitates that cause fouling of the heat exchanging surfaces – thus causing degradation of heat transfer [118]. In this study, SEM images of the heat exchanging surfaces were obtained to confirm the observations. These SEM images for the different surfaces and corresponding to the different experimental conditions (different wall temperatures) are shown in Figure 5-1 and Figure 5-2. These images were obtained after completion of the experiments that involved the flow of nanofluids containing SiO_2 at 0.1% mass concentration. Precipitated nanoparticles were detected on the TFT arrays – aswell as at locations away from the TFT arrays.Materials characterization was also performed to evaluate the nature of the precipitates. Energy Dispersive X-Ray (EDX) spectroscopy was performed to verify that the chemical composition of the precipitated particles do indeed correspond to that of the SiO_2 nanoparticles. EDX measurements are plotted in Figure 5-3.
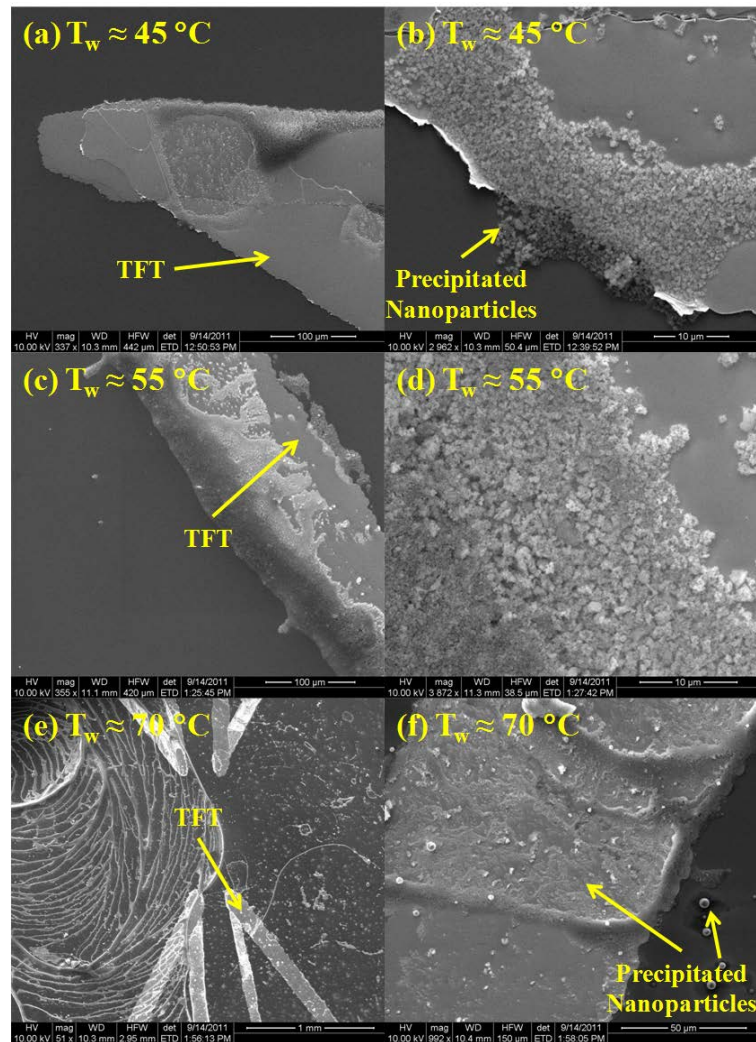
Figure 5-1 SEM images of nanoparticle precipitates on the bottom surface of the microchannel (at the location of the TFT array) – afterperforming forced convective heat transfer experiments using silica nanofluids
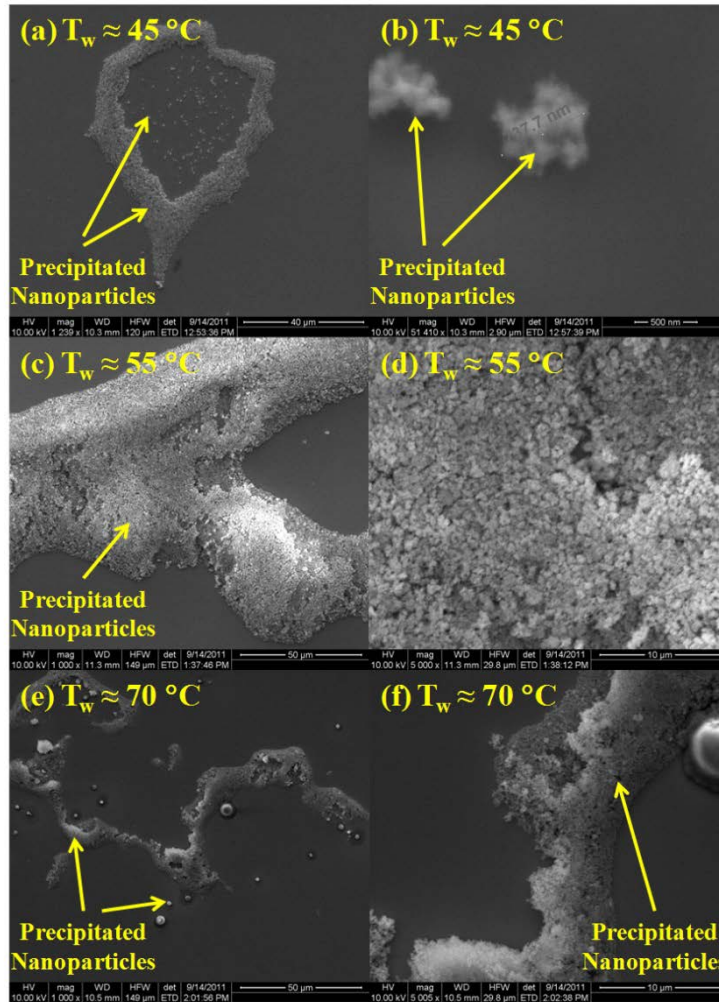
Figure 5-2 SEM images of nanoparticle precipitates on the bottom surface of the microchannel (at locations away from TFT array) - after performing forced convective heat transfer experiments using silica nanofluids
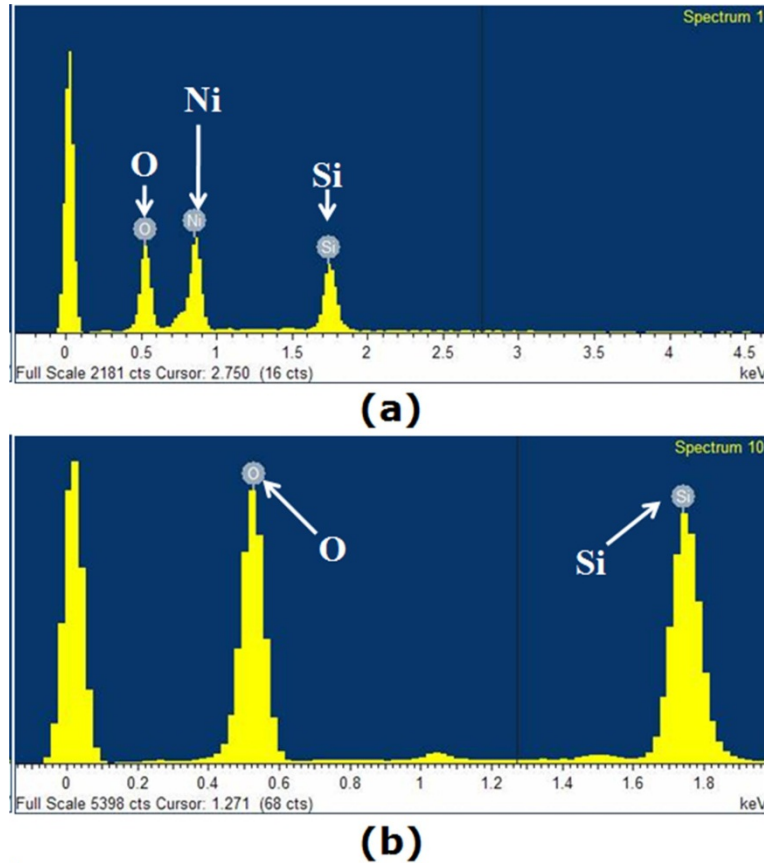
Figure 5-3 Materials characterization using Energy Dispersive X-Ray (EDX) spectroscopy of the precipitates on the bottom wall of the microchannel: (a) In regions at the location of the TFT array; and (b) away from the location of the TFT array. The Ni peak in (a) confirms the presence of the TFT array (which is composed of alloys with more than 90% Ni

The distinct peaks corresponding to Si and O in Figure 5-3confirm that the other impurities are not present in the precipitated particles. Nickel peak detected in Figure 5-3(a) is due to the TFT (both chromel and alumel) which contain more than 90 % nickel. According to Figure 5-1 and Figure 5-2, the agglomerated nanoparticle precipitates are ~200 - 700 nm in diameter. The precipitation is observed to occur in isolated regions with sufficient spacing between the precipitates (at $T_w \approx 45$ °C). These SEM results are

in good agreement with the results reported by Nelson et al. [18]. Hence, the isolated precipitates act as nanofins and enhance heat transfer by increasing the effective surface area for heat exchange between the hot surface and the coolant. However, particle precipitation is much more severe at higher wall temperatures as shown in Figure 5-1 and Figure 5-2.

(a)

(b)

(c)
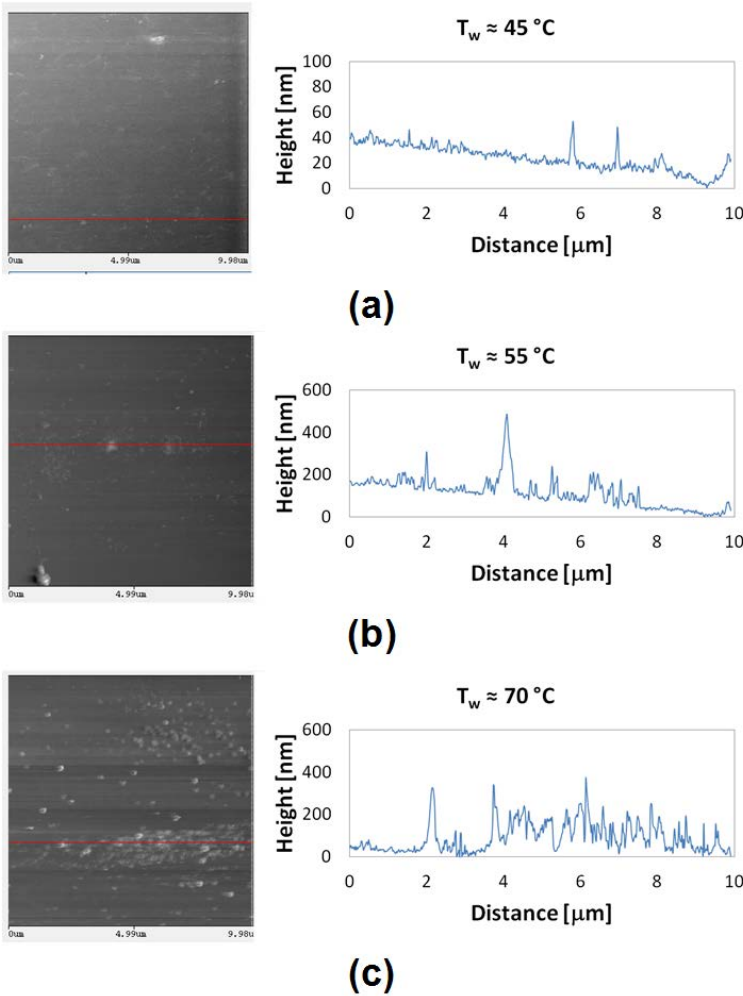
Figure 5-4 LFM images and line analysis results for (a) Tw ≈ 45 °C, (b) Tw ≈ 55 °C, and (c) Tw ≈ 70 °C

After performing the experiments, the surface of the substrates were also scanned using Lateral Force Microscopy (LFM), which is a technique often used in Atomic Force Microscopy (AFM). This measurement is used to obtain an estimate for the surface roughness of smooth substrates (and therefore shows the size and shape of the surface nano-structures). The results from the LFM measurements are shown in Figure 5-4. Figure 5-4 (a) shows the formation of nanofins, while Figure 5-4 (b) and (c) show that a film has been deposited over the substrates (rather than nanofins). This result is in good agreement with SEM analysis, discussed earlier.This leads to greater surface coverage of the heat exchanging surface by the precipitates – causing scaling (or fouling) and thus leading to higher thermal resistance for heat transfer between the silicon wafer surface and the working fluids. Thus, heat transfer rates are degraded when scaling occurs. It is presumed that the reason why excessive precipitation occurs at high heat fluxes (high average wall temperature) is the longer time of contact for the nanofluids with the heated surfaces, during progression to steady state conditions. It required 2 hours to reach steady state conditions (i.e., temperature fluctuations were less than $\pm$ 0.05 °C) at $T_w \approx$ 45 °C.Subsequent experiments resulted in cumulative contact time for the substrates with the nanofluids, where the contact time is estimated to be ~4 hours and ~6 hours, to reach steady state at $T_w \approx$ 55 °C and $T_w \approx$ 70 °C, respectively. Since these substrates are exposed to enhanced precipitation (due to longer time in contact with the nanofluids for the experiments performed at at $T_w \approx$ 55 °C and $T_w \approx$ 70 °C), particle precipitation is also more rampant leading to greater surface coverage by the precipitated nanoparticles and degradation in heat transfer (since silica fouling has lower thermal conductivity than

127

the exposed silicon substrate). In addition, increase in concentration of nanoparticles also accelerates the precipitation and agglomeration of nanoparticles, which results in inferior rates of convective heat transfer for these nanofluids.

Surprisingly, the level of degradation disappeared at higher values of wall temperature and mass concentration of nanoparticles. Vajjha and Das reported that for aqueous silica nanofluids – the specific heat capacity exceeded that of pure water for temperatures 70 °C [108]. Hence, at this temperature the higher specific heat capacity values result in higher convective heat transfer – which compensates for the lower conduction heat transfer due to surface fouling from the agglomerated silica nanoparticle precipitates. Therefore, these results suggest that the amount of precipitation of the nanoparticles can lead to different levels of modification of the surface topologies which can cause either increase or decrease in the rate of cooling. This precipitation is a function of the mass concentration, the exposure (contact) time and other material parameters (e.g., specific heat as a function of temperature) as well as surface interactions.

To summarize, while "moderate" levels of isolated precipitation can lead to the agglomerated nanoparticle precipitates behaving as isolated nanofins (enhanced surface area, therefore higher heat transfer) – excessive precipitation of nanoparticles can cause the formation of a continuous film of agglomerated nanoparticle precipitates leading to scaling (fouling) of the heat exchanging surfaces which results in degradation of heat transfer. Very few reports address (either positive or negative) influence of the

128

precipitation of nanoparticles on the forced convective heat transfer of nanofluids flowing in the microchannel [119-121].

These arguments are primarily focused on the surface modification of heat exchanging surfaces due to the precipitation of nanoparticles. Thus, close scrutiny is required in order to confirm the hypotheses suggested by those previous studies. In this study, characterization of surface modification of the heat exchanging surfaces was performed by utilizing Scanning Electron Microscopy (SEM). SEM images were obtained after the completion of the experiments using nanofluids and are shown in Figure 5-5, Figure 5-6, Figure 5-7, and Figure 5-8. Figure 5-5 and Figure 5-6 shows precipitation of SiO_2 nanoparticles at a location in the vicinity of the TFT arrays and also away from the TFT arrays, respectively. Precipitations of TiO_2 nanoparticles at a location in the vicinity of the TFT arrays and also away from the TFT arrays are shown in Figure 5-7 and Figure 5-8, respectively.
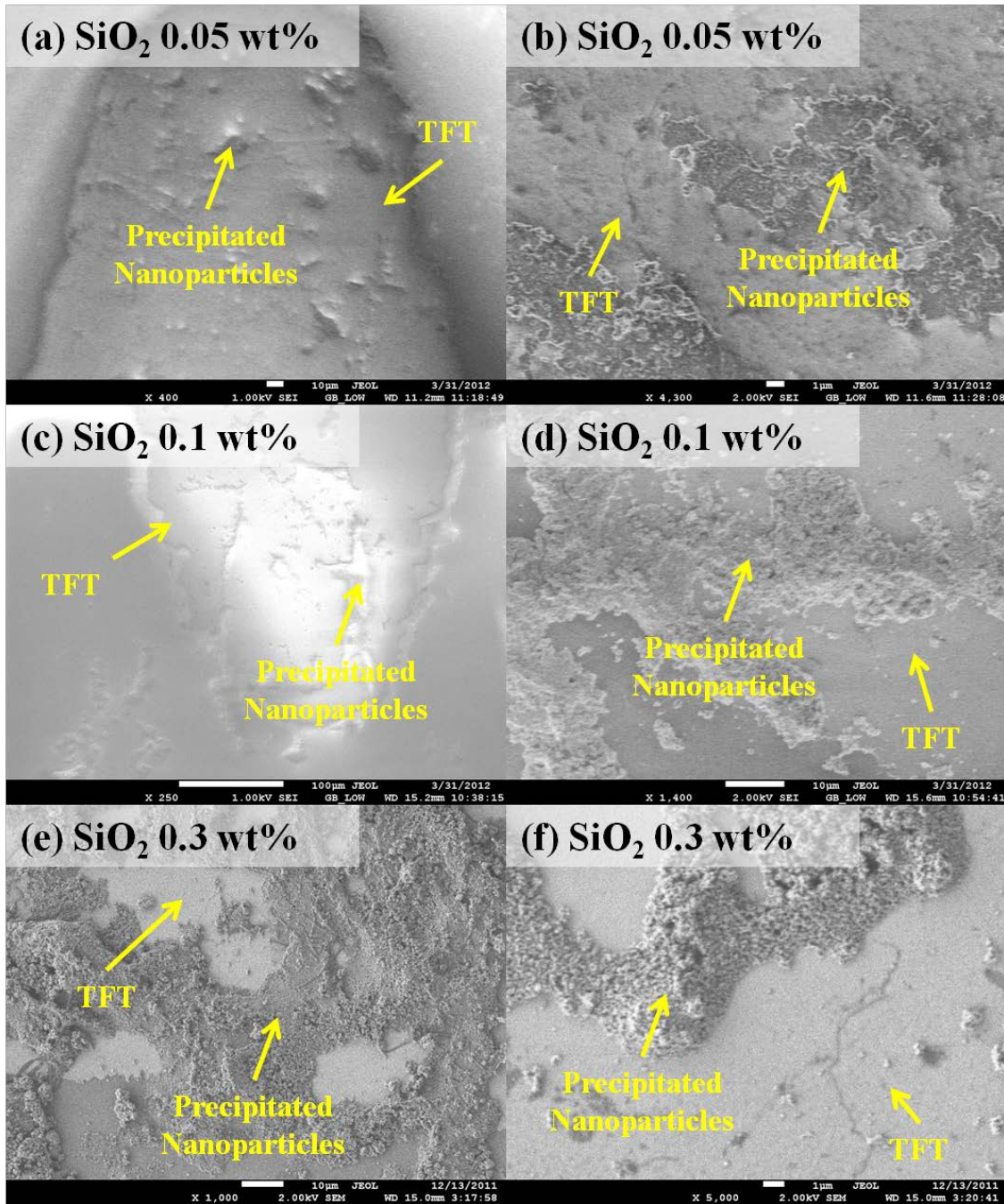
Figure 5-5 SEM images showing precipitation of nanoparticles on the bottom surface of the microchannel at the locations near the TFT array after performing forced convective heat transfer experiments using SiO₂ nanofluids
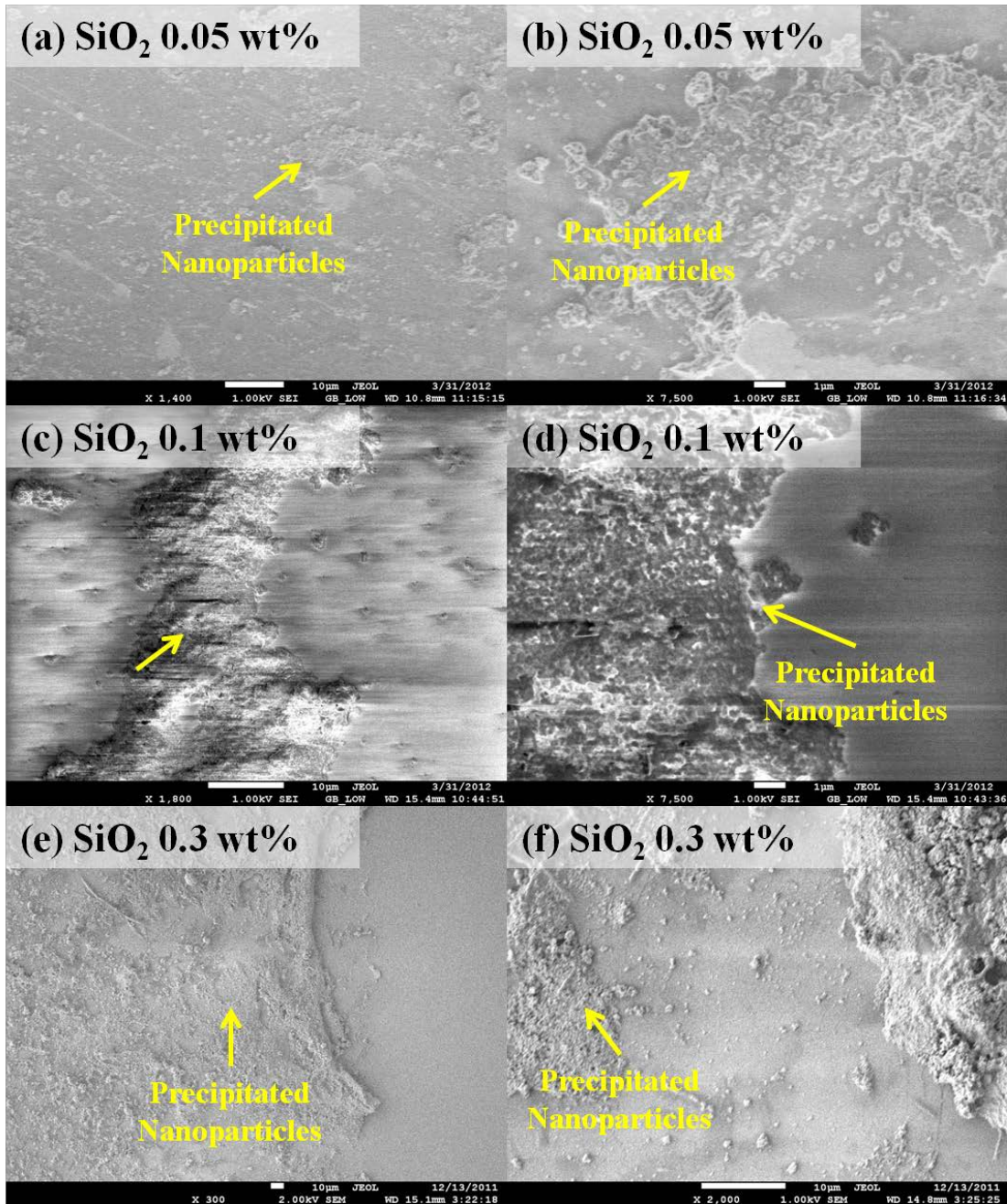
Figure 5-6 SEM images showing precipitation of nanoparticles on the bottom surface of the microchannel at the locations away from the TFT array after performing forced convective heat transfer experiments using SiO₂ nanofluids
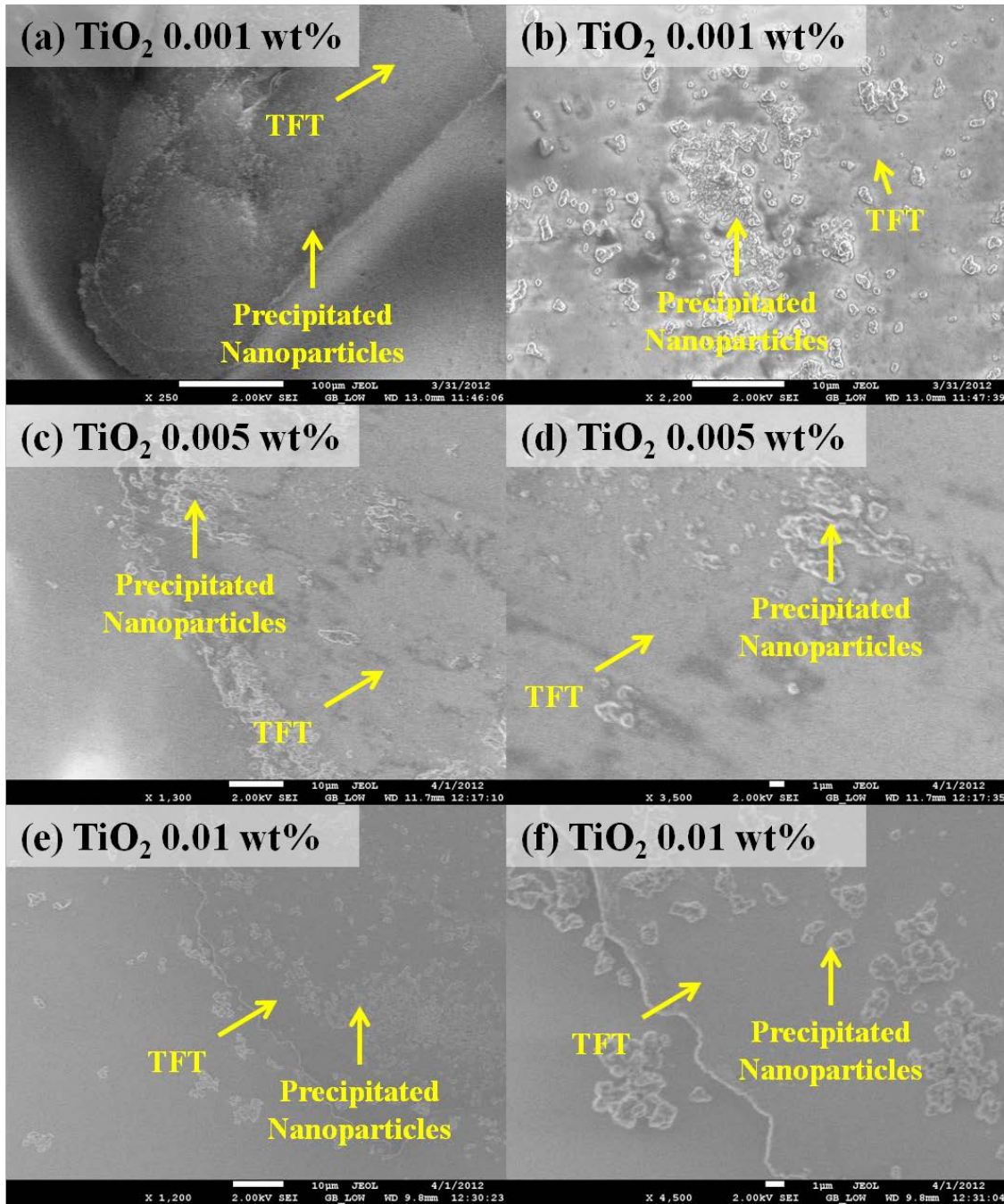
Figure 5-7 SEM images showing precipitation of nanoparticles on the bottom surface of the microchannel at the locations near the TFT array after performing forced convective heat transfer experiments using TiO₂ nanofluids
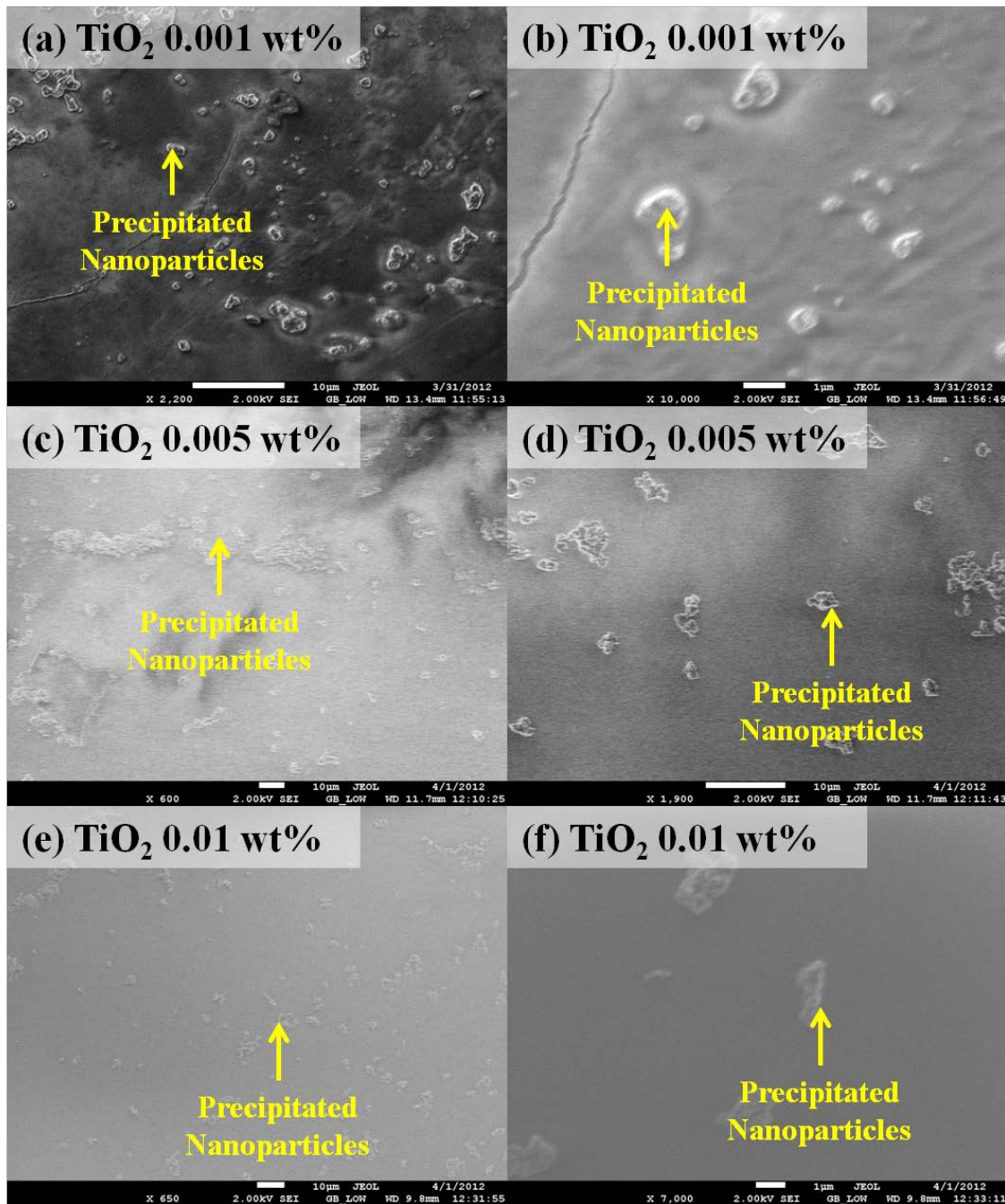
Figure 5-8 SEM images showing precipitation of nanoparticles on the bottom surface of the microchannel at the locations away from the TFT array after performing forced convective heat transfer experiments using TiO₂ nanofluids
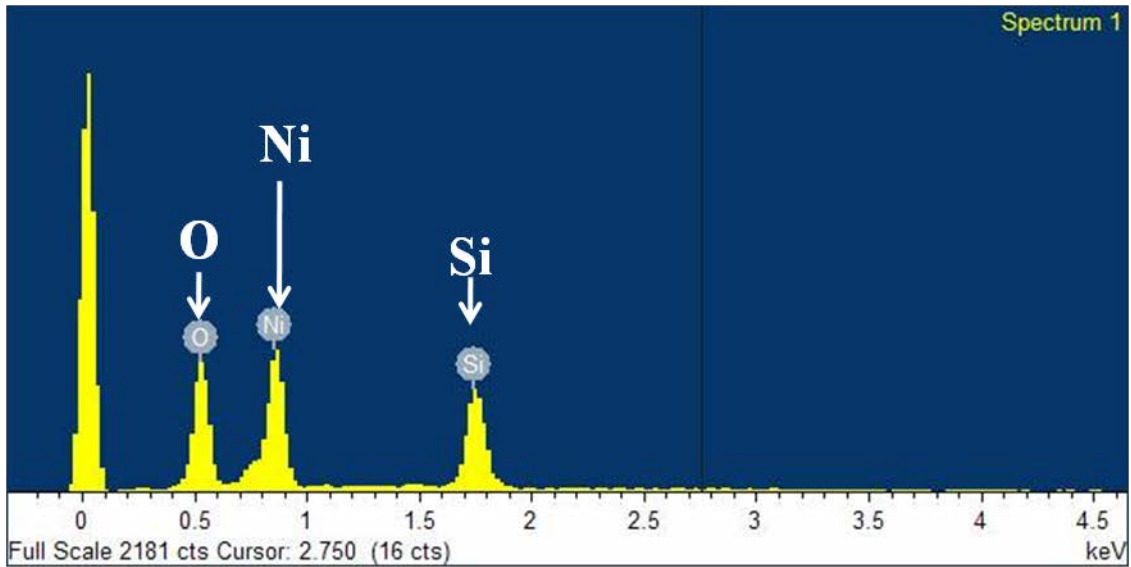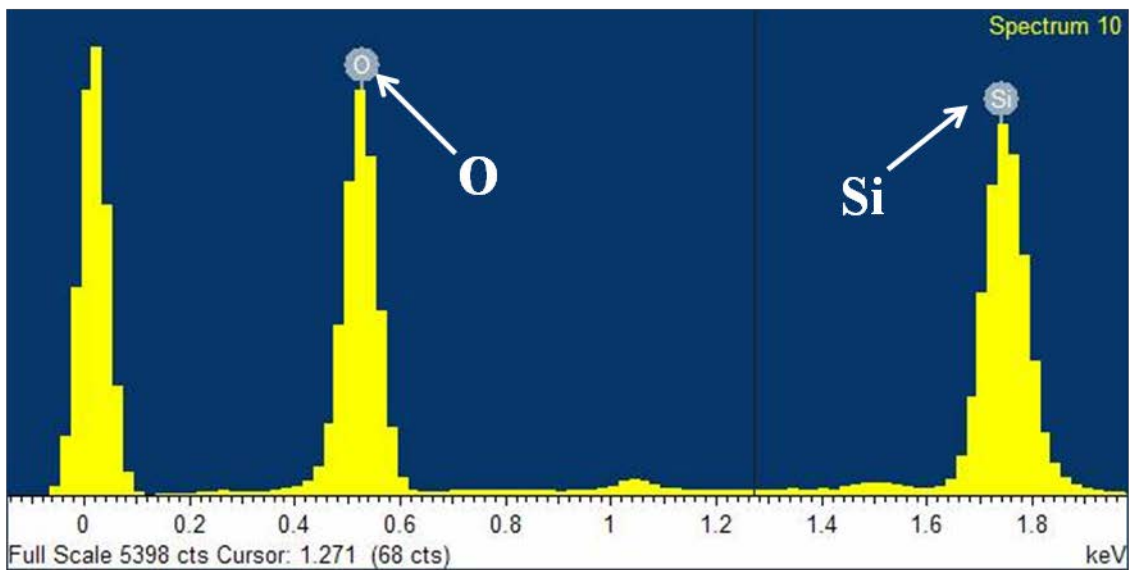
Figure 5-9 Energy Dispersive X-Ray (EDX) spectroscopy of the precipitated particles on the bottom surface of the microchannel after experiments using SiO$_2$ nanofluids at (a) the regions near the TFT array and (b) the regions away from the TFT array
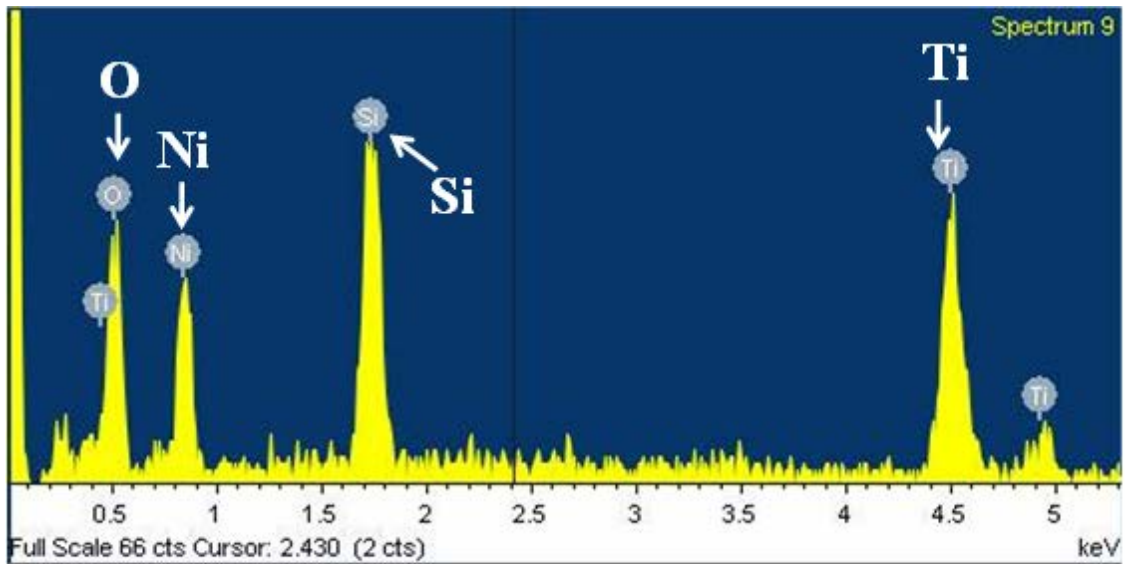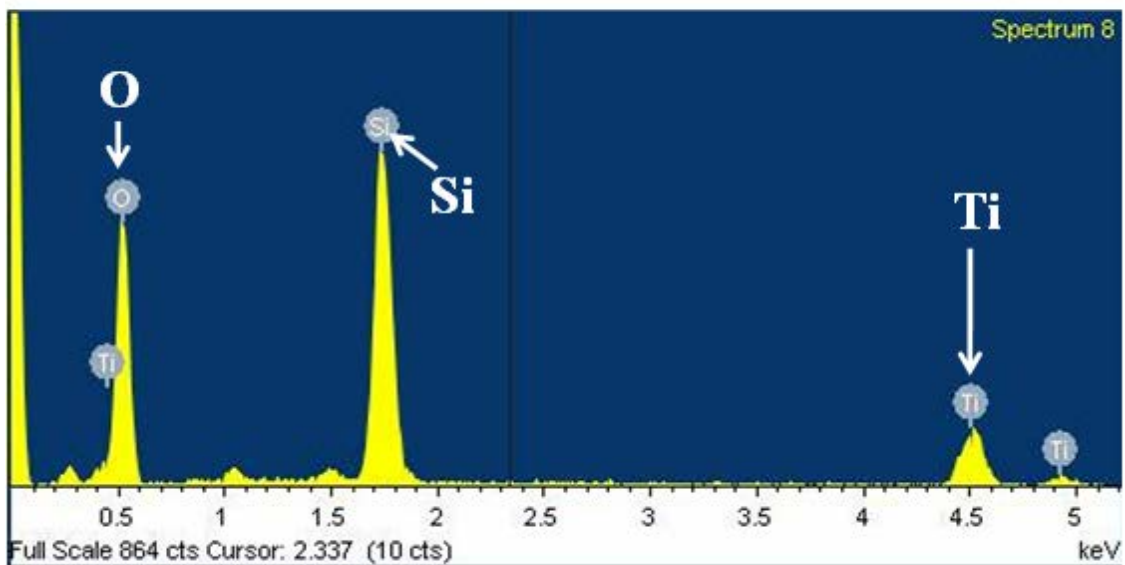
Figure 5-10 Energy Dispersive X-Ray (EDX) spectroscopy of the precipitated particles on the bottom surface of the microchannel after experiments using TiO₂ nanofluids at (a) the regions near the TFT array and (b) the regions away from the TFT array

In order to verify that the precipitated particles shown in these figures are either SiO$_2$ or TiO$_2$ nanoparticles, investigations were performed for materials characterization of these precipitates on the Pyrex wafer surface. Results from the Energy Dispersive X-Ray (EDX) spectroscopy measurement for these particles are plotted in Figure 5-9and Figure 5-10. The presence of peaks corresponding to Si and O in both Figure 5-9 (a) and (b) confirms that the precipitated material contains no impurities other than silica particles. The detection of Ni peak in Figure 5-9 (a) demonstrates the existence of TFT because TFT materials (both chromel and alumel) contain more than 90 % nickel. Similarly, presence of peaks corresponding to Ti and O in Figure 5-10 (a) and (b) shows precipitation particles are not impurities but TiO$_2$ particles. The presence of silicon peak in Figure 5-10 (a) and (b) is expected because the measurement was performed on the pyrex (glass) wafer.

As shown in Figure 5-5 and Figure 5-6, isolated precipitation is observed in some regions whereas other regions have heavier precipitation (which is composed of agglomerated nanoparticles). In contrast to the SEM images for the SiO$_2$ nanoparticle precipitates, the SEM images for TiO$_2$ nanoparticles show isolated precipitation (where the agglomerated nanoparticles have are less than 1μm in size and are prevalent within all SEM images that were obtained after flowing TiO$_2$ nanofluids in the microchannels – as shown in Figure 5-7 and Figure 5-8).

Isolated precipitation with smaller size nanoparticle precipitates possibly leads to enhancement of the surface area for heat exchange by acting as nanofins. In contrastexcessive agglomerationand precipitation can cause additional thermal

136

resistance/ barriers for heat transfer due to fouling of the surface and lead to degradation in heat flux values. For TiO_2 nanofluids the nanoparticles appear to be in stable suspension (and potentially have less affinity for the Pyrex wafer surface) and therefore the level of precipitation and agglomeration of the nanoparticles is significantly less (compared to that of SiO_2 nanoparticles). The dispersed and isolated precipitates of the TiO_2 nanoparticles are also distributed sparsely over a wide region (and therefore the precipitates are likely to enhance the effective surface area and serve as nanofins).The experimental data shows that there is marginal enhancement in the heat transfer for all experimental conditions for TiO_2 nanofluids; and the SEM images support the hypothesis that the precipitation of nanoparticles effectively leads to formation of nanofins (while large scale or excess precipitation of TiO_2 nanoparticles and fouling of the surface is effectively nonexistent); thus leading to consistent experiment results where enhance cooling performance is achieved with the TiO_2 nanofluids for all the experiments. In contrast, both types of precipitation, i.e., isolated precipitation and agglomerated precipitation of particles can be found in SEM images for the SiO_2 nanofluids experiments, as shown in Figure 5-5 and Figure 5-6. Therefore it is logical that the levels of enhancement for the SiO_2 nanofluid experiments are inferiorto TiO_2 nanofluids experiments (or leads to degradation in heat transfer, in some cases, when compared to the control experiments performed using DIW).

An alternate strategy for analyzing the effect of precipitation of the nanoparticles was also implemented in this study. If the anomalous thermal behavior is ascribed to nanoparticle agglomeration and precipitation, DIW is expected to show similar heat

137

transfer characteristics as that of nanofluids when the same microchannel is used (i.e., after the conclusion of the nanofluid experiments). Hence, DIW flowing in the microchannel may yield different thermal behavior before and after the channels are coated with nanoparticle precipitates (i.e., before and after the experiments using nanofluids are performed). Hence, the experiments were repeated using pure DIW right after the experiments involving nanofluids, for the same wafer substrate with the integrated TFT array. The results for these experiments are plotted in Figure 5-11 ~ Figure 5-18. In these plots the markers in blue, red, and green denote,successively, the data from the experiments for DIW (i.e., before performing experiments using nanofluids), data from experiments for nanofluids, and the data from experiments for DIW (after performing experiments using nanofluids), respectively.
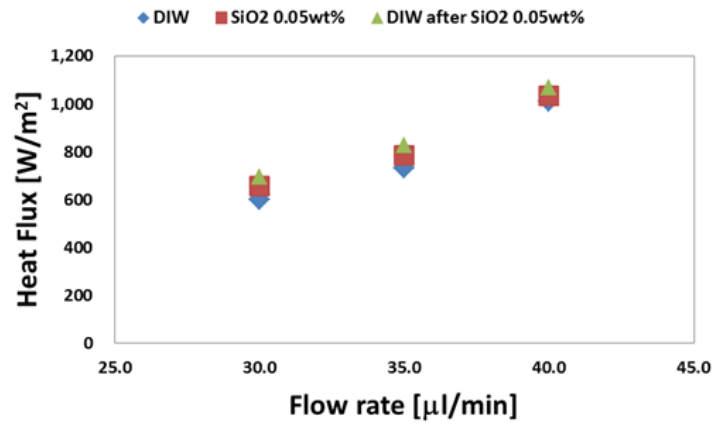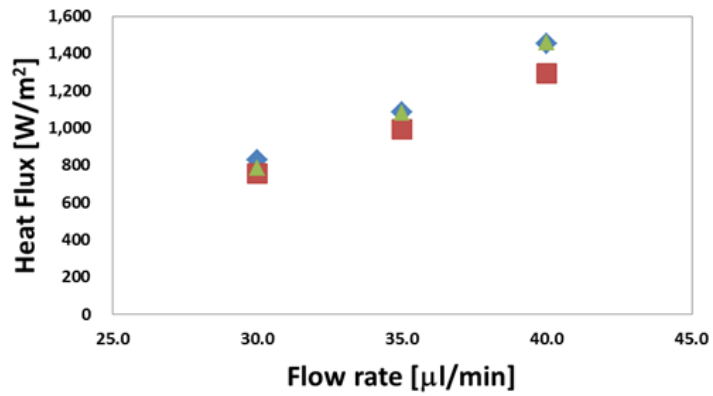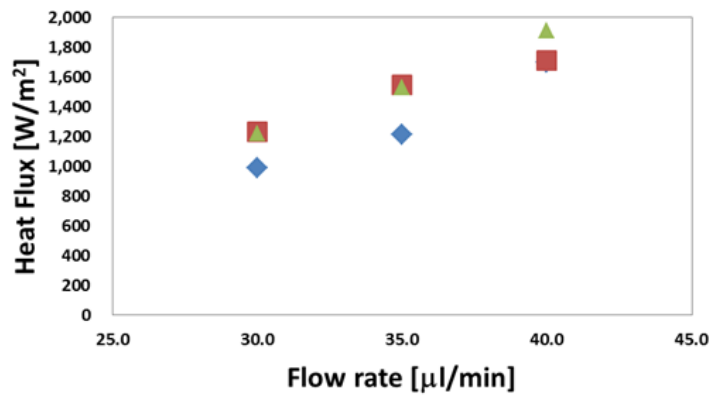
Figure 5-11 Heat removal ratecalculated using equation (8) including pure water experiments right after the experiments flowing nanofluids at SiO$_2$ 0.05 wt% as a function of flow rate at (a) T$_w$ ≈ 45 °C, (b) T$_w$ ≈ 60 °C, and (c) T$_w$ ≈ 75 °C
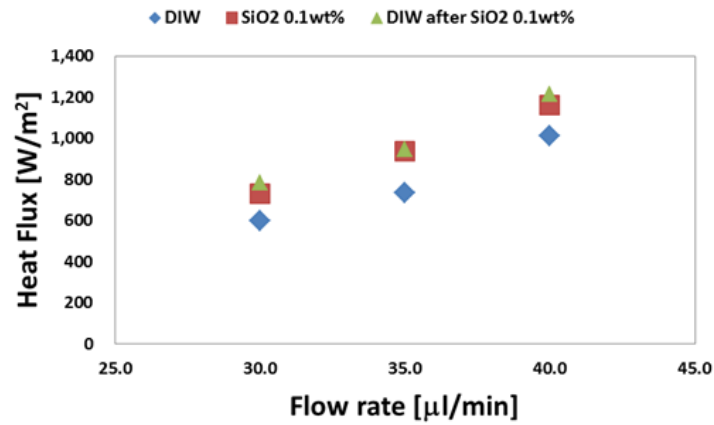
(a)
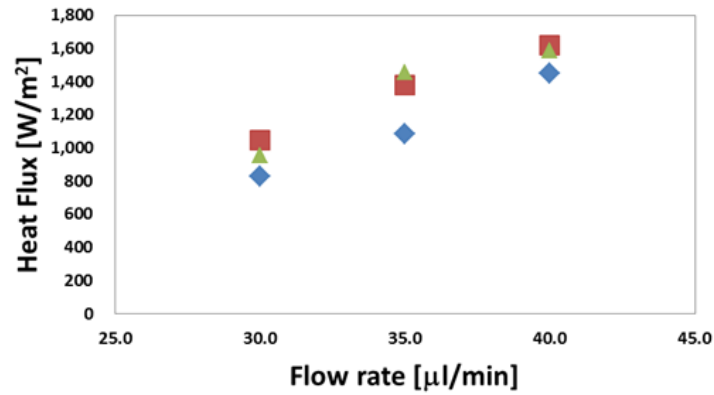
(b)
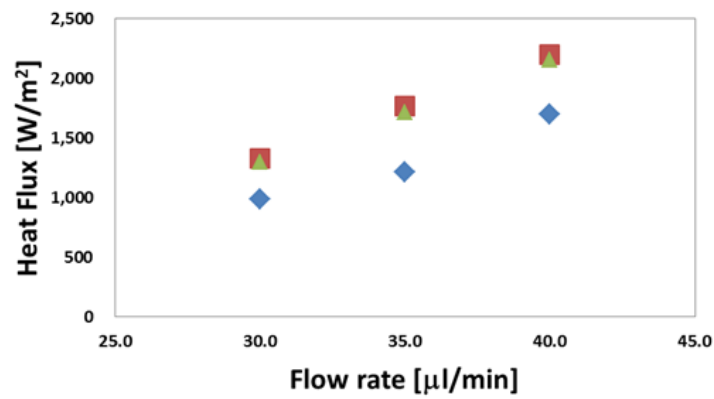
(c)

Figure 5-12 Heat removal rate calculated using equation (8) including pure water experiments right after the experiments flowing nanofluids at SiO$_2$ 0.1 wt% as a function of flow rate at (a) T$_w$ ≈ 45 °C, (b) T$_w$ ≈ 60 °C, and (c) T$_w$ ≈ 75 °C
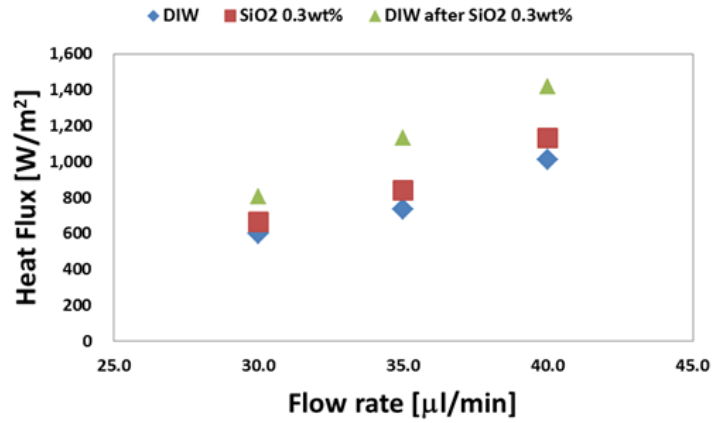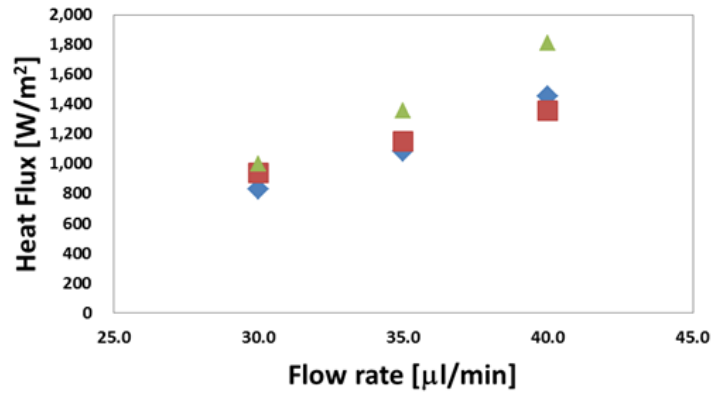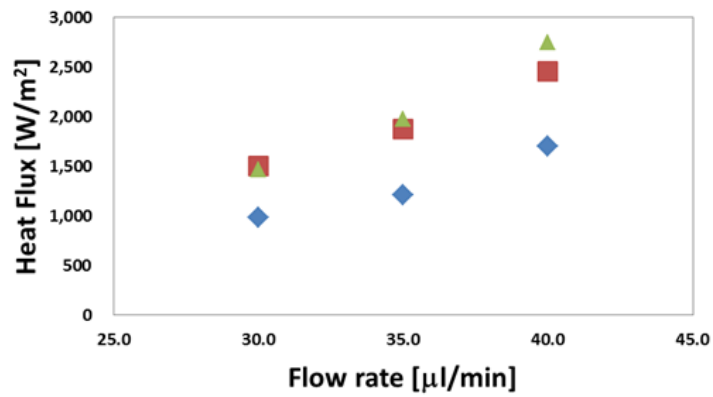
Figure 5-13 Heat removal ratecalculated using equation (8) including pure water experiments right after the experiments flowing nanofluids at SiO$_2$ 0.3 wt% as a function of flow rate at (a) T$_w$ ≈ 45 °C, (b) T$_w$ ≈ 60 °C, and (c) T$_w$ ≈ 75 °C
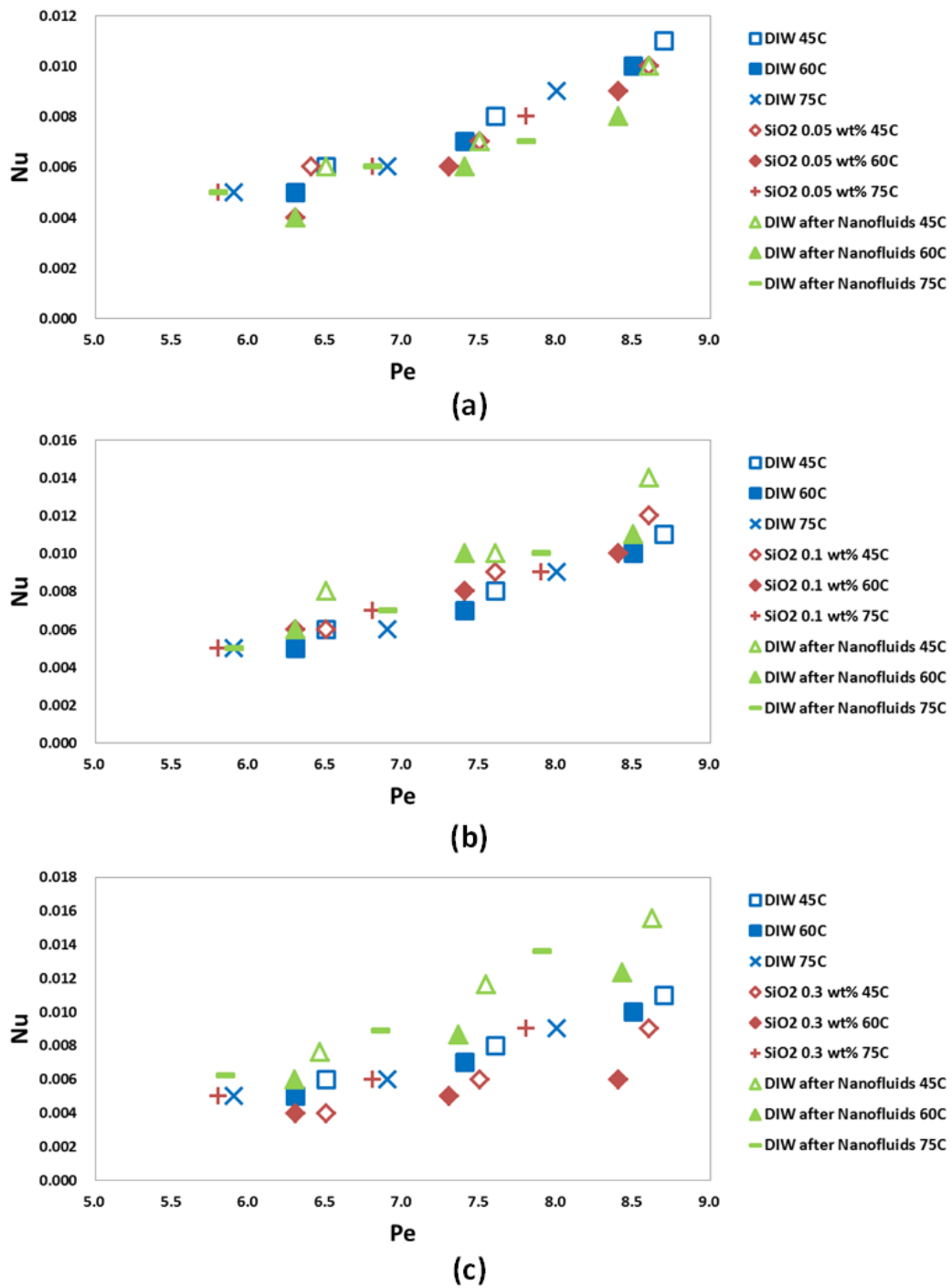
Figure 5-14 Nusselt number calculated using equation (11) as a function of Pêclet number for DIW, SiO$_2$ Nanofluids, and DIW after nanofluids experiments at (a) 0.05 wt%, (b) 0.1 wt%, and (c) 0.3 wt%

142
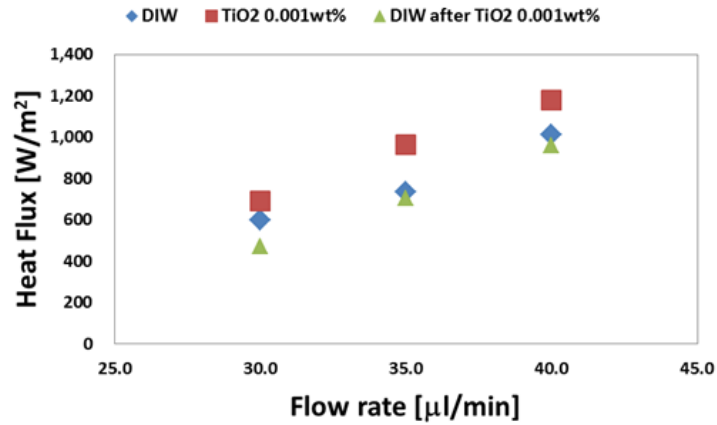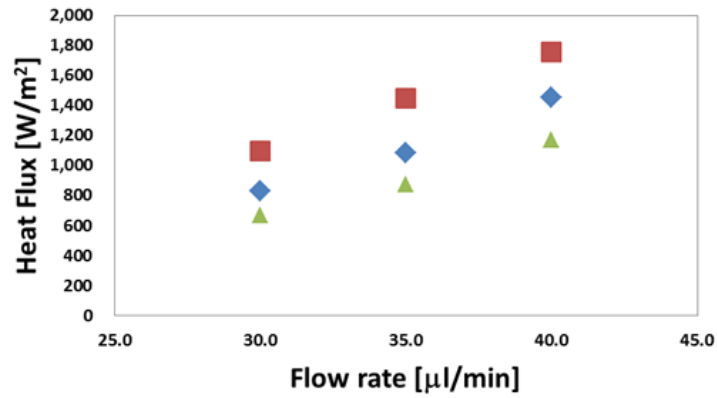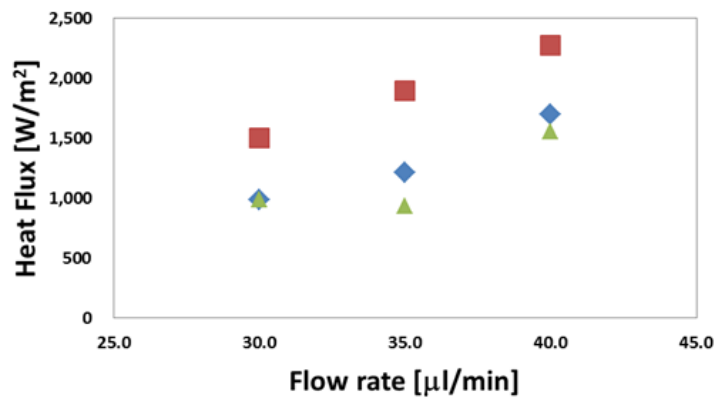
Figure 5-15 Heat removal ratecalculated using equation (8) including pure water experiments right after the experiments flowing nanofluids at TiO$_2$ 0.001 wt% as a function of flow rate at (a) T$_w$ ≈ 45 °C, (b) T$_w$ ≈ 60 °C, and (c) T$_w$ ≈ 75 °C

143
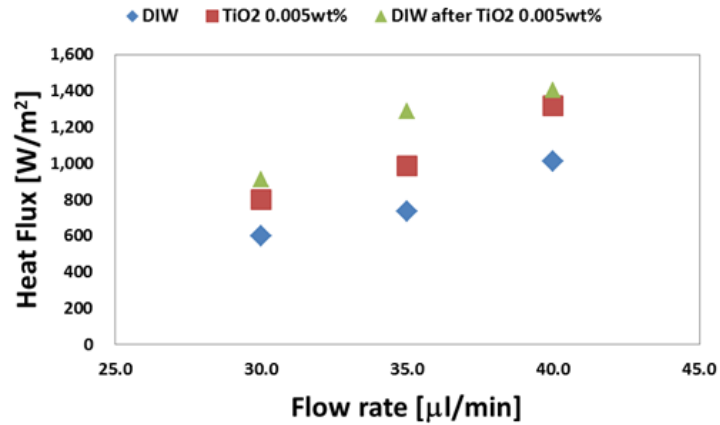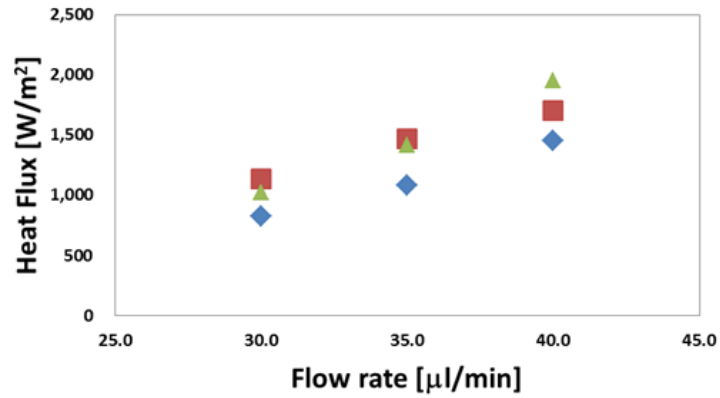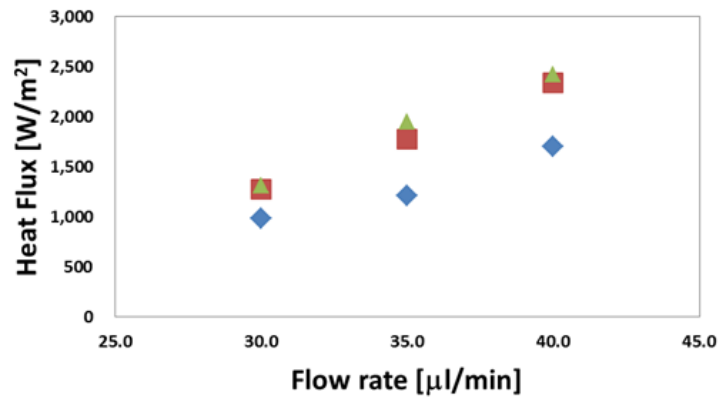
Figure 5-16 Heat removal rate calculated using equation (8) including pure water experiments right after the experiments flowing nanofluids at TiO$_2$ 0.005 wt% as a function of flow rate at (a) T$_w$ ≈ 45 °C, (b) T$_w$ ≈ 60 °C, and (c) T$_w$ ≈ 75 °C
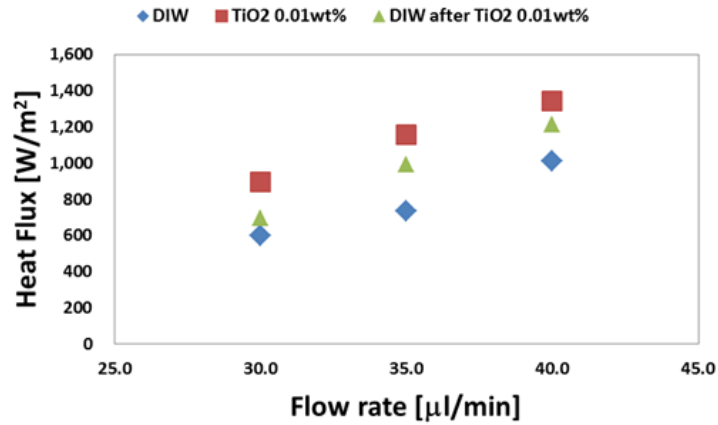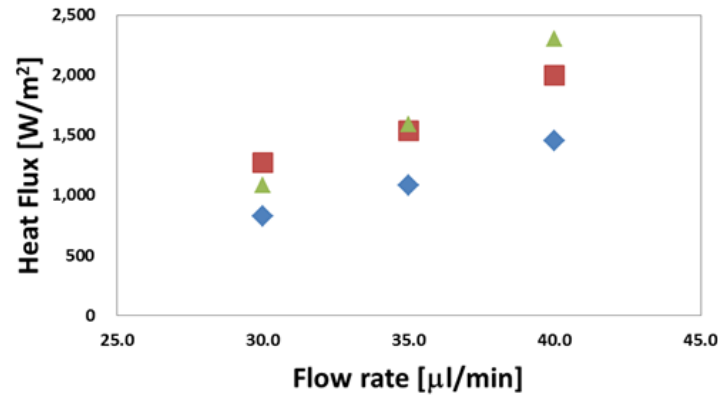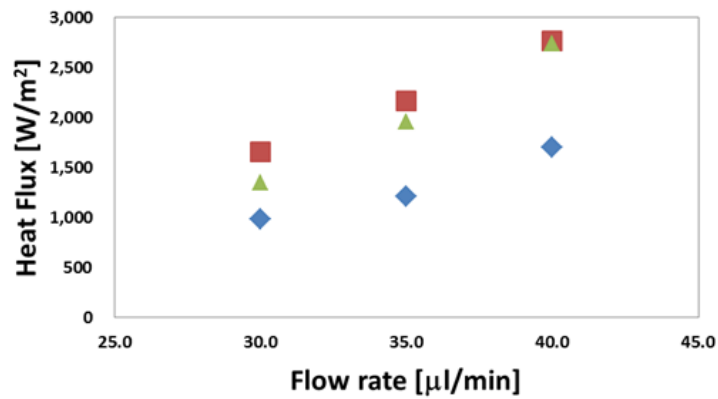
Figure 5-17 Heat removal rate calculated using equation (8) including pure water experiments right after the experiments flowing nanofluids at TiO₂ 0.01 wt% as a function of flow rate at (a) T_w ≈ 45 °C, (b) T_w ≈ 60 °C, and (c) T_w ≈ 75 °C

145
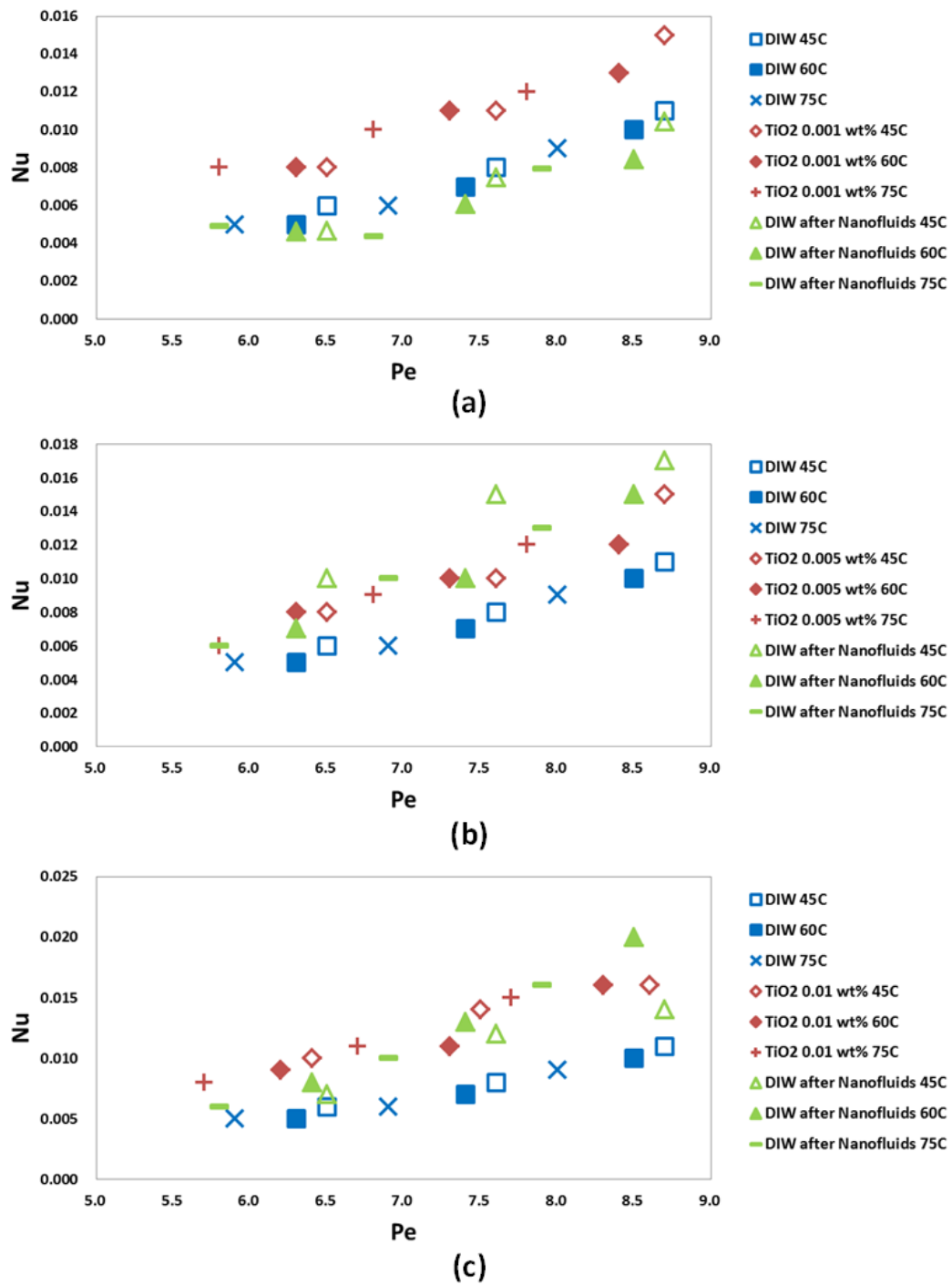
Figure 5-18 Nusselt number calculated using equation (11) as a function of Pêclet number for DIW, TiO₂ Nanofluids, and DIW after nanofluids experiments at (a) 0.001 wt%, (b) 0.005 wt%, and (c) 0.01 wt%

146

For the experiments performed using SiO_2 nanofluids, it is remarkable that the plots for the green color markers consistently overlap the markers in red color (or sometimes exceed the values for the markers plotted in red color) and also are consistently of higher value than the blue color markers. This demonstrates (as expected) that the heat flux results for the flow of DIW (after performing the nanofluids experiments)are in good agreement with the experimental data obtained from the flow ofnanofluids(and surprisingly –forall concentrations). Both heat removal rate and Nusselt number plots for flow of DIW (after experiments performed on nanofluids) show similar trend to that of the nanofluid experiments. The only exception to this trend is observed when the mass concentration of nanoparticles is 0.3% for SiO_2 and 0.001% for TiO_2 nanofluids. Significant increase in the evaluated thermal conductivity of SiO_2 nanofluids (at higher mass concentration) may dominate over the nanofin effect – and therefore result in significant difference for the thermo-fluidic performance for nanofluids (when compared to that of DIW even after the formation of the nanofins by precipitation). For TiO_2nanofluids at a mass concentration of 0.001%, it is possible that the level of precipitation (and therefore, the area density of nanofins) is not adequate to have significant effect on the thermo-fluidic behavior of the heat exchanging surface. It is also possible that the low surface affinity of the precipitated TiO_2 nanoparticles can cause them to be "eroded" from the wafer surface when DIW is used subsequent to the nanofluids experiments.

In summary, pure water (DIW) shows different trends in cooling performance depending on the history of usage and the order of experiments involving the

147

microchannel apparatus (i.e., before and after experiments using nanofluids are performed). These results provide the clues to conclude that the precipitation of nanoparticles influences thethermo-fluidic performance of the cooling system and can cause both enhancement as well as degradation of the heat transfer during forced convection of nanofluids in a microchannel.Precipitation of nanoparticles cause surface modification and change the surface topology during these experiments.

5.1.2. *Experiments on Surface With Artificial Nanofins*

An alternate strategy for proving the nanofin hypothesis is to investigate if similar levels of enhancement in forced convective heat transfer for flow of coolants (such as DIW) in microchannels by using plain microchannels and microchannels integrated with nanofins (e.g., that are fabricated using the SFIL process). If the experiments performed using microchannels containing nanofins show similar levels of (or match the) heat transfer enhancements observed in the previous experiments reported in this study – it will add credence to the nanofin hypothesis that has been proposed and validated in this study.Hence, experiments have been performed using microchannels containing nanofins on the heated surface (bottom surface of the microchannels) – thatare fabricated by SFIL process.

In order to perform the experiments, TFT is fabricated on nanofins which are fabricated using SFIL process (section 2.3), following the same protocol described in section 2.1. Figure 5-19 demonstrates SEM images of TFT junction on the surface containing nanofins at various magnifications. The average height of tested nanofins is

354 nm with 12 DRIE cycles. It is shown that TFT is successfully fabricated on nanofins and nanofins on TFT are slightly larger than nanofins on other regions due to the deposition of chromel and alumel.
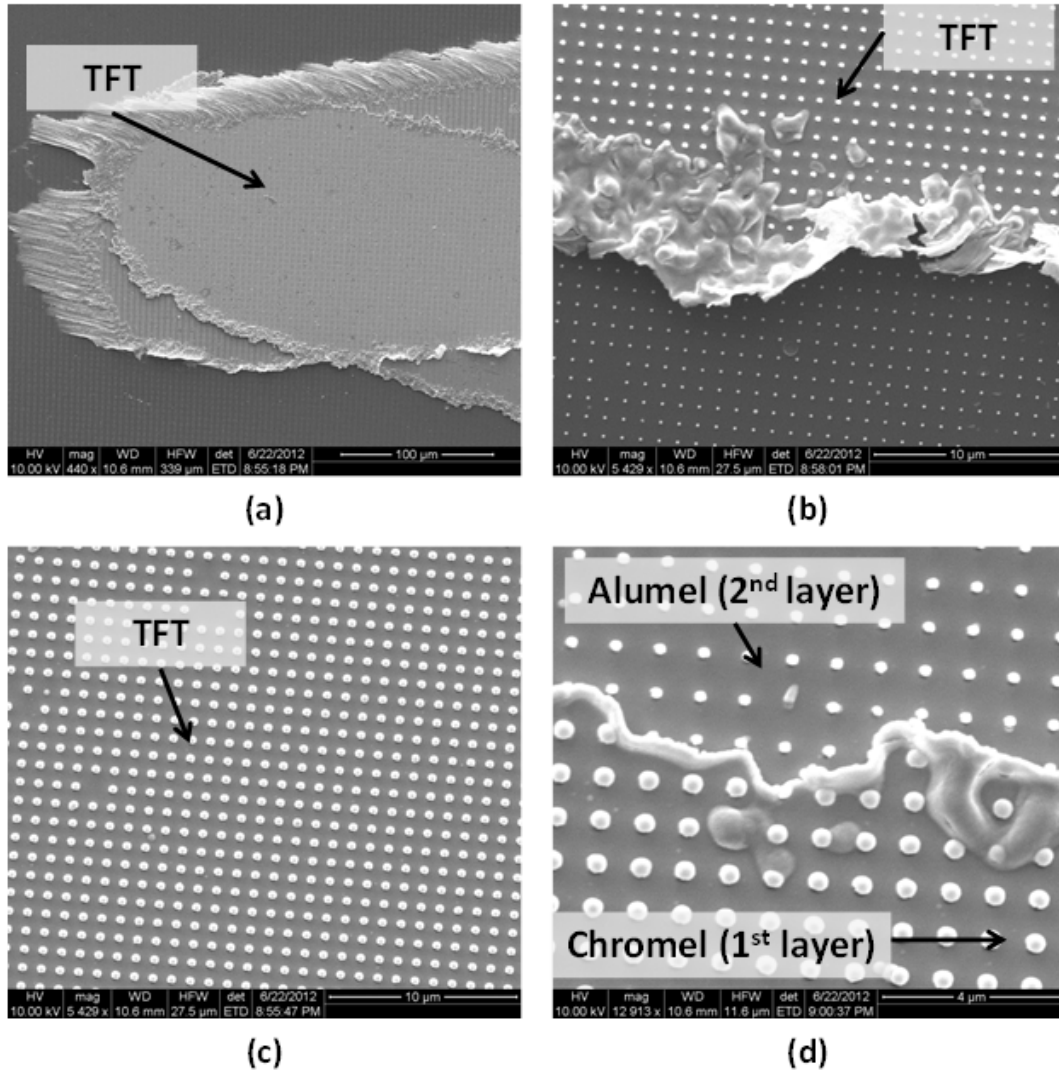
Figure 5-19 SEM images of TFT fabricated on artificial nanofins at different magnifications

Table 5-1 Experimental values for heat flux, heat transfer coefficients, and Nusselt number calculated using equation (8) – equation (11) for DIW flowing in the microchannel containing artificial nanofins on its surface

T_w [°C]	Flow Rate [µl/min]	Heat Flux [W/m^2]		h [W/m^{2}k]		Nu	
		DIW	SFIL	DIW	SFIL	DIW	SFIL
	30	599	769 (28.3%)	31	57 (82.2%)	0.006	0.010 (82.2%)
45	35	734	1026 (39.8%)	41	75 (81.2%)	0.008	0.014 (81.2%)
	40	1012	1277 (26.1%)	58	95 (64.2%)	0.011	0.017 (64.2%)
	30	828	1359 (64.0%)	29	56 (92.6%)	0.005	0.010 (92.6%)
60	35	1085	1628 (50.1%)	39	68 (73.6%)	0.007	0.012 (73.6%)
	40	1452	2119 (45.9%)	53	86 (61.7%)	0.010	0.016 (61.7%)
	30	986	2043 (107.3%)	26	53 (106.7%)	0.005	0.010 (106.7%)
75	35	1212	2688 (121.7%)	33	70 (110.6%)	0.006	0.013 (110.6%)
	40	1697	3244 (91.1%)	47	86 (81.0%)	0.009	0.016 (81.0%)
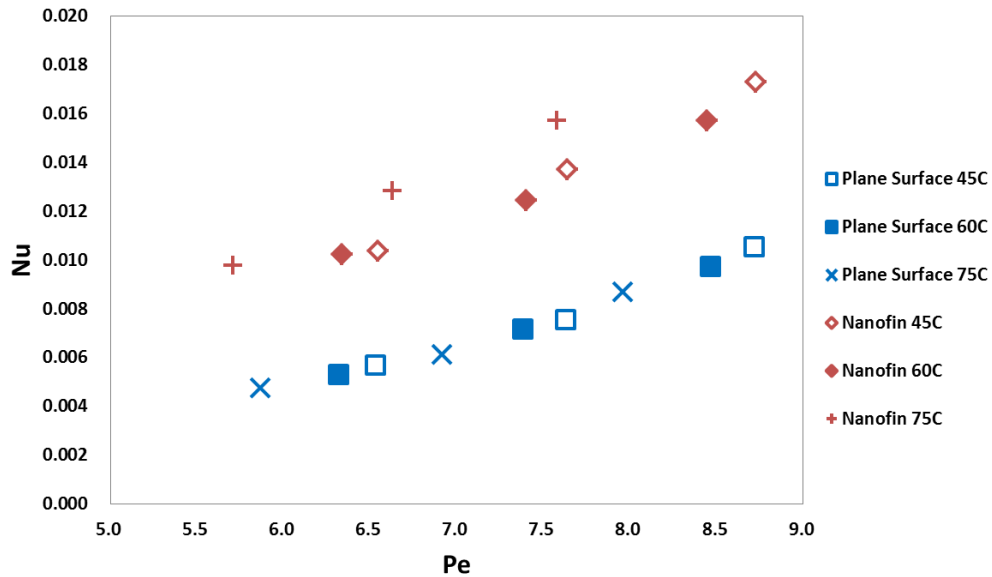
Figure 5-20 Nusselt number calculated using equation (11) as a function of Pêclet number for DIWflowing microchannel with plane surface (blue) and the surface containing artificial nanofins (red)

150

Results for the experiments on the surface with artificial nanofins are described in Table 5-1 and Figure 5-20. As can be seen, convective heat transfer is significantly enhanced on the surface with nanofins compared to plane surface. Specifically, heat removal rate from the heated surface enhanced from 25 % to 120 % and corresponding Nusselt number increased from 64 % to 110 %. These levels of enhancement in heat transfer are quite similar to those using nanofluids (up to 85 %). As earlier illustrated, these results support the hypothesis of the current study that modification of surface geometry due to the precipitation of nanoparticles during the experiments is the dominant mechanism in heat transfer enhancement observed in the experiments using nanofluids.

5.2. Potential Implications

5.2.1. Experimental Conditions

Precipitation of nanoparticles possibly affects temperature measurement on TFT surface. There exists temperature gradient within the precipitated nanoparticles, which may result in the difference between measured temperature by TFT and actual temperature at the bottom surface of microchannel. However, temperature gradient within the precipitated nanoparticles is expected to be small (less than 0.1 °C) since the dimension of the precipitates are extremely small. Considering the measurement uncertainty for temperature using TFT to be within 1 % (~ 0.5 °C), it can be concluded that the measurement error caused by precipitation of nanoparticles is expected to fall within the measurement uncertainty value. Thus, it is true that the precipitation of

nanoparticles may influence temperature measurement using TFT but this distortion is significantly lower than the measurement uncertainty and therefore is unlikely to distort the temperature measurements significantly.

Change of ΔT (= T_b − T_w) along microchannel is investigated to observe the characteristics heat transfer. Measurements are performed for control experiments (using DIW) and the results are summarized in Table 5-3. It is shown that the temperature difference between TFT and fluid temperature decreases along the flow direction. ΔT_1, ΔT_2, and ΔT_3 temperature difference between heated surface temperature and bulk fluid temperature at the location of 2 mm, 4 mm, 8 mm from the inlet, respectively. Surface temperature is directly measured by using TFT and the bulk fluid temperature is evaluated by assuming linear temperature gradient from inlet to outlet. According to the convection theory, it is constant for constant heat flux boundary condition and decreases for constant wall temperature boundary condition. The result indicates that heat transfer behavior of the current study seems to be similar to that under constant wall temperature boundary conditions. The result is compared to analytic values considering pure conduction (no flow) in Table 5-4. Derivation of analytic calculations is described in detail in appendix C.

It is conjectured that axial heat conduction also influences the result. As explained in detail in appendix D [122], axial heat conduction in the fluid near the inlet of the microchannel is significant, which leads to increasing difference between the wall and fluid temperature (this also leads to decrease in Nusselt number). In Table 5-2, the level of heat transfer in axial direction compared to in normal direction is roughly

estimated and shown. In this analytic estimation, the values for inlet temperature, outlet temperature, and wall temperature were 24.9 °C, 25.1 °C, and 46.0 °C, respectively, which is a boundary condition for DIW with 30 µl/min at given wall temperature. Although heat transfer in axial direction is shown to be negligible compared to that of in normal direction when there is no flow (values described in Table 5-2), it becomes significant when there is a flow. The ratio of axial heat transfer to heat transfer in normal direction is roughly estimated to 10 % when the flow is analytically considered at a given geometry of the microchannel in this study [122].

Table 5-2 <u>Comparison of the effect of heat transfer in axial direction [W/m^2]</u>

q"	q"$_{axial}$(Eq. (8))	q"$_{normal}$
rough estimation (equation (36))	245.9	2.917635×10^6
2D conduction (equation (C1))	1.41×10^{-9}	216.8

Also, additional levels of measurement uncertainty can be present for the thermocouples embedded at the inlet and outlet ports[118].When the temperature gradient is evaluated from the measurement of those thermocouples (especially at inlet and outlet), the experimental uncertainty is exacerbated because (1) the presence of the thermocouples possibly disturbs the flow and (2) the size of the tip of the thermocouples (~75 µm width) spans the dimension of the microchannel at the intlet and outlet – which can lead to additional experimental uncertainties.

Table 5-3 Change of ΔT (= T_b – T_w) along microchannel

T_w	Flow rate	ΔT_1 [°C]		ΔT_2 [°C]		ΔT_3 [°C]		ΔT_{out} [°C]	
45 °C	30 µl/min	18.0	(0.28)	17.0	(0.20)	15.0	(0.50)	12.4	(0.58)
	35 µl/min	17.2	(0.19)	16.5	(0.18)	14.0	(0.39)	10.6	(0.45)
	40 µl/min	16.8	(0.16)	16.8	(0.16)	14.2	(0.37)	11.4	(0.41)
60 °C	30 µl/min	26.3	(0.26)	25.2	(0.35)	21.4	(0.90)	18.1	(0.98)
	35 µl/min	25.8	(0.18)	25.4	(0.24)	21.6	(0.48)	17.7	(0.53)
	40 µl/min	25.3	(0.21)	24.4	(0.27)	20.7	(0.56)	16.9	(0.53)
75 °C	30 µl/min	37.9	(0.32)	36.0	(1.75)	30.4	(0.60)	28.0	(0.67)
	35 µl/min	35.6	(0.29)	34.5	(0.36)	29.0	(0.81)	25.3	(0.86)
	40 µl/min	34.2	(0.42)	33.4	(0.31)	27.5	(0.90)	23.3	(1.16)

Table 5-4 Comparison of experimental value of heat flux calculated using equation (8) with analytical valuecalculated using equation (C1) under constant wall temperature boundary condition with no flow

V_{in}	Flow Rate	q'' [W/m^2]	q''_{anal} [W/m^2]	T_w [°C]	T_{in} [°C]	T_{out} [°C]
20 V	30 µl/min	607	217	46.0	24.9	35.1
	35 µl/min	742	215	45.9	25.0	36.6
	40 µl/min	1050	215	45.2	24.3	35.5
25 V	30 µl/min	738	314	56.3	25.8	40.2
	35 µl/min	1135	320	56.2	25.0	40.8
	40 µl/min	1325	313	55.6	25.1	41.2
30 V	30 µl/min	1083	443	69.3	26.2	44.8
	35 µl/min	1428	431	68.1	26.1	46.2
	40 µl/min	1819	425	67.1	25.7	47.5

Heat flux results obtained by the heat balance model (enthalpy balance between inlet and outlet, i.e., based on temperature drop between inlet and outlet) is compared to those calculated based on wall temperature gradient (which assumes constant heat flux model) in Table 5-5–Table 5-8. It is shown that the values obtained from bulk fluid

temperature are approximately two times larger than those from TFT arrays. This significant discrepancy is basically from the additional experimental uncertainty for the thermocouples embedded at the inlet and outlet ports. When the temperature gradient is evaluated from the measurement of those thermocouples, the experimental uncertainty is exacerbated because (1) the presence of the thermocouples possibly disturbs the flow and (2) the size of the tip of the thermocouples (76 µm) are as large as the dimension of the microchannel which leads additional experimental uncertainties.

Table 5-5 Comparison of temperature gradient (for DIW experiment) evaluated from temperatures measured by TFT array and inlet/outlet port

T_w [°C]	Flow Rate [kg/s]	$\Delta T_{TFT}/\Delta x_{TFT}$ [°C/m] [a]	$\Delta T_{(Tout-Tin)}/\Delta x_{(Tout-Tin)}$ [°C/m] [b]	a / b
	0.009	286.9	661.8	43.4%
45	0.010	301.4	695.7	43.3%
	0.012	363.7	740.6	49.1%
	0.009	396.7	895.5	44.3%
60	0.010	445.3	956.0	46.6%
	0.012	521.7	1065.1	49.0%
	0.009	472.1	1208.7	39.1%
75	0.010	497.8	1258.0	39.6%
	0.012	609.8	1390.1	43.9%

Table 5-6 Comparison of temperature gradient (for TiO_2 0.001 wt.% experiment) evaluated from temperatures measured by TFT array and inlet/outlet port

T_w [°C]	Flow Rate [kg/s]	$\Delta T_{TFT}/\Delta x_{TFT}$[a]	$\Delta T_{(Tout-Tin)}/\Delta x_{(Tout-Tin)}$[b]	a / b
	0.009	332.9	800.7	41.6%
45	0.010	397.2	849.2	46.8%
	0.012	425.0	835.3	50.9%
	0.009	525.0	1200.5	43.7%
60	0.010	595.3	1253.9	47.5%
	0.012	632.5	1277.0	49.5%
	0.009	720.8	1670.2	43.2%
75	0.010	778.8	1718.5	45.3%
	0.012	816.5	1771.3	46.1%

Table 5-7 Comparison of temperature gradient (for TiO_2 0.005 wt.% experiment) evaluated from temperatures measured by TFT array and inlet/outlet port

T_w [°C]	Flow Rate [kg/s]	$\Delta T_{TFT}/\Delta x_{TFT}$[a]	$\Delta T_{(Tout-Tin)}/\Delta x_{(Tout-Tin)}$[b]	a / b
	0.009	385.8	710.5	54.3%
45	0.010	408.1	729.2	56.0%
	0.012	476.1	769.2	61.9%
	0.009	548.4	1019.2	53.8%
60	0.010	606.4	1075.1	56.4%
	0.012	616.5	1126.9	54.7%
	0.009	612.2	1426.3	42.9%
75	0.010	733.3	1449.0	50.6%
	0.012	845.4	1530.5	55.2%

Table 5-8 Comparison of temperature gradient (for TiO$_2$ 0.01 wt.% experiment) evaluated from temperatures measured by TFT array and inlet/outlet port

T$_w$ [°C]	Flow Rate [kg/s]	$\Delta T_{TFT}/\Delta x_{TFT}$[a]	$\Delta T_{(Tout-Tin)}/\Delta x_{(Tout-Tin)}$[b]	a / b
	0.009	436.0	563.6	77.4%
45	0.010	481.8	617.9	78.0%
	0.012	488.3	654.9	74.6%
	0.009	617.4	880.2	70.1%
60	0.010	639.5	963.0	66.4%
	0.012	727.1	955.3	76.1%
	0.009	802.7	1225.2	65.5%
75	0.010	900.2	1210.6	74.4%
	0.012	1005.6	1362.6	73.8%
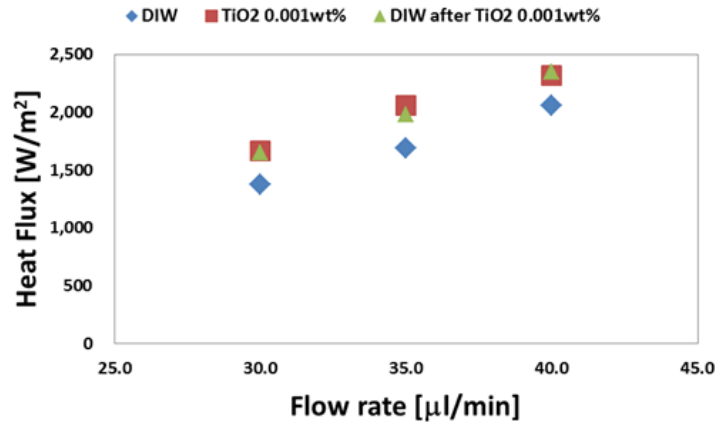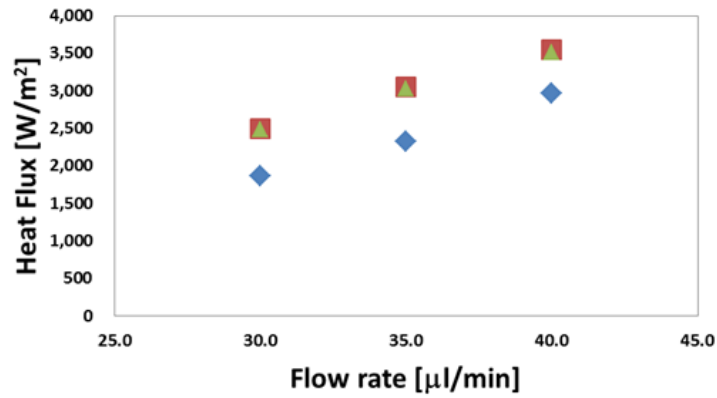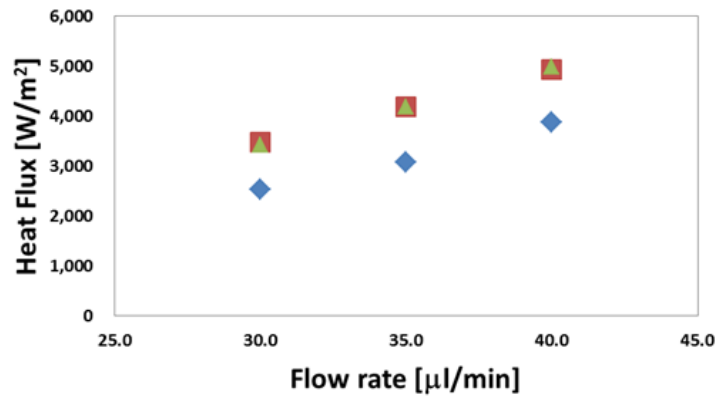
Figure 5-21 Heat flux values calculated using equation (27) plotted as a function of flow rate for TiO$_2$ nanofluids at mass concentration of 0.001% (a) T$_w$ ≈ 45 °C, (b) T$_w$ ≈ 60 °C, and (c) T$_w$ ≈ 75 °C

158
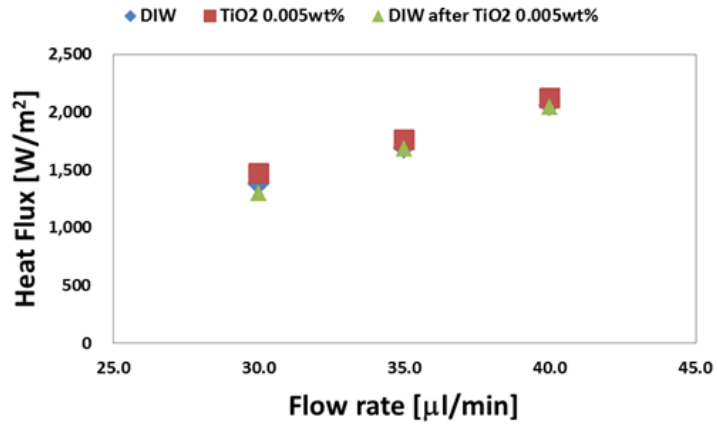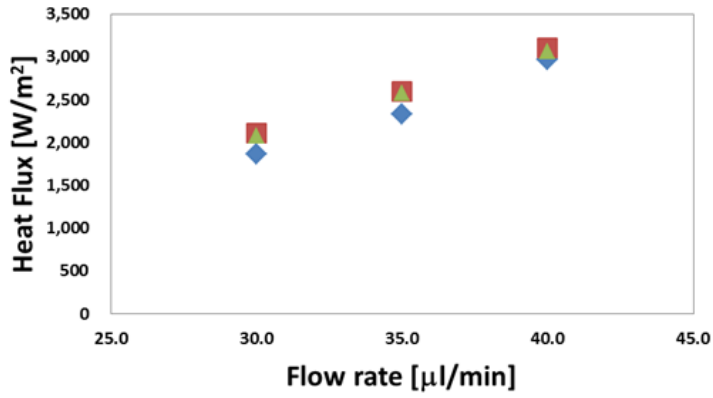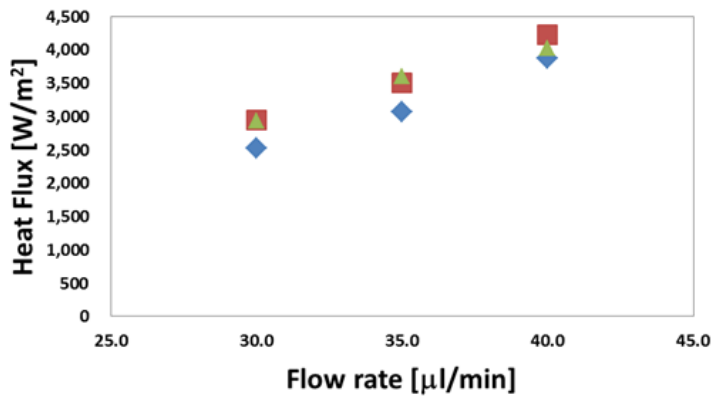
Figure 5-22 Heat flux values calculated using equation (27) plotted as a function of flow rate for TiO$_2$ nanofluids at mass concentration of 0.005 % (a) T$_w$ ≈ 45 °C, (b) T$_w$ ≈ 60 °C, and (c) T$_w$ ≈ 75 °C

159
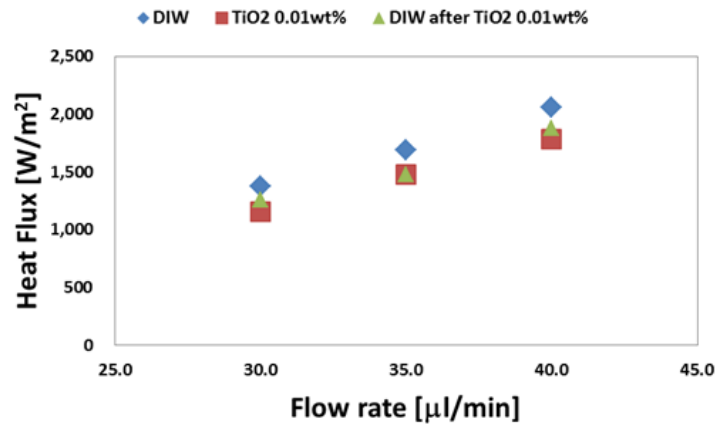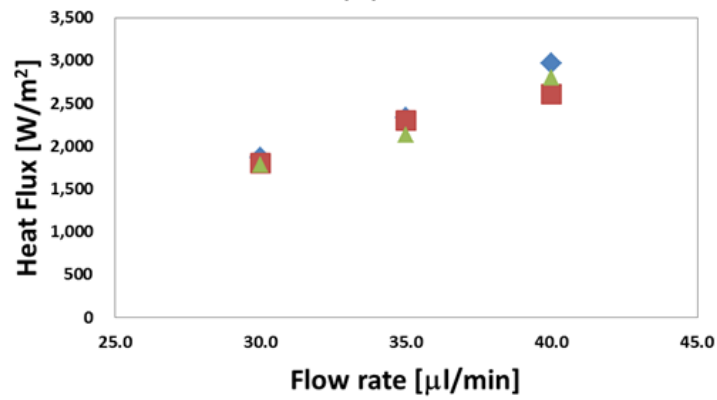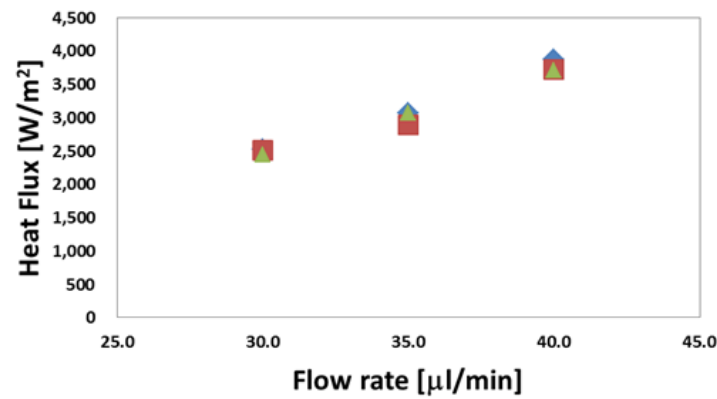
Figure 5-23 Heat flux values calculated using equation (27) plotted as a function of flow rate for TiO$_2$ nanofluids at mass concentration of 0.01 % (a) T$_w$ ≈ 45 °C, (b) T$_w$ ≈ 60 °C, and (c) T$_w$ ≈ 75 °C

160
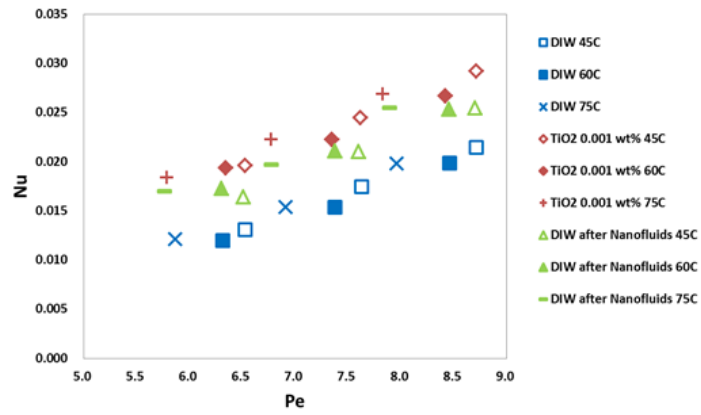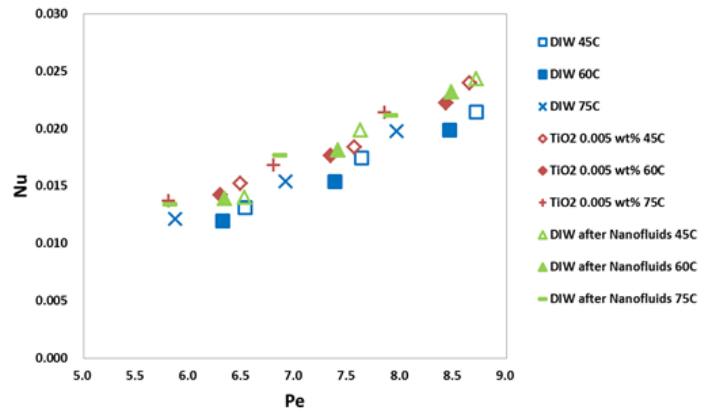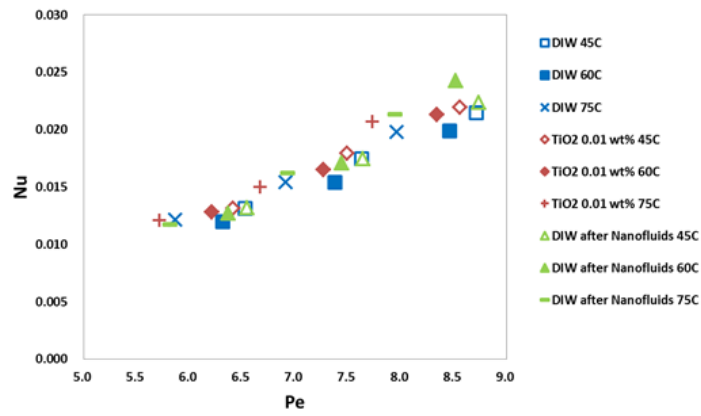
Figure 5-24 Nusselt number calculated using equation (11) and equation (27) as a function of Pêclet number for DIW, TiO$_2$ Nanofluids, and DIW after nanofluids experiments at (a) 0.001 wt%, (b) 0.005 wt%, and (c) 0.01 wt%

Stability of nanofluids is another issue which is of great importance in selection of nanofluids for the experiments because an unstable solution may result in significant errors and lack of repeatability for the experimental results. For example, it is known that aqueous Al_2O_3 nanofluids are quite unstable. This instability may result in significant difference between experimental results for the same experimental condition because nanoparticles are settled down during the experiments. Thus, it is inappropriate to study convective heat transfer of unstable suspensions like aqueous Al_2O_3 nanofluids, unless they are closely monitored at each step of the experiments – ensuring that agglomeration and precipitation of the nanoparticles have been minimized.

Also, it could be suspected that the existence of TFT might significantly influence on the heat transfer. Because the thickness of TFT (400 nm) is comparable to the height of the nanofins (350 nm), it is highly possible there is an enhancement in heat transfer due to TFT. Thus, measured convective heat transfer maybe locally exaggerated for microchannels even with plane surface. However, this localized enhancement does not significantly influence overall heat transfer as nanofins do because the number of TFT junctions is not as many as the number of nanofins. Whereas there are more than a million nanofins in the microchannel on the artificially fabricated nanofin surface, there are only eight TFT junctions. As a result, although heat transfer on plain microchannel can be locally exaggerated because of the existence of TFT, total amount of heat transfer changes very little. Thus, it is considered that the influence of TFT on the results is negligible in this study.

Tunable thermophysical properties afforded by nanomaterials can benefit several applications. For instance, the ability to tune the viscosity of a liquid has significant implications for the transportation of crude oil in pipelines. If the viscosity of crude oil can be reduced significantly using cheap additives the market price for crude oil can be decreased dramatically. However, viscosity of a fluid generally increases on mixing with nanoparticles [105, 123-125]. Also, specific heat capacity is also affected on mixing with nanoparticles, as discussed earlier. Literature reports show that the specific heat capacity decreases for aqueous nanofluids. However, Vajjha and Das reported that the specific heat capacity of aqueous silica nanofluids exceeded that of pure water for temperatures exceeding 70 °C [108]. Since higher specific heat capacity values results in higher convective heat transfer, heat transfer characteristics of silica nanofluids at higher temperature (75 °C) can be expected to be superior to those at lower temperatures (45 °C). This is also consistent with the experimental results of previous studies [118-121].

Monitoring precipitation of nanoparticles during the experiments can be the subject of a separate study in the future, using special techniques that are currently available commercially (e.g., using Surface Plasmon Resonance or "SPR" techniques). The oscillations at the boundary of a solid transparent material and the external medium such as air or water are extremely sensitive to minute changes that can occur at the boundary (or on the solid surface). For example, changes on a solid surface due to the absorption of molecules can affect the refractive index at the solid-liquid interface by modulating the surface plasmons. Surface plasmon resonance (SPR) affinity sensors are

utilized to detect the surface binding of chemical and biological materials by exploiting this phenomenon [126, 127]. This measurement technique can be adapted for in situ detection of the precipitation of the nanoparticles during the execution of the heat transfer experiments. Hence the experiments performed in this study can be repeated for real time monitoring of the precipitation of the nanoparticles when incorporated with a well-designed sensing system. This approach is recommended as future direction for this study.
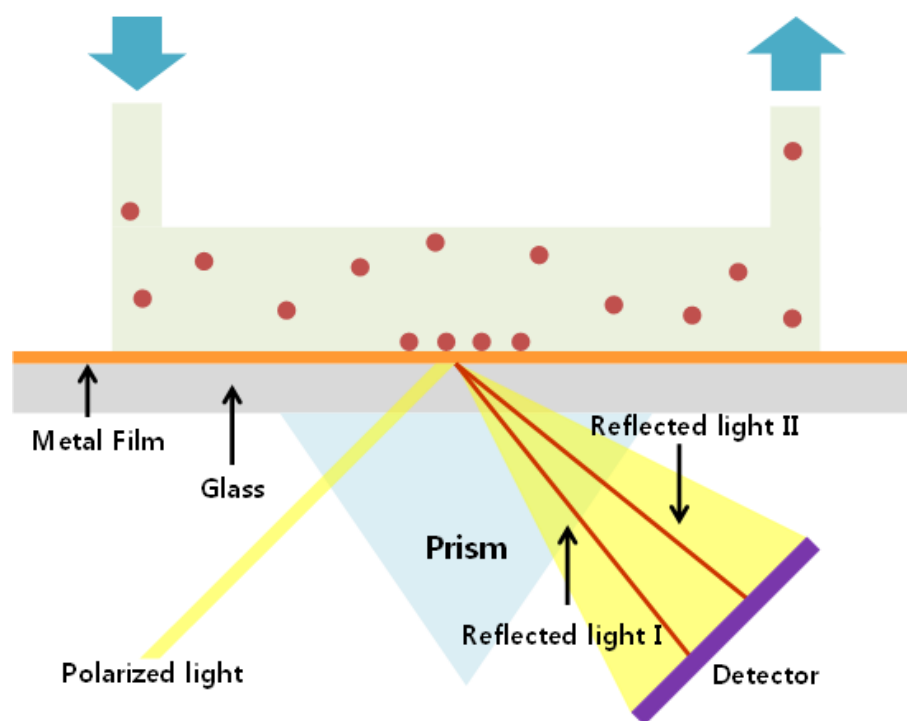
Figure 5-25 A diagram how surface plasmon resonance (SPR) can be utilized for detecting the precipitation of nanoparticles in-situ while flowing in the microchannel

Figure 5-25 describes the working principle of a SPR sensor. The light passes through a prism and strikes the surface of a flow at a fixed angle and is totally internally reflected at the solid-liquid interface. When the light strikes the surface, the evanescent wave (an electromagnetic component of the light or surface plasmon) propagates into the aqueous solution and interacts with the electrons in the metal film. Surface plasmon resonance (a surface plasmon is a wave of excited electrons) is produced by this interaction and is detected by the reflected light. The detector monitors the position of the reflected light and calculates the SPR angle. Since the SPR angle is very sensitive to the composition of the layer at the surface of the metal film, it is possible to monitor precipitation of nanoparticles in situ with high degree of accuracy and in real time.

5.2.2. *Persistency of Residual Effect and Surface Affinity Forces*

Initially it was not apparent if the precipitated nanoparticles were bound stably to the heat exchanging surfaces (i.e., if the precipitation is permanent) or if they could be flushed out from the surface at high enough flow rates (or shear rates). However, it was observed that the precipitated nanoparticles were bound stably and not flushed out during the control experiments that were performed immediately after performing the nanofluids experiments (which were performed over a period exceeding a minimum of four hours) Van der Waals forces predominantly result in adhesive forces [128]. Van der Waals force is proportional to particle diameter (D) whereas other forces such as electrical force and inertia force are proportional to D^2 and D^3, respectively. Since electrical force and inertia force decrease significantly as the size of a particle becomes

165

sub-micron scale, Van der Waals force becomes much larger than other forces for the smaller nanoparticles. Thus, it is very difficult to break adhesion forces binding the precipitated nanoparticles to the heat exchanging surface, which means that the precipitation and binding of the nanoparticles is virtually permanent and irreversible for the flow conditions used in this study.

Furthermore, Van der Waals (adhesion) force is dependent on the temperature as well as surface roughness. The free energy of this interaction is proportional to temperature in liquid-water mixture [129]. Also, changes in the surface roughness could result in the change of the total van der Waals force by up to several orders of magnitude [130-133]. The overall attraction force of van der Waals force between rough surface and smooth surface dramatically increases when the gap width is below 20 nm compared to that between smooth-smooth surfaces. In this sense, adhesion of precipitated nanoparticles on the wafer is rarely disrupted due to heating at higher temperature, especially for a rough surface.

Van der Waals adhesion force can be represented by Lennard – Jones (LJ) potential. This model describes the interaction potential between a pair of neutral atoms or molecules. Surface affinity between Si and SiO_2 and between Si and TiO_2 is evaluated using the classical "12 – 6" LJ potential. Standard "12 – 6" LJ potential is expressed as follows:

$$V_{LJ} = 4\varepsilon \left[\left(\frac{\sigma}{r} \right)^{12} - \left(\frac{\sigma}{r} \right)^{6} \right] \tag{28}$$

whereε is the depth of potential well which represents how strongly the two atoms attract each other and σ (referred to as the van der Waals radius) is proportional to the distance at which the intermolecular potential between two atoms is zero. This provides the information about how close two non-bonding atoms can be in equilibrium. The distance between two atoms which is measured from the center of one atom to the center of the other atom is denoted as r. In 12 – 6 LJ potential equation, the first term, $(\sigma/r)^{12}$, describes repulsive forces and the second term, $(\sigma/r)^6$, describes attraction forces.

When two non-bonding atoms are in an infinite distance apart, their bonding potential energy is zero. The bonding potential keeps decreasing from zero to negative values as the distance between two atoms decreases until two particles reach equilibrium. If it is forced to push two atoms closer to equilibrium, repulsion begins to occur and their bonding potential energy rapidly increases. Potential energy below equilibrium distance becomes positive values and such a large potential energy is not desirable. When two atoms are at equilibrium state, the potential energy between them reaches the minimum value and the pair of two atoms is the most stable and will remain in that state unless severe external force is exerted on them. The deeper the well depth (ε) is, the stronger the interaction between two atoms is.

In this study, values for pair coefficients, ε and σ, are obtained from Material Studio (Accelrys, Inc., 2008) using the"cvff" force field [134] and are summarized in Table 5-9. Pair coefficients for the non-bonding interactions between different atoms of type i and j are calculated using arithmetic mixing rule which is shown as follows.

$$\varepsilon_{ij} = \sqrt{\varepsilon_i \varepsilon_j} \tag{29}$$

167

$$\sigma_{ij} = \frac{\sigma_i + \sigma_j}{2} \tag{30}$$

Table 5-9 ε and σ values for various molecular sturctures

Interaction	ε [kcal/mol]	σ [Å]
Si-Si (Si wafer)	0.0400184175	4.0534337049
Si-Si (in SiO_2)	1.1E-09	7.2927965265
Ti-Ti	384.7899657314	1.1333858655
O-O (in SiO_2 / TiO_2)	0.000000023	11.2737516405
H-H	0	0
O-O (in H_2O)	0.155416412	3.165520088

Calculated values of the $12 - 6$ LJ potential for the pairing of Si (silicon wafer) – TiO_2, SO_2 (pyrex wafer) – TiO_2, Si (silicon wafer) – SiO_2, and SO_2 (pyrex wafer) – $SiO_2$are plotted in Figure 5-26 and Figure 5-27. In these figures, LJ potential values for Si – TiO_2 pair and SiO_2 – TiO_2 pairs are presented in the left axis with blue line and those for Si – SiO_2 pair and SiO_2 – SiO_2 pair are demonstrated in right axis with green dashed line.As shown in these figures, the well depth for Si – TiO_2 pair as well as SiO_2 – TiO_2 pairis significantly deeper than that for Si – SiO_2 pair and SiO_2 – SiO_2 pair, respectively. Theseresults indicate that the bonding force between silicon/pyrex glass wafer and TiO_2 nanoparticles is stronger than between silicon/pyrex glass wafer and SiO_2 nanoparticles. Thus, it could be stated that TiO_2 nanoparticles have stronger surface affinity to silicon/pyrex glass wafer than SiO_2 nanoparticles once the particles are precipitated on the wafer. However, larger force (and energy) is required to move TiO_2 nanoparticles from the infinity distance to the surface of the wafer because the area under the curve (between the plotted values and the x-axis) is significantly larger for

TiO$_2$. The area under the curve represents the force (or energy) required to move atoms from infinity distance to the given location. Obviously, this force for Si – TiO$_2$ pair as well as SiO$_2$ – TiO$_2$ pairs much larger than that for Si – SiO$_2$ pair as well as SiO$_2$ – SiO$_2$ pair, as shown in Figure 5-26. In other words, SiO$_2$ nanoparticles are more easily precipitated on the wafer than TiO$_2$ nanoparticles during the convective heat transfer experiments. Therefore, excessive precipitation is more likely to occur for SiO$_2$ nanoparticles.

Furthermore, it can be concluded from the comparison of each depth of well (i.e., the absolute value of the interaction potential at the location of the equilibrium distance)in Figure 5-26 and Figure 5-27 that silicon wafer is likely to have much larger surface affinity forces with nanoparticles than for that of thepyrex wafer. This also indicates that the total energy required to move atoms from infinity distance to the given location is much larger for silicon wafer than pyrex wafer. Thus, nanoparticles precipitate more spontaneously on the surface of the pyrex wafer than on the silicon wafer.
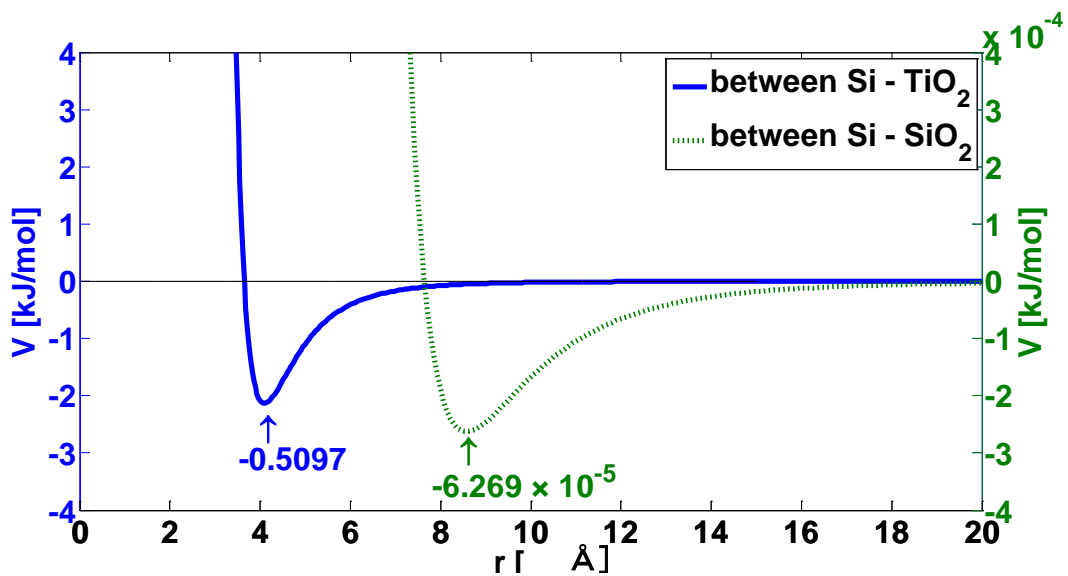
Figure 5-26 Lennard– Jones (LJ) potential between Si and TiO₂ (blue) and between Si and SiO₂ (green)
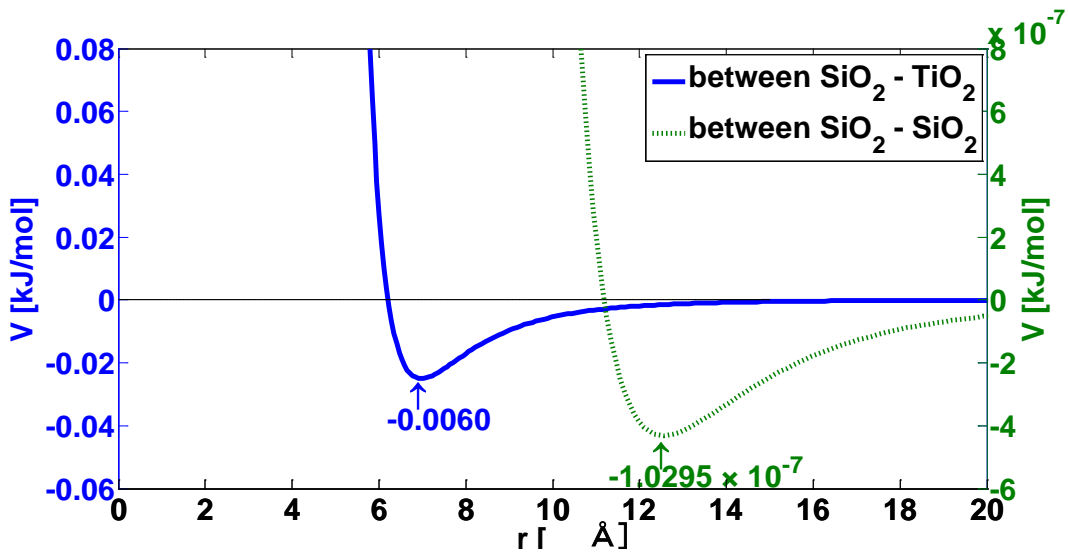
Figure 5-27 Lennard– Jones (LJ) potential between SiO₂ and TiO₂ (blue) and between SiO₂ and SiO₂ (green)
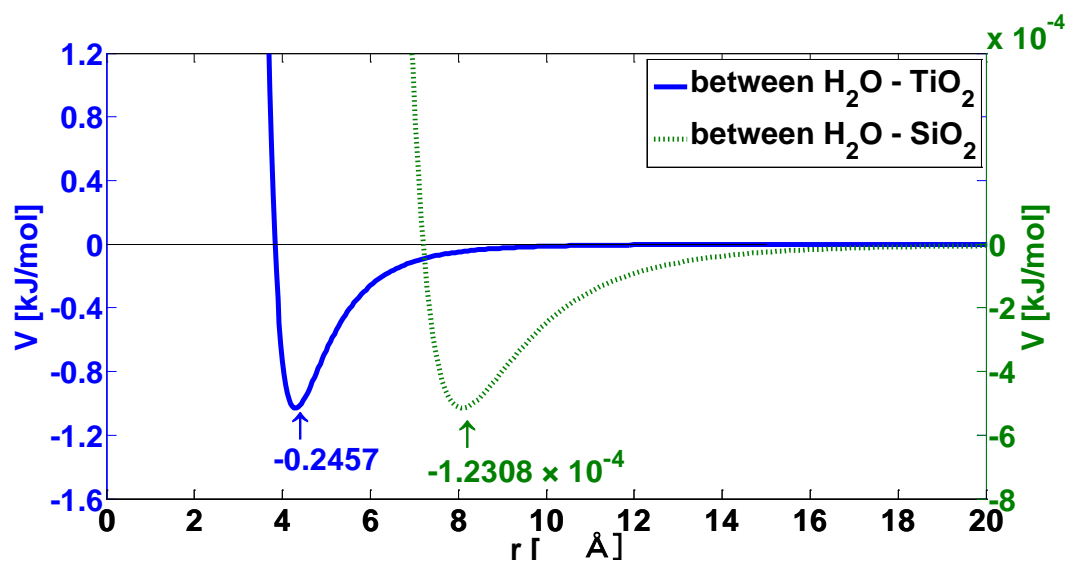
Figure 5-28 Lennard– Jones (LJ) potential between H₂O and TiO₂ (blue) and between H₂O and SiO₂ (green)

Calculated values of the 12 – 6 LJ potential for the pairing of H_2O (solvent molecules) – TiO_2 (nanoparticle) and H_2O (solvent molecules) – TiO_2 (nanoparticle) are plotted in Figure 5-28. In these figures, LJ potential values for H_2O – TiO_2 pair is presented in the left axis with blue line and those for and H_2O – SiO_2 pair is demonstrated in right axis with green dashed line.As shown in these figures, the well depth for and H_2O – TiO_2 pair is significantly deeper than that for and H_2O – SiO_2 pair. Theseresults indicate that the bonding force between water and TiO_2 nanoparticles is stronger than between water and SiO_2 nanoparticles. Thus, it could be stated that TiO_2 nanoparticles have stronger surface affinity for hydration than that for SiO_2 nanoparticles. Hence, larger force (and energy) is required to remove the hydration layer and cause the precipitation of the TiO_2 nanoparticles compared to that for the SiO_2 nanoparticles. The area under the curve represents the force (or energy) required to remove the atoms (or

molecules) from the surface of the nanoparticle. Obviously, this force (or energy) for $H_2O - TiO_2$ pair is much larger than that for $H_2O - SiO_2$ pair, as shown inFigure 5-28. In other words, SiO_2 nanoparticles are more easily precipitated due to a weaker hydration barrier than for that of TiO_2 nanoparticles during the convective heat transfer experiments. Therefore, excessive precipitation is more likely to occur for SiO_2 nanoparticles.

5.2.3. Enhancement of Surface Area

Enhancement of the effective surface area due to the precipitation of nanoparticles was evaluated by measuring the surface topography of the precipitated nanoparticles and analyzing the corresponding surface area of these precipitated protrusions which can act as "nanoflins". The surface profile was measured using Atomic Force Microscopy (AFM) techniques. The surface profiles obtained from the AFM measurements are expected to be accurate to nm resolution. However, since the AFM tip has a finite radius, the side of the tip contacts precipitated particles (instead of the end of the tip) which causes the measured diameter of the particle is broader than the real value (convolution effect). Thus, the effective diameter values of the surface nanostructures formed in-situ due to the precipitation of the nanoparticles (i.e., nanofins) are evaluated by using the full width at half maximum (FWHM) value from the surface topography measurements. Thus, the level of enhancement of the surface area is estimated by multiplying the height of the particle with the corresponding value of FWHM for the surface topography data.

172

Table 5-10 Enhancement of overall effective surface area due to the precipitation of nanoparticles

	Concentration	Enhancement
	0.05 wt. %	26.3%
SiO_2	0.1 wt %	38.4%
	0.3 wt %	50.4%
	0.001 wt. %	5.6%
TiO_2	0.005 wt %	17.6%
	0.01 wt %	21.8%

The results for these analyses are summarized in Table 5-10 and Figure 5-29. Figure 5-29 describes AFM scanning results on the precipitated surface under each experimental condition after completing experiments. The results for this analysis are illustrated in Table 5-10. The level of enhancement is plotted as a function of nanoparticles concentration and is shown in Figure 5-30. As can be seen in Figure 5-30, enhancement of surface area is significantly increase with minute addition of nanoparticles and the level of increase in the enhancement gradually decreases as nanoparticle concentration increases. Thus, it is proposed that there exists a saturation level of enhancement of surface area above saturation concentration.
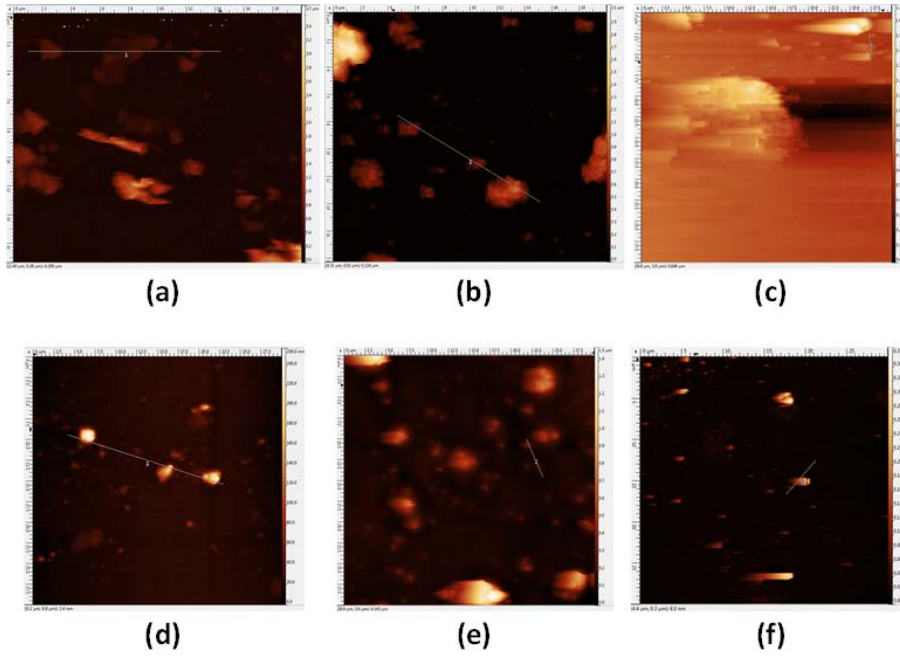
Figure 5-29 AFM images on the surface after flow SiO2 nanofluids at the mass concentration of (a) 0.05 %, (b) 0.1 %, (c) 0.3 % and TiO$_2$ nanofluids at the concentration of (d) 0.001 %, (e) 0.005 %, and (f) 0.01 %
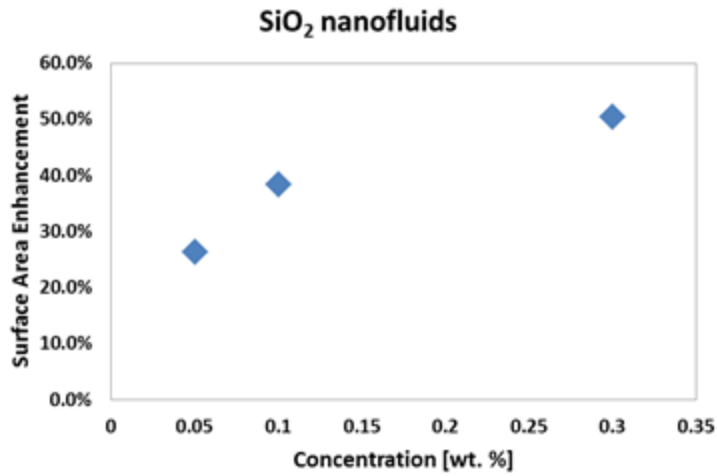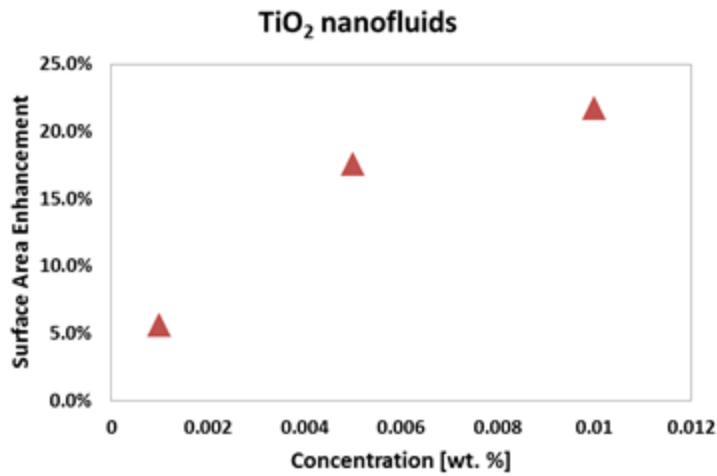
Figure 5-30 Enhancement of surface area for (a) SiO$_2$ nanofluids and (b) TiO$_2$ nanofluids as a function of nanoparticle concentration

The results listed in the table demonstrate that the effective surface area was enhanced by ~50 % and ~28 % for SiO$_2$ nanofluids and TiO$_2$ nanofluids, respectively. Since very large particles are formed by surface precipitation for the SiO$_2$ nanofluid experiments (i.e., formation of a fouling film due to the excessive precipitation of the

175

nanoparticles), the large agglomeration of nanoparticles leads to higher levels of enhancement of surface area compared to that of TiO_2 nanofluids. However, the underlying fouling film leads to lower levels of enhancement in the net heat transfer for the SiO_2 nanofluid experiments.

Artificial nanofins also enhance the effective surface area. For the sample containing nanofins with nominal diameter, height, and pitch to 140 nm and 350 nm, and 1 μm respectively, it is evaluated that the surface area enhancement is ~15 %. However, the level of heat transfer enhancement is significantly larger than the corresponding enhancement of the effective surface area. Therefore, it can be assumed that the precipitation of the nanoparticles also affects the transport phenomena in the near wall region compared to that of the plain surfaces (control experiments). This is apparent since the levels of enhancement in the values for the effective surface area due to the precipitates (which act as nanofins) do not completely account for the levels of enhancement in the heat transfer values. For example, precipitation of the nanoparticles can cause the local values of the concentration of the nanoparticles in the solvent in the near wall region to be significantly different than in the bulk ("far away" from the wall) – leading to modification of the velocity profiles and temperature profiles in the near wall region – in turn affecting the heat transfer and pressure drop values.

5.2.4. Other Possible Mechanisms

The level of heat transfer enhancement is significantly larger than the corresponding enhancement of the effective surface area. Therefore, it can be assumed

that the precipitation of the nanoparticles also affects the transport phenomena in the near wall region compared to that of the plain surfaces (control experiments). This is apparent since the levels of enhancement in the values for the effective surface area due to the precipitates (which act as nanofins) do not completely account for the levels of enhancement in the heat transfer values.For example, precipitation of the nanoparticles can cause the local values of the concentration of the nanoparticles in the solvent in the near wall region to be significantly different than in the bulk ("far away" from the wall) – leading to modification of the velocity profiles and temperature profiles in the near wall region – in turn affecting the heat transfer and pressure drop values.

Also, formation of bubbles with sub-micron scale dimensions (which is called "nanobubble") can affect heat transfer. Whereas bare silicon wafer has negligible surface roughness (i.e., to atomic scale roughness since it is a single crystal), silicon wafer containing etched nanofins has significant level of surface roughness. In general, surface roughness plays an important role in providing a conducive situation for the nucleation of bubbles and in enhancing the bubble nucleation site density [135]. Since formation of bubbles influences the heat transfer performance, it is worth investigating the effect of bubbles on the results in this study – eventhough the working temperature of the current study (~70 °C) is significantly lower than the boiling temperature of water (100 °C).

Discovery of bubble nucleation with sub-micron scale dimensions (which is called "nanobubble") has been reported recently. The nanobubbles have been reported to possess many interesting properties that can potentially be exploited for various

applications such as cleaning processed and drug delivery 9e.g., for cancer therapy) [136-138].

The topic nanobubble nucleation is controversial subject. The reason for the past controversies on the existence of nanobubbles arose from the inconsistency of the experimental results from various studies in the literature. Also, predictions from the conventional nucleation theory require very high values of wall superheat (i.e., heater temperatures) which makes it physically unrealistic for the existence of nanobubbles. To illustrate, classical Young-Laplace equation predicts that the pressure inside a bubble is greater than outside a bubble and the pressure difference is inversely proportional to the bubble diameter. As the size of bubble decreases, the pressure difference increases monotonically. For instance, 10 nm and 100 nm bubbles should have Laplace pressure on the order of 150 atm and 15 atm, respectively. It was reported that nanobubbles are unstable when subjected to these inherent high pressure values and eventually disappears (or collapses) within 10 ~ 100 μs [139]. Cavicchi and Avedisian had observed metastable nanobubbles on a hydrophilic, pulse-heated surface which they reported would exist for approximately ~1 ms [140].

However, numerous reports have demonstrated that nanobubbles are stable for several days. Since it is impossible to observe nano-sized bubbles using conventional microscopy techniques (e.g., optical microscopy or electron microscopy), the existence of nanobubbles have been primarily demonstrated by utilizing Atomic Force Microscopy (AFM). In general, AFM imaging has been conducted using tapping mode because contact mode tends to be too invasive [141-143]. It seems that the inconsistences of the

experimental processes results in the inconsistent experimental results. For example, nanobubbles are formed when the surface is cleaned using ethanol (due to the solvent exchange process) whereas nanobubbles were not observed when the solvent exchange process is not applied [144].

Theoretical efforts to explain these discrepancies have also been intensely controversial. According to the line tension theory, it is proposed that the macroscopic contact angle is modified because of changes in the volume of the bubble. However, this theory still predicts higher pressure difference than those observed in the experiments. Another theory suggested that a dynamic equilibrium condition is established such that the nanobubbles lose and gain gas at the same rate. This situation is plausible for hydrophobic surfaces because depletion layer at the interface has to be considered for nanobubbles [144]. The prediction for the size of bubbles from this theory is found to be consistent with the experimental results. However, this theory was incapable of explaining the existence of nanobubbles on hydrophilic surfaces [145]. Another theory proposes that surface contamination in the vicinity of a nanobubble reduces the surface tension at the vapor-liquid interface. However, this theory has invalidated by experiments where nanobubbles were generated using electrolysis after mixing with additives [146, 147]. Since there is a lack of a proper theoretical construct that can be used to predict the nucleation of nanobubbles, investigations continue with the motive ofunderstanding the stability of nanobubbles.

The existence of nanobubbles, though proven, remains controversial due to a lack of understanding of the physical processes responsible for the nucleation of the

179

nanobubbles. Therefore, it is difficult to characterize the effect of nanobubbles on the convective heat transfer in a microchannel because little is known about nature of the nanobubbles. Nevertheless, fabrication of artificial nanofins could influence the formation (nucleation) of nanobubbles which may enhance heat transfer. In addition, some studies suggest that nanobubbles can nucleate on heated nanoparticles [148, 149]. Such a phenomenon has significant scientific, commercial and societal implications since nanobubble nucleation on nanoparticles has been proposed for cancer therapy [149-151]. It is not clear if the formation of nanobubbles on nanoparticles as well as on nanofins and nanostructures (e.g. thin film thermocouples) that were used in this study – are responsible for the anomalous results reported in this study (e.g., both enhancement and degradation of transport phenomena in microchannel flows).

Recently, the existence of a semi-solid phase of the solvent molecules near the surface of nanoparticles (which is called "compressed layer") has been reported [91, 103, 105, 125, 152]. The existence of compressed layer has been validated both experimentally and theoretically.

Oh et al. has experimentally shown ordered liquid aluminum atoms adjacent to crystalline interface with sapphire [152]. Also, Yu et al. have experimentally studied the characteristics of liquid atoms within the solid-liquid interface [153]. By analyzing X-ray reflectivity data, the existence of a liquid layer at the solid-liquid interface was demonstrated experimentally and the experimental measurements showed that the thickness of the compressed layer can span a distance of three to six molecules from the surface of the crystalline interface.

In addition, the existence of compressed liquid layer has also been demonstrated by various research groups using molecular dynamic simulations [91, 154]. Li et al. demonstrated the existence of a dense layer of solvent molecules on the surface of a nanoparticle byplotting the mass density distribution of solvent molecules near the nanoparticle surface by analyzing the results obtained from MD simulations performed by the investigators of this study [155]. It was concluded from these results that the enhanced density of the solvent phase on the nanoparticle surface proves the existence of a compressed layer that nucleates around the nanoparticles with a thickness of approximately 0.5 nm.Solid-like characteristic of this layer due to increased density and significantly ordered atomic structure in this region could contribute to higher thermal conductivity of nanofluids. Xue et al. also investigated the effect of molecular ordering(within the compressed layer around nanoparticles) on the thermal conductivity of nanofluids. This investigation was performed using non-equilibrium molecular dynamics (MD) simulations [156]. The solvent molecules within the compressed layer are much more constrained than the solvent moleculesin the bulk phase (since these solvent molecules in the compressed layer tend to mimic the underlying lattice structure of the atoms on the surface of the nanoparticle, typically due to van der Waals interactions and ionic interactions). The solvent molecules in the compressed phase are, thus, expectedto have enhanced thermal properties including higher values of thermal conductivity.

In the compressed layer, the solvent molecules acquire an ordered structure (forming a compressed phase) by following the underlying lattice structure of the atoms

on the surface of the nanoparticle. This ordering of solvent molecules is quite different from the random motion of the molecules in the bulk liquid phase. Obviously, thermophysical properties of this layer are different from that of the bulk liquid phase, as was illustrated in earlier studies [155, 156]. However, it is very difficult to estimate the thermo-physical properties of the compressed layer since the crystalline structure of the compressed layer is a function of the lattice structure of the nanoparticle, which can be significantly different from that of the solid phase of the solvent material. Nevertheless, it is expected that the thermo-fluidic properties of the solvent phase can be modified significantly due to the existence of the compressed liquid layer that is nucleated on the surface of the nanoparticle. In addition, the nucleated compressed layer can form long-range structures as was demonstrated in previous studies [157, 158].
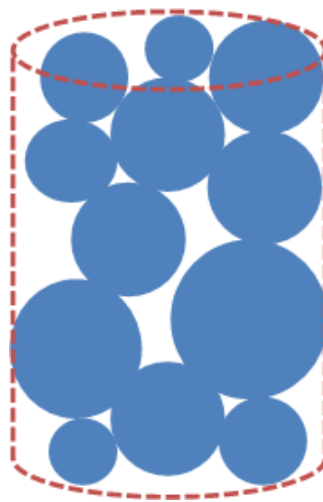
Figure 5-31 Schematic of a fractal structure potentially formed by the nanoparticle of precipitates (i.e., the resulting nanofin) on the heat exchanging surfaces. Red dashed line represents the equivalent cylindrical structure measured by the scanning probe tip that is then used in the current study to evaluate level of enhancement of the surface area by the resulting nanofin.

In addition, it is highly probable that the enhancement of surface area due to the precipitation of nanoparticles is underestimated in this study. In this study the surface area enhancement calculations are performed by assuming that the precipitates form cylindrical shaped nanofins where a simplified approach is adopted to estimate the dimensions of the nanofins (height is measured by AFM and diameter is assumed to be represented by FWHM). However, formation of the precipitate structures by the nanoparticles is much more complex. In fact, precipitation of nanoparticles has fractal structure as shown in Figure 5-31. As shown in Figure 5-31, surface area of the precipitated nanoparticles (blue spheres) is much larger than the simplified model used in this study (red dashed cylinder). Although it is very difficult to evaluated exact value of surface area enhancement, it is obvious that the level of evaluated enhancement of surface area due to the precipitation of nanoparticles is therefore underestimated in this study. It is possible that the precipitated nanoparticles form fractal structures whereby the fractal order of the nanostructures would determine the lower and upper bounds on the actual value of the surface area of the precipitates (e.g., the correlation dimension of the precipitated nanostructures would control the value of the surface area). Determining the fractal order of the precipitated nanostructures for a more accurate estimation of their surface area could be the subject of another study where the experimental variables could potentially affect the value of the fractal order – such as flow rate, wall temperature, heat flux, axial location along the flow direction, size distribution of the nanoparticles at the flow inlet, etc. Thus, underestimation of the surface area could be

183

one of the contributory factors for the discrepancy in the estimates compared to the levels of enhancement of heat transfer observed in the experiments.

In addition, although convective heat transfer experiments on the surface with artificial nanofins validated the hypothesis of the current study, there could be differences in transport mechanisms between nanofins formed from nanofluids and artificially engineered nanofin surface. Whereas artificial nanofins are well aligned on the surface with regularly defined dimensions, nanoparticles are randomly precipitated on the surface (with potentially fractal structures). Also, there could be a dynamic equilibrium and exchange mechanisms may exist for a fraction of the nanoparticles precipitated on a surface to be re-solvated into the solvent (it is not clear what fraction of the nanoparticles precipitated nanoparticles could be continuously deposited and re-solvated during the experiments). This dynamic equilibrium process may result in additional transport mechanisms (which may not exist for the artificial nanofins) because colder nanoparticles from the solvent may cause enhanced heat transfer during precipitation or when they are deflected (i.e., bounced off or re-solvated) after contact with the hot surface.

5.2.5. *Heat Transfer and Pressure Drop*

Only the convective heat transfer characteristics of nanofluids in a microchannel are investigated in this study. However, studies involving the pressure drop for internal flows arehistorically also a significant research area, especiallyfor practical applications such as turbomachinery. Such studies typically are focused on optimization of pressure

drop while trying to maximize heat transfer by using a complex combination of the coolant material and geometry for a range of flow rates. Since nanofluids have significantly higher viscosity values (as a function of shear rate) than that of the pure solvent –internal flow of nanofluids is associated with significantly higher pressure drop values (because nanofluids often have non-Newtonian rheological behavior even though the pure fluid can be Newtonian). For example, Ko et al. reported in their experimental study that the pressure drop of CNT nanofluids flowing in a horizontal pipe is increased significantly in the laminar flow regime [159]. The level of increase of the pressure drop in laminar flow regime was observed to be enhancedin this study as the nanoparticle concentration was increased. However, no significant increase in pressure drop was reported in the turbulent flow regime in this study. Arani and Amani also reported increase of friction factor with increasing nanoparticle concentration due to the increase of fluid viscosity [160]. Hence, there is a delicate balancing act in trying to maximize heat flux without significantly enhancing the pumping power requirement. This is a more difficult task to achieve in view of non-Newtonian rheological properties of nanofluid, compared to that of the typical Newtonian slvents/ coolants (such as air, water or refrigerants).

Recently, reduced pressure drop through microchannels using nano-textured surfaces was reported [161-163]. It was reported that high levels of surface roughness results in the increase of hydrophobicity of the surface with a concomitant decrease in the pressure drop for flow in microchannels and nanochannels, for the same flow rate (or conversely – higher flow rates for the same pressure drop). For example, Krupenkin et

al., illustrated super-hydrophobic surface with contact angles approaching 180° by fabricating an array of grass-like structure (nanoposts with 400 nm in diameter and 7 μm in height with 1.25 μm pitches) and coated the surface with hydrophobic polymer [164]. These engineered nanostructured surfaces were found to reduce pressure drop in internal flows. The authors rationalized their experimental data by assuming that the internal flow is modified due to trapping of air bubbles in the intervening space between the nanoposts. The space between nanoposts traps air to preserve non-wetting characteristic and effectively generate a surface in slip flow (at the air-liquid interface) which result in reduced drag force during internal flow.

In this study it is shown that the flow of nanofluids results in the precipitation of nanoparticles and the precipitates could behave as nanofins. These nanofins possibly play a role similar to that of the high aspect ratio nanoposts to generate effectively a super-hydrophobic surface on a local scale. Hence it is plausible that under certain conditions nanofluids may result in reduced pressure drop while simultaneously enhanced heat transfer compared to that of the pure solvent (e.g., water).

Modification of surface geometry has also been investigated to enhance heat transfer with minimal pressure loss. For example, Griffith et al. have studied heat transfer characteristics in rotating rectangular channels withcontacting dimples in turbulent flow regime [165]. In this study, they reported that dimpled channel creates smaller pressure drop compared to ribbed channel with similar levels of heat transfer enhancement. Also, Choi et al. reported that dimples on a spherecan cause reduction in the reduce drag force [166]. Dimples locally cause flow separation which initiate the

shear layer instabilityalong the separating shear layer. This results in the increased turbulence and the flow reattaches on the surface with a high momentumenabling the flow to overcome the adverse pressure gradient which is encountered in the rear (wake) of the sphere. As a result, the separation is delayed causing smaller wake and therefore pressure drop is reduced due to the presence of the dimples. Thus, in conventional situations the enhancement of heat transfer is associated with a concomitant increase in pressure drop (and pump power). However, for nanocoatings and nanostructured surfaces the pressure drop characteristics are counter-intuitive and can have opposite trends when the heat transfer is enhanced.

5.2.6. Non-Dimensional Analysis

Non-dimensional analysis for resulting values of Nusselt number was performed based on the raw experimental data. First of all, Nusselt number of DIW flowing in a rectangular microchannel (1 mm in width and 55 µm in height) is correlated to corresponding value of Pèclet number as shown in Figure 5-32. Linear fitting for the experimental results of control experiments using DIW suggested following correlation

$$Nu_0 = 0.0021Pe - 0.0078 \qquad (31)$$
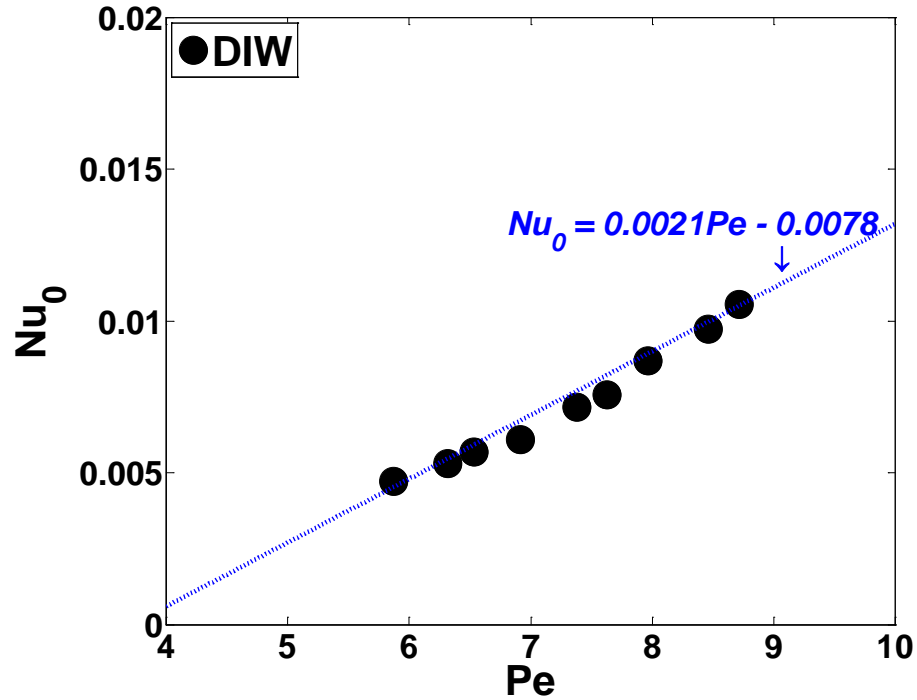
Figure 5-32 Linear fitting correlation for Nusselt number of DIW (control experiment) flowing in a rectangular microchannel (1 mm in width and 55 μm in height)

Values for Nusselt number of nanofluids (either SiO_2 nanofluids or TiO_2 nanofluids) were also correlated and compared to the Nusselt number values for the base fluid. The correlation is described in following equations and the plot is shown in Figure 5-33 and Figure 5-34.

$$Nu_{SiO2} = Nu_0 \left(1 + 0.3188\phi\right) \tag{32}$$

$$Nu_{TiO2} = Nu_0 \left(1 + 75.394\phi\right) \tag{33}$$

In these correlations, ϕ represents the value of mass concentration of nanofluids.
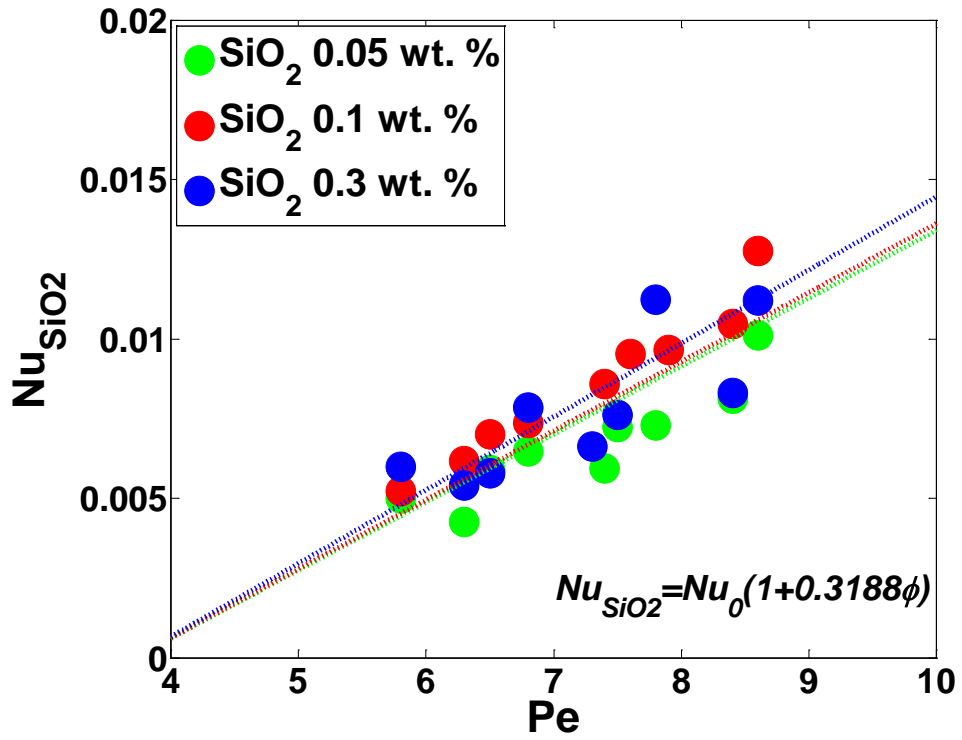
Figure 5-33 Nusselt number correlation for SiO₂ nanofluids under various mass concentrations compared to the values of Nusselt number of control experiment
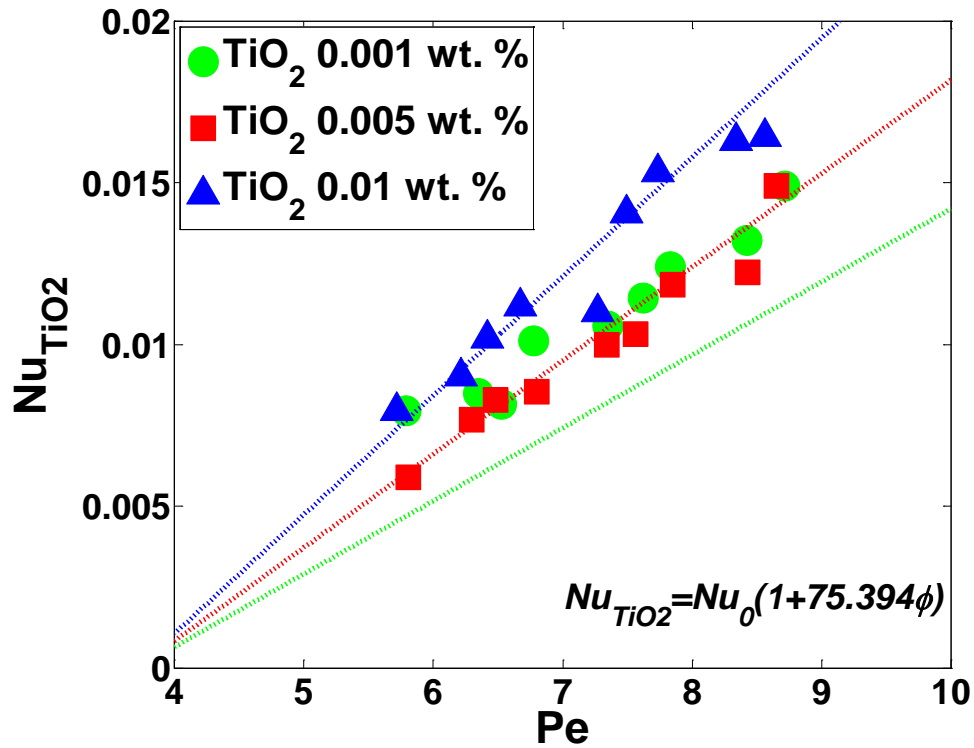
Figure 5-34 Nusselt number correlation for TiO$_2$ nanofluids under various mass concentrations compared to the values of Nusselt number of control experiment

Values for Nusselt number of control experiments which are conducted after nanofluids experiments (either SiO$_2$ nanofluids or TiO$_2$ nanofluids) were also obtained for the correlations. The correlation is described in following equations and the plot is shown in Figure 5-35 and Figure 5-36.

$$Nu_{DIW \ after \ SiO2} = Nu_0 \left(1+1.1808\phi\right) \tag{34}$$

$$Nu_{DIW \ after \ TiO2} = Nu_0 \left(1+60.112\phi\right) \tag{35}$$
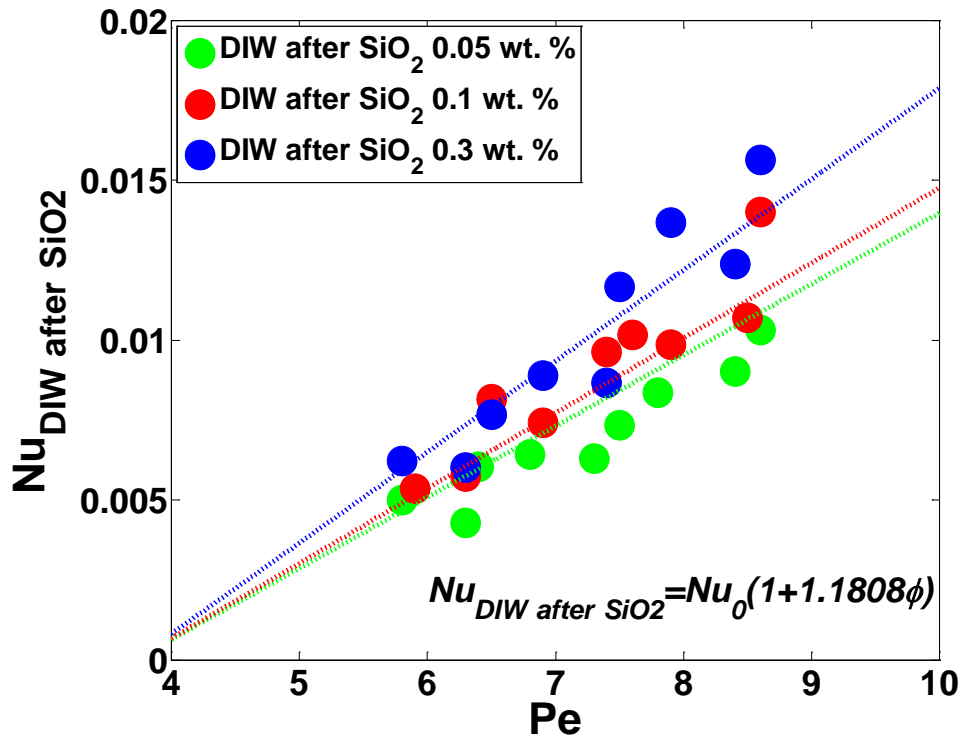
Figure 5-35 Nusselt number correlation for control experiment conducted after flowing SiO₂ nanofluids under various mass concentrations compared to the values of Nusselt number of control experiment
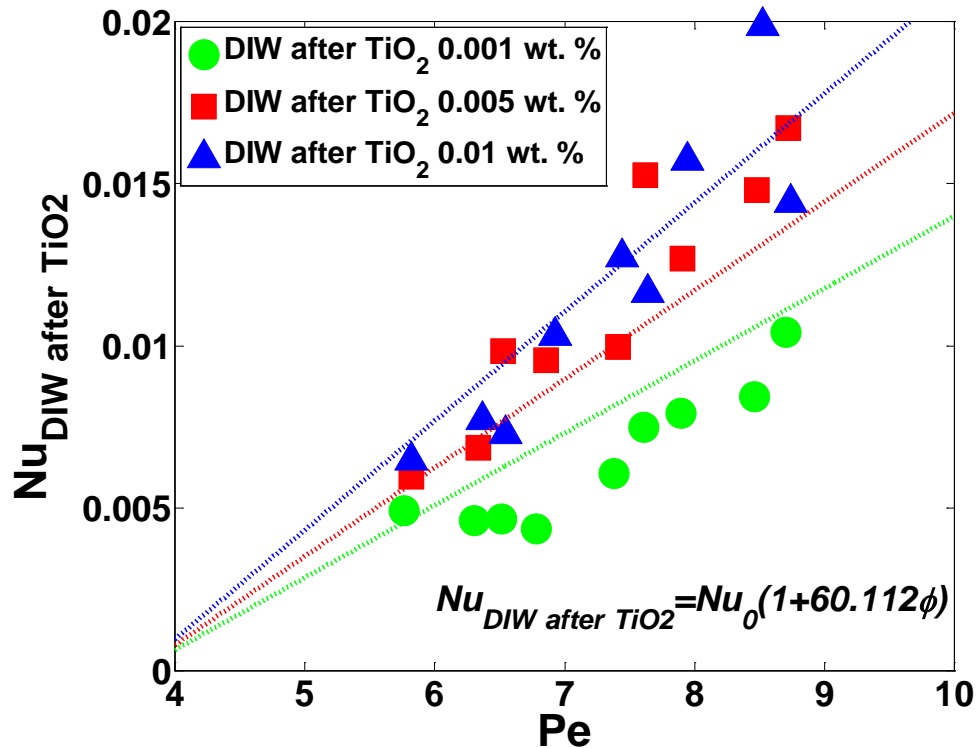
Figure 5-36 Nusselt number correlation for control experiment conducted after flowing TiO₂ nanofluids under various mass concentrations compared to the values of Nusselt number of control experiment

5.3. Experiments Using Confocal Microscopy Setup

5.3.1. Calculation of Heat Flux

Temperature gradient near the heat exchanging surface is measured using laser induced fluorescence (LIF) thermography. As described in the previous section, aqueous fluorecein and quantum dot solutions displayed temperature dependence characteristics where the intensity of the emission decreased with increase in temperature (for the same concentration). In the literature reports this behavior as exploited successfully for

thermography of miniaturized systems (e.g.,biological cells). In this study, this behavior was exploited to determine the temperature profile in the coolant. The results demonstrate that the coolant temperature decreases as the point of measurement shifts from the wall (hot surface) to a location away from the wall. The advantage of this metrology technique is that the wall heat flux values can be directly estimated using Fourier's law of conduction equation, which is expressed as:

$$q'' = -k\frac{\partial T}{\partial y} \tag{36}$$

where, k is thermal conductivity of heat transfer medium (water in the current study). Using the value of thermal conductivity of water, (0.58 W/m·K), heat flux is calculated and summarized in Table 5-11.

Table 5-11 Heat flux (W/cm^2) data obtained from LIF and QD experiments calculated by assuming the value for thermal conductivity is water, ice, or maximum reported value of SiO$_2$ nanofluids (flow rate is 40 µl/min)

	used k value	20 V	30 V	40 V
	k_w	-11.8	18.0	20.9
Fluorecein	k_{ice}	-45.0	69.0	80.0
	k_{SiO2}	-14.1	21.6	25.1
	k_w	46.6	44.8	44.7
Quantum Dot	k_{ice}	178.4	171.5	171.3
	k_{SiO2}	55.9	53.8	53.7

The results show that the magnitude of heat flux in the LIF experiments is lower than that of the QD experiments. In the LIF experiments the dye molecules are estimated

193

to have a Stoke's diameter of 1 nm or less – hence the coolant is expected to have characteristics of the pure solvent. On the other hand, the QD nanoparticles have size ranging from 17 to 29 nm (manufacturer's introduction is from 15 to 20 nm) as can be seen in Figure 5-37. Agglomeration of QD is also found in some regions in Figure 5-37. Therefore the coolant of QD solution is expected to behave like a nanofluid. Hence, the heat transfer in the QD experiments is found to be higher than that of the LIF experiments.
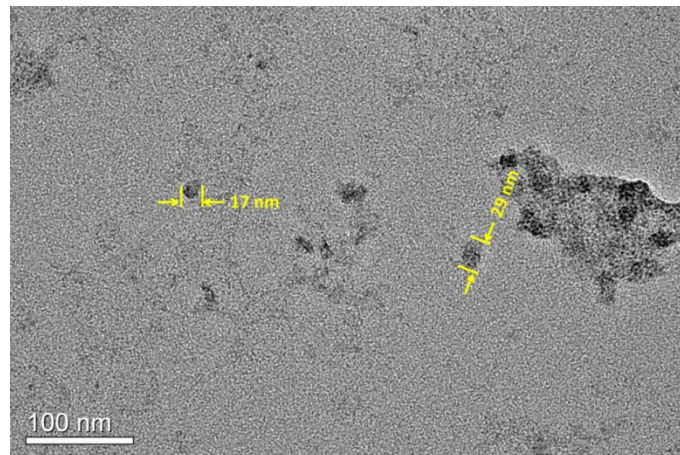
Figure 5-37 TEM image of QD

It should be noted that the measurement uncertainty of the heat flux values in the flow visualization experiments is expected to be high. Hence, it is not surprising that the heat flux values evaluated using the confocal microscopy apparatus (which are illustrated in Table 5-11) disagrees significantly with those calculated using the TFT array (which are shown in Table 4-2). The major reason for the discrepancies can be attributed to the differences in the experimental apparatus and measurement approaches.

In the TFT apparatus the temperature gradient is estimated from temperature drops recorded over length scales that span ~2 mm. On the other hand, heat flux values obtained from the flow visualization apparatus spans a length scale less than 10 microns. Hence, the TFT apparatus provides data based on line measurement while the flow visualization apparatus provides data based on point measurements(area averaged values ascribed to a point). In addition for the TFT experiments – the microchannel is heated from the entire bottom surface of the Pyrex wafer. For the confocal microscopy experiments, only part of the bottom surface (in the vicinity of the flow inlet) is accessible for acquiring experimental data – since the flexible film electrical heater is opaque and interferes with the optical access required for the measurements. Also, laser illumination of the microchannel wall can cause localized heating (as well as volumetric heat generation in the coolant) and nucleation of nanobubbles [142, 167-170] which are below the wavelength of the illumination source leading to high heat flux values. Since the confocal microscopy experiments provide the local values of temperature gradients (i.e., local heat flux values at a particular location on the wall)– it can be expected that these data will be of higher magnitude. In contrast, TFT experiments enable the measurement of global values and are therefore expected to be significantly lower. Localized heat flux values are expected to be higher because particles concentration at the location of measurement could significantly different (higher) than average value. To illustrate this effect, three different thermal conductivity values (water–0.58 W/m·K, ice–2.22 W/m·K, and maximum reported value of SiO_2nanofluilds–0.696 W/m·K [171]) are used for evaluating heat flux values as described Table 5-11.As can be seen in this

table, heat flux values are significantly changes depending on the values of thermal conductivity. Thus, local concentration affects the measurement results and is needed to be significantly considered especially in flow visualization experiments. To summarize, the heat flux values obtained from the TFT experiments (and enthalpy balance approaches)are lower than that of the confocal microscopy experiments, potentially due to the following reasons:

1. Higher experimental uncertainty for flow visualization data.

2. Higher temperature gradients due to non-uniformity of heating in confocal setup (due to laser illumination and asymmetric placement of flexible film heater).

3. Localized heating and phase change (nanobubbles) by laser illumination.

4. Variation of local concentration of solution.

5. Local heat flux values recorded by confocal microscopy (global values by TFT)

It is shown that both fluorecein and QD showed good performance as a temperature sensor. It is generally known that QDs have several superior optical characteristics over organic fluorescence dye, such as fluorecein [84-86]. Whereas organic dyes loss their emission intensity very fast once they are exposed to light("quenching"),QDs have higher photo-stability for extended periodsof time. Also, QDs are capable of wider range of excitation and emission wavelengths than organic dyes. However, the experimental results of the current study show that fluorecein is a better material than QD in the point of view for temperature measurement itself. First of

all, measurement uncertainty for fluorecein (5.2 %) is significantly less than that of QD (17.3 %). In addition, it is revealed that QD solution behaves as nanofluids, which may influence the heat transfer characteristics of target system and possibly distort the accuracy of the measurement.

5.3.2. QD Solution as a Nanofluid

The results obtained from flow visualization experiments using confocal microscope suggest that the QD solution effectively behaves as a nanofluids. SEM images were obtained after performing the flow visualization experiments and are shown inFigure 5-38.The figure validates the premise that the QD solution behaves similar to a nanofluid whereas the fluorecein solution does not. As can be seen in this figure, although precipitation has been observed (either near TFT or away from TFT) on the wafer after QD experiment, no precipitation has been found for the samples performed with organic dye, fluorecein. These results are as expectedbecause the size of QD and organic dye is 17 ~ 29 nm and under 1 nm, respectively.
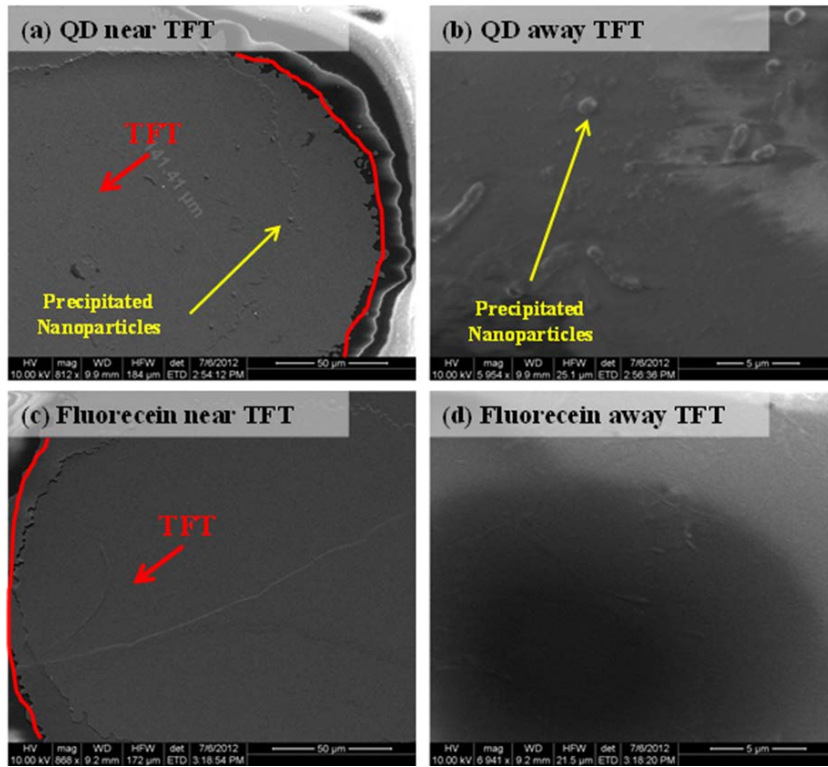
Figure 5-38 SEM images after flow visualization experiment for (a), (b) QD and (c), (d) fluorecein

Further investigations were performed to verify if QD solution behaves likea nanofluid. Thermal response of QD solution at 0.08 µM molar concentration was measured using TFT integrated microchannel experiment setup. The results are shown in Figure 5-39, Table 5-12, Table 5-13, and Table 5-14.The measured values of the heat removal rate, the heat transfer coefficient, and the Nusselt number, thermophysical properties of QD solution are approximated to those of DIW, since these values are not available un the literature.Such an approach could provide a glimpse into the behavior of QD solution. As can be seen in these figure and tables, significantly higher levels of enhancement in heat transfer is observed for QD solution compared to pure solvent

(DIW). Also, control experiment using DIW conducted right after the experiment using QD solution shows similar heat transfer characteristics closer to that QD solution than that of control experiment using DIW before the experiment of QD solution. These results demonstrate that the QD solution behaves as a nanofluid.
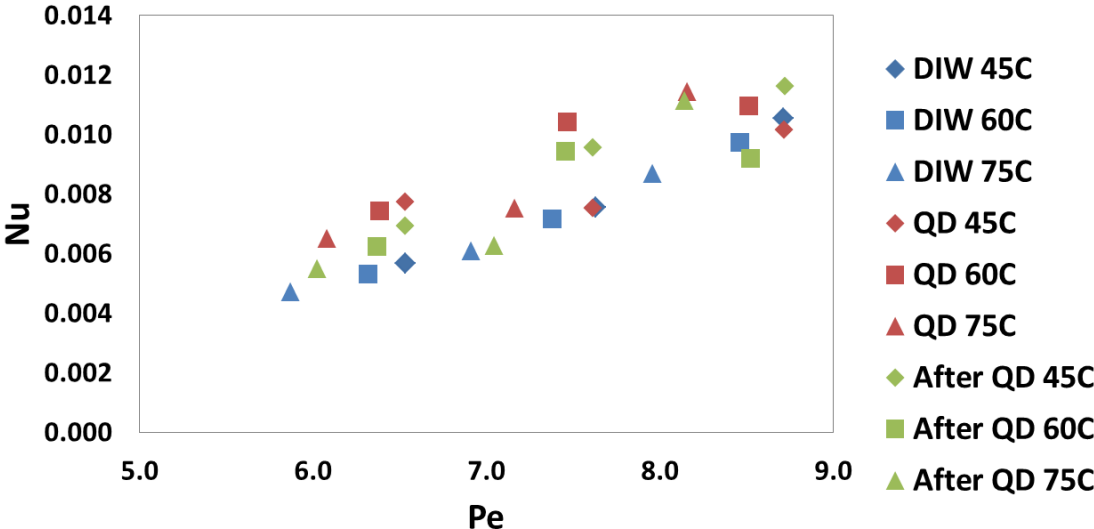
Figure 5-39 Nusselt number calculated using equation (11) versus Pèclet number for QD solution and DIW before and after the experiment using QD solution

Table 5-12 Heat removal rate calculated using equation (8) for various conditions including wall temperature and flow rate using QD solutions at molar concentration of 0.08 μM (enhancement levels in braces)

T_w [°C]	Flow Rate [μl/min]	Heat Flux [W/m^2]		
		DIW	QD	after QD
45	30	599	685 (14.4 %)	627 (4.6 %)
	35	734	707 (-3.7%)	859 (17.0 %)
	40	1012	905 (-10.6%)	969 (-4.3%)
60	30	828	951 (14.8 %)	855 (3.2 %)
	35	1085	1277 (17.8 %)	1197 (10.3 %)
	40	1452	1413 (-2.7%)	1221 (-15.9%)
75	30	986	1177 (19.4 %)	1029 (4.5 %)
	35	1212	1351 (11.4 %)	1185 (-2.3%)
	40	1697	1952 (15.0 %)	1891 (11.4 %)

Table 5-13 Convective heat transfer coefficient calculated using equation (9) for various conditions including wall temperature and flow rate using QD solutions at molar concentration of 0.08 μM (enhancement levels in braces)

T_w [°C]	Flow Rate [μl/min]	h [W/m^{2}K]		
		DIW	QD	after QD
45	30	31	42 (35.9 %)	38 (21.9 %)
	35	41	41 (-0.4%)	52 (26.5 %)
	40	58	56 (-3.5%)	63 (10.1 %)
60	30	29	41 (40.1 %)	34 (17.5 %)
	35	39	57 (45.3 %)	52 (31.7 %)
	40	53	60 (12.6 %)	50 (-5.4%)
75	30	26	36 (37.4 %)	30 (16.2 %)
	35	33	41 (23.3 %)	34 (3.1 %)
	40	47	63 (31.7 %)	61 (28.2 %)

Table 5-14 Nusselt number calculated using equation (11) for various conditions including wall temperature and flow rate using QD solutions at molar concentration of 0.08 μM (enhancement levels in braces)

T_w [°C]	Flow Rate [μl/min]	Nu		
		DIW	QD	after QD
	30	0.006	0.008 (35.9 %)	0.007 (21.9 %)
45	35	0.008	0.008 (-0.4%)	0.010 (26.5 %)
	40	0.011	0.010 (-3.5%)	0.012 (10.1 %)
	30	0.005	0.007 (40.1 %)	0.006 (17.5 %)
60	35	0.007	0.010 (45.3 %)	0.009 (31.7 %)
	40	0.010	0.011 (12.6 %)	0.009 (-5.4%)
	30	0.005	0.006 (37.4 %)	0.005 (16.2 %)
75	35	0.006	0.008 (23.3 %)	0.006 (3.1 %)
	40	0.009	0.011 (31.7 %)	0.011 (28.2 %)

6. CONCLUSION (FUTURE DIRECTION)

6.1. Summary and Conclusions

In this study, the forced convective heat transfer performance of different coolants during flow in a microchannel was measured. The coolants used in this study are: de-ionized water (DIW) and aqueous nanofluids. The aqueous nanofluids consisted of: SiO_2 nanofluids (at mass concentration of 0.05%, 0.1% and 0.3%; and nanoparticle diameter of 10~100 nm), TiO_2 nanofluids (at mass concentration of 0.001%, 0.005% and 0.01%; and nanoparticle diameter of 10~50 nm) and Quntum Dot (QD) suspensions (which can be effectively considered to be a nanofluid: since the QDs are nanoparticles with a nominal diameters of ~ 29 nm.

Different configurations of the experimental apparatus were utilized in this study. Initial experiments were performed using a microchannel apparatus integrated with TFT array that were fabricated in-situ. This experimental apparatus was then mounted on the stage of a confocal microscope for performing flow visualization experiments. The flow visualization experiments were performed using: (1) Laser Induced Fluorescence (LIF) techniques using organic dye, fluorecein; and (2) Quantum Dots (QDs). In addition, the level of precipitation of the nanoparticles was monitored after each experiment using materials characterization techniques such as SEM and EDX.

Furthermore, different strategies were implemented in the experimental procedure. The order of performance of the experiments was found to affect the heat flux values. For example, a control experiment is performed by flowing DIW in the heated

microchannel. This was followed by experiments performed using nanofluid coolants (SiO_2 nanofluids or TiO_2 nanofluids). Subsequently, the control experiment is repeated by flowing DIW in the same heated microchannel. It was observed that repeating the control experiment after the nanofluid experiments, consistently yielded heat flux values that matched (or in certain cases exceeded) that of the nanofluids experiments and almost always exceeded the heated flux values obtained from the initial control experiments.

Also, artificial nanofins are fabricated using SFIL technique. The height of nanofins can be easily controlled by varying DRIE cycles during the fabrication processes. TFT arrays are fabricated on nanofin surface and the experiments were performed using DIW as a test fluid. These experiments showed that the heat transfer coefficient of DIW on nanofin-surface is higher than that of DIW on plain surface, which supports the hypothesis of the current study.

6.1.1. The Nanofin Hypothesis

Hence, these experiments were used to prove the hypothesis central to this study: that the isolated precipitation of the nanoparticles leads to formation of nanofins on the heated surface that enhances the effective surface area for forced convective heat transfer in microchannels and this is the most dominant transport mechanism of nanofluids flowing in the microchannel. That is, thermo-physical properties of the nanofluids coolant plays minor role in transport mechanism compared to the surface modification. In addition, the implication of this hypothesis was also proven that

excessive agglomeration and precipitation of nanoparticles lead to the formation of a fouling film that acts as an additional thermal barrier/ resistance to heat transfer due to scaling – thus causing degradation of the forced convective heat transfer (compared to that of the control experiments performed using DIW coolant).

6.1.2. Anomalous Results

Several anomalous (or counter-intuitive) behavior of the nanofluid coolants were also observed in these experiments. These are summarized as follows:

1. SiO_2 nanofluids were observed to cause either enhancement or degradation of the heat flux values, depending on the level of precipitation (and surface fouling). In contrast, TiO_2 nanofluids were consistently observed to cause enhancement in heat flux (compared to the control experiments performed using DIW).

2. The level of precipitation for TiO_2 nanofluids was observed to be much less compared to that of the SiO_2 nanofluids in the SEM images (possibly due to better stability of the nanofluids and lower affinity of the nanoparticles for the Pyrex wafer substrate).

3. TFT experiments were observed to yield lower values of heat flux than that of the flow visualization experiments (possibly due to non-uniform heat flux distribution, localized heating leading potentially to phase change/ formation

of nano-bubbles due to laser illumination, higher local values of heat flux obtained by point-measurements rather than the lower values of global heat flux measured due to line-average measurements, etc.).

4. The nanofluids experiments seem to render "system memory" to the experimental apparatus – due to formation of nanoparticle precipitates. Thus when the control experiment is repeated before and after the nanofluids experiments – consistently higher values of heat flux are obtained that usually matches (or exceeds) the heat flux values obtained from the nanofluids experiments. This proves the hypothesis central to this study (i.e., nanofin effect dominates over the thermo-physical property effects and is the primary driver in the heat flux enhancements that are observed in nanofluids experiments).

5. Artificial nanofins are successfully fabricated using SFIL process. TFT is integrated with these nanofins and convective heat transfer experiments were performed on this apparatus using DIW as a testing fluid. The results showed higher heat flux values compared to those on the plain surface using the same fluid. The level of enhancement is quite similar to that of using nanofluids. These results add credence to the nanofin hypothesis that has been proposed and validated in this study.

6.2. Conclusion

Forced convection heat transfer using nanofluids in a microchannel is evaluated in this study. It is revealed that the precipitation of nanoparticles is the most dominant heat transfer mechanism of nanofluids. Isolated precipitation of nanoparticles behaves as nanofins, which results in significant enhancement of heat transfer coefficient. However, excessive precipitation forms fouling film and cause the degradation of heat transfer. Artificial nanofins are fabricated using SFIL process to evaluate the significance of precipitation effect. When these nanofins are tested in the experiment, similar level of enhancement in forced convection heat transfer coefficient has been observed compared to those of nanofluids. This result demonstrates and validates nanofin hypothesis that the precipitation of nanoparticles is predominant mechanism of heat transfer enhancement using nanofluids.

Considering the experimental results of the current study, there are several benefits to utilize nanofins and microchannel with respect to the effective method for the enhancement of heat transfer. First of all, a microchannel has an advantage over a macrochannel in that a former provides much larger surface area with the same volume. Therefore, the level of enhancement of heat transfer in microchannel by introducing either nanofins or isolated precipitation of nanoparticles would be greater than that of in macrochannel. Using nanofins are much reliable than using nanofluids if the technique is adopted in the applications because repeated use of nanofluids possibly leads excessive precipitation of nanoparticles and degradation of heat transfer. In addition, nanofluids cause increase of pumping cost since the viscosity of nanofluids is higher than pure

solvent, which does not have to be worried about when nanofins are used. However, fabrication of nanofins is expensive compared to just using nanofluids. Thus, in practical point of view, it is suggested to flow nanofluids for a short period time to let nanoparticles precipitate in isolation and then use pure solvent (i.e. water).

6.3. Future Directions

Monitoring change of nanoparticle concentration at the exit of the microchannel is another good approach to evaluate precipitation of nanoparticles. By comparing the value of mass concentration between inlet and outlet of the microchannel, it is possible to estimate total amount of precipitated nanoparticles within the microchannel. However, measuring the concentration of nanofluids at the exit of the flow is very difficult. It is proposed that use of filters to capture nanoparticles at the outlet is one of the effective ways to indirectly measure the concentration at the exit in future studies.

An alternative strategy could be the selective and partial removal ofthe precipitates when excessive precipitation has caused fouling (and therefore degradation in heat transfer). As discussedearlier, it is difficult to remove nanoparticles once they have precipitated on the surface (due to the energy barrier caused by the van der Waal's interaction and ionic interactions). The existence of fouling layer due to excessive precipitation of the nanoparticles mayalso be undesirable in various semiconductor applications. Moreover, it would be very useful if it is possible to reliably execute selective and partial removalof precipitated nanoparticles on the surface because this technique will make it possible to control formation of the fouling film due to excessive

precipitation of nanoparticles and obviate the heat transfer degradation issues (as well as reliability issues) encountered with nanofluid coolants. Prior studies allude to potential techniques that can be leveraged for partial and selective removal of the fouling layer formed by the nanoparticle precipitates. For example, it is reported that formation of nanobubbles effectively removes nanoparticles on the surface of a substrate [136, 172]. Considering erosion of precipitated nanoparticles and long term stability of the precipitated system, it is important to develop effective technology to remove precipitates. In this sense, further study on cleaning precipitated nanoparticles may enable the development of new and more reliable techniques to control enhancement of heat transfer using nanofluids.

In addition, the current study can be extended to the study of hybrid system to utilize nanofluids on engineered nanofin surface. The physics of this hybrid system will become much more complex and could be more nuanced. Nevertheless, it is suggested that studying heat transfer characteristics on hybrid system will open new research interests.

In this study for each experiment it was not possible to quantitatively evaluate whether the precipitation wasoptimum (isolated) or excessive (fouling) due to the limitation of image processing techniques in this study. However, monitoring this parameter is suggested as a topic of future study.

The implications of this study are envisioned in: (1) computer chip cooling applications; (2) oil and gas exploration (e.g., use of nanofluids as nanotracers, for prevention or remediation of breakthrough in oil and gas reservoirs by utilizing

nanoparticle precipitation from drilling muds containing nanofluid/ surfactant formulations, fracking fluids containing nanofluid formulations, etc.); (3) solar thermal power generation (e.g., in concentrated solar power/ CSP –nanofluids can be used as thermal energy storage/ TES materials, heat transfer fluid/ HTF materials, working fluid in dish-Sterling engines or other thermodynamic cycles); (4) solar photo-voltaic/ PV power generation (e.g., nanofluid coolants for CSP-PV arrays); (5) geothermal energy harvesting (e.g., nanofluids as working fluids in enhancing heat exchanger performance and for exploitation in thermodynamic cycles); (6) Nuclear power applications (e.g., using nanofluids for enhancing the thermodynamic performance, cooling of fuel rod bundles and nuclear safety applications for prevention of "loss of coolant accidents"/ LOCA).

In addition, although the current study is limited to low temperature ranges (i.e., below the saturation temperature of the solvent), the study can be extended to multi-phase flows. An experimental strategy similar to the current study can be adopted for flow boiling experiments in a microchannel using nanofluids. Preliminary experiments for flow boiling of microchannels were performed to demonstrate the feasibility. These experiment exhibited similar behavior that of the single phase convective heat transfer, i.e., the control experiments repeated after the nanofluids experiments were found to replicate the heat flux values for the nanofluids experiments (barring a few cases). Also the level of flow boiling heat flux values were ~ 104 times higher than that for the flows without phase change, for the same inlet (liquid only) flow rate. Also, the flow boiling

heat flux values for the nanofluids were enhanced by 50-80% compared to that of the pure solvent (DIW).

The results obtained from this study have made contributions) to the fundamental understanding of the thermal-fluid sciences and nanotechnology (nanofabrication) in the following ways:

- Developed nano-scale temperature metrology platform for monitoring convective heat transfer phenomena of simple (Newtonian) fluids and complex fluids (nanofluids).

- Designed and fabricated high quality and stable thin film nano-sensors which can be utilized to measure temperature of coolants in microchannel, while minimizing the perturbation of the transport mechanisms under investigation.

- Utilized nano-fabrication techniques using Step and Flash Imprinting Lithography (SFIL) for obtaining surface nanostructures (nanofins) with the aim of enhancing surface area for augmenting convective heat transfer.

- Evaluated the contribution of various parameters such as nanoparticle concentration, wall temperature, and flow velocity on the forced convective heat transfer characteristics of nanofluid coolants during flow in a microchannel.

- Addressed the effect of surface nano-structures ("nanofins") on heat transfer and correlate the behavior with the thermal efficacy of nanofluids flowing in a microchannel (i.e., prove that nanoparticle precipitates from nanofluids can act as "nanofins"). Hence, this can help prove that the surface interactions are more dominant in determining the thermal efficacy of nanofluids than their bulk property values.

- Demonstrated the feasibility of non-contact temperature metrology techniques for experimental flow visualization and heat transfer measurements (especially in the near wall region) using quantum dots (QDs) and laser-induced-fluorescence (LIF) techniques.

- Demonstrated the feasibility of flow boiling experiments in microchannels using temperature nano-sensor array for both pure solvent (DIW) and aqueous nanofluids.

- Demonstrated high levels of enhancement for flow boiling experiments in microchannels (compared to the cases without phase change).

- Demonstrated significant enhancement of flow boiling heat transfer for nanofluids compared to that of the pure solvent.

- It is observed that even for flow boiling experiments, repeating the control experiments (flow of pure solvent) after the nanofluids experiments, results in identical levels of heat transfer to that of the nanofluid (barring a few experiments that were exceptions to this trend). This alludes to the possibility that even for flow boiling in microchannels the nanofin effect could be the dominant mechanism for heat transfer enhancement and the properties of the coolant is probably of secondary importance.

REFERENCES

[1] Wyss, H. M., Blair, D. L., Morris, J. F., 2006, "Mechanism for Clogging of Microchannels," Physical Review E - Statistical, Nonlinear, and Soft Matter Physics, **74**(6) .

[2] Dai, J., and Grace, J. R., 2010, "Blockage of Constrictions by Particles in Fluid-Solid Transport," International Journal of Multiphase Flow, **36**(1) pp. 78-87.

[3] Eastman, J. A., Choi, U. S., Li, S., 1997, "Enhanced thermal conductivity through the development of nanofluids," Proceedings of the 1996 MRS Fall Symposium, December 2, 1996 - December 5, Materials Research Society, Boston, MA, USA, **457,** pp. 3-11.

[4] Eastman, J. A., Choi, S. U. S., Li, S., 2001, "Anomalously Increased Effective Thermal Conductivities of Ethylene Glycol-Based Nanofluids Containing Copper Nanoparticles," Applied Physics Letters, **78**(6) pp. 718-720.

[5] Hong, T., Yang, H., and Choi, C. J., 2005, "Study of the Enhanced Thermal Conductivity of Fe Nanofluids," Journal of Applied Physics, **97**(6) .

[6] Patel, H. E., Das, S. K., Sundararajan, T., 2003, "Thermal Conductivities of Naked and Monolayer Protected Metal Nanoparticle Based Nanofluids: Manifestation of Anomalous Enhancement and Chemical Effects," Applied Physics Letters, **83**(14) pp. 2931-2933.

[7] Shalkevich, N., Escher, W., Burgi, T., 2010, "On the Thermal Conductivity of Gold Nanoparticle Colloids," Langmuir, **26**(2) pp. 663-670.

[8] Das, S. K., Putra, N., Thiesen, P., 2003, "Temperature Dependence of Thermal Conductivity Enhancement for Nanofluids," Journal of Heat Transfer, **125**(4) pp. 567-574.

[9] Li, C. H., and Peterson, G. P., 2006, "Experimental Investigation of Temperature and Volume Fraction Variations on the Effective Thermal Conductivity of Nanoparticle Suspensions (Nanofluids)," Journal of Applied Physics, **99**(8) .

[10] Wang, X., Xu, X., and Choi, S. U. S., 1999, "Thermal Conductivity of Nanoparticle-Fluid Mixture," Journal of Thermophysics and Heat Transfer, **13**(4) pp. 474-480.

[11] Lee, S., Choi, S. U. -., Li, S., 1999, "Measuring Thermal Conductivity of Fluids Containing Oxide Nanoparticles," Journal of Heat Transfer, **121**(2) pp. 280-289.

[12] Murshed, S. M. S., Leong, K. C., and Yang, C., 2005, "Enhanced Thermal Conductivity of TiO2 - Water Based Nanofluids," International Journal of Thermal Sciences, **44**(4) pp. 367-373.

[13] Sinnott, S. B., and Andrews, R., 2001, "Carbon Nanotubes: Synthesis, Properties, and Applications," Critical Reviews in Solid State and Materials Sciences, **26**(3) .

[14] Assael, M. J., Chen, C. -., Metaxa, I., 2004, "Thermal Conductivity of Suspensions of Carbon Nanotubes in Water," International Journal of Thermophysics, **25**(4) pp. 971-985.

[15] Wen, D., and Ding, Y., 2004, "Effective Thermal Conductivity of Aqueous Suspensions of Carbon Nanotubes (Carbon Nanotube Nanofluids)," Journal of Thermophysics and Heat Transfer, **18**(4) pp. 481-485.

[16] Xie, H., Lee, H., Youn, W., 2003, "Nanofluids Containing Multiwalled Carbon Nanotubes and their Enhanced Thermal Conductivities," Journal of Applied Physics, **94**(8) pp. 4967-4971.

[17] Choi, E. S., Brooks, J. S., Eaton, D. L., 2003, "Enhancement of Thermal and Electrical Properties of Carbon Nanotube Polymer Composites by Magnetic Field Processing," Journal of Applied Physics, **94**(9) pp. 6034-6039.

[18] Nelson, I. C., Banerjee, D., and Ponnappan, R., 2009, "Flow Loop Experiments using Polyalphaolefin Nanofluids," Journal of Thermophysics and Heat Transfer, **23**(4) pp. 752-761.

[19] Wang, L., and Wei, X., 2009, "Nanofluids: Synthesis, Heat Conduction, and Extension," Journal of Heat Transfer, **131**(3) pp. 1-7.

[20] Wei, X., Zhu, H., Kong, T., 2009, "Synthesis and Thermal Conductivity of Cu2O Nanofluids," International Journal of Heat and Mass Transfer, **52**(19-20) pp. 4371-4374.

[21] Wei, X., Kong, T., Zhu, H., 2010, "CuS/Cu2S Nanofluids: Synthesis and Thermal Conductivity," International Journal of Heat and Mass Transfer, **53**(9-10) pp. 1841-1843.

[22] Buongiorno, J., Venerus, D. C., Prabhat, N., 2009, "A Benchmark Study on the Thermal Conductivity of Nanofluids," Journal of Applied Physics, **106**(9) .

[23] Pak, B. C., and Cho, Y. I., 1998, "Hydrodynamic and Heat Transfer Study of Dispersed Fluids with Submicron Metallic Oxide Particles," Experimental Heat Transfer, **11**(2) pp. 151-170.

214

[24] Xuan, Y., and Li, Q., 2003, "Investigation on Convective Heat Transfer and Flow Features of Nanofluids," Journal of Heat Transfer, **125**(1) pp. 151-155.

[25] Wen, D., and Ding, Y., 2004, "Experimental Investigation into Convective Heat Transfer of Nanofluids at the Entrance Region Under Laminar Flow Conditions," International Journal of Heat and Mass Transfer, **47**(24) pp. 5181-5188.

[26] Kulkarni, D. P., Namburu, P. K., Ed Bargar, H., 2008, "Convective Heat Transfer and Fluid Dynamic Characteristics of SiO 2 - Ethylene glycol/water Nanofluid," Heat Transfer Engineering, **29**(12) pp. 1027-1035.

[27] Hwang, K. S., Jang, S. P., and Choi, S. U. S., 2009, "Flow and Convective Heat Transfer Characteristics of Water-Based Al2O3 Nanofluids in Fully Developed Laminar Flow Regime," International Journal of Heat and Mass Transfer, **52**(1-2) pp. 193-199.

[28] Nassan, T. H., Heris, S. Z., and Noie, S. H., 2010, "A Comparison of Experimental Heat Transfer Characteristics for Al2O3/water and CuO/water Nanofluids in Square Cross-Section Duct," International Communications in Heat and Mass Transfer, **37**(7) pp. 924-928.

[29] Ding, Y., Alias, H., Wen, D., 2006, "Heat Transfer of Aqueous Suspensions of Carbon Nanotubes (CNT Nanofluids)," International Journal of Heat and Mass Transfer, **49**(1-2) pp. 240-250.

[30] Amrollahi, A., Rashidi, A. M., Lotfi, R., 2010, "Convection Heat Transfer of Functionalized MWNT in Aqueous Fluids in Laminar and Turbulent Flow at the Entrance Region," International Communications in Heat and Mass Transfer, **37**(6) pp. 717-723.

[31] Terekhov, V. I., Kalinina, S. V., and Lemanov, V. V., 2010, "The Mechanism of Heat Transfer in Nanofluids: State of the Art (Review). Part 2. Convective Heat Transfer," Thermophysics and Aeromechanics, **17**(2) pp. 157-171.

[32] Buongiorno, J., 2006, "Convective Transport in Nanofluids," Journal of Heat Transfer, **128**(3) pp. 240-250.

[33] Heyhat, M. M., and Kowsary, F., 2010, "Effect of Particle Migration on Flow and Convective Heat Transfer of Nanofluids Flowing through a Circular Pipe," Journal of Heat Transfer, **132**(6) pp. 1-9.

[34] Tuckerman, D. B., and Pease, R. F. W., 1981, "High-Performance Heat Sinking for VLSI," Electron Device Letters, **EDL-2**(5) pp. 126-129.

[35] Jiang, P., Fan, M., Si, G., 2001, "Thermal-Hydraulic Performance of Small Scale Micro-Channel and Porous-Media Heat-Exchangers," International Journal of Heat and Mass Transfer, **44**(5) pp. 1039-1051.

[36] Nguyen, N. T., Bochnia, D., Kiehnscherf, R., 1996, "Investigation of Forced Convection in Microfluid Systems," Sensors and Actuators, A: Physical, **55**(1) pp. 49-55.

[37] Wu, H. Y., and Cheng, P., 2003, "An Experimental Study of Convective Heat Transfer in Silicon Microchannels with Different Surface Conditions," International Journal of Heat and Mass Transfer, **46**(14) pp. 2547-2556.

[38] Qu, W., Mala, G. M., and Li, D., 2000, "Heat Transfer for Water Flow in Trapezoidal Silicon Microchannels," International Journal of Heat and Mass Transfer, **43**(21) pp. 3925-3936.

[39] Peng, X. F., and Wang, B. -., 1993, "Forced Convection and Flow Boiling Heat Transfer for Liquid Flowing through Microchannels," International Journal of Heat and Mass Transfer, **36**(14) pp. 3421-3427.

[40] Peng, X. F., Wang, B. X., Peterson, G. P., 1995, "Experimental Investigation of Heat Transfer in Flat Plates with Rectangular Microchannels," International Journal of Heat and Mass Transfer, **38**(1) pp. 127-137.

[41] Tso, C. P., and Mahulikar, S. P., 2000, "Experimental Verification of the Role of Brinkman Number in Microchannels using Local Parameters," International Journal of Heat and Mass Transfer, **43**(10) pp. 1837-1849.

[42] Peng, X. F., Peterson, G. P., and Wang, B. X., 1994, "Frictional Flow Characteristics of Water Flowing through Rectangular Microchannels," Experimental Heat Transfer, **7**(4) pp. 249-264.

[43] Peng, X. F., and Peterson, G. P., 1996, "Convective Heat Transfer and Flow Friction for Water Flow in Microchannel Structures," International Journal of Heat and Mass Transfer, **39**(12) pp. 2599-2608.

[44] Kandlikar, S. G., Joshi, S., and Tian, S., 2003, "Effect of Surface Roughness on Heat Transfer and Fluid Flow Characteristics at Low Reynolds Numbers in Small Diameter Tubes," Heat Transfer Engineering, **24**(3) pp. 4-16.

[45] Liu, Y., Cui, J., Li, W., 2011, "Effect of Surface Microstructure on Microchannel Heat Transfer Performance," Journal of Heat Transfer, **133**(12) pp. 124501 (6 pp.).

[46] Jang, S. P., and Choi, S. U. S., 2006, "Cooling Performance of a Microchannel Heat Sink with Nanofluids," Applied Thermal Engineering, **26**(17-18) pp. 2457-2463.

[47] Valencia, G. E., Ramos, M. A., and Bula, A. J., 2008, "Experimental evaluation of the convective heat transfer coefficients in a nanofluid-cooled milli channels heat sink," ASME International Mechanical Engineering Congress and Exposition, IMECE 2007, November 11, 2007 - November 15, American Society of Mechanical Engineers, Seattle, WA, United States, **6,** pp. 31-37.

[48] Vaziee, P., and Abouali, O., 2008, "Numerical Study of Forced Convection of Nanofluids in a Microchannel Heat Sink," ASME International Conference on Nanochannels, Microchannels, and Minichannels, ICNMM 2008, June 23, 2008 - June 25, American Society of Mechanical Engineers, New York, NY, United States, pp. 1083.

[49] Lee, J., and Mudawar, I., 2007, "Assessment of the Effectiveness of Nanofluids for Single-Phase and Two-Phase Heat Transfer in Micro-Channels," International Journal of Heat and Mass Transfer, **50**(3-4) pp. 452-463.

[50] Jung, J., Oh, H., and Kwak, H., 2009, "Forced Convective Heat Transfer of Nanofluids in Microchannels," International Journal of Heat and Mass Transfer, **52**(1-2) pp. 466-472.

[51] Singh, P. K., Harikrishna, P. V., Sundararajan, T., 2011, "Experimental and Numerical Investigation into the Heat Transfer Study of Nanofluids in Microchannel," Journal of Heat Transfer, **133**(12) .

[52] Wen, D., and Ding, Y., 2005, "Effect of Particle Migration on Heat Transfer in Suspensions of Nanoparticles Flowing through Minichannels," Microfluidics and Nanofluidics, **1**(2) pp. 183-189.

[53] Glaninger, A., Jachimowicz, A., Kohl, F., 2000, "Wide Range Semiconductor Flow Sensors," Sensors and Actuators, A: Physical, **85**(1) pp. 139-146.

[54] Wu, S., Lin, Q., Yuen, Y., 2001, "MEMS Flow Sensors for Nano-Fluidic Applications," Sensors and Actuators, A: Physical, **89**(1-2) pp. 152-158.

[55] Ernst, H., Jachimowicz, A., and Urban, G. A., 2002, "High Resolution Flow Characterization in Bio-MEMS," Sensors and Actuators, A: Physical, **100**(1) pp. 54-62.

[56] [56] Marshall, R., Atlas, L., and Putner, T., 1966, "The Preparation and Performance of Thin Film Thermocouples," Journal of Scientific Instruments, **43**(3) pp. 144-149.

[57] Nguyen, N. T., and Kiehnscherf, R., 1995, "Low-Cost Silicon Sensors for Mass Flow Measurement of Liquids and Gases," Sensors and Actuators, A: Physical, **49**(1-2) pp. 17-20.

[58] Martin, L. C., Wrbanek, J. D., and Fralick, G. C., 2001, "Thin film sensors for surface measurements," 19th International Congress on Instrumentation in Aerospace Simulation Facilities (ICIASF 2001), August 27, 2001 - August 30, Institute of Electrical and Electronics Engineers Inc, Cleveland, OH, United states, pp. 196-203.

[59] Golan, G., Axelevitch, A., Sigalov, B., 2003, "Integrated thin film heater-thermocouple systems," Elsevier Ltd, **43,** pp. 509-512.

[60] Heichal, Y., Chandra, S., and Bordatchev, E., 2005, "A Fast-Response Thin Film Thermocouple to Measure Rapid Surface Temperature Changes," Experimental Thermal and Fluid Science, **30**(2) pp. 153-159.

[61] Kim, T. H., and Kim, S. J., 2006, "Development of a Micro-Thermal Flow Sensor with Thin-Film Thermocouples," Journal of Micromechanics and Microengineering, **16**(11) pp. 2502-2508.

[62] Fujiki, H., 2007, "New Thin-Film Multijunction Thermal Converter Design for Improved High-Frequency Performance," IEEE Sensors Journal, **7**(9) pp. 1243-1247.

[63] Kumar, S. R. S., and Kasiviswanathan, S., 2009, "Transparent ITO-Mn:ITO Thin-Film Thermocouples," IEEE Sensors Journal, **9**(7) pp. 809-13.

[64] Sunder, M., and Banerjee, D., 2009, "Experimental Investigation of Micro-Scale Temperature Transients in Sub-Cooled Flow Boiling on a Horizontal Heater," International Journal of Heat and Fluid Flow, **30**(1) pp. 140-149.

[65] Van, D. W., Linder, C., de Rooij, N. F., 1993, "Liquid Velocity Sensor Based on the Hot-Wire Principle," Sensors and Actuators, A: Physical, **37-38**(2) pp. 693-697.

[66] Kersjes, R., Eichholz, J., Langerbein, A., 1993, "Integrated Sensor for Invasive Blood-Velocity Measurement," Sensors and Actuators, A: Physical, **37-38**(2) pp. 674-678.

[67] Jeon, S., 2011, "Development of micro/nano-Scale Sensors for Investigation of Heat Transfer in Multi-Phase Flows," Ph.D Dissertation, Texas A&M University, College Station.

[68] Hansen, S., 2012, "Experimental Study of Droplet Impingement using Photo-Activated Nano-Coatings and Temperature Nano-Sensors Integrated with High-Speed Visualization," MS. Thesis, Texas A&M University, College Station.

[69] Baughn, J. W., 1995, "Liquid Crystal Methods for Studying Turbulent Heat Transfer," International Journal of Heat and Fluid Flow, **16**(5) pp. 365-375.

[70] Jeschke, P., Biertumpfel, R., and Beer, H., 2000, "Liquid-Crystal Thermography for Heat-Transfer Measurements in the Presence of Longitudinal Vortices in a Natural Convection Flow," Measurement Science and Technology, **11**(5) pp. 447-453.

[71] Richards, C. D., and Richards, R. F., 1998, "Transient Temperature Measurements in a Convectively Cooled Droplet," Experiments in Fluids, **25**(5) pp. 392-400.

[72] Stasiek, J. A., and Kowalewski, T. A., 2002, "The use of thermochromic liquid crystals in heat transfer research," XIV Conference on Liquid Crystals: Chemistry, Physics, and Applications, September 3, 2001 - September 7, SPIE, Zakopane, Poland, **4759,** pp. 374-383.

[73] Saunders, P. M., 1967, "Aerial Measurement of Sea Surface Temperature in the Infrared," Journal of Geophysical Research, **72**(16) pp. 4109-4117.

[74] Sturm, J. C., and Reaves, C. M., 1992, "Silicon Temperature Measurement by Infrared Absorption: Fundamental Processes and Doping Effects," IEEE Transactions on Electron Devices, **39**(1) pp. 81-88.

[75] Buffone, C., and Sefiane, K., 2004, "IR Measurements of Interfacial Temperature during Phase Change in a Confined Environment," Experimental Thermal and Fluid Science, **29**(1) pp. 65-74.

[76] Hetsroni, G., Mosyak, A., and Segal, Z., 2001, "Nonuniform Temperature Distribution in Electronic Devices Cooled by Flow in Parallel Microchannels," IEEE Transactions on Components and Packaging Technologies, **24**(1) pp. 16-23.

[77] Chan, C., and Daily, J. W., 1980, "Measurement of Temperature in Flames using Laser Induced Fluorescence Spectroscopy of OH," Applied Optics, **19**(12) pp. 1963-1968.

[78] Omenetto, N., Benetti, P., and Rossi, G., 1972, "Flame Temperature Measurements by Means of Atomic Fluorescence Spectrometry," Spectrochimica Acta, Part A (Molecular Spectroscopy), **27B**(10) pp. 453-61.

[79] Lavieille, P., Lemoine, F., Lavergne, G., 2000, "Temperature Measurements on Droplets in Monodisperse Stream using Laser-Induced Fluorescence," Experiments in Fluids, **29**(5) pp. 429-437.

[80] Sakakibara, J., Hishida, K., and Maeda, M., 1997, "Vortex Structure and Heat Transfer in the Stagnation Region of an Impinging Plane Jet (Simultaneous Measurements of Velocity and Temperature Fields by Digital Particle Image Velocimetry and Laser-Induced Fluorescence)," International Journal of Heat and Mass Transfer, **40**(13) pp. 3163-3176.

[81] Ozturk, S., Hassan, Y. A., and Ugaz, V. M., 2010, "Interfacial Complexation Explains Anomalous Diffusion in Nanofluids," Nano Letters, **10**(2) pp. 665-671.

[82] Hardin, R., Sun, X., and Scime, E. E., 2004, "Three-dimensional laser-induced fluorescence measurements in a helicon plasma," Review of Scientific Instruments, **75**(10) pp. 4103-4105

[83] Chamarthy, P., Garimella, S. V., and Wereley, S. T., 2010, "Measurement of the Temperature Non-Uniformity in a Microchannel Heat Sink using Microscale Laser-Induced Fluorescence," International Journal of Heat and Mass Transfer, **53**(15-16) pp. 3275-3283.

[84] Jamieson, T., Bakhshi, R., Petrova, D., 2007, "Biological Applications of Quantum Dots," Biomaterials, **28**(31) pp. 4717-4732.

[85] Smith, A. M., Duan, H., Mohs, A. M., 2008, "Bioconjugated Quantum Dots for in Vivo Molecular and Cellular Imaging," Advanced Drug Delivery Reviews, **60**(11) pp. 1226-1240.

[86] Resch-Genger, U., Grabolle, M., Cavaliere-Jaricot, S., 2008, "Quantum Dots Versus Organic Dyes as Fluorescent Labels," Nature Methods, **5**(9) pp. 763-775.

[87] Yang, J., Yang, H., and Lin, L., 2011, "Quantum Dot Nano Thermometers Reveal Heterogeneous Local Thermogenesis in Living Cells," ACS Nano, **5**(6) pp. 5067-5071.

[88] Li, S., Zhang, K., Yang, J., 2007, "Single Quantum Dots as Local Temperature Markers," Nano Letters, **7**(10) pp. 3102-3105.

[89] Ahn, H. S., 2007, "Heat Transfer Enhancement in Single-Phase Forced Convection with Blockages and in Two-Phase Pool Boiling with Nano-Structured Surfaces," Ph.D Dissertation, Texas A&M University, College Station.

[90] Sathyamurthi, V., 2009, "Experimental & Numerical Investigation of Pool Boiling on Engineered Surfaces with Integrated Thin Film Temperature Sensors," Ph.D Dissertation, Texas A&M University, College Station.

[91] Singh, N., 2010, "Computational Analysis of Thermo-Fluidic Characteristics of a Carbon Nano-Fin," Ph.D Dissertation, Texas A&M University, College Station..

[92] Sriraman, S. R., 2007, "Pool Boiling on Nano Finned Surfaces," MS. Thesis, Texas A&M University, College Station.

[93] Xia, Y., and Whitesides, G.M., 1998, Annual Reviews Inc, Palo Alto, CA, United States, pp. 153-184. (DOI: 10.1146/annurev.matsci.28.1.153)

[94] Kane, R. S., Takayama, S., Ostuni, E., 1999, "Patterning Proteins and Cells using Soft Lithography," Biomaterials, **20**(23-24) pp. 2363-2376.

[95] Chou, S. Y., Krauss, P. R., and Renstrom, P. J., 1996, "Nanoimprint Lithography," Journal of Vacuum Science & Technology B: Microelectronics Processing and Phenomena, **14**(6) pp. 4129-4129.

[96] Johnson, S. C., 2005, "Step and Flash Imprint Lithography: Materials and Process Development," Ph.D Dissertation, Department of Chemical Engineering, University of Texas at Austin, .

[97] Bodas, D., and Khan-Malek, C., 2006, "Formation of More Stable Hydrophilic Surfaces of PDMS by Plasma and Chemical Treatments," Microelectronic Engineering, **83**(4-9) pp. 1277-1279.

[98] Hong, S. M., Kim, S. H., Kim, J. H., 2006, "Hydrophilic surface modification of PDMS using atmospheric RF plasma," International MEMS Conference 2006, IOP Publishing, UK, **34,** pp. 656-61.

[99] Incropera, F.P., Dewitt, D.P., Bergman, T.L., 2006, "Fundamentals of Heat and Mass Transfer," Wiley, Chichester, UK.

[100] Bergman, T. L., 2009, "Effect of Reduced Specific Heats of Nanofluids on Single Phase, Laminar Internal Forced Convection," International Journal of Heat and Mass Transfer, **52**(5-6) pp. 1240-1244.

[101] Zhou, S., and Ni, R., 2008, "Measurement of the Specific Heat Capacity of Water-Based Al_2O_3 Nanofluid," Applied Physics Letters, **92**(9) pp. 093123-1 - 093123-3.

221

[102] Namburu, P. K., Kulkarni, D. P., Dandekar, A., 2007, "Experimental Investigation of Viscosity and Specific Heat of Silicon Dioxide Nanofluids," Micro and Nano Letters, **2**(3) pp. 67-71.

[103] Shin, D., and Banerjee, D., 2011, "Enhancement of Specific Heat Capacity of High-Temperature Silica-Nanofluids Synthesized in Alkali Chloride Salt Eutectics for Solar Thermal-Energy Storage Applications," International Journal of Heat and Mass Transfer, **54**(5-6) pp. 1064-1070.

[104] Bridges, N. J., Visser, A. E., and Fox, E. B., 2011, "Potential of Nanoparticle-Enhanced Ionic Liquids (NEILs) as Advanced Heat-Transfer Fluids," Energy and Fuels, **25**(10) pp. 4862-4864.

[105] Jung, S., 2012, "Numerical and Experimental Investigation of Inorganic Nanomaterials for Thermal Energy Storage (TES) and Concentrated Solar Power (CSP) Applications," Ph.D Dissertation, Texas A&M University, College Station.

[106] Kline, S. J., and McClintock, F. A., 1953, "Describing Uncertainties in SingleSample Experiments," Mechanical Engineering, **75**(1) pp. 38.

[107] Fox, R.W., Pritchard, P.J., and McDonald, A.T., 2008, "Introduction to fluid mechanics, seventh edition," Wiley, Chichester, UK, pp. xvi+684.

[108] Vajjha, R. S., and Das, D. K., 2009, "Specific Heat Measurement of Three Nanofluids and Development of New Correlations," Journal of Heat Transfer, **131**(7) pp. 1-7.

[109] Ferrouillat, S., Bontemps, A., Ribeiro, J., 2011, "Hydraulic and Heat Transfer Study of SiO2/water Nanofluids in Horizontal Tubes with Imposed Wall Temperature Boundary Conditions," International Journal of Heat and Fluid Flow, **32**(2) pp. 424-439.

[110] Evans, W., Fish, J., and Keblinski, P., 2006, "Role of Brownian Motion Hydrodynamics on Nanofluid Thermal Conductivity," Applied Physics Letters, **88**(9) .

[111] Hamilton, R. L., and Crosser, O. K., 1962, "Thermal Conductivity of Heterogeneous Two-Component Systems," Industrial and Engineering Chemistry -- Fundamentals, **1**(3) pp. 187-191.

222

[112] Ding, Z. W., Cheah, S. C., and Saeid, N. H., 2009, "Parametric study of heat transfer enhancement using nanofluids," 2009 3rd International Conference on Energy and Environment: Advancement Towards Global Sustainability, ICEE 2009, December 7, 2009 - December 8, IEEE Computer Society, Malacca, Malaysia, pp. 294-298.

[113] He, Y., Men, Y., Zhao, Y., 2009, "Numerical Investigation into the Convective Heat Transfer of TiO2 Nanofluids Flowing through a Straight Tube Under the Laminar Flow Conditions," Applied Thermal Engineering, **29**(10) pp. 1965-1972.

[114] Peng, X., Manna, L., Yang, W., 2000, "Shape Control of CdSe Nanocrystals," Nature, (404) pp. 59-61.

[115] Donegá, C. d. M., Bode, M., and Meijerink, A., 2006, "Size- and Temperature-Dependence of Exciton Lifetimes in CdSe Quantum Dots," Physical Review B, **74**(8) pp. 085320.

[116] Sahu, M., Singh, P., Mahapatra, S. S., 2012, "Prediction of Entrance Length for Low Reynolds Number Flow in Pipe using Neuro-Fuzzy Inference System," Expert Systems with Applications, **39**(4) pp. 4545-4557.

[117] Sparrow, E. M., Lin, S. H., and Lundgren, T. S., 1964, "Flow Development in the Hydrodynamic Entrance Region of Tubes and Ducts," Physics of Fluids, **7**(3) pp. 338-347.

[118] Yu, J., Kang, S., Jeon, S., and Banerjee, D., 2012, "Heat Transfer Measurements for Flow of Nanofluids in Microchannels using Temperature Nano-Sensors," Frontiers in Heat and Mass Transfer (FHMT), **3**(013004) .

[119] Jeon, S., Kang, S., and Banerjee, D., 2010, "Investigation of Thermal Characteristics of Nanofluids during Flow in a Micro-channel using an Array of Surface Temperature-nano-sensors," Paper No. SAE-10PSC-0135, SAE Power Systems Conference, November 2-4, Fort Worth, Texas, .

[120] Kang, S., Jeon, S., and Banerjee, D., 2011, "Experimental Study of Thermal Performance of Nanofluids During Flow in Microchannels using Surface Temperature-Nano-Sensors," Paper No. AJTEC2011-44374, 8th Thermal Engineering Joint Conference, March 13-17, Honolulu, Hawaii, .

[121] Yu, J., Kang, S., Jeon, S., 2011, "Investigation of Convective Heat Transfer of Aqueous Nanofluids in Microchannels integrated with temperature nanosensors," Paper No. IMECE2011-64082, Proceedings of the ASME 2011 International Mechanical Engineering Congress & Exposition, November 11-17, Denver, Colorado, .

223

[122] Yarin, L.P., Mosyak, A., and Hetsroni, G., 2009, "Fluid Flow, Heat Transfer and Boiling in Micro-Channels," Springer, pp. 145-194.

[123] Chevalier, J., Tillement, O., and Ayela, F., 2007, "Rheological Properties of Nanofluids Flowing through Microchannels," Applied Physics Letters, **91**(23) .

[124] Murshed, S. M. S., Leong, K. C., and Yang, C., 2008, "Investigations of Thermal Conductivity and Viscosity of Nanofluids," International Journal of Thermal Sciences, **47**(5) pp. 560-568.

[125] Jo, B., 2012, "Numerical and Experimental Investigation of Organic Nanomaterials for Thermal Energy Storage and for Concentrating Solar Power Applications," Ph.D Dissertation, Texas A&M University, College Station.

[126] Chinowsky, T. M., Quinn, J. G., Bartholomew, D. U., 2003, "Performance of the Spreeta 2000 Integrated Surface Plasmon Resonance Affinity Sensor," Sensors and Actuators, B: Chemical, **91**(1-3) pp. 266-274.

[127] Locharoenrat, K., Sano, H., and Mizutani, G., 2007, "Phenomenological Studies of Optical Properties of Cu Nanowires," Science and Technology of Advanced Materials, **8**(4) pp. 277-281.

[128] Lam, K. K., and Newton, J. M., 1992, "Influence of Particle Size on the Adhesion Behaviour of Powders, After Application of an Initial Press-on Force," Powder Technology, **73**(2) pp. 117-125.

[129] Ninham, B. W., Parsegian, V. A., and Weiss, G. H., 1970, "On the Macroscopic Theory of Temperature-Dependent Van Der Waals Forces," Journal of Statistical Physics, **2**(4) pp. 323-8.

[130] Cooper, K., Ohler, N., Gupta, A., 2000, "Analysis of Contact Interactions between a Rough Deformable Colloid and a Smooth Substrate," Journal of Colloid and Interface Science, **222**(1) pp. 63-74.

[131] Suresh, L., and Walz, J. Y., 1996, "Effect of Surface Roughness on the Interaction Energy between a Colloidal Sphere and a Flat Plate," Journal of Colloid and Interface Science, **183**(1) pp. 199-199.

[132] Sun, N., and Walz, J. Y., 2001, "A Model for Calculating Electrostatic Interactions between Colloidal Particles of Arbitrary Surface Topology," Journal of Colloid and Interface Science, **234**(1) pp. 90-105.

[133] Eichenlaub, S., Gelb, A., and Beaudoin, S., 2004, "Roughness Models for Particle Adhesion," Journal of Colloid and Interface Science, **280**(2) pp. 289-298.

[134] Dauber-Osguthorpe, P., Roberts, V. A., Osguthorpe, D. J., 1988, "Structure and Energetics of Ligand Binding to Proteins: Escherichia Colidihydrofolate Reductase-Trimethoprim, a Drug-Receptor System," Proteins, **4**(1) pp. 31-47.

[135] Honda, H., Takamatsu, H., and Wei, J. J., 2002, "Enhanced Boiling of FC-72 on Silicon Chips with Micro-Pin-Fins and Submicron-Scale Roughness," Journal of Heat Transfer, **124**(2) pp. 383-390.

[136] Wu, Z., Chen, H., Dong, Y., 2008, "Cleaning using Nanobubbles: Defouling by Electrochemical Generation of Bubbles," Journal of Colloid and Interface Science, **328**(1) pp. 10-14.

[137] Wang, Y., Li, X., Zhou, Y., 2010, "Preparation of Nanobubbles for Ultrasound Imaging and Intracelluar Drug Delivery," International Journal of Pharmaceutics, **384**(1–2) pp. 148-153.

[138] Suzuki, M., Koshiyama, K., Shinohara, F., 2005, "Nanobubbles Enhanced Drug Susceptibility of Cancer Cells using Ultrasound," International Congress Series, **1284**(0) pp. 338-339.

[139] Ljunggren, S., and Eriksson, J. C., 1997, "The Lifetime of a Colloid-Sized Gas Bubble in Water and the Cause of the Hydrophobic Attraction," Colloids and Surfaces A: Physicochemical and Engineering Aspects, **129–130**(0) pp. 151-155.

[140] Cavicchi, R. E., and Avedisian, C. T., 2007, "Bubble Nucleation and Growth Anomaly for a Hydrophilic Microheater Attributed to Metastable Nanobubbles," Physical Review Letters, **98**(12) .

[141] Attard, P., Moody, M. P., and Tyrrell, J. W. G., 2002, "Nanobubbles: The big picture," Elsevier, **314,** pp. 696-705.

[142] Ishida, N., Inoue, T., Miyahara, M., 2000, "Nano Bubbles on a Hydrophobic Surface in Water Observed by Tapping-Mode Atomic Force Microscopy," Langmuir, **16**(16) pp. 6377-6380.

[143] Lou, S., Ouyang, Z., Zhang, Y., 2000, "Nanobubbles on Solid Surface Imaged by Atomic Force Microscopy," Journal of Vacuum Science and Technology B: Microelectronics and Nanometer Structures, **18**(5) pp. 2573-2575.

[144] Hampton, M. A., and Nguyen, A. V., 2010, "Nanobubbles and the Nanobubble Bridging Capillary Force," Advances in Colloid and Interface Science, **154**(1-2) pp. 30-55.

[145] Zhang, X. H., Zhang, X. D., Lou, S. T., 2004, "Degassing and Temperature Effects on the Formation of Nanobubbles at the mica/water Interface," Langmuir, **20**(9) pp. 3813-3815.

[146] Yang, S., Tsai, P., Kooij, E. S., 2009, "Electrolytically Generated Nanobubbles on Highly Orientated Pyrolytic Graphite Surfaces," Langmuir, **25**(3) pp. 1466-1474.

[147] Zhang, L., Zhang, Y., Zhang, X., 2006, "Electrochemically Controlled Formation and Growth of Hydrogen Nanobubbles," Langmuir, **22**(19) pp. 8109-8113.

[148] Siems, A., Weber, S. A. L., Boneberg, J., 2011, "Thermodynamics of Nanosecond Nanobubble Formation at Laser-Excited Metal Nanoparticles," New Journal of Physics, **13**.

[149] Lukianova-Hleb, E., Kashinath, S., and Lapotko, D. O., 2012, "Plasmonic nanobubbles for cell theranostics," Plasmonics in Biology and Medicine IX, January 22, 2012 - January 24, SPIE, San Francisco, CA, United states, **8234,** pp. The Society of Photo-Optical Instrumentation Engineers (SPIE).

[150] Lukianova-Hleb, E., Hanna, E. Y., Hafner, J. H., 2010, "Tunable Plasmonic Nanobubbles for Cell Theranostics," Nanotechnology, **21**(8) .

[151] Lapotko, D., 2011, "Plasmonic Nanobubbles as Tunable Cellular Probes for Cancer Theranostics," Cancers, **3**pp. 802-840.

[152] Oh, S. H., Kauffmann, Y., Scheu, C., 2005, "Ordered Liquid Aluminum at the Interface with Sapphire," Science, **310**(5748) pp. 661-663.

[153] Yu, C. -., Richter, A. G., Kmetko, J., 2001, "Structure of Interfacial Liquids: X-Ray Scattering Studies," Physical Review E - Statistical, Nonlinear, and Soft Matter Physics, **63**(2) pp. 021205-021201.

[154] Walther, J. H., Jaffe, R., Halicioglu, T., 2001, "Carbon Nanotubes in Water: Structural Characteristics and Energetics," Journal of Physical Chemistry B, **105**(41) pp. 9980-9987.

[155] Li, L., Zhang, Y., Ma, H., 2010, "Molecular Dynamics Simulation of Effect of Liquid Layering Around the Nanoparticle on the Enhanced Thermal Conductivity of Nanofluids," Journal of Nanoparticle Research, **12**(3) pp. 811-821.

[156] Xue, L., Keblinski, P., Phillpot, S. R., 2004, "Effect of Liquid Layering at the Liquid-Solid Interface on Thermal Transport," International Journal of Heat and Mass Transfer, **47**(19-20) pp. 4277-4284.

[157] Shin, D. H., 2011, "Molten Salt Nanomaterials for Thermal Energy Storage and Concentrated Solar Power Applications," Ph.D Dissertation, Texas A&M University, College Station.

[158] Shin, D., and Banerjee, D., 2011, "Enhanced Specific Heat of Silica Nanofluid," Journal of Heat Transfer, **133**(2) .

[159] Ko, G. H., Heo, K., Lee, K., 2007, "An Experimental Study on the Pressure Drop of Nanofluids Containing Carbon Nanotubes in a Horizontal Tube," International Journal of Heat and Mass Transfer, **50**(23-24) pp. 4749-4753.

[160] Abbasian Arani, A. A., and Amani, J., 2012, "Experimental Study on the Effect of TiO2–water Nanofluid on Heat Transfer and Pressure Drop," Experimental Thermal and Fluid Science, **42**(0) pp. 107-115.

[161] Dalton, T., Hodes, M., Eason, C., 2006, "Challenges in using nano-textured surfaces to reduce pressure drop through microchannels," 7th International Conference on Thermal, Mechanical and Multiphysics Simulation and Experiments in Micro-Electronics and Micro-Systems, EuroSimE 2006, April 24, 2006 - April 26, Inst. of Elec. and Elec. Eng. Computer Society, Como, Italy, **2006,** .

[162] Enright, R., Eason, C., Dalton, T., 2006, "Friction factors and nusselt numbers in microchannels with superhydrophobic walls," 4th International Conference on Nanochannels, Microchannels and Minichannels, ICNMM2006, June 19, 2006 - June 21, American Society of Mechanical Engineers, Limerick, Ireland, **2006 A,** pp. 599-609.

[163] Henoch, C., Krupenkin, T. N., Kolodner, P., 2006, "Turbulent drag reduction using superhydrophobic surfaces," 3rd AIAA Flow Control Conference, June 5, 2006 - June 8, American Institute of Aeronautics and Astronautics Inc, San Francisco, CA, United states, **2,** pp. 840-844.

[164] Krupenkin, T. N., Taylor, J. A., Schneider, T. M., 2004, "From Rolling Ball to Complete Wetting: The Dynamic Tuning of Liquids on Nanostructured Surfaces," Langmuir, **20**(10) pp. 3824-3827.

[165] Griffith, T. S., Al-Hadhrami, L., and Han, J., 2003, "Heat Transfer in Rotating Rectangular Cooling Channels (AR = 4) with Dimples," Journal of Turbomachinery, **125**(3) pp. 555-563.

[166] Choi, J., Jeon, W., and Choi, H., 2006, "Mechanism of Drag Reduction by Dimples on a Sphere," Physics of Fluids, **18**(4) .

[167] Holmberg, M., Kuhle, A., Garns, J., 2003, "Nanobubble Trouble on Gold Surfaces," Langmuir, **19**(25) pp. 10510-10513.

[168] Lauga, E., and Brenner, M. P., 2004, "Dynamic Mechanisms for Apparent Slip on Hydrophobic Surfaces," Physical Review E - Statistical, Nonlinear, and Soft Matter Physics, **70**(2) pp. 026311-1-026311-7.

[169] Nagayama, G., Tsuruta, T., and Cheng, P., 2006, "Molecular Dynamics Simulation on Bubble Formation in a Nanochannel," International Journal of Heat and Mass Transfer, **49**(23-24) pp. 4437-4443.

[170] Matsumoto, M., and Tanaka, K., 2008, "Nano Bubble-Size Dependence of Surface Tension and Inside Pressure," Fluid Dynamics Research, **40**(7-8) pp. 546-553.

[171] Venerus, D. C., and Jiang, Y., 2011, "Investigation of Thermal Transport in Colloidal Silica Dispersions (Nanofluids)," Journal of Nanoparticle Research, **13**(7) pp. 3075-3083.

[172] Yang, S., and Duisterwinkel, A., 2011, "Removal of Nanoparticles from Plain and Patterned Surfaces using Nanobubbles," Langmuir, **27**(18) pp. 11430-11435.
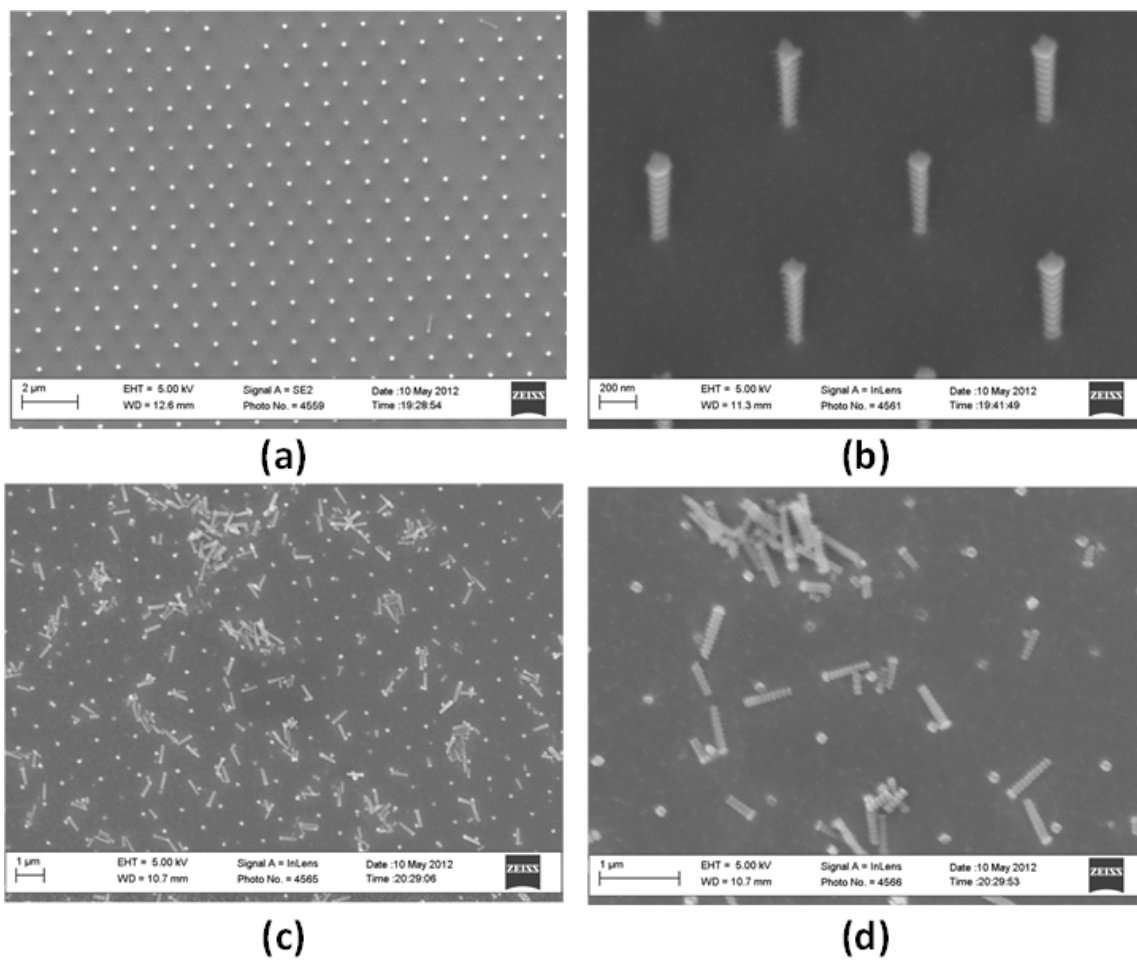
Figure A - 1SEM images: (a) Before piranha cleaning (without tilting), (b) Before piranha cleaning (SEM stage tilted at 35°), (c) After piranha cleaning (without tilting), (d) After piranha cleaning (without tilting 45°)

APPENDIX B : DERIVATION OF NUSSELT NUMBER

- **Governing Equation**

  - Continuity : $\dfrac{\partial u}{\partial x} + \dfrac{\partial v}{\partial y} = 0$

  - X-momentum : $u\dfrac{\partial u}{\partial x} + v\dfrac{\partial u}{\partial y} = -\dfrac{1}{\rho}\dfrac{\partial P}{\partial x} + \upsilon\left(\dfrac{\partial^2 u}{\partial x^2} + \dfrac{\partial^2 u}{\partial y^2}\right)$

  - Energy : $u\dfrac{\partial T}{\partial x} + v\dfrac{\partial T}{\partial y} = \alpha\left(\dfrac{\partial^2 T}{\partial x^2} + \dfrac{\partial^2 T}{\partial y^2}\right)$

- **Hydro-dynamically Fully Developed Condition**

  - $\dfrac{u}{U_{max}} = \dfrac{u-0}{U_{max}-0} = f(y) \neq f(x)$ $\quad\rightarrow\quad$ $\dfrac{\partial u}{\partial x} = 0$

- **Thermally Fully Developed Condition**

  - $\dfrac{T-T_w}{T_b-T_w} = f(y) \neq f(x)$ $\quad\rightarrow\quad$ $\dfrac{\partial}{\partial x}\left(\dfrac{T-T_w}{T_b-T_w}\right) = 0$

- **Simplified Governing Equation**

  - Continuity : $v = 0$

  - X-momentum : $0 = -\dfrac{1}{\rho}\dfrac{\partial P}{\partial x} + \upsilon\dfrac{\partial^2 u}{\partial y^2}$ $\quad\rightarrow\quad$ $0 = -\dfrac{1}{\mu}\dfrac{\partial P}{\partial x} + \dfrac{\partial^2 u}{\partial y^2}$

230

> Energy   : $u\dfrac{\partial T}{\partial x} = \alpha\dfrac{\partial^2 T}{\partial y^2}$

- **Solving Velocity Profile (solve x-momentum equation)**

  ➢ Boundary Conditions

    ▪ $\left.\dfrac{\partial u}{\partial y}\right|_{y=b} = 0$ ---------- B.C. (1)

    ▪ $u(b) = 0$ ---------- B.C. (2)

  ➢ General Solution

    ▪ $u(y) = \dfrac{1}{2\mu}\dfrac{\partial P}{\partial x}y^2 + C_1 y + C_2$

  ➢ Apply Boundary Conditions

    ▪ B.C. (1) : $0 = \dfrac{1}{\mu}\dfrac{\partial P}{\partial x}b + C_1$ → $C_1 = -\dfrac{b}{\mu}\dfrac{\partial P}{\partial x}$

    ▪ B.C. (2) : $0 = \dfrac{1}{2\mu}\dfrac{\partial P}{\partial x}b^2 + C_1 b + C_2$ → $C_2 = \dfrac{b}{\mu}\dfrac{\partial P}{\partial x}\left(1 - \dfrac{b}{2}\right)$

  ➢ Solution

    ▪ $u(y) = \dfrac{1}{2\mu}\dfrac{\partial P}{\partial x}y^2 - \dfrac{b}{\mu}\dfrac{\partial P}{\partial x}y + \dfrac{b}{\mu}\dfrac{\partial P}{\partial x}\left(1 - \dfrac{b}{2}\right)$

    $= -\dfrac{b^2}{2\mu}\dfrac{\partial P}{\partial x}\left[1 - \left(\dfrac{y}{b}\right)^2\right]$

    $= u_{max}\left[1 - \left(\dfrac{y}{b}\right)^2\right]$

➤ Mean Velocity

■ $\bar{u} = \dfrac{\displaystyle\int_{-b}^{b} u(y)\,dy}{\displaystyle\int_{-b}^{b} dy}$

$$= \dfrac{\displaystyle\int_{-b}^{b} u_{max}\left[1-\left(\dfrac{y}{b}\right)^2\right]dy}{2b}$$

$$= \dfrac{u_{max}}{2b}\int_{-b}^{b}\left(1-\dfrac{y^2}{b^2}\right)dy$$

$$= \dfrac{u_{max}}{2b}\left(y-\dfrac{y^3}{3b^2}\right)\Bigg|_{-b}^{b}$$

$$= \dfrac{2}{3}u_{max}$$

➤ Final Soultion

■ $u(y) = \dfrac{3}{2}\bar{u}\left[1-\left(\dfrac{y}{b}\right)^2\right]$

Figure B - 1Modeling of convective heat transfer between two parallel plate

- **Solving Temperature Profile (solve energy equation)**

  ➢ Boundary Conditions

  - $\left.\dfrac{\partial T}{\partial y}\right|_{y=b} = 0$ ---------- B.C. (1)   :

    Insulated Condition

  - $T(0) = T_{CL}$ ---------- B.C. (2)

  ➢ General Solution

  - $u\dfrac{\partial T}{\partial x} = \alpha\dfrac{\partial^2 T}{\partial y^2}$ → $\dfrac{3}{2}\bar{u}\left[1-\left(\dfrac{y}{b}\right)^2\right]\dfrac{\partial T}{\partial x} = \alpha\dfrac{\partial^2 T}{\partial y^2}$

  ➢ Apply Boundary Conditions

  - B.C. (1) : $0 = \dfrac{3\bar{u}}{2\alpha}\dfrac{\partial T}{\partial x}\left[b - \dfrac{1}{3}\dfrac{b^3}{b^2}\right] + C_1$ → $C_1 = \dfrac{3\bar{u}}{2\alpha}\dfrac{\partial T}{\partial x}\left(-\dfrac{2}{3}b\right)$

  - B.C. (2) : $T_{CL} = C_2$ → $C_2 = T_{CL}$

233

> Solution

- $$T(y) = \frac{3\bar{u}}{2\alpha}\frac{\partial T}{\partial x}\left[\frac{y^2}{2} - \frac{1}{12}\frac{y^4}{b^2}\right] + \frac{3\bar{u}}{2\alpha}\frac{\partial T}{\partial x}\left(-\frac{2}{3}b\right)y + T_{CL}$$

$$= \frac{3\bar{u}b^2}{2\alpha}\frac{\partial T}{\partial x}\left[\frac{1}{2}\left(\frac{y^2}{b^2}\right) - \frac{1}{12}\left(\frac{y^4}{b^4}\right) - \frac{2}{3}\left(\frac{y}{b}\right)\right] + T_{CL}$$

> Bulk Mean Temperature

- $$T_b = \frac{\displaystyle\int_{-b}^{b}\rho c_p u(y)T(y)dy}{\displaystyle\int_{-b}^{b}\rho c_p u(y)dy}$$

$$= \frac{\displaystyle\int_{-b}^{b}\frac{3}{2}\bar{u}\left[1-\left(\frac{y}{b}\right)^2\right]\frac{3\bar{u}b^2}{2\alpha}\frac{\partial T}{\partial x}\left[\frac{1}{2}\left(\frac{y^2}{b^2}\right) - \frac{1}{12}\left(\frac{y^4}{b^4}\right) - \frac{2}{3}\left(\frac{y}{b}\right)\right]dy}{\displaystyle\int_{-b}^{b}\frac{3}{2}\bar{u}\left[1-\left(\frac{y}{b}\right)^2\right]dy} + T_{CL}$$

$$= \frac{3\bar{u}b^2}{2\alpha}\frac{\partial T}{\partial x}\frac{\displaystyle\int_{-b}^{b}\left[\frac{1}{2}\left(\frac{y^2}{b^2}\right) - \frac{1}{12}\left(\frac{y^4}{b^4}\right) - \frac{2}{3}\left(\frac{y}{b}\right) - \frac{1}{2}\left(\frac{y^4}{b^4}\right) + \frac{1}{12}\left(\frac{y^6}{b^6}\right) + \frac{2}{3}\left(\frac{y^3}{b^3}\right)\right]dy}{\displaystyle\int_{-b}^{b}\left[1-\left(\frac{y}{b}\right)^2\right]dy} + T_{CL}$$

$$= \frac{3\bar{u}b^2}{2\alpha}\frac{\partial T}{\partial x}\frac{\left[\frac{1}{6}\frac{y^3}{b^2} - \frac{1}{60}\frac{y^5}{b^4} - \frac{1}{3}\frac{y^2}{b} - \frac{1}{10}\frac{y^5}{b^4} + \frac{1}{84}\frac{y^7}{b^6} + \frac{2}{12}\frac{y^4}{b^3}\right]_{-b}^{b}}{\left[y - \frac{1}{3}\frac{y^3}{b^2}\right]_{-b}^{b}} + T_{CL}$$

234

$$= \frac{3\bar{u}b^2}{2\alpha} \frac{\partial T}{\partial x} \frac{\frac{1}{6} - \frac{1}{60} - \frac{1}{10} + \frac{1}{84}}{1 - \frac{1}{3}} + T_{CL}$$

$$= \frac{3\bar{u}b^2}{2\alpha} \frac{\partial T}{\partial x} \frac{\frac{70 - 7 - 42 + 5}{420}}{\frac{2}{3}} + T_{CL}$$

$$= \frac{3\bar{u}b^2}{2\alpha} \frac{\partial T}{\partial x} \frac{13}{140} + T_{CL}$$

➢ Wall Temperature

- $T_w = T(-b) = \dfrac{3\bar{u}b^2}{2\alpha} \dfrac{\partial T}{\partial x} \left[\dfrac{1}{2} - \dfrac{1}{12} + \dfrac{2}{3} \right] + T_{CL} = \dfrac{3\bar{u}b^2}{2\alpha} \dfrac{\partial T}{\partial x} \dfrac{13}{12} + T_{CL}$

- $T_w - T_b = \left[\dfrac{3\bar{u}b^2}{2\alpha} \dfrac{\partial T}{\partial x} \dfrac{13}{12} + T_{CL} \right] - \left[\dfrac{3\bar{u}b^2}{2\alpha} \dfrac{\partial T}{\partial x} \dfrac{13}{140} + T_{CL} \right] = \dfrac{3\bar{u}b^2}{2\alpha} \dfrac{\partial T}{\partial x} \dfrac{104}{105}$

- **Conditions when Uniform Heat Flux is applied…**

➢ $q_w^{"} = h\left(T_w - T_b \right)$

➢ $T_w - T_b = \dfrac{q_w^{"}}{h}$

➢ $\dfrac{\partial T_w}{\partial x} - \dfrac{\partial T_b}{\partial x} = 0$

➢ $\dfrac{\partial T_w}{\partial x} = \dfrac{\partial T_b}{\partial x}$

➢ $\dfrac{\partial}{\partial x} \left(\dfrac{T - T_w}{T_b - T_w} \right) = 0$ → $\dfrac{\partial T_w}{\partial x} = \dfrac{\partial T_b}{\partial x} = \dfrac{\partial T}{\partial x} = c$: Thermally Fully Developed

235

- **Calculation of Nusselt Number**

$$q_w'' \cdot w \cdot dx = \frac{\partial}{\partial x}\left(\rho \bar{u} A c_p T_b\right) dx = \rho \bar{u}\left(2bw\right) c_p \frac{\partial T_b}{\partial x} dx$$

$$q_w'' = 2\rho \bar{u} b c_p \frac{\partial T_b}{\partial x} = h\left(T_w - T_b\right)$$

$$2\rho \bar{u} b c_p \frac{\partial T_b}{\partial x} = h \frac{3\bar{u}b^2}{2\alpha} \frac{\partial T}{\partial x} \frac{104}{105}$$

$$h = \frac{105}{104} \frac{4k}{3b} = 1.346 \frac{k}{b}$$

$$Nu = \frac{hD_h}{k} = \frac{h\left(4b\right)}{k} = 5.384$$

APPENDIX C : ANALYTIC CALCULATION OF PURE CONDUCTION UNDER
CONSTANT WALL TEMPERATURE BOUNDARY CONDITION

Q″ = 0

$\theta_{in} = T_{in} - T_{in} = 0$

H

L

$\theta_{out} = T_{out} - T_{in}$

$\theta_w = T_w - T_{in}$
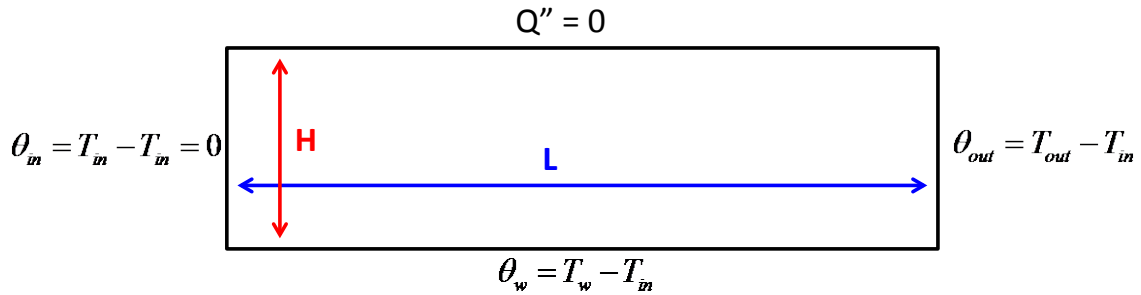
Figure C - 1 Modeling and boundary conditions (constant wall temperature) for analytic calculation of pure conduction without any flow in the microchannel

- **Governing Equation& Boundary Conditions**

  ➢ $\dfrac{\partial^2 \theta}{\partial x^2} + \dfrac{\partial^2 \theta}{\partial y^2} = 0$

  - $\theta(0, y) = 0$ ---------- B.C. (1)
  - $\theta(L, y) = \theta_{out}$ ---------- B.C. (2)
  - $\theta(x, 0) = \theta_w$ ---------- B.C. (3)
  - $\dfrac{\partial \theta}{\partial y}(x, H) = 0$ ---------- B.C. (4)

- **Modified equation (θ = θ₁ + θ₂)**

  ➢ $\dfrac{\partial^2 \theta_1}{\partial x^2} + \dfrac{\partial^2 \theta_1}{\partial y^2} = 0$

  - $\theta_1(0, y) = 0$ ---------- B.C. (1)
  - $\theta_1(L, y) = 0$ ---------- B.C. (2)

237

- $\theta_1(x,0) = \theta_w$ --------- B.C. (3)

- $\dfrac{\partial \theta_1}{\partial y}(x,H) = 0$ --------- B.C. (4)

➢ $\dfrac{\partial^2 \theta_2}{\partial x^2} + \dfrac{\partial^2 \theta_2}{\partial y^2} = 0$

- $\theta_2(0,y) = 0$ --------- B.C. (1)

- $\theta_2(L,y) = \theta_{out}$ --------- B.C. (2)

- $\theta_2(x,0) = 0$ --------- B.C. (3)

- $\dfrac{\partial \theta_2}{\partial y}(x,H) = 0$ --------- B.C. (4)

- **Solution**

➢ $\theta_1(x,y) = \sum A_n \sin\left(\dfrac{n\pi}{L} x\right) \cosh\left[\dfrac{n\pi}{L}(H-y)\right]$

- $A_n = \dfrac{\theta_w \int_0^L \sin\left(\dfrac{n\pi}{L} x\right) dx}{\cosh\left(\dfrac{n\pi H}{L}\right)\int_0^L \sin^2\left(\dfrac{n\pi}{L} x\right) dx} = \dfrac{2\theta_w}{n\pi} \dfrac{1-(-1)^n}{\cosh\left(\dfrac{n\pi H}{L}\right)}$

➢ $\theta_2(x,y) = \sum B_n \sin\left(\dfrac{(2n-1)\pi}{2H} y\right) \sinh\left(\dfrac{(2n-1)\pi}{2H} x\right)$

- $B_n = \dfrac{\theta_{out} \int_0^H \sin\left(\dfrac{(2n-1)\pi}{2H} y\right) dy}{\sinh\left(\dfrac{(2n-1)\pi L}{2H}\right)\int_0^H \sin^2\left(\dfrac{(2n-1)\pi}{2H} y\right) dy} = \dfrac{4\theta_{out}}{(2n-1)\pi} \dfrac{1}{\sinh\left(\dfrac{(2n-1)\pi L}{2H}\right)}$

- **Heat flux at the wall (Equation C1)**

$$q_w^{"} = -k\frac{\partial T}{\partial y}\bigg|_{y=0} = -k\frac{\partial \theta}{\partial y}\bigg|_{y=0}$$

$$= -k\left[\sum A_n \frac{-n\pi}{L}\sin\left(\frac{n\pi}{L}x\right)\sinh\left(\frac{n\pi H}{L}\right) + \sum B_n \frac{(2n-1)\pi}{2H}\sinh\left(\frac{(2n-1)\pi}{2H}x\right)\right]$$

APPENDIX D :AXIAL CONDUCTION IN THE FLUID

The energy equation for steady state incompressible flow in a tube with constant physical properties is expressed as follows with an assumption that energy dissipation is negligible [122].

$$\rho u c_p \frac{\partial T}{\partial x} = k \left\{ \frac{1}{r} \frac{\partial}{\partial r} \left(r \frac{\partial T}{\partial r} \right) + \frac{\partial^2 T}{\partial x^2} \right\}$$

In this equation, ρ, c_p, and k represents density, specific heat capacity, and thermal conductivity of a fluid, respectively. Also, x and r are the longitudinal and radial coordinates. Following dimensionless variables can be introduced under constant heat flux boundary conditions.

$$\tilde{u} = \frac{u}{U_{ax}}, \quad R = \frac{r}{r_0}, \quad X^+ = \frac{2}{Pe} \frac{x}{d}, \quad \theta = \frac{T - T_0}{qd/k}$$

Pèclet number, Pe, is defined as $Pe = \frac{Ud}{\alpha}$ where $U = \frac{U_{ax}}{2}$ is the average velocity (U_{ax} is axial velocity) and $d = 2r_0$. T_0 and q represents the fluid temperature at the inlet and heat flux on the wall, respectively. The original equation becomes dimensionless equation as follows:

$$\tilde{u} \frac{\partial \theta}{\partial X^+} = \frac{1}{R} \frac{\partial}{\partial R} \left(R \frac{\partial \theta}{\partial R} \right) + \frac{1}{Pe^2} \frac{\partial^2 \theta}{\partial X^{+2}}$$

When it is assumed that (1) the exit of microchannel is adiabatic and (2) θ is a weak function of R, the solution of dimensionless equation is:

$$\frac{\partial^2 \bar{\theta}}{\partial X^{+2}} - \frac{1}{4} Pe^2 \frac{\partial \bar{\theta}}{\partial X^+} + \frac{1}{2} Pe^2 = 0$$

where $\bar{\theta}\left(= \int_0^1 \theta R dR\right)$ is the average temperature. The solution of this equation is as

follows under adiabatic boundary condition at the outlet.

$$\bar{\theta} = C + C\exp\left(\frac{Pe^2}{4}X^+\right) + 2X^+, \quad C = -\frac{2}{\left(Pe^2/4\right)}\exp\left(-\frac{Pe^2}{4}X_{outlet}^+\right)$$

Dimensionless parameter, $M = \left|\dfrac{q_{cond}}{q_{conv}}\right|$, is introduced to express the contribution ratio of

heat flux due conduction and convection.

$$q_{conv} = \rho U c_p \left(T - T_0\right)$$

$$q_{cond} = -k \frac{dT}{dx}$$

by substituting the above result,

$$M = \frac{1}{4} \frac{1 - \exp\left(\chi^+ - \chi_{outlet}^+\right)}{\chi^+ - \exp\left(\chi^+ - \chi_{outlet}^+\right) + \exp\left(-\chi_{outlet}^+\right)}$$

where $\chi^+ = \dfrac{Pe^2 X^+}{4}$. Dimensionless parameter χ+ is very large. To illustrate, the order

of magnitude of this parameter is ~1000 for the microchannel used in the current study.

$$\chi_{outlet}^+ = \frac{Pe^2 X_{outlet}^+}{4} = \frac{Pe}{2} \frac{L}{d} \sim 1000 \gg 1$$

Considering χ_{outlet}^+ is larger than χ^+, exponential terms become negligible and following

equation is obtained.

$$M \approx \frac{1}{4}\frac{1}{\chi^+}$$

The last equation shows that heat conduction is very significant compared to convection near the entrance of the microchannel. The temperature difference between wall and fluid becomes larger due to the existence of heat conduction along axial direction of the flow. In addition, axial conduction contributes on decreasing value of Nusselt number at the entrance.

APPENDIX E : FLOW BOILING IN A MICROCHANNEL

The current study can be extended to studies on phase-change heat transfer (flow boiling in micro-channels). By increasing input power into the heater, the temperature of the wafer was increased to exceed the saturation temperature of water. Flow boiling experiments in a microchannel were conducted using exactly the same apparatus and nanofluids (i.e., titania nanoparticles at a mass concentration of 0.001%). The results are shown in Figure E - 1and Table E - 1. Heat flux values are calculated using equation (27) and maximum measurement uncertainty evaluated using Kline and McClintock method [106] is 16.1 %.

Table E - 1 Heat flux [W/m^2] values for flow boiling experiments in the microchannel using different working fluids

Voltage In	Flow Rate [µl/min]	DIW	TiO$_2$ 0.001 wt. %	DIW after TiO$_2$
	5	184.9	203.1	246.4
47.5V	10	375.8	618.6	681.5
	15	868.0	1170.7	1179.5
	5	94.0	260.7	245.6
50.0 V	10	606.3	697.4	533.8
	15	1114.5	1106.5	686.0
	5	206.2	251.9	234.2
52.5V	10	574.9	711.8	760.1
	15	1188.3	1520.7	1322.1
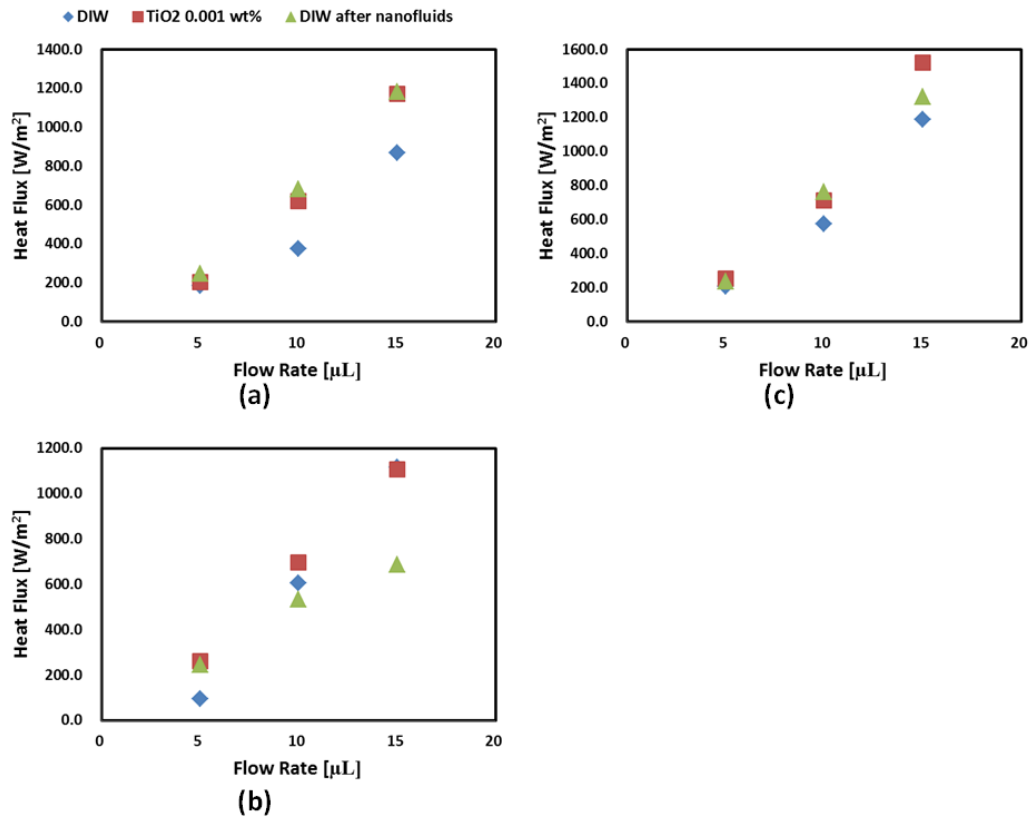
Figure E - 1 Removed heat flux values for input voltage (a) 47.5 V, (b) 50.0 V, and (c) 52.5 V

Heat flux values for DIW experiments are shown to be higher than the corresponding values without phase change. Also, nanofluids yielded higher heat flux values compared to the base fluid (DIW) as can be easily seen in this figure and table. Furthermore, the when the control experiments were repeated after the nanofluids experiments, similar heat flux values (to that of the nanofluids experiments) were obtained – except for the experiments performed for an input voltage of 50.0 V. In other words, DIW showed different values of heat flux depending on the sequence of the experiments. These results show that for flow boiling experiments in microchannels, the experiments performed

244

with nanofluids and pure solvent (control experiments) display similar behavior to that of the experiments without phase change. Hence the nanofin effect is found to exist even for flow boiling configurations.

SEM images obtained for the heat exchanging surface with the intent of observing the level of precipitation of the nanoparticles after the completion of all the experiments are shown in Figure E - 2 and Figure E - 3. In the images nanoparticle precipitates are observed both near the TFT junctions and away from the TFT junctions. In addition, materials characterization of the precipitates using EDX confirms that the precipitates have the same composition as the nanoparticles (not impurities). This is confirmed from the existence of Ti peak in the EDX results.
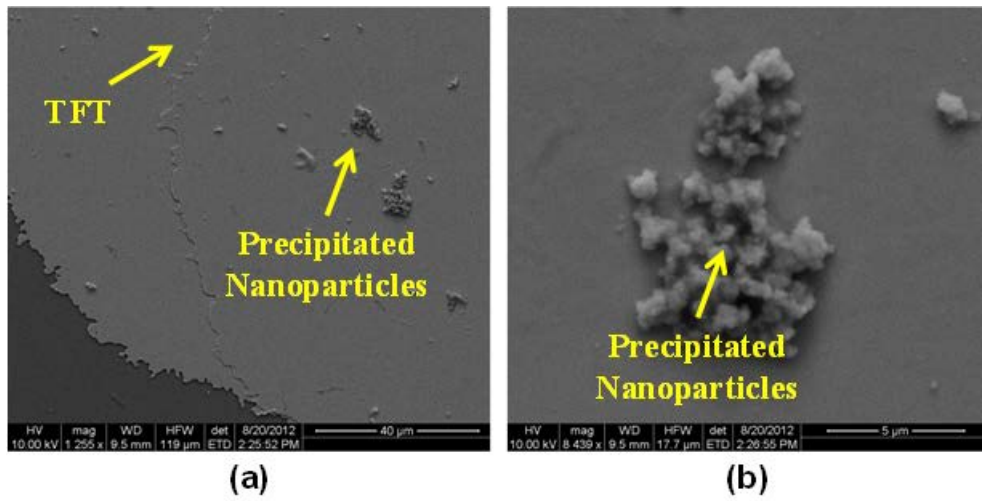
Figure E - 2 SEM images showing the precipitation of the nanoparticles at the region of TFT junction at the magnification of (a) 1255X and (b) 8439X and corresponding EDX result
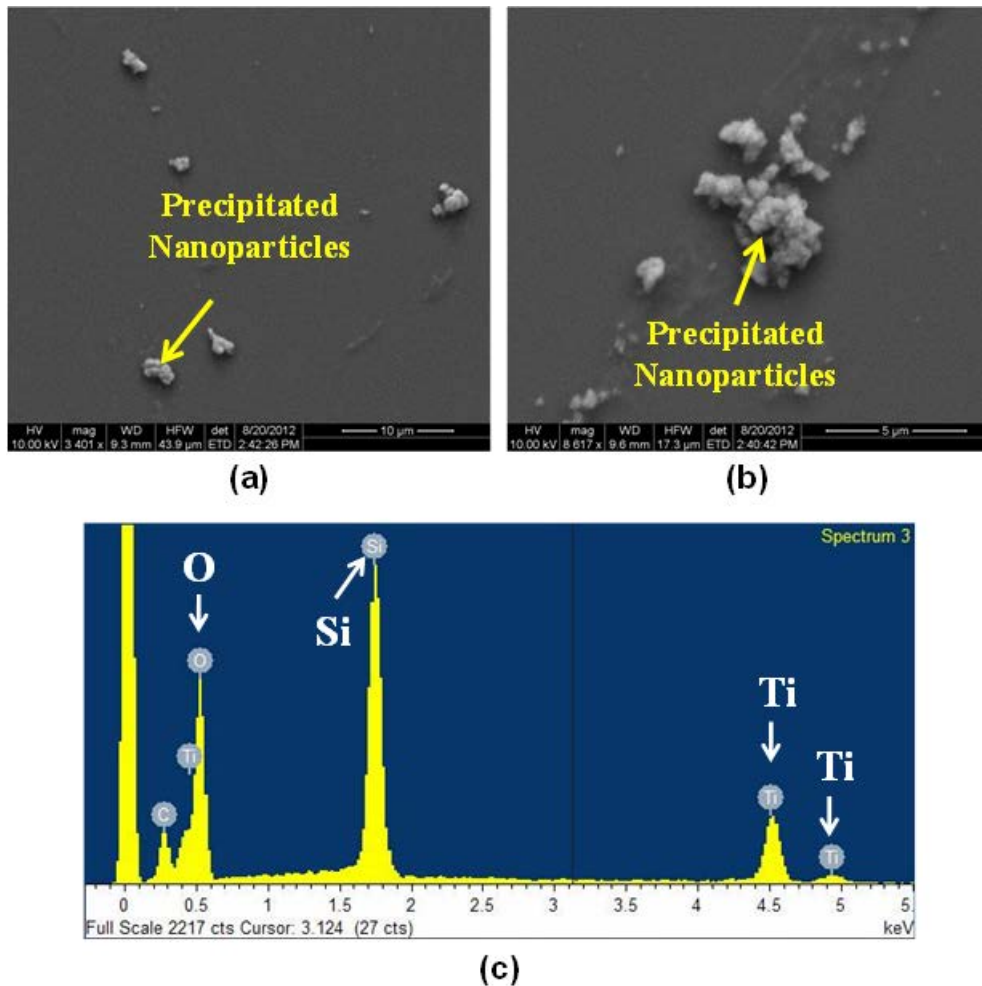
Figure E - 3 SEM images showing the precipitation of the nanoparticles at the region away from TFT junction at the magnification of (a) 3401X and (b) 8617X and corresponding EDX result

Figure E - 4 to Figure E - 12show the pictures obtained during the flow boiling experiments. These images demonstrate the morphology of the bubbles in the microchannel (i.e., bubbly flow and primarily slug flow).

(a)

(b)

(c)

248
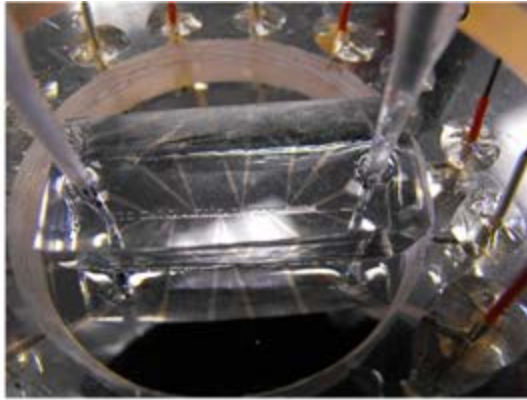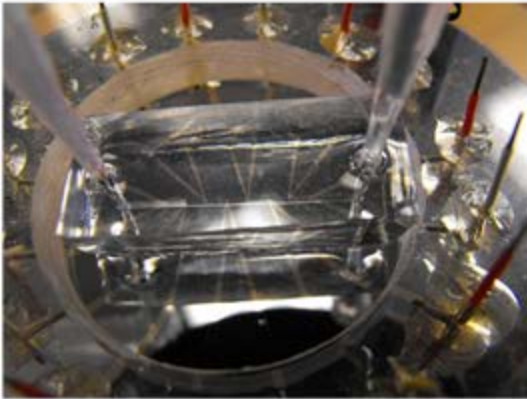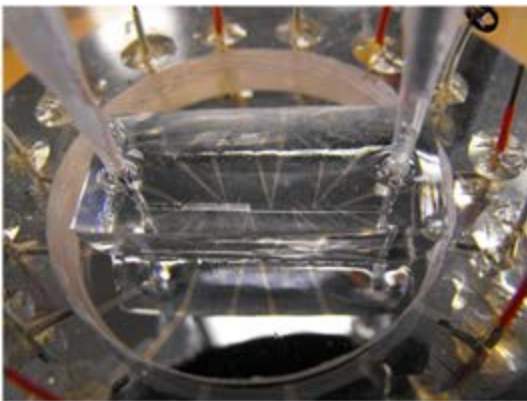
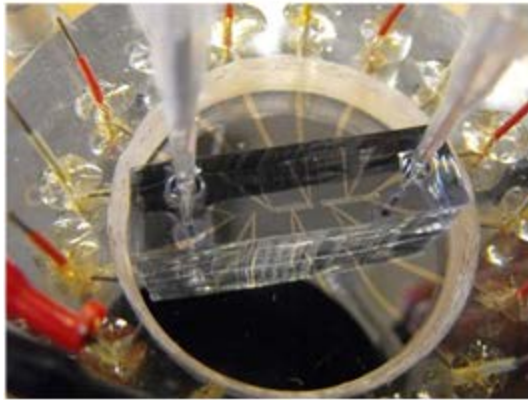**Figure E - 4Pictures showing bubbles in the microchannel for DIW at the flow rate of (a, d) 5 µl/min, (b, e) 10 µl/min, and (c, f) 15 µl/min when input voltage is 47.5 V**
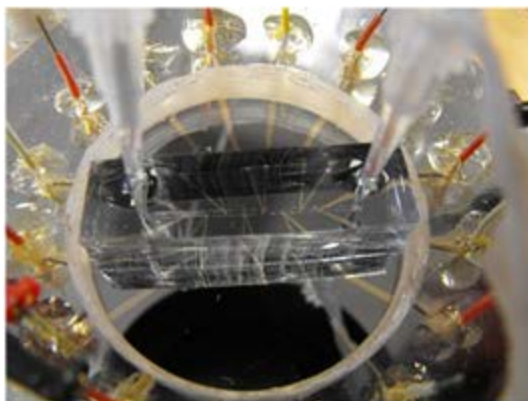
(a)

(b)

(c)

250
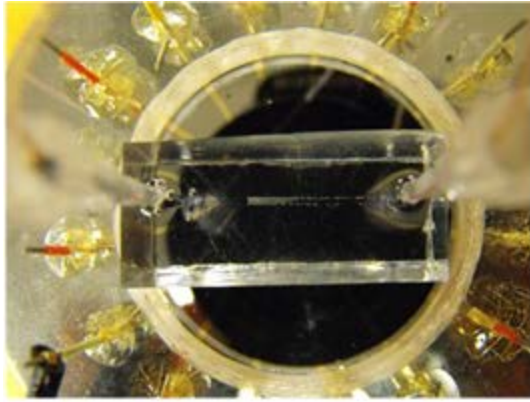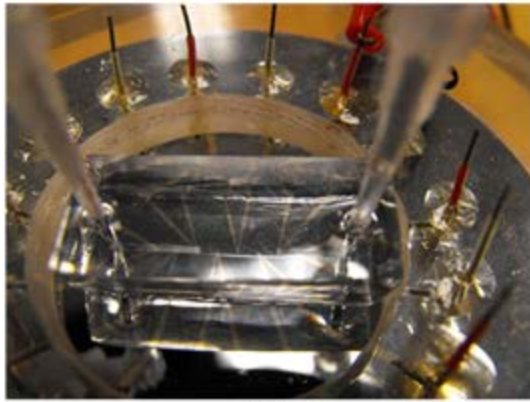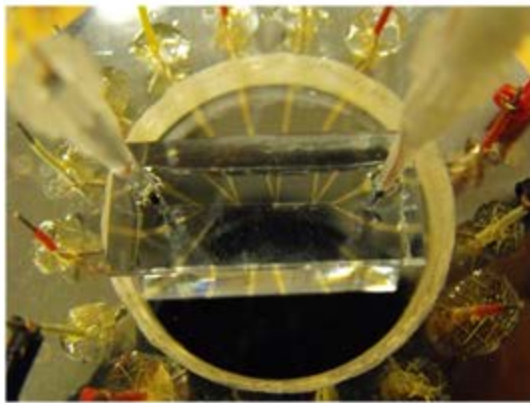
Figure E - 5 Pictures showing bubbles in the microchannel for DIW at the flow rate of (a, d) 5 µl/min, (b, e) 10 µl/min, and (c, f) 15 µl/min when input voltage is 50.0 V

(a)

(b)

(c)
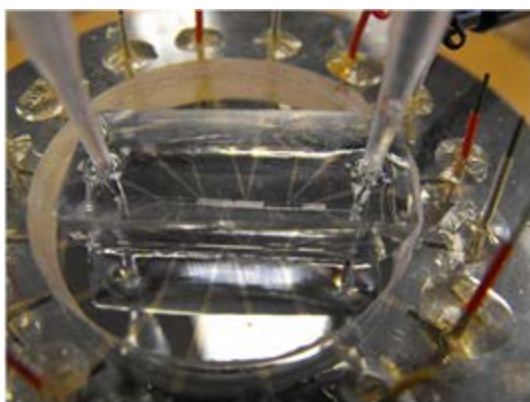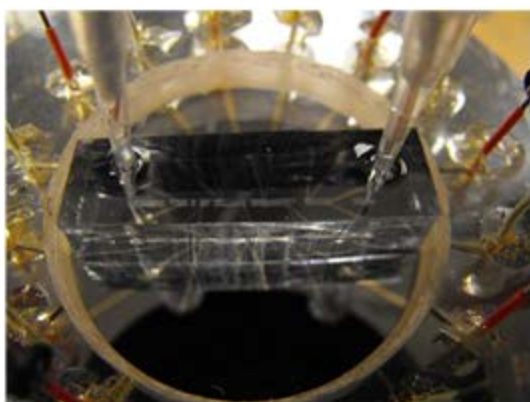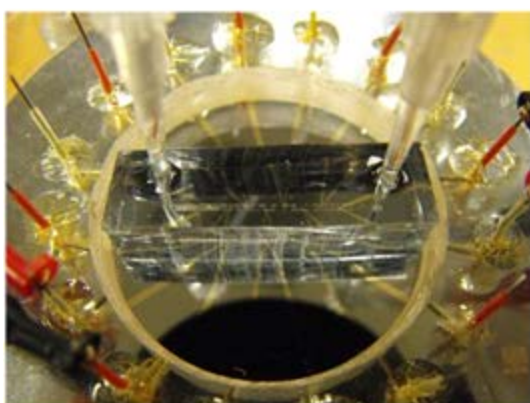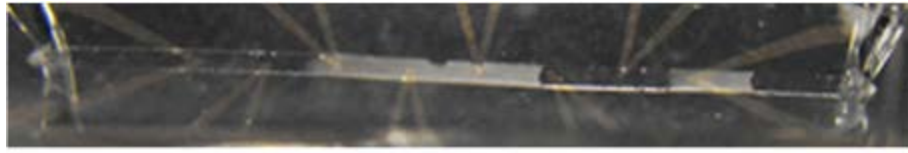
Figure E - 6 Pictures showing bubbles in the microchannel for DIW at the flow rate of (a, d) 5 µl/min, (b, e) 10 µl/min, and (c, f) 15 µl/min when input voltage is 52.5 V

(a)

(b)

(c)
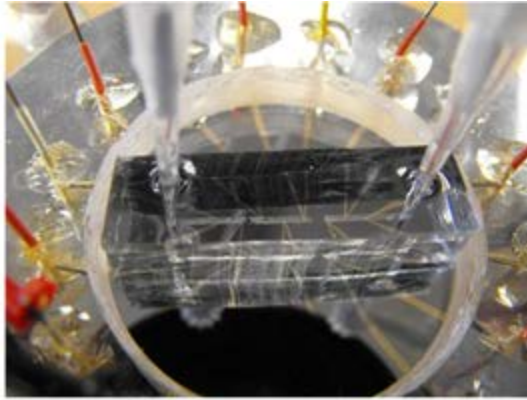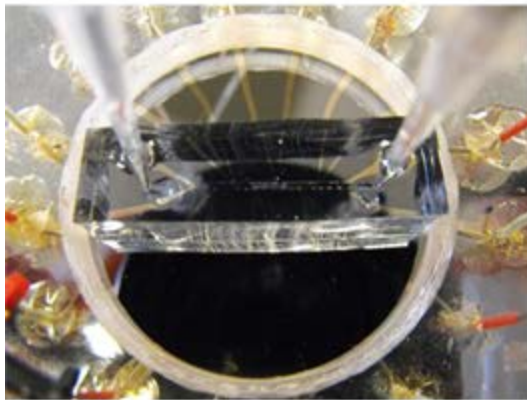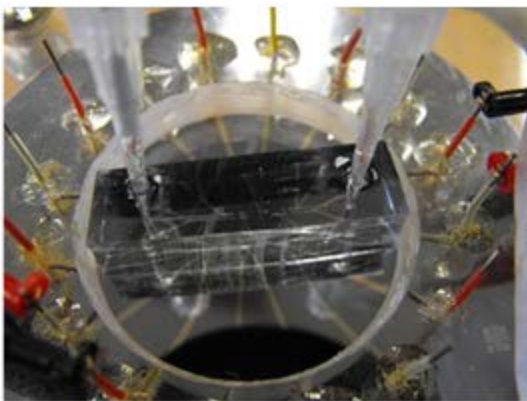
Figure E - 7 Pictures showing bubbles in the microchannel for TiO$_2$ 0.001 wt. % nanofluids at the flow rate of (a, d) 5 μl/min, (b, e) 10 μl/min, and (c, f) 15 μl/min when input voltage is 47.5 V
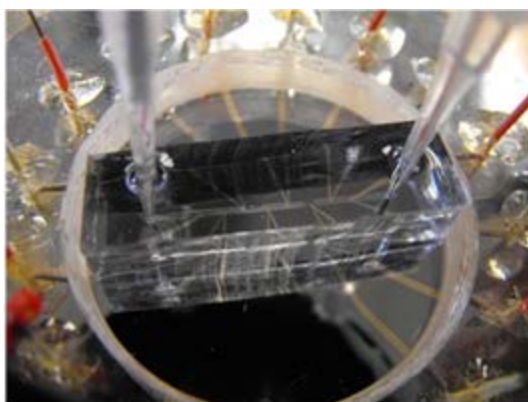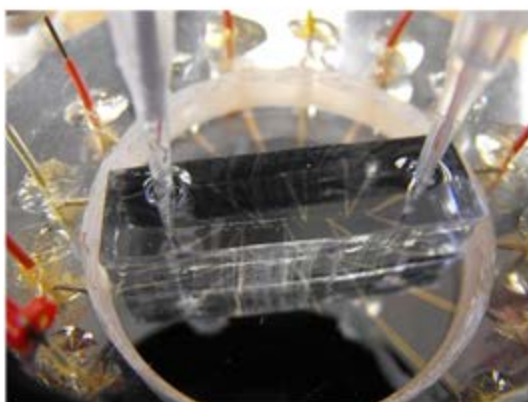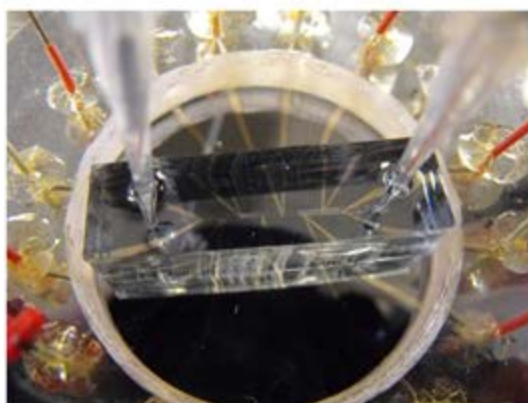
(a)

(b)

(c)

256
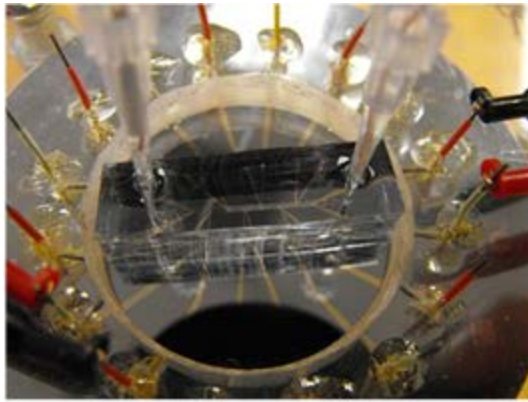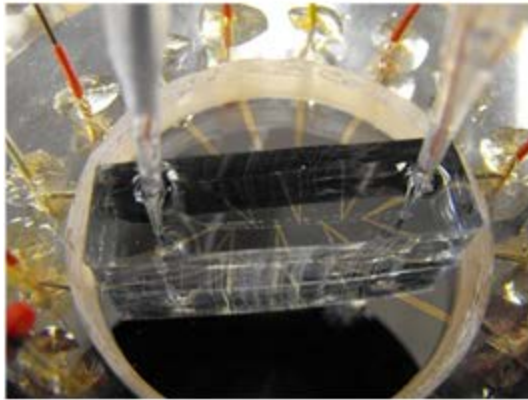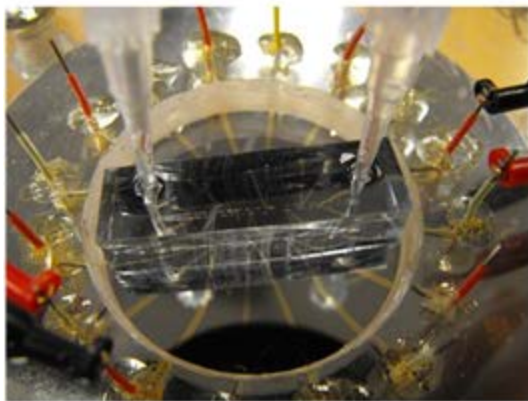
(d)

(e)

(f)

**Figure E - 8 Pictures showing bubbles in the microchannel for TiO$_2$ 0.001 wt. %
nanofluids at the flow rate of (a, d) 5 μl/min, (b, e) 10 μl/min, and (c, f) 15 μl/min
when input voltage is 50.0 V**

(a)

(b)

(c)
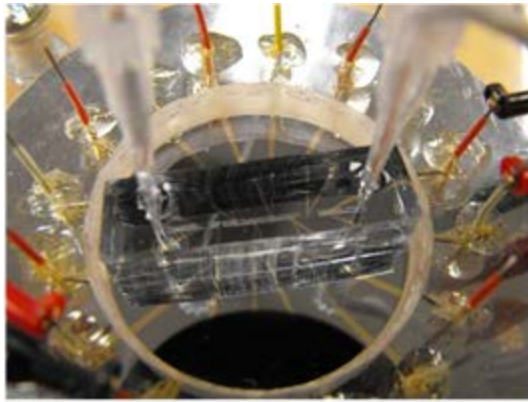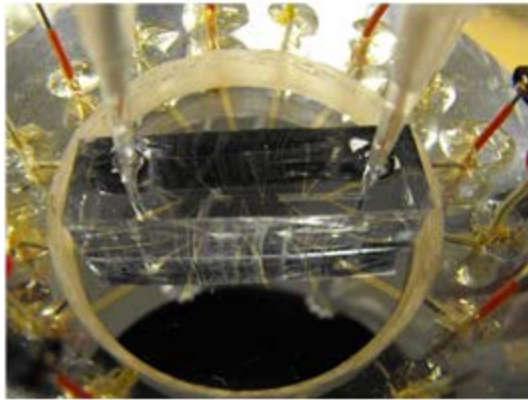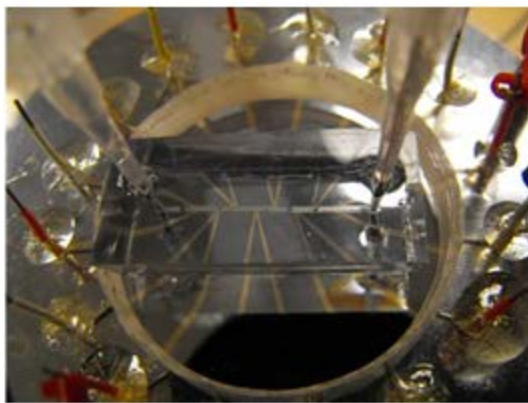
**Figure E - 9 Pictures showing bubbles in the microchannel for TiO$_2$ 0.001 wt. %
nanofluids at the flow rate of (a, d) 5 µl/min, (b, e) 10 µl/min, and (c, f) 15 µl/min
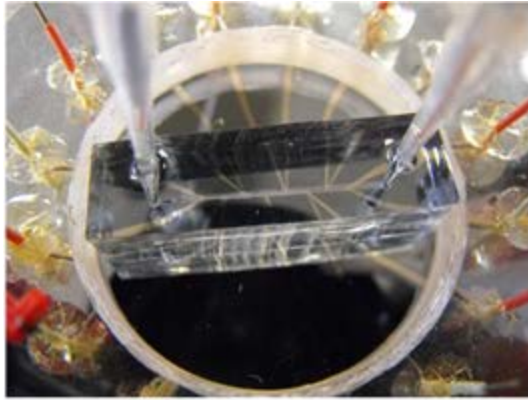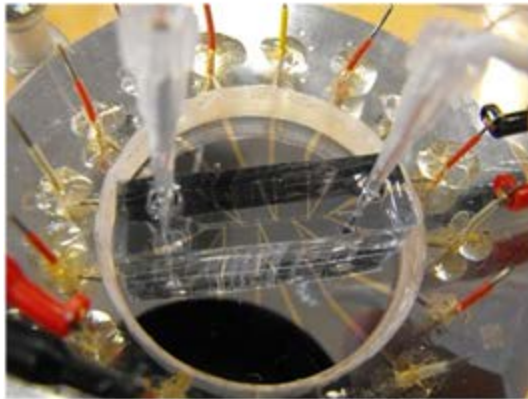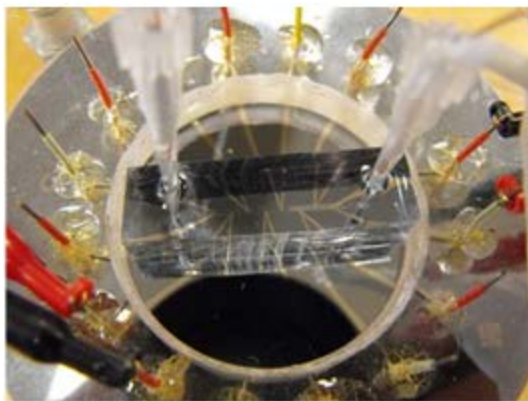when input voltage is 52.5 V**

(a)

(b)

(c)
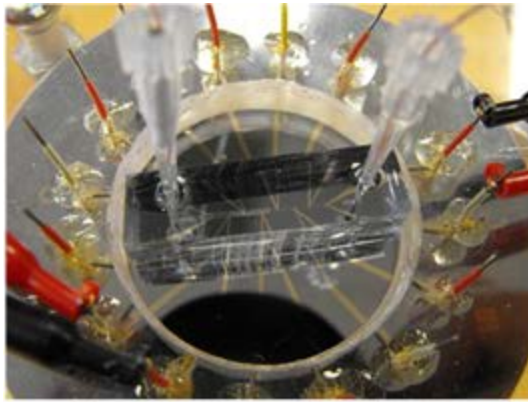
Figure E - 10 Pictures showing bubbles in the microchannel for DIW after nanofluids experiments at the flow rate of (a, d) 5 µl/min, (b, e) 10 µl/min, and (c, f) 15 µl/min when input voltage is 47.5 V

(a)

(b)

(c)

Figure E - 11 Pictures showing bubbles in the microchannel for DIW after nanofluids experiments at the flow rate of (a, d) 5 µl/min, (b, e) 10 µl/min, and (c, f) 15 µl/min when input voltage is 50.0 V

(a)

(b)

(c)

(d)

(e)

(f)

Figure E - 12 Pictures showing bubbles in the microchannel for DIW after nanofluids experiments at the flow rate of (a, d) 5 µl/min, (b, e) 10 µl/min, and (c, f) 15 µl/min when input voltage is 52.5 V